

¹ Observation of the Higgs boson in the WW^*
² channel and search for Higgs boson pair
³ production in the $b\bar{b}b\bar{b}$ channel with the
⁴ ATLAS detector

⁵ A DISSERTATION PRESENTED
⁶ BY
⁷ TOMO LAZOVICH
⁸ TO
⁹ THE DEPARTMENT OF PHYSICS

¹⁰ IN PARTIAL FULFILLMENT OF THE REQUIREMENTS
¹¹ FOR THE DEGREE OF
¹² DOCTOR OF PHILOSOPHY
¹³ IN THE SUBJECT OF
¹⁴ PHYSICS

¹⁵ HARVARD UNIVERSITY
¹⁶ CAMBRIDGE, MASSACHUSETTS
¹⁷ MAY 2016

¹⁸ ©2016 – TOMO LAZOVICH

¹⁹ ALL RIGHTS RESERVED.

20 **Observation of the Higgs boson in the WW^* channel and search
 21 for Higgs boson pair production in the $b\bar{b}b\bar{b}$ channel with the
 22 ATLAS detector**

23 ABSTRACT

24 This dissertation presents two studies: the observation and measurement of the Higgs boson in the
 25 $H \rightarrow WW^* \rightarrow \ell\nu\ell\nu$ channel at $\sqrt{s} = 7$ TeV and $\sqrt{s} = 8$ TeV and a search for Higgs pair pro-
 26 duction in the $HH \rightarrow b\bar{b}b\bar{b}$ channel at $\sqrt{s} = 13$ TeV with the ATLAS detector in pp collisions at the
 27 Large Hadron Collider.

28 First, the discovery of a particle consistent with the Higgs in 4.8 fb^{-1} at $\sqrt{s} = 7$ TeV and 5.8 fb^{-1} at
 29 $\sqrt{s} = 8$ TeV is discussed. Then, the measurement of the Higgs boson signal strength and cross section
 30 in both the gluon fusion and vector boson fusion (VBF) production modes using 20.3 fb^{-1} of $\sqrt{s} =$
 31 8 TeV data combined with 4.8 fb^{-1} of 7 TeV data is shown. The combined signal strength is measured
 32 to be $\mu = 1.09^{+0.23}_{-0.21}$. The total observed significance of the $H \rightarrow WW^*$ process is observed to be
 33 6.1σ (with 5.8σ expected). Advanced methods for background reduction and estimation, particularly in
 34 same-flavor lepton final states, are shown. The VBF signal strength is measured to be $\mu_{\text{VBF}} = 1.27^{+0.53}_{-0.45}$
 35 with an observed significance of 3.2σ (with 2.7σ expected). In the VBF channel, a selection requirement
 36 based method, the precursor to the final multivariate technique used for the result, is detailed.

37 Finally, a search for Higgs pair production in the $b\bar{b}b\bar{b}$ final state with 3.2 fb^{-1} at $\sqrt{s} = 13$ TeV
 38 is presented. A particular focus is placed on a tailored signal region for resonant production of Higgs
 39 pairs at high masses, utilizing novel techniques in object reconstruction to increase signal acceptance in
 40 boosted final state topologies. No significant excesses are observed, and upper limits on cross sections are
 41 placed for spin-2 Randall Sundrum gravitons (RSG) and narrow spin-0 resonances. The cross section of
 42 $\sigma(pp \rightarrow G_{\text{KK}}^* \rightarrow hh \rightarrow b\bar{b}b\bar{b})$ with $k/\bar{M}_{\text{Pl}} = 1$ is constrained to be less than 70 fb for masses in the
 43 range $600 < m_{G_{\text{KK}}^*} < 3000 \text{ GeV}$. For the RSG model with $k/\bar{M}_{\text{Pl}} = 2$, cross sections limits between
 44 40 fb and 200 fb are set for the mass range of $500 < m_{G_{\text{KK}}^*} < 3000 \text{ GeV}$. The cross section upper
 45 limits for $\sigma(pp \rightarrow H \rightarrow hh \rightarrow b\bar{b}b\bar{b})$ ranges from 30 to 300 fb in the mass range of $500 < m_H <$
 46 3000 GeV .

Contents

47

48	o INTRODUCTION	I
49	I Theoretical and Experimental Background	5
50	I.1 THE PHYSICS OF THE HIGGS BOSON	6
51	I.1.1 The Standard Model of Particle Physics	6
52	I.1.2 Electroweak Symmetry Breaking and the Higgs	8
53	I.1.3 Higgs Boson Production and Decay	II
54	I.1.4 Higgs Pair Production in the Standard Model	15
55	I.1.5 Higgs Pair Production in Theories Beyond the Standard Model	16
56	I.1.6 Conclusion	21
57	2 THE ATLAS DETECTOR AND THE LARGE HADRON COLLIDER	22
58	2.1 The Large Hadron Collider	23
59	2.2 The ATLAS Detector	25
60	2.3 The ATLAS Muon New Small Wheel Upgrade	36
61	2.4 Object Reconstruction in ATLAS	40
62	II Observation and measurement of Higgs boson decays to WW^* in LHC	
63	Run I at $\sqrt{s} = 7$ and 8 TeV	49
64	3 $H \rightarrow WW^* \rightarrow \ell\nu\ell\nu$ ANALYSIS STRATEGY	50
65	3.1 Introduction	50
66	3.2 The $H \rightarrow WW^* \rightarrow \ell\nu\ell\nu$ signal in ATLAS	51
67	3.3 Background processes	52
68	3.4 Shared signal region selection requirements	56
69	3.5 Background reduction in same-flavor final states	58
70	3.6 Parameters of interest and statistical treatment	64
71	4 THE DISCOVERY OF THE HIGGS BOSON AND THE ROLE OF THE $H \rightarrow WW^* \rightarrow \ell\nu\ell\nu$ CHANNEL	
72	4.1 Introduction	70

74	4.2	Data and simulation samples	71
75	4.3	$H \rightarrow WW \rightarrow e\nu\mu\nu$ search	71
76	4.4	$H \rightarrow \gamma\gamma$ search	76
77	4.5	$H \rightarrow ZZ \rightarrow 4\ell$ search	77
78	4.6	Combined results	79
79	4.7	Conclusion	81
80	5	OBSERVATION OF VECTOR BOSON FUSION PRODUCTION OF $H \rightarrow WW^* \rightarrow \ell\nu\ell\nu$	83
81	5.1	Introduction	83
82	5.2	Data and simulation samples	84
83	5.3	Object selection	88
84	5.4	Analysis selection	91
85	5.5	Background estimation	99
86	5.6	Systematic uncertainties	110
87	5.7	Results	114
88	6	COMBINED RUN I $H \rightarrow WW^* \rightarrow \ell\nu\ell\nu$ RESULTS	119
89	6.1	Introduction	119
90	6.2	Results of dedicated gluon fusion $H \rightarrow WW^* \rightarrow \ell\nu\ell\nu$ search	120
91	6.3	Signal strength measurements in ggF and VBF production	122
92	6.4	Measurement of Higgs couplings to vector bosons and fermions	125
93	6.5	Higgs production cross section measurement	126
94	6.6	Conclusion	127
95	III	Search for Higgs pair production in the $HH \rightarrow b\bar{b}b\bar{b}$ channel in LHC	
96		Run 2 at $\sqrt{s} = 13$ TeV	129
97	7	SEARCH FOR HIGGS PAIR PRODUCTION IN BOOSTED $b\bar{b}b\bar{b}$ FINAL STATES	130
98	7.1	Introduction	130
99	7.2	Motivation	131
100	7.3	Data and simulation samples	133
101	7.4	Event reconstruction and object selection	135
102	7.5	Event selection	138
103	7.6	Data-driven background estimation	141
104	7.7	Systematic uncertainties	147
105	7.8	Results	150

106	8 COMBINED LIMITS FROM BOOSTED AND RESOLVED SEARCHES	152
107	8.1 Introduction	152
108	8.2 Resolved results	153
109	8.3 Search technique and results	153
110	8.4 Limit setting	154
111	IV Looking ahead	158
112	9 CONCLUSION	159
113	APPENDIX A OPTIMIZATION OF b -TAGGING WORKING POINT IN $X \rightarrow HH \rightarrow b\bar{b}b\bar{b}$	
114	SEARCH	161
115	APPENDIX B b -TAGGING PERFORMANCE AT HIGH p_T	163
116	B.1 MV2 algorithm overview	163
117	B.2 Changes in MV2 score at high p_T	164
118	REFERENCES	176

Listing of figures

120	1.1	The particles of the Standard Model and their properties[1].	7
121	1.2	The four most common Higgs boson production modes at the LHC: (a) gluon-gluon fusion, (b) vector boson fusion, (c) $W/Z + H$ production, (d) $t\bar{t}H$ production	ii
122	1.3	Higgs production cross sections as a function of center of mass energy (\sqrt{s}) at a pp collider[2].	12
123	1.4	Higgs boson branching ratios as a function of m_H [2].	14
124	1.5	The two leading diagrams for Standard Model di-Higgs production at the LHC: (a) box diagram, (b) Higgs self coupling	16
125	1.6	Diagrams with new vertices for non-resonant Higgs pair production arising in composite Higgs models	17
126	1.7	Generic Feynman diagram for resonant Higgs pair production in BSM theories	18
127	1.8	Branching ratios for a spin-2 Randall-Sundrum graviton as a function of mass computed in MadGraph with the CP3-Origins implementation [3, 4]	18
128	1.9	$\sigma \times BR(HH)$ for RSG as a function of mass computed in MadGraph with the CP3-Origins implementation [3, 4]	19
129	1.10	RSG width as a function of mass computed in MadGraph with the CP3-Origins implementation [3, 4]	20
130	1.11	Branching ratios for heavy Higgs H in Type I (left) and Type II (right) 2HDM models with $\tan \beta = 1.5$ and $\cos(\beta - \alpha) = 0.1(0.01)$ for Type I (Type II). [5]	21
131			
132	2.1	A schematic view of the LHC ring [6]	23
133	2.2	A full diagram of the ATLAS detector [7]	26
134	2.3	The ATLAS coordinate system	27
135	2.4	Layout of the ATLAS Inner Detector system [8]	28
136	2.5	Layout of the ATLAS calorimeter system [7]	30
137	2.6	Layout of the ATLAS muon system [7]	32
138	2.7	Predicted field integral as a function of $ \eta $ for the ATLAS magnet system [7]	34
139	2.8	ATLAS trigger rates for Level-1 triggers as a function of instantaneous luminosity in 2012 and 2015 operation. These are single object triggers for electromagnetic clusters (EM), muons (MU), jets (J), missing energy (XE), and τ leptons (TAU). The threshold of the trigger is given in the name in GeV. [9]	35
140	2.9	Instantaneous luminosity as a function of time for data recorded by ATLAS at different center of mass energies [10, ii]	36

151	2.10	MDT tube hit (solid) and segment (dashed) efficiency as a function of hit rate per tube [12]	38
152	2.11	Trigger rate as a function of p_T threshold with and without the NSW upgrade [12]	38
153	2.12	Illustrations of the geometry (left) and operating principle (right) of the micromegas detector [12]	39
154	2.13	Geometry of the sTGC detector [12]	40
155	2.14	Illustration of particle interactions in ATLAS [13]	41
156	2.15	Electron performance: (a) reconstruction efficiency as a function of electron E_T [14] (b) energy resolution in simulation as a function of $ \eta $ for different energy electrons [15]	42
157	2.16	Muon performance: (a) reconstruction efficiency as a function of muon p_T (b) dimuon mass resolution as a function of average p_T [16]	44
158	2.17	Jet energy response after calibration as a function of true p_T in simulation [17]	45
159	2.18	Light jet rejection (1/efficiency) vs. b -jet efficiency for MV1 and its input algorithms (a) [18] and MV2 (b) [19] in simulated $t\bar{t}$ events. The numbers in the algorithm names in (b) refer to the fraction of charm events used in the MV2 training.	46
160	2.19	Resolution of E_T^{miss} components as a function of $\sum E_T$ before pileup suppression with different pileup techniques [20]	48
161	3.1	Branching ratios for a WW system. q refers to quarks. ℓ can be either an electron or muon, and the leptonic branching ratios of the τ are included. For example, the $\ell\nu qq$ final state includes one W decaying to $e\nu$, $\mu\nu$, or $\tau\nu$. τ_h refer to hadronic decays of the τ	52
162	3.2	Feynman diagram for Standard Model WW production	53
163	3.3	Feynman diagrams for top pair production (left) and Wt production (right)	54
164	3.4	An example Feynman diagram of $W + \text{jets}$ production	54
165	3.5	An example Feynman diagram of $Z + \text{jets}$ production	55
166	3.6	An illustration of the unique analysis signal regions[21]	56
167	3.7	A graphical illustration of the $E_{T,\text{rel}}^{\text{miss}}$ calculation	58
168	3.8	Predicted backgrounds (compared with data) as a function of n_j (a and b) and n_b (c)	59
169	3.9	An event display of a $Z/\gamma^* + \text{jets}$ event illustrating the effect of pileup interactions	60
170	3.10	The RMS of different missing transverse momentum definitions as a function of the average number of interactions per bunch crossing	61
171	3.11	The difference between the true and reconstructed values of the missing transverse momentum (a) and m_T (b) in a gluon fusion signal sample	62
172	3.12	Comparison of f_{recoil} distributions for $Z/\gamma^* + \text{jets}$, $H \rightarrow WW^*$, and other backgrounds with real neutrinos.	63
173	3.13	Signal significance as a function of required value for f_{recoil} and $p_{T,\text{rel}}^{\text{miss}(\text{trk})}$ in the ggF $H \rightarrow WW^*$ with $n_j = 0$	64

186	4.1	Jet multiplicity distribution in data and MC after applying lepton, jet, and $E_{\text{T},\text{rel}}^{\text{miss}}$ selections.	
187		The WW and top backgrounds have been normalized using control samples, and the hashed	
188		band indicates the total uncertainty on the prediction. [22]	72
189	4.2	Comparison of m_{T} between data and simulation in the $n_j = 0$ WW (a) and $n_j = 1$	
190		top (b) control samples [22]	74
191	4.3	m_{T} distribution in the $H \rightarrow WW \rightarrow e\nu\mu\nu n_j \leq 1$ channels for 8 TeV data[22].	76
192	4.4	Diphoton mass spectrum in 7 and 8 TeV data. Panel a) shows the unweighted data distri-	
193		bution superimposed on the background fit, while panel c) shows the data where each event	
194		category is weighted by its signal to background ratio. Panels b) and d) show the respective	
195		distributions with background subtracted[22].	77
196	4.5	Four lepton invariant mass spectrum ($m_{4\ell}$) in 7 and 8 TeV data compared to background	
197		estimate. A 125 GeV SM Higgs signal is shown in blue[22].	78
198	4.6	Local p_0 distribution as a function of hypothesized Higgs mass for the $H \rightarrow ZZ^* \rightarrow 4\ell$	
199		(a), $H \rightarrow \gamma\gamma$ (b), and $H \rightarrow WW^* \rightarrow \ell\nu\ell\nu$ (c) channels. Dashed curves show expected	
200		results, while solid curves show observed. Red curves are from 7 TeV data, blue curves from	
201		8 TeV, and black curved combined[22].	80
202	4.7	Combined 95% CL limits (a), local p_0 values (b), and signal strength measurement (c) as a	
203		function of Higgs mass[22].	81
204	4.8	Comparison of measured signal strength μ for a 126 GeV Higgs in the 7 and 8 TeV datasets[22].	82
205	4.9	Two dimensional likelihood as a function of signal strength μ and Higgs mass m_H [22].	82
206	5.1	A comparison of the subleading lepton p_{T} spectrum between VBF $H \rightarrow WW^*$ production	
207		and $t\bar{t}$ background	85
208	5.2	Leading jet η in VBF $H \rightarrow WW^*$ (red) and $t\bar{t}$ (black)	93
209	5.3	Distributions of (a) m_{jj} , (b) Δy_{jj} , (c) $C_{\ell 1}$, and (d) $\Sigma m_{\ell j}$, for the VBF analysis. The top	
210		panels compare simulation and data, while the bottom panels show normalized distributions	
211		for all background processes and signal[21].	95
212	5.4	A cartoon of the WW final state. Momenta are represented with thin arrows, spins with thick	
213		arrows. [21]	96
214	5.5	Event display of a VBF candidate event[21].	97
215	5.6	Distributions of $m_{\ell\ell}$ (top left), $\Delta\phi_{\ell\ell}$ (top right), and m_{T} (bottom), Higgs topology vari-	
216		ables used in the selection requirements of the cut-based signal region and as inputs to the	
217		BDT result. These are plotted after all of the BDT pre-training selection cuts[21].	100
218	5.7	Distributions of m_{jj} (top left), Δy_{jj} (top right), $\sum C_{\ell}$ (bottom), VBF topology variables	
219		used in the selection requirements of the cut-based signal region and as inputs to the BDT	
220		result. These are plotted after all of the BDT pre-training selection cuts[21].	101
221	5.8	Distributions of m_{jj} (a) and O_{BDT} (b) in the VBF $n_b = 1$ top CR [21].	103

222	5.9	Comparison of m_{jj} shape in a same flavor $Z \rightarrow \ell\ell$ control region and the VBF cut-based signal region.	105
223	5.10	General illustration of the ABCD region definitions for $Z/\gamma^* \rightarrow \ell\ell$ background estimation.	106
224	5.11	Distribution of m_{T2} in the WW validation region of the VBF analysis[21].	107
225	5.12	Extrapolation factors for the $W + \text{jets}$ estimate derived for muons (a) and electrons (b) as a function of lepton p_T [21].	109
226	5.13	Background composition in final VBF signal region[21].	110
227	5.14	Variations in the top background extrapolation factor in the cut-based analysis due to PDF uncertainties, binned in m_T	112
228	5.15	Variations in the top background extrapolation factor in the cut-based analysis due to QCD scale uncertainties, binned in m_T	113
229	5.16	Postfit distributions in the cut-based VBF analysis. Panel (a) shows the one-dimensional m_T distribution, while (b) shows the data candidates split into the bins of m_T and m_{jj} used in the final fit[21].	116
230	5.17	Postfit distributions in the BDT VBF analysis[21].	117
231	5.18	Overlap between cut-based and BDT VBF signal region candidates in the m_{jj} - m_T plane. .	117
232	6.1	Post-fit m_T distribution in the $n_j \leq 1$ regions[21].	121
233	6.2	Best fit signal strength $\hat{\mu}$ as a function of hypothesized m_H [21].	123
234	6.3	Local p_0 as a function of m_H [21].	123
235	6.4	Likelihood as a function of $\mu_{\text{VBF}}/\mu_{\text{ggF}}$ [21].	124
236	6.5	Likelihood scan as a function of μ_{VBF} and μ_{ggF} [21].	125
237	6.6	Likelihood scan as a function of κ_F and κ_V [21].	126
238	6.7	Comparison of signal strength measurements in different Higgs decay channels on ATLAS[23].	128
239	7.1	Parton luminosity ratios as a function of resonance mass M_X for 13/8 TeV and 7/8 TeV [24].	131
240	7.2	Summary of HH branching ratios [25].	132
241	7.3	Minimum ΔR between B decay vertices for different RSG masses in a $G_{\text{KK}}^* \rightarrow HH \rightarrow 4b$ sample with $c = 1$	133
242	7.4	Trigger efficiency for events passing all signal region selections as a function of mass in $G_{\text{KK}}^* \rightarrow HH \rightarrow 4b$ samples with $c = 1$ [26]. In the trigger names, “j” refers to a jet or jets. “ht” refers to H_T , the scalar sum of transverse momenta in the event. “bloose” refers to a loose b -tagging requirement applied to the jet. “aior” refers to anti- k_T jets with $R = 1.0$. The numbers at the end are the thresholds on the given quantity in GeV.	135
243	7.5	Comparison of untrimmed and trimmed jet masses for large radius jets in a RSG sample with $m_{G_{\text{KK}}^*} = 1$ TeV. JES (JMS) refers to the standard jet energy (mass) scale calibration for ATLAS [17].	136

257	7.6	Efficiency of finding two b -jets from each Higgs in an RSG event using calorimeter jets with $R = 0.3$ or different track jet radii [27]	137
258	7.7	Illustration of the boosted selection requirements on Higgs candidates. Each large-radius calorime- ter jet (Higgs candidate) must contain two track jets	139
259	7.8	Acceptance \times efficiency as a function of mass for (a) RSG and (b) narrow heavy scalar sig- nal models [28].	140
260	7.9	Efficiency of requiring 3 or 4 b -tagged track jets vs. RSG mass. The efficiency quoted is rel- ative to the previous selection requirements (rather than an absolute efficiency).	141
261	7.10	M_J^{sublead} vs. M_J^{lead} in a 2 b -tag data sample. The signal region is defined by the inner black contour ($X_{hh} < 1.6$) and the sideband region is defined by the outer contour ($R_{hh} >$ 35.8 GeV). The region between the black contours is the control region. The mass region which is enriched in $t\bar{t}$ background is also shown for illustration. [28]	143
262	7.11	An illustration of the data-driven background estimation technique for the boosted anal- ysis	144
263	7.12	Leading large-R jet mass in the 3 b (a) and 4 b (b) sideband regions. The multijet and $t\bar{t}$ back- grounds are estimated using the data-driven methods described above. Because their normal- izations are derived in the sideband region, the total background normalization is constrained by default to match the normalization of the data [28].	145
264	7.13	Di-jet invariant mass ($M_{2,J}$) in the 3 b (a) and 4 b (b) control regions. The multijet and $t\bar{t}$ back- grounds are estimated using the data-driven methods described above [28].	146
265	7.14	Di-jet invariant mass ($M_{2,J}$) in the 3 b (a) and 4 b (b) signal regions. The multijet and $t\bar{t}$ back- grounds are estimated using the data-driven methods described above. In the 3 b region, a graviton signal with $m_{G_{KK}^*} = 1.8$ TeV and $c = 1$ is overlaid, with the cross section mul- tiplied by a factor of 50 so that the signal is visible. In the 4 b region, signals with $m_{G_{KK}^*} =$ 1.0 TeV and $m_{G_{KK}^*} = 1.5$ TeV are overlaid, both with $c = 1$ and the yields multiplied by factors of 2 and 5 respectively [28].	151
266	8.1	Di-jet invariant mass ($M_{2,J}$) in the resolved signal region. Agraviton signal with $m_{G_{KK}^*} =$ 800 GeV and $c = 1$ is overlaid. [28].	154
267	8.2	Expected and observed upper limit as a function of mass for G_{KK}^* in the RSG model with (a) $c = 1$ and (b) $c = 2$, as well as (c) H with fixed $\Gamma_H = 1$ GeV, at the 95% confidence level in the CL_s method. [28]	157
268	A.1	Estimated significance as a function of signal mass for RSG $c = 1$ models in the 3 b (a) and 4 b (b) regions for different b -tagging efficiency working points	162
269	B.1	Summary of the inputs to the MV2 b -tagging algorithm	164
270	B.2	p_T of the leading track jet in the leading calorimeter jet for different signal masses in RSG $c =$ 1 models	165

293	B.3	MV _{2C2O} score for the leading track jet (a) and subleading track jet (b) of the leading calorime-	
294		ter jet for different signal masses in RSG $c = 1$ models	165
295	B.4	IP _{3D} log-likelihood ratio ($\log(p_b/p_u)$) of the leading track jet in the leading calorimeter jet	
296		for different signal masses in RSG $c = 1$ models	166
297	B.5	Mass (a) and number of tracks (b) for the secondary vertices computed with the SV1 algo-	
298		rithm. When no secondary vertex is found, the quantiites are assigned to default negative val-	
299		ues.	166
300	B.6	Mass (a) and number of tracks (b) for vertices computed with the JetFitter algorithm. When	
301		no vertices are found, the quantiites are assigned to default negative values.	167

Listing of tables

302

303	1.1 Production cross sections for a 125 GeV Higgs boson at $\sqrt{s} = 8$ TeV with scale and PDF uncertainties [2].	13
304		
305	1.2 Branching ratios for a 125 GeV Higgs boson[2].	15
306		
307	1.3 Possible channels for Higgs searches. Checkmarks denote the most sensitive production modes [29].	15
308		
309	1.4 Production cross sections for pair production of a 125 GeV Higgs boson at $\sqrt{s} = 14$ TeV with total uncertainty [30]. The uncertainties include QCD scale and PDF variations as well as uncertainties on α_S	16
310		
311	2.1 Evolution of LHC machine conditions [31, 32]	25
312		
313	2.2 Performance requirements for the ATLAS detector [7].	37
314		
315	2.3 Signal efficiencies for WH production with $H \rightarrow b\bar{b}$ and $H \rightarrow WW^* \rightarrow \mu\nu qq$ under different trigger configurations [12].	40
316		
317	3.1 A summary of backgrounds to the $H \rightarrow WW^* \rightarrow \ell\nu\ell\nu$ signal	55
318		
319	4.1 Monte carlo generators used to model signal and background for the Higgs search[22].	71
320		
321	4.2 Normalization factors (ratio of data and MC yields in a control sample) for the Standard Model WW and top backgrounds in the $H \rightarrow WW^* \rightarrow \ell\nu\ell\nu$ analysis [22]. Only statistical uncertainties are shown.	74
322		
323	4.3 Data and expected yields for signal and background in the final $H \rightarrow WW^* \rightarrow \ell\nu\ell\nu$ signal region. Uncertainties shown are both statistical and systematic. [22]	75
324		
325	4.4 Summary of the expected and observed significance and measured signal strengths in the combined 7 and 8 TeV datasets for the Higgs discovery analysis[22].	79
326		
327	5.1 Single lepton triggers used for electrons and muons. A logical “or” of the triggers listed for each lepton type is taken. Units are in GeV, and the i denotes an isolation requirement in the trigger.	85
328		
329	5.2 Di-lepton triggers used for different flavor combinations. The two thresholds listed refer to leading and sub-leading leptons, respectively. The di-muon trigger only requires a single lepton at level-i.	85

330	5.3	Trigger efficiency for signal events and relative gain of adding a dilepton trigger on top of the single lepton trigger selection. The first lepton is the leading, while the second is the sub-leading. Efficiencies shown here are for the ggF signal in the $n_j = 0$ category but are comparable for the VBF signal.	86
331			
332	5.4	Monte Carlo samples used to model the signal and background processes[21].	87
333			
334	5.5	p_T dependent isolation requirements for muons. Muons are required to have the amount of calorimeter or track based cone sums be less than this fraction of their p_T	89
335			
336	5.6	p_T dependent requirements for electrons. Electrons are required to have the amount of calorimeter or track based cone sums be less than this fraction of their E_T	90
337			
338	5.7	Event selection for the $n_j \geq 2$ VBF analysis in the 8 TeV cut-based analysis[21].	98
339			
340	5.8	Top normalization factors computed at each stage of the cut-based selection. Uncertainties are statistical only.	102
341			
342	5.9	Top normalization factors computed for each bin of O_{BDT} . Uncertainties are statistical only.	102
343			
344	5.10	$Z/\gamma^* \rightarrow \tau\tau$ correction factors for the VBF cut-based analysis. Uncertainties are statistical only.	105
345			
346	5.11	$Z/\gamma^* \rightarrow \ell\ell$ normalization factors for cut-based and BDT analyses. Uncertainties are statistical only.	107
347			
348	5.12	Systematic uncertainties for various processes in the cut-based VBF analysis, given in units of % change in yield. Values are given for the low m_{jj} signal region.	111
349			
350	5.13	Composition of the post-fit uncertainties (in %) on the total signal (N_{sig}), total background (N_{bkg}), and individual background yields in the VBF analysis[21].	114
351			
352	5.14	Event selection for the VBF BDT analysis. The event yields in (a) are shown after the pre-selection and the additional requirements applied before the BDT classification (see text). The event yields in (b) are given in bins in O_{BDT} after the classification[21].	115
353			
354	6.1	All signal regions definitions input into final statistical fit[21].	120
355	6.2	Post-fit yields in the different ggF and VBF dedicated signal regions[21].	121
356			
357	7.1	Summary of requirements on objects used in the $X \rightarrow HH \rightarrow b\bar{b}b\bar{b}$ search	138
358	7.2	Effect of boosted selection on data, RSG signal models, $t\bar{t}$, and $Z+\text{jets}$. The numbers from simulation are normalized with the MC generator cross section and do not take into account the data driven estimates described in section 7.6 [33].	142
359			
360	7.3	Mass region definitions used for background estimation	143
361	7.4	Parameters derived for exponential fit to background M_{2J} shape in the 3 b and 4 b signal regions [33]	146
362			
363	7.5	The number of events in data and predicted background events in the boosted 3-tag and 4-tag sideband and control regions. The uncertainties shown are statistical only. [28]	147
364			

365	7.6	Summary of systematic uncertainties in the total background and signal event yields (expressed in %) in the boosted 3-tag and 4-tag signal regions. Systematic uncertainties on the signal normalization are shown for models with $m_{G_{KK}^*} = 1.5$ TeV and both $c = 1$ and $c = 2$ as well as a narrow width heavy scalar.	149
366			
367	7.7	Alternate fit functions used to model the M_{JJ} distribution in the QCD multijet background. In the equations, $x = M_{JJ}/\sqrt{s}$	150
368			
369	7.8	Observed yields in the 3-tag and 4-tag signal regions for the boosted analysis compared to the predicted number of background events Errors correspond to the total uncertainties in the predicted event yields. The yields for a graviton with $m_{G_{KK}^*} = 1$ TeV and $c = 1$ are also shown. [28]	151
370			
371	8.1	Observed yields in the resolve selection 4-tag signal region compared to the predicted num- ber of background events Errors correspond to the total uncertainties in the predicted event yields. The yields for a graviton with $m_{G_{KK}^*} = 800$ GeV and $c = 1$ are also shown. [28] . .	153
372			
373			
374			
375			
376			
377			

Acknowledgments

380 I have been a member of the Harvard ATLAS group for many years now, first as an undergraduate
 381 and then as a graduate student. As a result, I have had the privilege of interacting with many amazing
 382 people there over the years and have accumulated a large list of folks to thank.

383 First and foremost, I must thank the two people who have effectively been my academic parents since
 384 I started in the Harvard group: Joao Guimaraes da Costa and Melissa Franklin. Melissa Franklin and
 385 Joao Guimaraes da Costa. They have both been so important to both my academic and personal devel-
 386 opment that I can't even put one before the other. Joao has been an excellent PhD advisor, showing me
 387 how to look at the big picture and helping me navigate the sometimes complicated politics of ATLAS.
 388 He got me started on my first projects with ATLAS as a young college sophomore before there was even
 389 beam in the LHC (go cosmic ray muons!). He has also been a constant source of advice and support,
 390 even when we have been on different continents. Melissa gave me my start in HEP as a summer student
 391 on CDF and has been an unbelievable mentor throughout my time at Harvard. I still remember our
 392 weekly chalkboard particle physics lessons after that first summer. She also graciously took me on as a
 393 co-advisee after Joao moved on to his new position at IHEP. I am incredibly lucky to have had both of
 394 them as advisors.

395 Another mentor who was essential to my development as a graduate student is Paolo Giromini. His
 396 uncanny knowledge and intuition about detectors is unmatched and I am very grateful to have had
 397 the chance to work with him on the micromegas for the ATLAS New Small Wheel upgrade project. I
 398 owe essentially all my practical knowledge about detectors (and building things in general) to him. I also
 399 appreciated his unique sense of humor which made sometimes difficult tasks much easier to get through.

400 I am grateful to John Huth and Masahiro Morii for their helpful advice as the other professors in the
 401 Harvard ATLAS group as well. I especially thank John for helping me get started on the micromegas
 402 trigger project and being a great professor to TF particle physics for.

403 I also owe enormous thanks to Hugh Skottowe, the postdoc that I worked most closely with in my
 404 early years as a graduate student. He was always able to help me through complicated tasks in everything
 405 from writing code to understanding difficult physics concepts. I particularly enjoyed walking down to
 406 his office in Palfrey at random times and talking through whatever problem I was tackling on that day.

407 Alex Tuna, the second postdoc that I worked closely with at Harvard, deserves great thanks as well.
 408 He helped me push through to the end of my graduate career and offered great advice along the way.

409 Being at Harvard, I have seen an incredible array of graduate students graduate before me: Ben Smith,
 410 Verena Martinez Outschoorn, Srivas Prasad, Michael Kagan, Giovanni Zevi Della Porta, Laura Jeanty,
 411 Kevin Mercurio, William Spearman, and Andy Yen. I want to thank them all for showing me what a

412 good physicist looks like and for patiently answering my questions and offering insightful advice about
413 physics and life.

414 Getting through graduate school would not have been possible without the support and friendship
415 of the other students in our group. Thanks to Emma Tolley for geeking out with me about cool com-
416 puting stuff, going to taste delicious beers with me, and helping start the Palfrey tradition of Taco Tues-
417 days. Thanks to Brian Clark for being a great friend and housing companion both in Kirkland House
418 and in our tiny summer apartment in Geneva (and thanks to his partner Allison Goff for the same rea-
419 sons!). Thanks to Siyuan Sun for giving me my first aikido lesson and always being there for great con-
420 versations, big and small. Tony (Baojia) Tong deserves special recognition for working with me on the
421 $4b$ analysis and putting up with my sometimes strange requests (and giving me rides to the Val Thoiry
422 Migros so I wouldn't have to pay exorbitant Geneva grocery prices!). Stephen Chan is probably the only
423 student in the group who both understands my references to the Sopranos and makes some of his own.
424 To the younger graduate students - Karri Di Petrillo, Jennifer Roloff, Julia Gonski, and Ann Wang - I
425 want to say thank you for making the group a fun and lively place to be and giving all of us energy that
426 the older graduate students like myself can sometimes lack.

427 I'd like to thank Annie Wei and Gray Putnam, the two undergraduates I have worked with as a gradu-
428 ate student. Their unbelievable intuition and quickness in picking up difficult particle physics concepts
429 is inspiring.

430 I would also like to thank all of the postdocs that I have interacted with in my time in the Harvard
431 group: Kevin Black, Alberto Belloni (who would always ask me "Do you have it?"...I can now say that
432 I do!), Shulamit Moed, Corrinne Mills, Geraldine Conti, David Lopez Mateos, Chris Rogan, Valerio
433 Ippolito, and Stefano Zambito.

434 There are many people on ATLAS who have helped me get to this point as well. In the WW group,
435 I have to thank Jonathan Long, Joana Machado Miguens, Ben Cerio, Philip Chang, Bonnie Chow,
436 Richard Polifka, Heberth Torres, Tae Min Hong, and Jennifer Hsu for being wonderful colleagues and
437 making the entire analysis run smoothly. In the $4b$ group, I have to thank Qi Zeng, Tony Tong, Alex
438 Tuna, Michael Kagan, Max Bellomo, John Alison, and Patrick Bryant.

439 Kirkland House was my home for the last three years of graduate school and was an wonderful envi-
440 ronment and support system. I want to thank my fellow tutors, especially Brian Clark and Allison Goff
441 (again), Zach Abel, Kelly Bodwin, Alex Lupsasca, John and Pam Park, Luke and Erin Walczewski, and
442 Philip Gant for their friendship and support. I also want to thank Kate Drizos Cavell, Bob Butler, and
443 the Faculty Deans Tom and Verena Conley.

444 There are still a few friends that haven't been covered yet and deserve great thanks. Jake Connors and
445 Meredith MacGregor have been absolutely wonderful friends and I thank them in particular for the
446 many home-cooked meals and great conversations we've had in their apartment. Nihar Shah has been
447 my friend and confidant since we were both wee freshmen in Harvard Yard. Gareth Kafka, though he
448 sits on the "neutrino" side of Palfrey House, has made days there more fun and has also been an enthusi-

449 astic participant in the Palfrey Taco Tuesdays.

450 Being at Harvard necessarily means having to navigate through bureaucracy at some point or another.
451 I thank Lisa Cacciabaudo, Carol Davis, and Jacob Barandes for always having open doors and being the
452 most kind, helpful people in the Physics department.

453 I thank Venky Narayananamurti for putting on a great SPU course that I was proud to be a part of and
454 TF for. I'd also like to thank Jim Waldo for offering me much advice about working in Computer Science
455 and giving me a fun data project to be a part of in my free time.

456 I grew up in a very tight knit Serbian community on the south side of Chicago which helped make
457 me the person I am today. I would like to thank all of the people at St. Simeon Mirotochivi Serbian
458 Orthodox Church who have always been sources of enthusiasm and support in my life.

459 I would not be here without the unconditional love and constant support and encouragaement of my
460 family. To my pokojni Dendas Branko and Miloje, my pokojni Baba Milka, and my Baba Desa, I want to
461 say thank you for instilling in me at an early age the love of curiosity and storytelling that I have carried
462 throughout my life. To my sister Angelina, I want to say thank you for always loving me and being my
463 partner in crime throughout our childhoods. To my parents, Miroljub and Nada, Tata and Mama, I
464 really cannot express how grateful I am to you and how much I owe you. As I look back now I see how
465 I am a combination of both of your best qualities and every day I am in situations where I understand
466 more and more the lessons you made sure to teach me and the sacrifices you made to make sure I got the
467 best possible education. I love you all.

468 Finally, I have to thank my soul mate, the one person in my life who understands me more than any-
469 one else, my fiancee Kelly Brock. You are my sounding board, my support system, my cheerleader (fig-
470 uratively and literally!), my best friend, my role model, and my everything. I would not have gotten
471 through graduate school without you and my life would not be the same without you. I cannot wait to
472 start our new lives together as the married doctors, tackling whatever comes our way with the same zeal
473 with which we tackled graduate school. I love you with all my heart and soul.

0

474

475

Introduction

476 The Higgs boson is often described as one of the cornerstones of the Standard Model. Since the con-
477 ception of the Higgs mechanism as the source of electroweak symmetry breaking in the early 1960s,
478 countless collider experiments have searched for this elusive particle. This dissertation presents multi-
479 ple studies of the Higgs boson with the ATLAS detector at the Large Hadron Collider (LHC).

480 One of the first priorities of the early LHC was the search for the Higgs boson. This search was first
481 tackled in three main channels: $H \rightarrow \gamma\gamma$, $H \rightarrow ZZ^*$, and $H \rightarrow WW^*$. Each channel has its own
482 merits, but the WW^* is particularly suited to searching over a wide range of masses. The $H \rightarrow WW$
483 branching ratio is large and it is the primary decay channel above the $2m_W$ mass threshold.

484 While the rate of events produced in $H \rightarrow WW^*$ is large, the channel poses some challenges. First,
485 the most common mode of study for this channel is $H \rightarrow WW^* \rightarrow \ell\nu\ell\nu$. With neutrinos in the
486 final state, it is not possible to fully reconstruct the invariant mass of the parent Higgs like the $\gamma\gamma$ and
487 $ZZ \rightarrow 4\ell$ channels. Second, the final state topology is mimicked by a wide variety of backgrounds that

488 need to be properly estimated. This means tailored selection requirements for background reduction
489 and robust background estimation techniques must both be developed.

490 In 2012, the ATLAS and CMS experiments announced the discovery of a new particle consistent with
491 the Higgs boson [22, 34]. In ATLAS, this discovery was made with 4.8 fb^{-1} collected at $\sqrt{s} = 7 \text{ TeV}$
492 and 5.8 fb^{-1} at $\sqrt{s} = 8 \text{ TeV}$. The $H \rightarrow WW^* \rightarrow \ell\nu\ell\nu$ analysis played an important role in this
493 discovery. After the discovery, measurement of the properties of the newly discovered particle and con-
494 firmation of its consistency with the Standard Model Higgs were the main priorities. The WW^* chan-
495 nel is also uniquely suited to these types of measurements. Because of its good rate, it offers some of the
496 best cross section measurements available among the various Higgs decay modes. It is also suited for
497 measurement of multiple Higgs production modes, like the vector boson fusion (VBF) mode, where in-
498 coming quarks radiate W/Z bosons which fuse to make a Higgs. In VBF production with the WW^*
499 decay channel, the coupling of the Higgs to the W boson is present in both the production and decay
500 which allows for more precise measurements of this coupling than other channels which rely on gluon
501 fusion production (where gluons couple to the Higgs through a top loop in the production). The mea-
502 surement of VBF carries the additional challenge that its cross section is an order of magnitude smaller
503 than that of gluon fusion, meaning that the large branching ratio to WW^* offers an additional advan-
504 tage in isolating this production mode. In the final ATLAS Run 1 results, combining 20.3 fb^{-1} taken at
505 $\sqrt{s} = 8 \text{ TeV}$ with the 4.8 fb^{-1} collected at $\sqrt{s} = 7 \text{ TeV}$, the WW^* channel achieved its first observa-
506 tion of VBF production of the Higgs.

507 After Run 1 of the LHC, with the existence of the Higgs now firmly established, the focus shifted to
508 searches for physics beyond the Standard Model. In particular, searches for high mass resonances benefit
509 from the LHC’s increase to $\sqrt{s} = 13 \text{ TeV}$ in Run 2. The newly discovered Higgs can be used as a tool
510 in these searches. Higgs pair production in the Standard Model has a low cross section that requires large
511 datasets (on the order of the LHC’s lifetime) for full measurement. However, new physics can modify
512 this cross section, especially new resonances which decay to two Higgs bosons. A search for Higgs pair
513 production in the $HH \rightarrow b\bar{b}b\bar{b}$ final state was performed with 3.2 fb^{-1} collected with ATLAS at $\sqrt{s} =$
514 13 TeV in 2015.

515 This dissertation begins by discussing the discovery of the Higgs and the role of the $H \rightarrow WW^* \rightarrow$
516 $\ell\nu\ell\nu$ channel. It then discusses the first observation of the VBF production mode in $H \rightarrow WW^* \rightarrow$
517 $\ell\nu\ell\nu$ with the full ATLAS Run 1 dataset, as well as the final combined Run 1 measurements from this
518 channel. Finally, it presents a search for Higgs pair production in the $HH \rightarrow b\bar{b}b\bar{b}$ channel. It is orga-
519 nized into four parts.

520 Part 1 presents the theoretical and experimental background required for the subsequent parts. Chap-
521 ter 1 gives an overview of Higgs physics, particularly single and double Higgs production in the Standard
522 Model and beyond. Chapter 2 presents details regarding the Large Hadron Collider and the ATLAS
523 experiment. The evolution of machine conditions, descriptions of the ATLAS sub-detectors, and an
524 overview of object reconstruction in ATLAS are all shown. A brief interlude on the ATLAS Muon New
525 Small Wheel upgrade is also given, as this upgrade has been a focus of my graduate work and will have
526 important impact on ATLAS' ability to study the Higgs at the High Luminosity LHC.

527 Part 2 discusses the observation and measurement of the Higgs in the $H \rightarrow WW^* \rightarrow \ell\nu\ell\nu$
528 channel in the ATLAS Run 1 dataset at $\sqrt{s} = 7$ and 8 TeV. Because I worked in this channel from
529 before the discovery through to the final analysis of the Run 1 dataset, Part 2 is organized in such a way
530 to allow easy presentation of multiple analyses on different subsets of the full Run 1 dataset. Chapter 3
531 presents a general overview of the $H \rightarrow WW^*$ analysis strategy and defines many of the variables and
532 common elements used in the rest of Part 2. Chapter 4 presents the discovery of the Higgs boson, fo-
533 cusing on the role of the WW^* channel in this discovery. Chapter 5 presents the first observation of the
534 VBF production mode of the Higgs in the WW^* channel, a study which was done on the full Run 1
535 ATLAS dataset. In this chapter, the focus is mainly on the selection cut-based VBF analysis. The cut-
536 based analysis was an important first step to the final VBF result which used a Boosted Decision Tree
537 (BDT). Where appropriate, connections between the cut-based and BDT analyses are shown and their
538 compatibility is discussed. Finally, the VBF analysis was an important input into the combined Run 1
539 $H \rightarrow WW^* \rightarrow \ell\nu\ell\nu$ result, which used both the gluon fusion and VBF channels in a combined
540 fit to infer properties of the Higgs, including its couplings to the gauge bosons and its production cross
541 section. This is the topic of Chapter 6.

542 Part 3 presents a search for Higgs pair production in the $HH \rightarrow b\bar{b}b\bar{b}$ channel. Chapter 7 presents
543 an overview of this search in the boosted regime, where the Higgs pairs are the result of the decay of a
544 heavy resonance. Chapter 8 shows the combined results between the boosted regime and the resolved
545 regime, which is sensitive to lower mass resonances and non-resonant Higgs pair production. Finally,
546 Part 4 presents a conclusion and brief outlook of future Higgs physics with ATLAS.

⁵⁴⁷

Part I

⁵⁴⁸

Theoretical and Experimental Background

1

549

550

The Physics of the Higgs Boson

551 This chapter presents an overview of the Standard Model of Particle Physics and in particular the physics
552 of the Higgs boson. First, a brief overview of the Standard Model and its history are presented. Then, a
553 description of the Higgs mechanism of electroweak symmetry breaking is given. Next, the physics of sin-
554 gle Higgs boson production and decay is described. The Standard Model also allows for production of
555 two Higgs bosons and this is detailed as well. Finally, di-Higgs production in two beyond the Standard
556 Model (BSM) theories - Randall-Sundrum gravitons (RSG) and Two Higgs Doublet Models (2HDM) -
557 is shown.

558 **I.I THE STANDARD MODEL OF PARTICLE PHYSICS**

559 The Standard Model (SM) of Particle Physics is a quantum field theory describing the fundamental
560 particles of nature and the forces that govern their interactions. Several comprehensive treatments of
561 the SM already exist in the literature[1, 29, 35–38] and this section will not rehash those. Rather, this

562 section presents a brief overview of the SM particles and forces in order to define them for subsequent
 563 discussions.

564 The Standard Model consists of two primary categories of fundamental particles: fermions (spin 1/2
 565 particles) and bosons (integer spin particles). The SM also describes three forces: electromagnetism, the
 566 weak nuclear force, and the strong nuclear force. Gravity is not included in the theory and is largely irrele-
 567 evant at the scales currently probed by collider experiments. Within the fermions, there are both quarks
 568 (which interact via all three forces) and the leptons. The charged leptons interact via electromagnetic and
 569 weak interactions, while neutrinos (neutral leptons) interact only via the weak force. Within the bosons,
 570 there are the W^\pm and Z bosons (the mediators of the weak force), the gluon (g , the mediator of the
 571 strong force), and the photon (γ), the mediator of the electromagnetic force. Finally, there is the Higgs
 572 boson, a fundamental spin-0 particle resulting from the Higgs mechanism of electroweak symmetry
 573 breaking. Figure 1.1 summarizes the fermions and bosons of the SM.

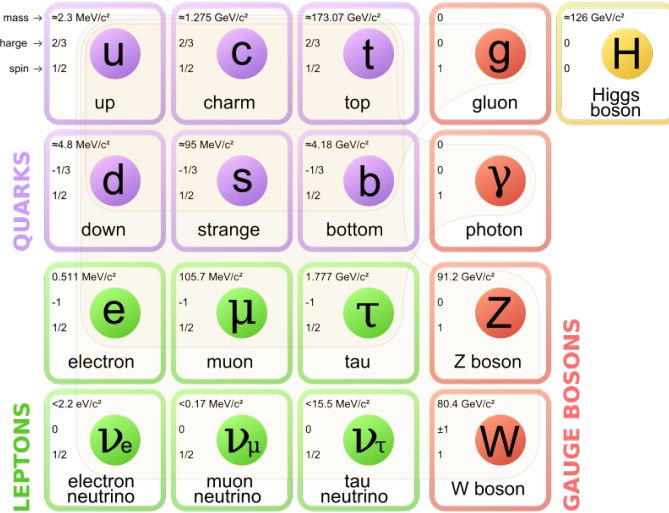


Figure 1.1: The particles of the Standard Model and their properties[1].

574 The Standard Model coalesced into a unified theoretical framework in the 1960s through the work of
 575 Glashow, Weinberg, Salam, and others on the theory of electroweak interactions[39–42]. This theory
 576 characterized both the electromagnetic and weak interactions as unified under a single gauge symme-
 577 try group, namely $SU(2) \times U(1)$. At low enough energy scales (on the order of the W and Z masses,
 578 the electroweak symmetry is broken, as evidenced by the fact that the weak bosons have mass while the

579 photon does not. The discovery of the Higgs boson in 2012 confirmed the Higgs mechanism as the most
 580 likely candidate for this electroweak symmetry breaking[22, 34]. The electroweak theory is then com-
 581 bined with the theory of quantum chromodynamics (which models the strong sector as a non-Abelian
 582 $SU(3)$ gauge group) to form the complete SM[43].

583 1.2 ELECTROWEAK SYMMETRY BREAKING AND THE HIGGS

584 In the Standard Model Lagrangian, it is difficult to include mass terms for the W and Z bosons without
 585 breaking the fundamental gauge symmetry of the Lagrangian. A traditional mass term does not preserve
 586 the $SU(2) \times U(1)$ symmetry. Additionally, scattering of massive W and Z bosons violate unitarity
 587 and these diagrams diverge at high energy scales. In the 1960s, Higgs, Brout, Englert, Guralnik, Kibble,
 588 and Hagen developed a mechanism for spontaneous symmetry breaking via the addition of a complex
 589 scalar doublet to the SM. Three of the four real degrees of freedom of this complex field would go to the
 590 longitudinal modes of the W^\pm and Z , thus allowing them to have mass[44–47]. The remaining degree
 591 of freedom would manifest as an additional scalar, known now as the Higgs boson.

592 The mechanism works by introducing a Lagrangian for the newly introduced field that still respects
 593 the symmetry of the Standard Model inherently, but with a minimum at a non-zero vacuum expecta-
 594 tion value for the field. In this minimum of the potential, the electroweak symmetry is broken. Specifi-
 595 cally, consider a complex scalar doublet Φ with four degrees of freedom, as shown in equation 1.1.

$$\Phi = \begin{pmatrix} \phi^+ \\ \phi^0 \end{pmatrix} = \frac{1}{\sqrt{2}} \begin{pmatrix} \phi_1^+ + i\phi_2^+ \\ \phi_1^0 + i\phi_2^0 \end{pmatrix} \quad (1.1)$$

596 The minimal potential of a self-interacting Higgs that still respects the SM symmetry is given in equa-
 597 tion 1.2.

$$V(\Phi) = \mu^2 \Phi^\dagger \Phi + \lambda (\Phi^\dagger \Phi)^2 \quad (1.2)$$

598 If the μ^2 term of this potential is positive, then the potential has a minimum at $\Phi = 0$ and the SM

⁵⁹⁹ symmetry is preserved. However, if instead $\mu^2 < 0$, then the minimum is at a finite value of Φ , namely

$$\Phi_{\min} = \frac{1}{\sqrt{2}} \begin{pmatrix} 0 \\ v \end{pmatrix} \quad (1.3)$$

⁶⁰⁰ where $v = \sqrt{\mu^2/\lambda}$. Because this is the location of the minimum, it corresponds to the vacuum expecta-
⁶⁰¹ tion value for the field ($\langle \Phi \rangle = \Phi_{\min}$). The excitations of the Higgs can then be parameterized as

$$\Phi = \frac{1}{\sqrt{2}} \begin{pmatrix} 0 \\ v + H \end{pmatrix} \quad (1.4)$$

⁶⁰² The full scalar Lagrangian, including the kinetic term, is then given as

$$\mathcal{L}_s = (D^\mu \Phi)^\dagger (D_\mu \Phi) - V(\Phi) \quad (1.5)$$

⁶⁰³ where the covariant derivative is defined as

$$D_\mu = \partial_\mu + \frac{ig}{2} \tau^a W_\mu^a + ig' Y B_\mu \quad (1.6)$$

⁶⁰⁴ and W^1, W^2, W^3 and B are the $SU(2)$ and $U(1)$ gauge fields of the electroweak theory, respectively. g
⁶⁰⁵ and g' are the corresponding coupling constants. With the scalar Lagrangian in place, the physical gauge
⁶⁰⁶ fields can then be written as

$$W_\mu^\pm = \frac{1}{\sqrt{2}} (W_\mu^1 \mp i W_\mu^2) \quad (1.7)$$

⁶⁰⁷

$$Z_\mu = \frac{-g' B_\mu + g W_\mu^3}{\sqrt{g^2 + g'^2}} \quad (1.8)$$

⁶⁰⁸

$$A_\mu = \frac{g B_\mu + g' W_\mu^3}{\sqrt{g^2 + g'^2}} \quad (1.9)$$

⁶⁰⁹ Equation 1.7 corresponds to the charged W^+ and W^- bosons, equation 1.8 corresponds to the neutral

610 Z boson, and equation 1.9 corresponds to the neutral photon. The masses of the particles also arise from
 611 the Lagrangian. The photon has zero mass, while the masses of the W and Z bosons are given in equa-
 612 tion 1.10.

$$\begin{aligned} M_W^2 &= \frac{1}{4}g^2v^2 \\ M_Z^2 &= \frac{1}{4}(g^2 + g'^2)v^2 \end{aligned} \quad (1.10)$$

613 The fermion masses also arise through a coupling with the Higgs via the Yukawa interaction (for a de-
 614 tailed description, see [38]). In this case the coupling between the Higgs and the fermions goes as

$$g_{Hf\bar{f}} = \frac{m_f}{v} \quad (1.11)$$

615 The full Lagrangian of Higgs interactions can be written as

$$\mathcal{L}_{\text{Higgs}} = -g_{Hf\bar{f}}\bar{f}fH + \frac{g_{HHH}}{6}H^3 + \frac{g_{HHHH}}{24}H^4 + \delta_V V_\mu V^\mu \left(g_{HVV}H + \frac{g_{HHVV}}{2}H^2 \right) \quad (1.12)$$

616 with

$$\begin{aligned} g_{HVV} &= \frac{2m_V^2}{v} & g_{HHVV} &= \frac{2m_V^2}{v^2} \\ g_{HHH} &= \frac{3m_H^2}{v} & g_{HHHH} &= \frac{3m_H^2}{v^2} \end{aligned} \quad (1.13)$$

617 Here, V refers to the W^\pm and Z , and $\delta_W = 1$ while $\delta_Z = 1/2$. Phenomenologically, there are a few
 618 features of this Lagrangian that are useful to note. First, note that the Higgs mass is a free parameter
 619 of the theory that must be determined experimentally. Second, note that the coupling of the Higgs to
 620 the vector bosons and fermions scales with the masses of these particles, a fact that is important when
 621 considering both the production and decays of the particle. Also note that the branching ratio of the
 622 Higgs to W bosons will be twice that of the branching ratio to Z if the Higgs mass is large enough to
 623 produce the particles on shell because of the extra symmetry factor associated with the W coupling.
 624 Finally, note the presence of the cubic and quartic Higgs self interaction terms, which can lead to final
 625 states with multiple Higgs bosons produced.

626 1.3 HIGGS BOSON PRODUCTION AND DECAY

627 This section discusses the properties of Higgs production and decay mechanisms. The details presented
 628 here will focus on the properties of a 125 GeV Higgs boson, as this is the mass closest to that of the
 629 newly discovered Higgs.

630 1.3.1 HIGGS PRODUCTION

631 The Higgs is produced by four main production modes at the Large Hadron Collider - gluon-gluon
 632 fusion (ggF), vector boson fusion (VBF), associated production with a W or Z boson, or associated
 633 production with top quarks ($t\bar{t}H$). Figure 1.2 shows the Feynman diagrams for these four modes.

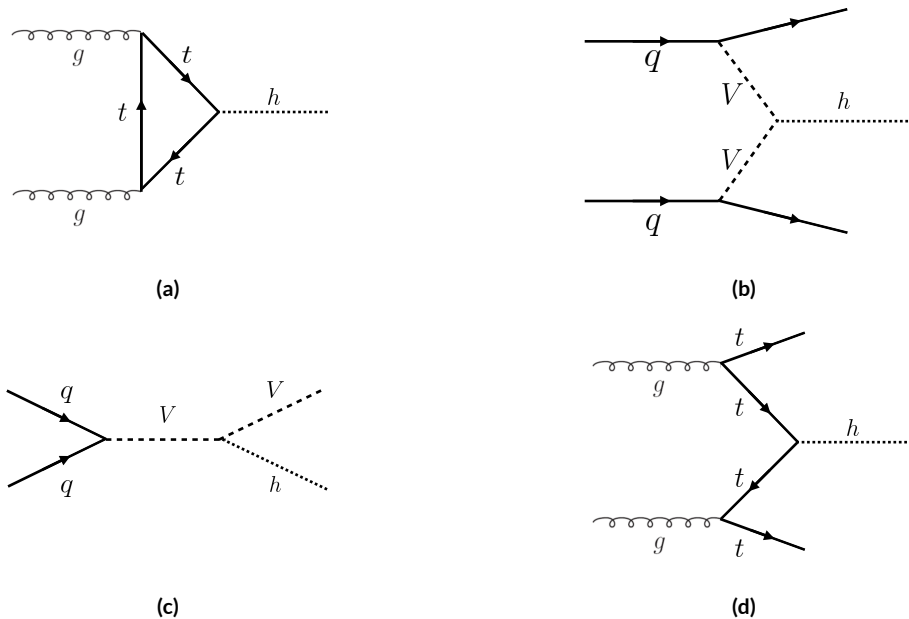


Figure 1.2: The four most common Higgs boson production modes at the LHC: (a) gluon-gluon fusion, (b) vector boson fusion, (c) $W/Z + H$ production, (d) $t\bar{t}H$ production

634 In gluon-gluon fusion, gluons from the incoming protons fuse via a top-quark loop to produce a
 635 Higgs. The top quark is the dominant contribution in the loop due to its heavy mass and the fact that
 636 the Higgs-fermion coupling constant scales with fermion mass. In vector boson fusion, the incoming
 637 quarks each radiate a W or Z boson which fuse to produce the Higgs. This production mode results in
 638 a final state with a Higgs boson and two additional jets which tend to be forward because they carry the

639 longitudinal momentum of the incoming partons. The Higgs can also be produced in association with a
 640 W or Z boson. The W/Z is produced normally and then radiates a Higgs (this mode is also sometimes
 641 known as “Higgs-strahlung”). Finally, the Higgs can be produced in association with two top quarks.
 642 Each incoming gluon splits into a $t\bar{t}$ pair, and one of the top pairs combines to create a Higgs.

643 Figure 1.3 shows the production cross section for a 125 GeV Higgs boson in each of these modes at a
 644 pp collider as a function of center of mass energy.

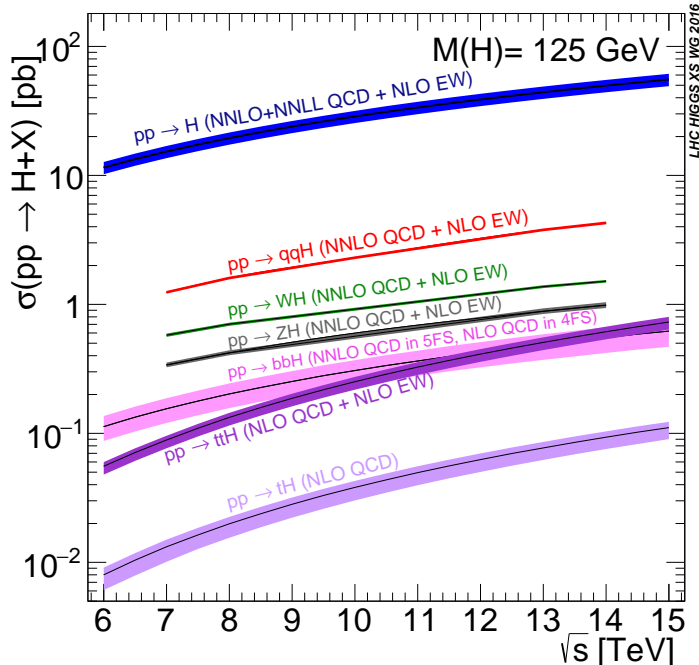


Figure 1.3: Higgs production cross sections as a function of center of mass energy (\sqrt{s}) at a pp collider[2].

645 In figure 1.3, note that gluon fusion has the largest cross section, while VBF is the second largest at
 646 approximately a factor of 10 smaller. The figure also includes the less commonly studied $b\bar{b}H$ and tH
 647 modes. The $b\bar{b}H$ and tH modes are not studied as commonly as $t\bar{t}H$ due to the larger background con-
 648 tributions and lower cross sections, respectively. At $\sqrt{s} = 8$ TeV, ggF production of a 125 GeV Higgs
 649 has a cross section of 19.47 pb, while VBF has a cross section of 1.601 pb[2]. The cross sections of all
 650 of the main Higgs production modes at this center of mass energy, as well as their uncertainties from
 651 varying the renormalization and factorization scales and PDFs, are summarized in table 1.1 for a 125 GeV
 652 Higgs.

Production mode	σ (pb)	QCD scale uncert. (%)	PDF + α_s uncert. (%)
Gluon fusion	19.47	+7.3 / - 8.0	3.1
Vector boson fusion	1.601	+0.3 / - 0.2	2.2
WH	0.7026	+0.6 / - 0.9	2.0
ZH	0.4208	+2.9 / - 2.4	1.7
$t\bar{t}H$	0.1330	+4.1 / - 9.2	4.3
$b\bar{b}H$	0.2021	+20.7 / - 22.3	
tH (t -channel)	0.01869	+7.3 / - 16.5	4.6
tH (s -channel)	1.214×10^{-3}	+2.8 / - 2.4	2.8

Table 1.1: Production cross sections for a 125 GeV Higgs boson at $\sqrt{s} = 8$ TeV with scale and PDF uncertainties [2].

653 1.3.2 HIGGS BRANCHING RATIOS

654 The fact that the Higgs couples more strongly to more massive particles is crucial for understanding its
 655 branching ratios. The width for Higgs decays to fermions is given in equation 1.14 [29].

$$\Gamma(H \rightarrow f\bar{f}) = \frac{N_c \sqrt{2} G_F m_f^2 m_H}{8\pi} \quad (1.14)$$

656 In this case, N_c is the number of colors, G_F is the Fermi constant, m_f is the mass of the fermion, and
 657 m_H is the mass of the Higgs. Note that the width scales with the square of the fermion mass. (This also
 658 assumes that the Higgs mass is large enough to decay with both the fermions on shell.)

659 The decay width to WW is given in equation 1.15 [29].

$$\Gamma(H \rightarrow W^+W^-) = \frac{\sqrt{2} G_F M_W^2 m_H}{16\pi} \frac{\sqrt{1-x_W}}{x_W} (3x_W^2 - 4x_W + 4) \quad (1.15)$$

660 where m_W is the mass of the W and $x_W = 4M_W^2/m_H^2$. To get the branching ratio to ZZ , the
 661 equation is divided by 2 to account for identical particles in the final state, and x_W is replaced with
 662 $x_Z = 4M_Z^2/m_H^2$. This is shown in equation 1.16 [29].

$$\Gamma(H \rightarrow ZZ) = \frac{\sqrt{2} G_F M_Z^2 m_H}{32\pi} \frac{\sqrt{1-x_Z}}{x_Z} (3x_Z^2 - 4x_Z + 4) \quad (1.16)$$

663 These formulas can also be visualized as a function of Higgs mass. Figure 1.4 shows the branching

664 ratios as a function of the Higgs mass.

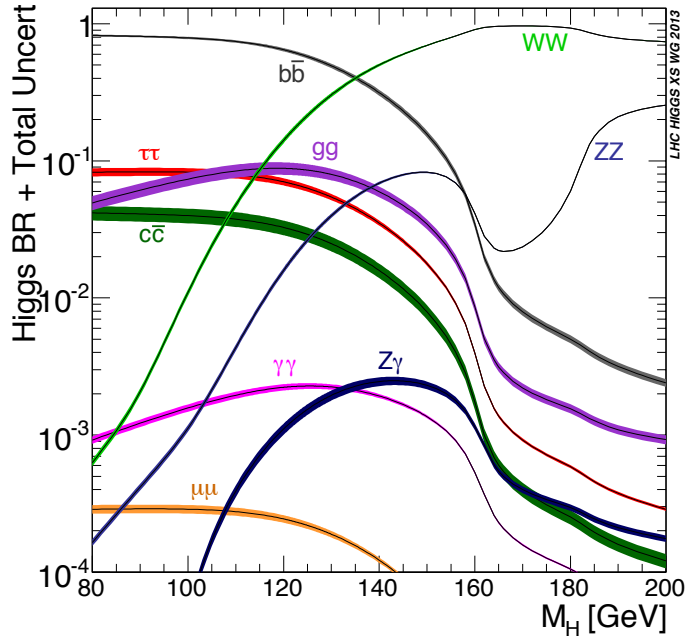


Figure 1.4: Higgs boson branching ratios as a function of m_H [2].

665 There are a few interesting features to note in this figure. First, note that at high Higgs masses, once
 666 on-shell production of both W and Z bosons is possible, these two decays are the dominant ones due to
 667 the large masses of the W/Z . Also note that the branching ratio to W s is twice that of Z s at these large
 668 masses due to the δ_V symmetry factor noted previously. At 125 GeV, the Higgs is accessible through
 669 many different decay modes. The largest branching ratio is the decay $H \rightarrow b\bar{b}$ at 58.24% [2]. This
 670 branching is larger than the WW/ZZ decays because one of the two bosons must be produced off-
 671 shell for $m_H = 125$ GeV. The second largest branching ratio is to WW^* at 21.37 % (before taking
 672 into account the branching ratios of the W). Table 1.2 summarizes the branching ratios for a 125 GeV
 673 Higgs. Note that there is in fact a Higgs branching ratio to $\gamma\gamma$ even though photons are massless. This
 674 decay happens through a loop (the largest contributions to the loop are top and W) which suppresses
 675 the branching ratio.

676 Note that the branching ratios alone do not tell the full story of which Higgs channels are the most
 677 sensitive. For example, a $H \rightarrow b\bar{b}$ search in gluon fusion production is incredibly difficult due to the

Decay	Branching ratio (%)
$b\bar{b}$	58.24
WW^*	21.37
gg	8.187
$\tau\tau$	6.272
$c\bar{c}$	2.891
ZZ^*	2.619
$\gamma\gamma$	0.2270
$Z\gamma$	0.1533
$\mu\mu$	0.02176

Table 1.2: Branching ratios for a 125 GeV Higgs boson[2].

large QCD dijet background at the LHC. However, in associated production of the Higgs, where a W or Z gives additional final state particles that can be used to reduce background, a search for $H \rightarrow b\bar{b}$ can be sensitive. The combinations of production and decay modes that are most commonly studied are summarized in table 1.3 [29].

Decay	Inclusive (incl. ggF)	VBF	WH/ZH	$t\bar{t}H$
$H \rightarrow \gamma\gamma$	✓	✓	✓	✓
$H \rightarrow b\bar{b}$			✓	✓
$H \rightarrow \tau^+\tau^-$		✓		
$H \rightarrow WW^* \rightarrow \ell\nu\ell\nu$	✓	✓	✓	
$H \rightarrow ZZ \rightarrow 4\ell$	✓			
$H \rightarrow Z\gamma \rightarrow \ell\ell\gamma$	very low			

Table 1.3: Possible channels for Higgs searches. Checkmarks denote the most sensitive production modes [29].

1.4 HIGGS PAIR PRODUCTION IN THE STANDARD MODEL

The Standard Model also allows for processes that produce two Higgs bosons in the final state, known as Higgs pair production or di-Higgs production. The two main production mechanisms are shown in figure 1.5.

The two diagrams in figure 1.5 interfere destructively with one another, resulting in a low overall cross section for di-Higgs production at the LHC. Nevertheless, Higgs pair production is quite interesting to study because it gives direct access to the λ parameter of the Higgs potential, also known as the Higgs self

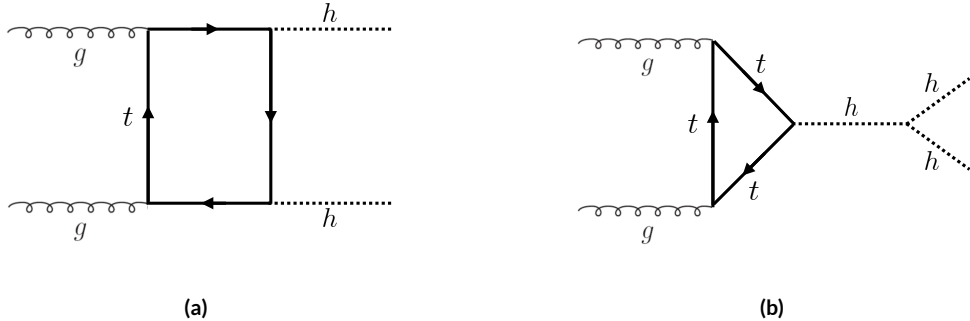


Figure 1.5: The two leading diagrams for Standard Model di-Higgs production at the LHC: (a) box diagram, (b) Higgs self coupling

coupling. The diagram in figure 1.5(b) is sensitive to this coupling through the triple Higgs vertex.

One can substitute the gluon fusion production of diagram 1.5(b) with any of the other production modes previously discussed. These other modes do not suffer from interference with the box diagram in figure 1.5(a) due to the presence of additional particles in the final state. They still have a lower cross section than the gluon fusion mode, however. The cross sections for di-Higgs production in the different modes, as well as their uncertainties, are shown in table 1.4 [30]. These are shown for $\sqrt{s} = 14$ TeV as the higher center of mass energy is more sensitive to this process. Note that the scale of cross section quoted is now in fb rather than pb.

Production mode	σ (fb)	Total uncrt. (%)
Gluon fusion	33.89	+37.2 / - 27.8
Vector boson fusion	2.01	+7.6 / - 5.1
$W H H$	0.57	+3.7 / - 3.3
$Z H H$	0.42	+7.0 / - 5.5
$t\bar{t}H$	1.02	-

Table 1.4: Production cross sections for pair production of a 125 GeV Higgs boson at $\sqrt{s} = 14$ TeV with total uncertainty [30]. The uncertainties include QCD scale and PDF variations as well as uncertainties on α_S .

696

1.5 HIGGS PAIR PRODUCTION IN THEORIES BEYOND THE STANDARD MODEL

698 The Standard Model Higgs pair production cross section is rather small, and datasets on the scale of the
699 full lifetime of the LHC will be required to obtain sensitive measurements of the Higgs self-coupling.

700 However, the discovery of the Higgs also gives particle physicists a new tool that can be exploited in the
 701 search for new physics beyond the Standard Model. In particular, Higgs pair production is a promising
 702 channel in the search for new physics. The cross section for di-Higgs production can be altered through
 703 both resonant and non-resonant production of Higgs pairs. In non-resonant production, di-Higgs pro-
 704 duction vertices can arise from the presence of a new strong sector and additional colored particles[48–
 705 50]. Figure 1.6 shows examples of the types of vertices that can arise. In the resonant case, new heavy
 706 particle can decay to Higgs pairs. Such new particles can include heavy Higgs bosons arising in two
 707 Higgs doublet models (2HDM) or Higgs portal models as well as heavy gravitons in Randall-Sundrum
 708 theories[3, 5, 48, 51–55]. Figure 1.7 shows a generic diagram for a heavy resonance decaying to two Higgs
 709 bosons. In the 2HDM, X corresponds to the heavy CP-even scalar H . In the Randall-Sundrum model,
 710 X corresponds to a heavy spin-2 graviton G .

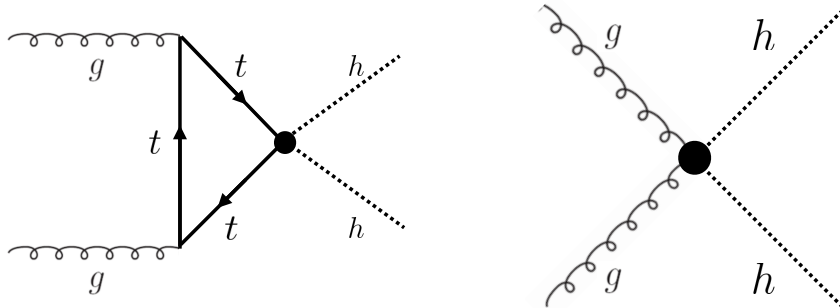


Figure 1.6: Diagrams with new vertices for non-resonant Higgs pair production arising in composite Higgs models

711 The next sections provide more detail on the phenomenology of resonant Higgs production in
 712 Randall-Sundrum and 2HDM models, as these models will later be tested in a dedicated search for reso-
 713 nant production of boosted Higgs pairs.

714 1.5.1 RANDALL-SUNDRUM GRAVITONS

715 The Randall-Sundrum model is a proposed solution to the hierarchy problem that posits a five-dimensional
 716 warped spacetime that contains two branes: one where the force of gravity is very strong and a second
 717 brane at the TeV scale corresponding to the known Standard Model sector [51]. In the theory, the
 718 branes are weakly coupled and the graviton probability function drops exponentially going from the

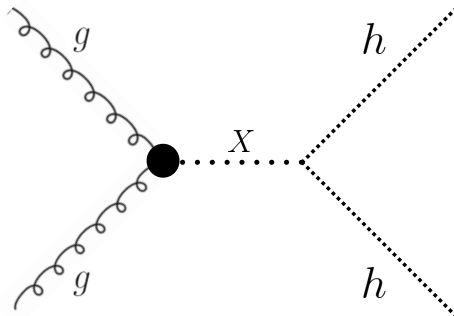


Figure 1.7: Generic Feynman diagram for resonant Higgs pair production in BSM theories

719 gravity brane to the SM brane, rendering gravity weak on the SM brane. The experimental consequence
 720 of this theory is a tower of widely spaced (in mass) Kaluza-Klein graviton resonances. In theories where
 721 the fermions are localized to the SM brane, production of gravitons from fermion pairs is suppressed
 722 and the primary mode of production is gluon fusion[3]. These gravitons have a substantial branching
 723 fraction to Higgs pairs, ranging from 6.43% for gravitons with a mass of 500 GeV to 7.66% at 3 TeV.
 724 Figure 1.8 shows the branching ratios of the spin-2 Randall Sundrum graviton (RSG) as a function of its
 725 mass. The predominant decays are to $t\bar{t}$ above the mass threshold for that channel.

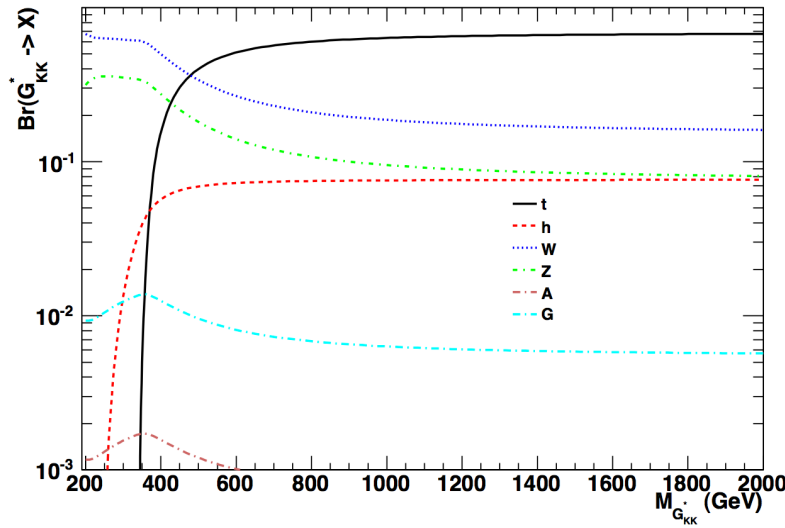


Figure 1.8: Branching ratios for a spin-2 Randall-Sundrum graviton as a function of mass computed in MadGraph with the CP3-Origins implementation [3, 4]

726 These models have two free parameters - the mass of the graviton and a curvature parameter k . Typ-

727 ically, rather than k , the theory is parameterized using $c \equiv k/\bar{M}_{\text{pl}}$, where \bar{M}_{pl} is the reduced Planck
 728 mass. The cross section for production of the RSG decreases as a function of mass and is strongly depen-
 729 dent on the gluon PDF. The increase in center of mass energy from 8 to 13 TeV in LHC Run 2 greatly
 730 increases the cross section at higher mass. Figure 1.9 shows the cross section as a function of graviton
 731 mass at $\sqrt{s} = 13$ TeV for RSG models with $c = 1.0$ and $c = 2.0$.

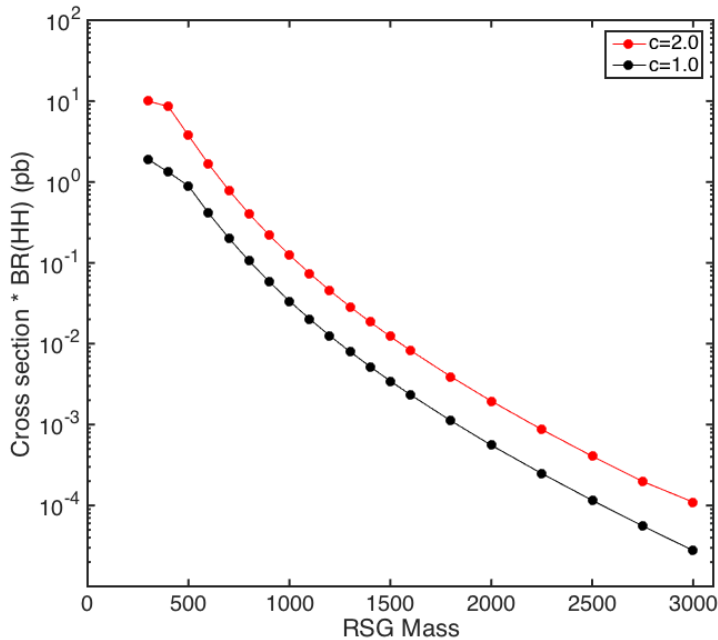


Figure 1.9: $\sigma \times \text{BR}(HH)$ for RSG as a function of mass computed in MadGraph with the CP3-Origins implementation [3, 4]

732 Another interesting feature of the theory is that the width of the graviton increases with both c and
 733 m_G . Figure 1.10 shows the graviton width for both $c = 1.0$ and $c = 2.0$ as a function of mass. In
 734 $c = 1.0$, the width starts at 8.365 GeV for a mass of 300 GeV and increases to 187.2 GeV at a mass of
 735 3 TeV. Similarly, with $c = 2.0$, the width starts at 33.46 GeV for $m_G = 300$ GeV and increases to
 736 748.8 GeV at a mass of 3 TeV.

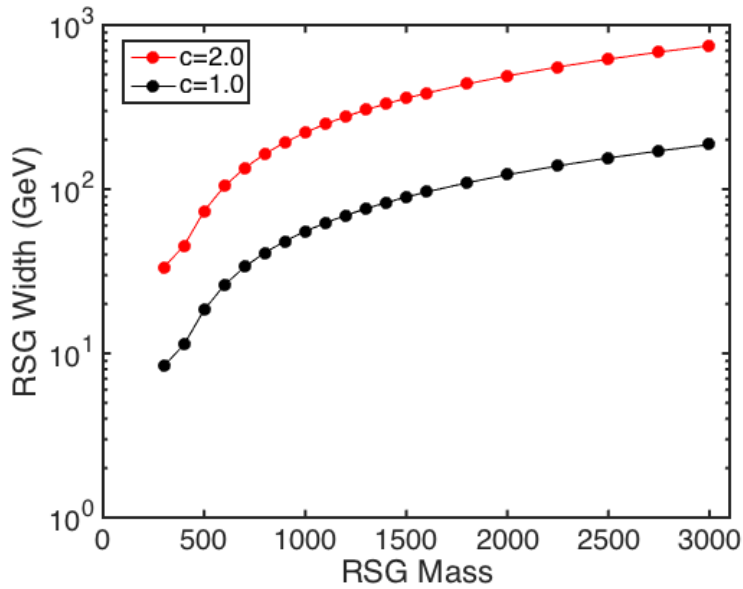


Figure 1.10: RSG width as a function of mass computed in MadGraph with the CP3-Origins implementation [3, 4]

737 1.5.2 TWO HIGGS DOUBLET MODELS

738 In Two Higgs Doublet Models (2HDM), a second complex scalar doublet is added to SM[5, 53, 54]. In
 739 this case, all four degrees of freedom in the second doublet correspond to new particles, meaning that
 740 there are five total scalars from the two Higgs doublets - h (light CP-even Higgs), H (heavy CP-even
 741 Higgs), A (heavy CP-odd Higgs), and H^\pm (charged Higgs). The model is parameterized by two main
 742 parameters. The first, $\tan \beta \equiv \frac{v_2}{v_1}$, is the ratio of the vacuum expectation values of the two Higgs dou-
 743 blets (where v_1 corresponds to the v in the SM Higgs model described above). The second parameter
 744 is α , a mixing angle between the heavy and light Higgs fields. Models are also often parameterized with
 745 $\cos(\beta - \alpha)$ rather than α directly. The limit where $\cos(\beta - \alpha) = 0$ is called the alignment limit, and
 746 it is in this limit that the light Higgs h has the same couplings as a Standard Model Higgs.

747 2HDM models are usually separated into two main types - Type I and Type II. In Type I models, the
 748 charged fermions only couple to the second Higgs doublet, leading to a fermiophobic light Higgs. In
 749 Type II models, up-type quarks couple to the first doublet while down-type quarks couple to the second
 750 doublet. One specific realization of a Type II 2HDM is the Minimal Supersymmetric Standard Model
 751 (MSSM).

752 Resonant di-Higgs production in this model can proceed through decays of the heavy CP-even Higgs
 753 $H \rightarrow hh$. The branching ratio for $H \rightarrow hh$ depends on the model type as well as the values of $\tan \beta$
 754 and $\cos(\beta - \alpha)$. Figure 1.11 shows the branching ratios as a function of the mass of the heavy scalar H for
 755 both Type I and Type II models. Depending on the type of model hh can be a substantial fraction of the
 756 decays of H .

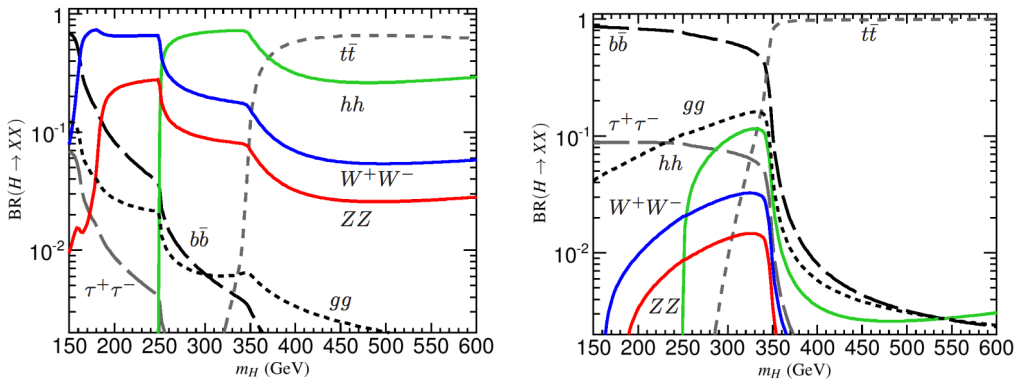


Figure 1.11: Branching ratios for heavy Higgs H in Type I (left) and Type II (right) 2HDM models with $\tan \beta = 1.5$ and $\cos(\beta - \alpha) = 0.1$ (Type I) (0.01 for Type II). [5]

757 1.6 CONCLUSION

758 Studying the Higgs sector is essential for understanding the details of how mass arises in the Standard
 759 Model and how the electroweak symmetry is broken. The discovery of the Higgs boson also opens the
 760 door for its use as a tool to search for new physics, and Higgs pair production is an ideal candidate for
 761 this study. Even if no BSM physics is found in Higgs pair production, searches for Higgs pairs will put
 762 constraints on the Higgs self coupling and thus further knowledge of the Standard Model and the details
 763 of the Higgs potential.

This is some random quote to start off the chapter.

Firstname lastname

2

764

765

766

The ATLAS detector and the Large Hadron Collider

767 This chapter presents an overview of the experimental systems used to conduct the measurements pre-
768 sented in this thesis. First, a brief overview of the accelerator, the Large Hadron Collider, will be given.
769 In this section, the accelerator conditions relevant to data-taking are presented as well. Next, an overview
770 of the ATLAS experiment is given. The basics of each sub-detector's role are summarized, as well as the
771 details of the datasets accumulated. Then, a brief interlude on the ATLAS Muon New Small Wheel up-
772 grade is presented. While this new detector does not have a direct impact on any of the datasets taken
773 so far, it will have an impact on future analyses and the work done on it is briefly summarized here. Fi-
774 nally, an overview of object reconstruction in ATLAS is given. While the details of all of the algorithms
775 will not be presented in detail, aspects of the reconstruction performance such as object resolutions are
776 shown as these are relevant to the two studies presented later in this thesis.

777 2.1 THE LARGE HADRON COLLIDER

778 The Large Hadron Collider (LHC) is a proton-proton collider at the CERN laboratory in Geneva,
779 Switzerland[56]. It is designed for a maximum collision center of mass energy of $\sqrt{s} = 14 \text{ TeV}$ and
780 has a circumference of 26.7 kilometers. Four main experiments are located at the interaction points (IP)
781 of the accelerator: ATLAS (A Toroidal LHC ApparatuS), CMS (the Compact Muon Solenoid), ALICE
782 (A Large Ion Collider Experiment), and LHCb [7, 57–59]. The studies performed in this thesis were all
783 completed with the ATLAS detector.

784 Figure 2.1 shows a schematic of the LHC ring and the various experiments.

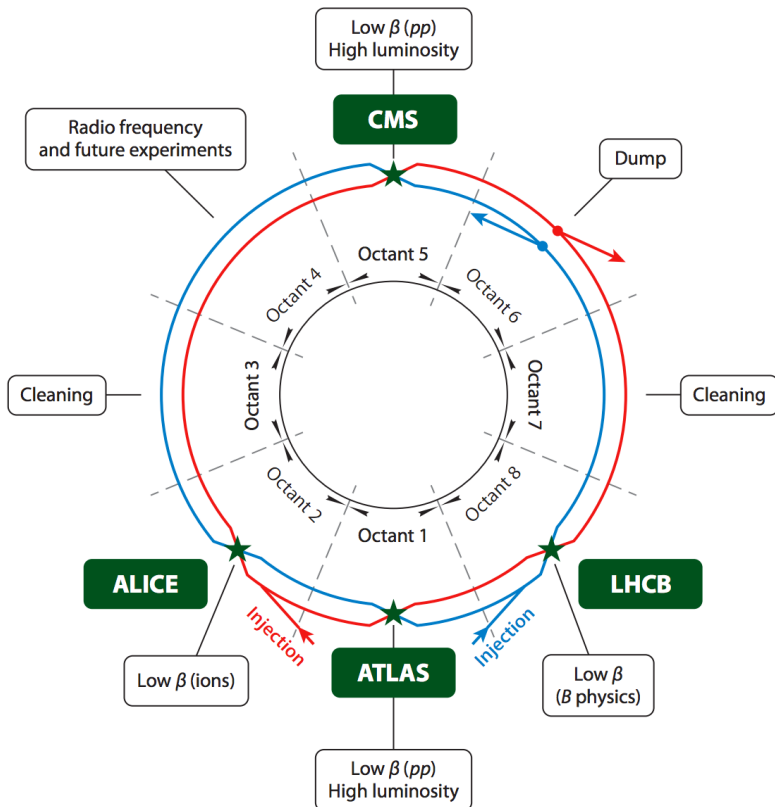


Figure 2.1: A schematic view of the LHC ring [6]

785 One of the most interesting features of the LHC is in its magnet design. Because the tunnel does not
786 have room for separate superconducting magnets for each of the beam pipes, the LHC employs a twin-
787 bore magnet design. Each magnet must hold an 8.3 Tesla magnetic field in order to bend the proton

788 beams at $\sqrt{s} = 14$ TeV. The superconducting magnets are cooled to a temperature of 1.9 Kelvin with
 789 superfluid helium.

790 2.1.1 INSTANTANEOUS LUMINOSITY

791 The rate of physics events expected from the accelerator is dependent on the instantaneous luminosity
 792 of the machine and the cross section of the physics process, $R_{\text{events}} = L\sigma$. Here, R_{events} is the number
 793 of events per second, L is the instantaneous luminosity of the machine, and σ is the cross section for the
 794 physics process being measured. The instantaneous luminosity of the LHC is determined by numerous
 795 factors related to machine conditions. Equation 2.1 gives the equation for instantaneous luminosity of
 796 Gaussian beam profile [6].

$$L = \frac{N_b^2 n_b f_{\text{rev}} \gamma_r}{4\pi \epsilon_n \beta^*} F \quad (2.1)$$

797 The LHC collides protons in bunches, and in the above equation N_b is the number of protons per
 798 bunch while n_b is the number of bunches per beam. Nominally, the LHC can hold up to 2808 pro-
 799 ton bunches. f_{rev} is the revolution frequency. ϵ_n is the normalized transverse beam emittance, a mea-
 800 surement of the average spread of the particles position-momentum space which has the dimension of
 801 length. β^* is the value of the *beta* function for the beam at the interaction point. It relates the emmi-
 802 tance to the Gaussian width of the beam with $\sigma_{\text{beam}} = \sqrt{\epsilon \cdot \beta}$. F is a reduction factor that corrects for
 803 the fact that the beams are colliding at an angle at the IP.

804 Another way of writing the instantaneous luminosity is shown in equation 2.2. In this case, the in-
 805 stantaneous luminosity is written as the ratio of the rate of inelastic collisions with the inelastic cross
 806 section[60].

$$L = \frac{R_{\text{inel}}}{\sigma_{\text{inel}}} = \frac{\mu n_b f_{\text{rev}}}{\sigma_{\text{inel}}} \quad (2.2)$$

807 In this case, μ is the average number of interactions per bunch crossing in the accelerator. μ is a useful
 808 parameter for characterizing the amount of activity recorded in an experiment. As the instantaneous

809 luminosity and thus μ increase, there are more interactions per bunch crossing and more activity in the
 810 detector. This is often characterized with $\langle \mu \rangle$, the measured per bunch crossing μ value averaged over
 811 all bunch crossings. The interactions inside each bunch crossing that are not the main physics process of
 812 interest are often referred to as “pileup” interactions, and $\langle \mu \rangle$ is a measurement of the level of pileup in
 813 the detector.

814 2.1.2 EVOLUTION OF MACHINE CONDITIONS

815 This thesis uses datasets taken at three different center of mass energies: $\sqrt{s} = 7$ TeV data taken in the
 816 year 2011, $\sqrt{s} = 8$ TeV data taken in the year 2012, and $\sqrt{s} = 13$ TeV dataa taken in the year 2015. In
 817 addition to increasing center of mass energy, the instananeous luminosity and parameters that determine
 818 it were evolving. Table 2.1 summarizes that machine conditions in each of these datasets.

	2011	2012	2015	Design
\sqrt{s} [TeV]	7	8	13	14
Number of bunches	1380	1380	1825	2808
Max. protons per bunch	1.45×10^{11}	1.7×10^{11}		1.15×10^{11}
Bunch spacing [ns]	50	50	25	25
Max. instantaneous luminosity [$\text{cm}^{-2}\text{s}^{-1}$]	3.7×10^{33}	7.7×10^{33}	5×10^{33}	10^{34}
β^* [m]	1.0	0.6	0.8	0.55
$\langle \mu \rangle$	11.6	20.7	13.7	-

Table 2.1: Evolution of LHC machine conditions [31, 32]

819 2.2 THE ATLAS DETECTOR

820 The ATLAS detector is a multi-purpose particle detector experiment at the LHC’s Point 1 [7]. It has
 821 nearly 4π coverage in solid angle around the interaction point. It consists of an inner detector for mea-
 822 suring charged particles, electromagnetic and hadronic calorimeters, and a muon spectrometer. Fig-
 823 ure 2.2 gives an overview of the detector.

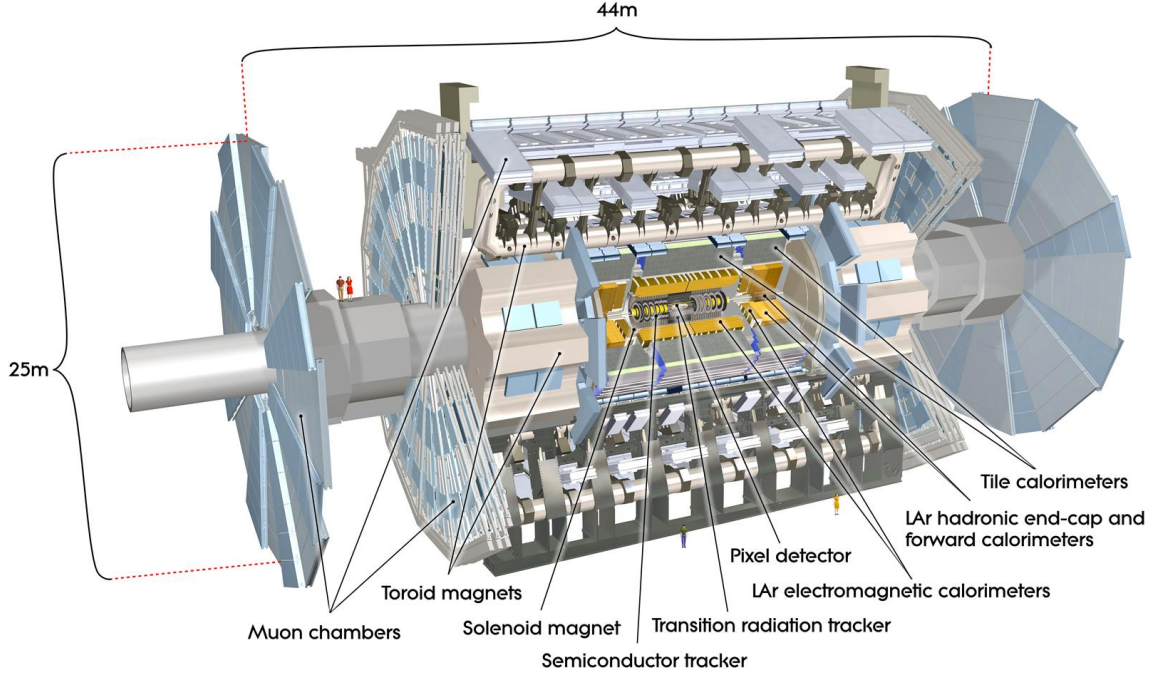


Figure 2.2: A full diagram of the ATLAS detector [7]

824 2.2.1 COORDINATE SYSTEM

825 Before defining the properties of the individual detectors, it is important to establish the coordinate
 826 system used. Figure 2.3 shows a schematic of the coordinate system. The azimuthal plane (perpendicular
 827 to the beam line) is defined as the x - y plane. The angle in this plane is referred to as ϕ . The angle relative
 828 to the beam axis is referred to as θ . Rather than using θ directly as a coordinate, the experiment often
 829 uses the pseudorapidity η . η is defined in equation 2.3.

$$\eta = \ln \left(\tan \left(\frac{\theta}{2} \right) \right) \quad (2.3)$$

830 Pseudorapidity is the massless approximation of rapidity, the angle used to parameterize boosts in
 831 special relativity. This is important for two reasons. First, it means that differences in η are Lorentz in-
 832 variant. Second, particle production is roughly constant in pseudorapidity. Particles with η close to zero
 833 are referred to as “central”, while those at high $|\eta|$ are called “forward”. In general, two main detector

834 topologies can be seen in figure 2.2. There are “barrel” elements, which surround the beam line cylind-
 835 drically and are in the central region of the detector. In the forward region, there are “endcap” regions
 836 which are arranged as disks perpendicular to the beam line.

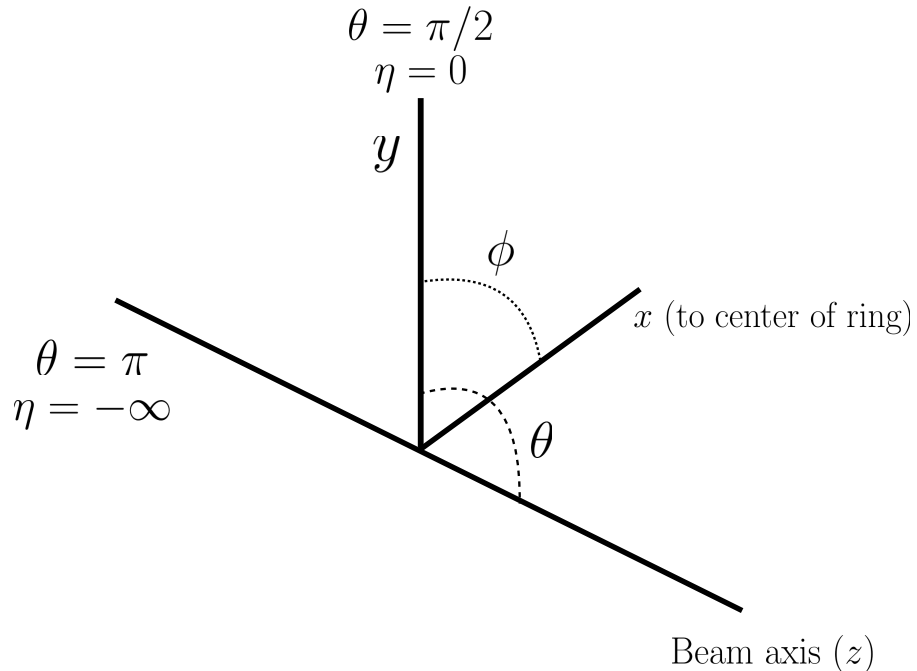


Figure 2.3: The ATLAS coordinate system

837 2.2.2 INNER DETECTOR

838 The ATLAS Inner Detector (ID) system is built for precision tracking of charged particles. It covers the
 839 range $|\eta| < 2.5$. In this range, approximately 1000 particles are generated every bunch crossing in the
 840 detector. This requires having fine granularity to achieve the resolutions required for good momentum
 841 measurement and vertex reconstruction.

842 The ID consists of three sub-components: the pixel detector, semiconductor tracker (SCT), and trans-
 843 sition radiation tracker (TRT). It is surrounded by a solenoid providing a 2 T axial magnetic field which
 844 bends particles in the transverse plane to allow for momentum measurement. Figure 2.4 shows the layout
 845 of each of these components.

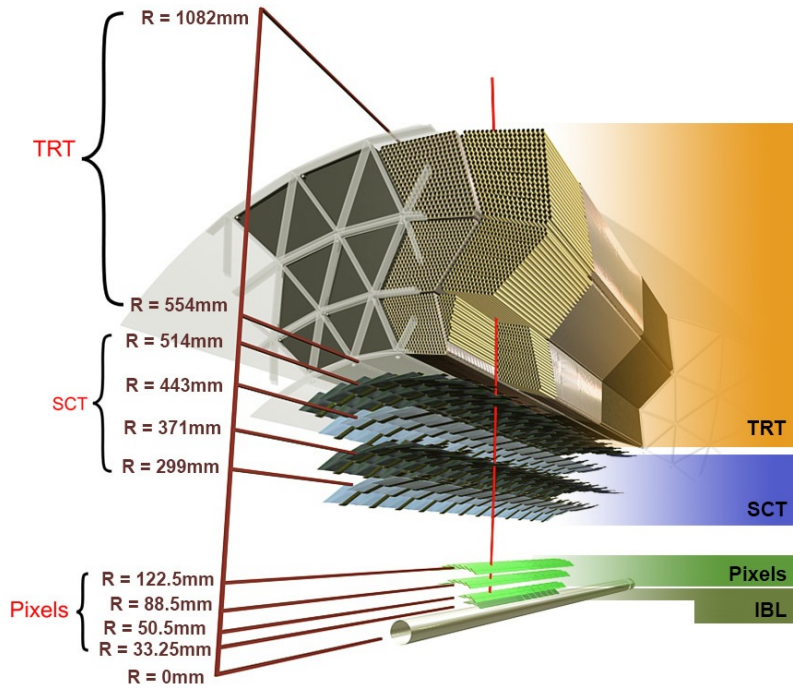


Figure 2.4: Layout of the ATLAS Inner Detector system [8]

846 PIXEL DETECTOR

847 The pixel detector is the first detector particles traverse after being generated in proton collisions and is
 848 the most granular detector. Its operation is crucial for precision tracking and vertex reconstruction as
 849 well as higher level object reconstruction like tagging of jets from b -quarks. The basic sensing element in
 850 this subdetector is a silicon pixel detector. The operating principle for the silicon pixels is that of a p - n
 851 junction. When a charged particle passes through, it creates electron-hole pairs that are then separated
 852 by the electric field. The sensors are $250 \mu\text{m}$ thick and use oxygenated n -type wafers with readout pixels
 853 on the n^+ side of the detector [7]. Overall, the pixel detector has 1744 sensors and 80.4 million readout
 854 channels.

855 In the barrel region, the pixel detector has three concentric layers of sensors surrounding the beam-
 856 line. In the endcap region, it consists of disks perpendicular to the beam axis. The detector is segmented
 857 in the R - ϕ plane and in z . Usually, three pixel layers are crossed by a charged particle track. The intrinsic
 858 accuracies of the sensors are $10 \mu\text{m}$ in R - ϕ and $115 \mu\text{m}$ in z (or R for the endcap).

859 **INSERTABLE B-LAYER**

860 In Run 2, a new innermost pixel layer, known as the insertable B-layer (IBL), was added to the Inner
861 Detector [61]. This layer was added to cope with the higher luminosities planned in LHC Run 2 and
862 at the high luminosity HL-LHC. Additionally it improves tracking position resolution which in turn
863 improves the vertexing and b -tagging capabilities in ATLAS. The detector sits directly on a new beam
864 pipe, only 33.25 mm away from the collision points in the azimuthal plane.

865 **SEMICONDUCTOR TRACKER (SCT)**

866 The semiconductor tracker (SCT) consists of silicon microstrips and comprises the next four layers of
867 the ID. This sub-detector has 6.4cm long sensors that are daisy-chained into strips with a strip pitch of
868 $80 \mu\text{m}$ [7]. Some of the strips have a small stereo angle to allow for measurement of both angular coor-
869 dinates. In total there are 6.3 million readout channels. The intrinsic accuracies are $17 \mu\text{m}$ in $R\text{-}\phi$ and
870 $580 \mu\text{m}$ in z (or R in the endcap).

871 **TRANSITION RADIATION TRACKER (TRT)**

872 The transition radiation tracker (TRT) serves two purposes. First, it consists of 4mm diameter straw
873 tubes filled with a 70/27/3% gas mixture of xenon, carbon dioxide, and oxygen to provide tracking of
874 charged particles. Particles typically have 36 TRT straw tube hits per track. The material in between
875 the straws is designed to induce transition radiation which can be useful for particle identification. As
876 particles pass between media with different dielectric constants, they emit transition radiation that can
877 cause additional showers in the TRT. In particular it is useful for discrimination between electrons and
878 pions or other charged hadrons, as the amount of transition radiation is proportional to the Lorentz
879 factor of the particle.

880 **2.2.3 CALORIMETERS**

881 The calorimeter system consists of two main sub-components: a fine granularity electromagnetic calorime-
882 ter tailored for the measurement of photons and electrons and multiple coarser hadronic calorimeters

883 dedicated to the measurement of hadronic showers [7]. The calorimeter system has broader coverage
884 than the inner detector, covering the region out to $|\eta| < 4.9$. It is also designed to deliver good contain-
885 ment of showers so as to limit leakage into the muon system. Figure 2.5 shows the layout of the calorime-
886 ter system.

887 Both the electromagnetic and hadronic calorimeters are sampling calorimeters. They alternate active
888 material for energy measurement with passive material for energy absorption. The materials used for
889 each purpose vary based on the type of calorimeter and its location in the detector.

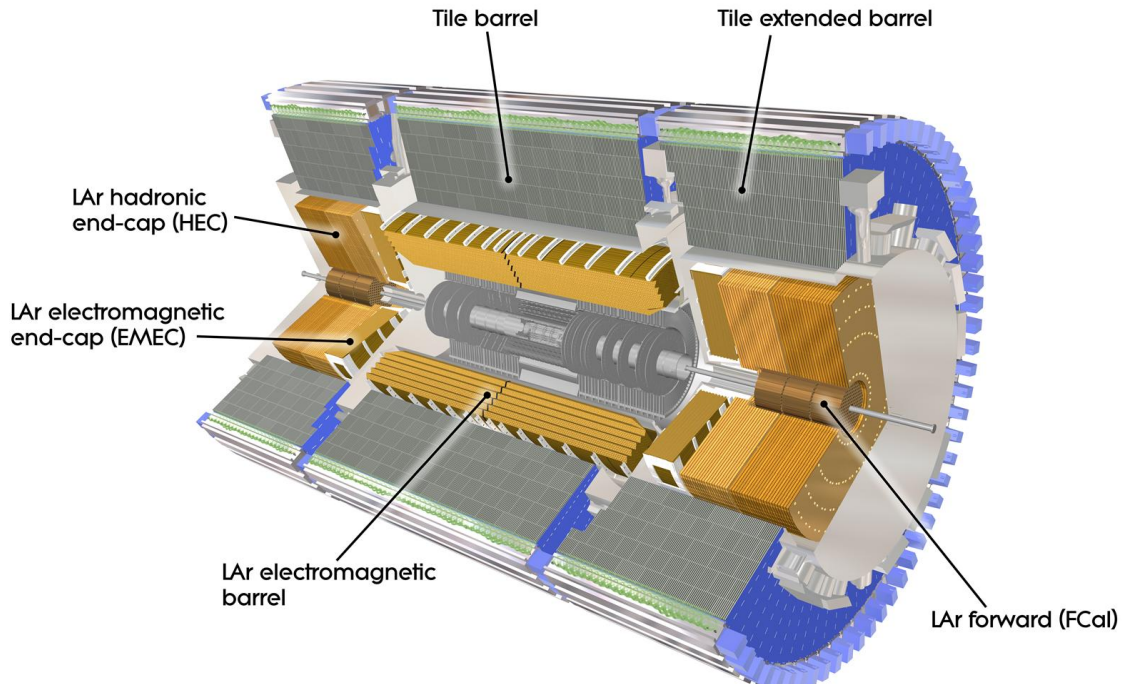


Figure 2.5: Layout of the ATLAS calorimeter system [7]

890 ELECTROMAGNETIC CALORIMETER

891 The electromagnetic calorimeter (EM calorimeter) use liquid Argon (LAr) as its active material and lead
892 as its passive material. It is arrange in an accordion geometry to increase the absorption area while still
893 allowing it to have no azimuthal cracks (complete symmetry in ϕ). The EM calorimeter is divided into a

894 barrel portion that extends to $|\eta| < 1.475$ and an endcap portion going from $1.375 < |\eta| < 3.2$. The
895 region where these two units overlap is called the “transition region”.

896 In order to provide good containment the calorimeter depth must be optimized. Typically, for elec-
897 tromagnetic calorimeters the depth is measured in radiation lengths. In general, the intensity of a par-
898 ticle beam attenuates exponentially in distance with a constant equal to the radiation length. That is,
899 $I(x) = I_0 e^{-x/X_0}$, where I is the intensity, x is the distance traveled, and X_0 is the radiation length.
900 The ATLAS EM calorimeter is designed to have > 22 radiation lengths in the barrel and > 24 in the
901 endcap [7].

902 **HADRONIC CALORIMETERS**

903 There are three types of hadronic calorimeters present in ATLAS: the tile calorimeter (TileCal), hadronic
904 endcap (HEC), and forward calorimeter (FCal). Each one is optimized for stopping of hadronic showers
905 and the materials chosen are specific to their placement in the detector.

906 The TileCal is a scintillating tile calorimeter placed directly outside the EM calorimeter. It uses steel as
907 the absorber and plastic scintillator tiles as the active material. It has coverage in the barrel at $|\eta| < 1.0$
908 and in the “extended barrel” region of $0.8 < |\eta| < 1.7$.

909 The HEC had two wheels perpendicular to the beam line per endcap and is located directly behind
910 the EM calorimeter endcap modules. The HEC covers the region from $1.5 < |\eta| < 3.2$, overlapping
911 slightly with both the tile calorimeter and the forward calorimeter. Like the EM calorimeter, it uses liq-
912 uid Argon as the active material, but it uses copper as the absorber.

913 The FCal covers the most forward regions of the calorimeter system, extending to the region of $3.1 <$
914 $|\eta| < 4.9$. It again uses liquid argon as its active material. For absorber, it consists of an innermost
915 module made of copper followed by a module made of tungsten.

916 The hadronic equivalent of radiation length is called the interaction length and is denoted as λ . In the
917 barrel, the hadronic calorimeter depth is approximately 9.7λ , while in the endcap is is 10λ . The outer
918 supports contribute an additional 1.3λ . This is been shown to be sufficient to limit punch-through of
919 showers to the muon system [7].

920 2.2.4 MUON SPECTROMETER

921 The muon spectrometer is dedicated to measuring the momentum and position of muons. It consists
922 of tracking and trigger chambers which are unique in the barrel and endcap regions. The magnetic field
923 for bending of muons is provided by a system of three large air-core toroid magnets (from which ATLAS
924 derives its name.) These magnets provide 1.5 to 5.5 Tm of bending power at $0 < |\eta| < 1.4$ and approx-
925 imately 1 to 7.5 Tm in the endcap region of $1.6 < |\eta| < 2.7$. The entire muon system covers the range
926 $0 < |\eta| < 2.7$. Monitored drift tubes (MDTs) are used for tracking in the barrel and the two outer
927 layers of the endcap, while cathode strip chambers (CSCs) are used to provide tracking in the innermost
928 endcap wheel. In the barrel, resistive plate chambers (RPCs) are used as trigger chambers while thin gap
929 chambers (TGCs) are used in the endcap. Figure 2.6 shows the layout of the ATLAS muon system. The
930 entire muon system is designed with the specification of providing a 10% momentum resolution for a
931 1 TeV muon.

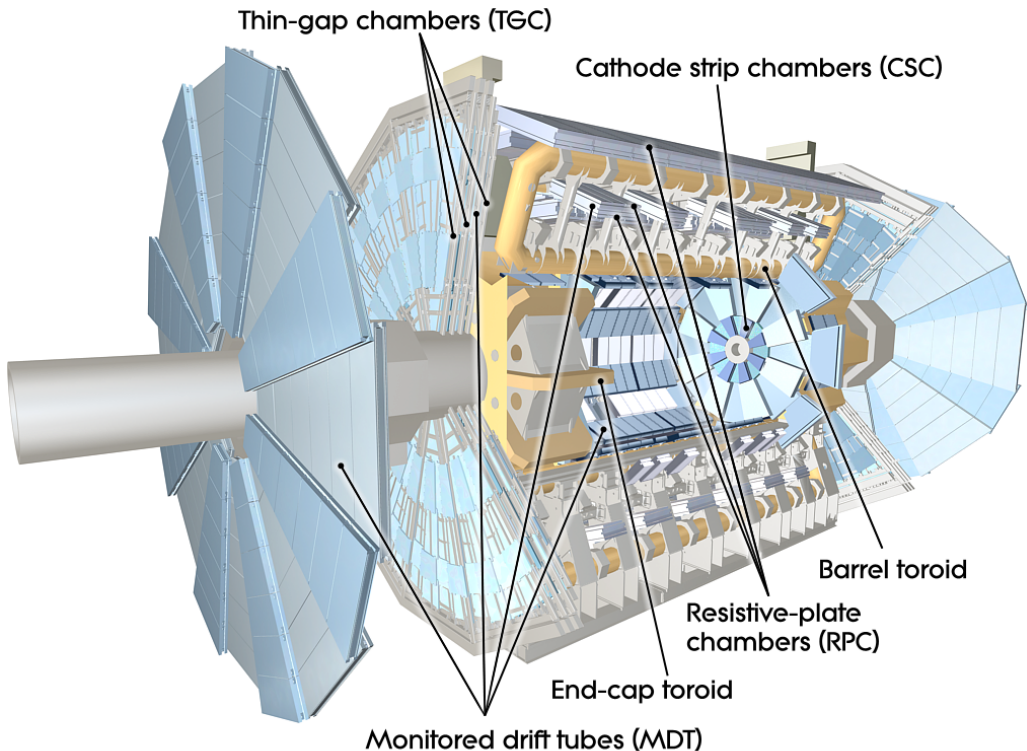


Figure 2.6: Layout of the ATLAS muon system [7]

932 MONITORED DRIFT TUBES (MDTs)

933 The monitored drift tubes (MDTs) are aluminum 3cm diameter tubes filled with a 93/7 % mixture of
934 Argon and CO₂, with trace amounts of water. As a charged particle traverses the tube, it ionizes the gas
935 and the ions drift to a wire at the center of the tube. The radial distance of traversal of the particle in the
936 tube is determined by the drift time of the electrons, allowing for fine position resolution. The tubes
937 have an average resolution of 80 μm per tube and a maximum drift time of approximately 700ns. The
938 tubes are oriented so that they give precision measurement in η and run along ϕ . They cover $|\eta| < 2.7$,
939 except in the innermost layer of the endcap where they only go to $|\eta| < 2.0$ [7].

940 CATHODE STRIP CHAMBERS (CSCs)

941 The cathode strip chambers cover a narrow window of the innermost endcap region at $2.0 < |\eta| <$
942 2.7. In this region the background rates in the cavern are particularly high and the CSCs are designed
943 to handle these higher rates. The CSCs are multiwire proportional chambers with wires pointing in
944 the radial direction (away from the beam pipe). The wire serves as an anode and there are two types of
945 segmented cathode strip, one perpendicular to the wires which gives the precision measurement and one
946 parallel which provides the transverse coordinate. It has an 80/20 gas mixture of Argon and CO₂ [7].

947 RESISTIVE PLATE CHAMBERS (RPCs)

948 The resistive plate chambers (RPCs) are gaseous electrode-plate detectors covering the region $|\eta| <$
949 1.05. They consist of two resistive plates separated by a distance of 2 mm. The gas mixture used is a
950 94.7/5/0.3% mixture of C₂H₂F₄, Iso-C₄H₁₀, and SF₆. It has readout strips with a pitch of 23-35 mm
951 for both η and ϕ measurement and thus provides measurement of the azimuthal coordinate in the barrel
952 that the MDTs do not. The thin gas gap allows for a quick response time which makes it ideal for use in
953 the trigger. There are three layers of RPCs which are referred to as the three trigger stations. They allwo
954 for both a low p_T and high p_T trigger. The coincidence of hits in the innermost chambers allows for
955 triggering of muons between 6 and 9 GeV, while the outermost layer allows the trigger to select high
956 momentum tracks in the range of 9 to 35 GeV [7].

957 THIN GAP CHAMBERS (TGCs)

958 The thin gap chambers (TGCs) are multiwire proportional chambers where the wire to cathode dis-
959 tance (1.4mm) is smaller than the wire-to-wire distance (1.8 mm). They contain a gas mixture of CO₂
960 and *n*-pentane and use a hih electric field to gain good time resolution. They serve two functions in the
961 end-cap system. First, they serve as the trigger chambers. Second, they also provide azimuthal coordi-
962 nate measurement which the MDTs do not. They sit on the inner and middle layers of the endcap. The
963 outermost layer's azimuthal coordinate is determined by extrapolation [7].

964 2.2.5 MAGNET SYSTEM

965 As mentioned previously, there are two independent magnet systems in ATLAS. The first is a 2 T solenoid
966 field in the inner detector which provides bending in the azimuthal plane. The second is an approxi-
967 mately 0.5 T toroidal field in the muon system which provides bending in η . Figure 2.7 shows the pre-
968 dicted field integral as a function of $|\eta|$ [7].

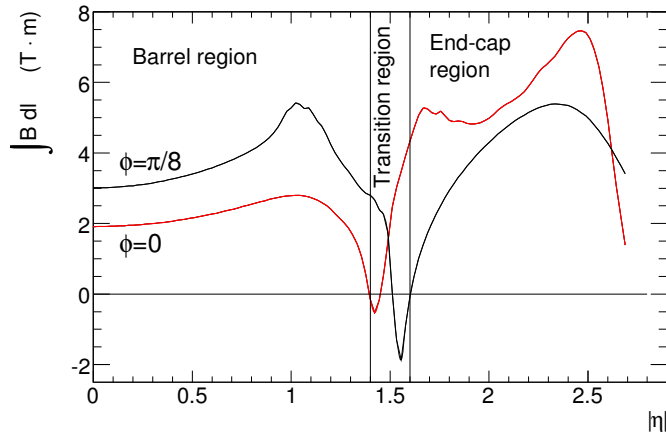


Figure 2.7: Predicted field integral as a function of $|\eta|$ for the ATLAS magnet system [7]

969 2.2.6 TRIGGER SYSTEM

970 The ATLAS trigger system searches for signatures of muons, electrons, photons, hadronically decay-
971 ing τ leptons, and jets in order to save these events for further analysis. The trigger system in ATLAS

972 is designed to reduce the maximum LHC event rate of 40 MHz to a more reasonable rate that can be
 973 recorded. The trigger first consists of a fast, hardware based system called the Level-1 (L1) trigger. The
 974 L1 trigger consists of independent dedicated detector sub-components that can seed regions of in-
 975 terest (RoIs) for further analysis downstream. For muons, the RPCs and TGCs are used, while in the
 976 calorimeter coarsely grained sections of calorimeter cells called towers are used. Once regions of interest
 977 are seeded, a software based system called the High Level Trigger (HLT) is used to reconstruct objects
 978 and integrate information from different parts of the detector. In Run 1 of ATLAS, the HLT consisted
 979 of two separate stages: the level 2 (L2) trigger and the event filter (EF).

980 The maximum trigger rate that the L1 trigger can handle is 75 kHz. In the HLT, the rate of events
 981 written to disk is approximately 200 Hz. Figure 2.8 shows the trigger rates for different L1 triggers in
 982 2012 and 2015 for ATLAS [9].

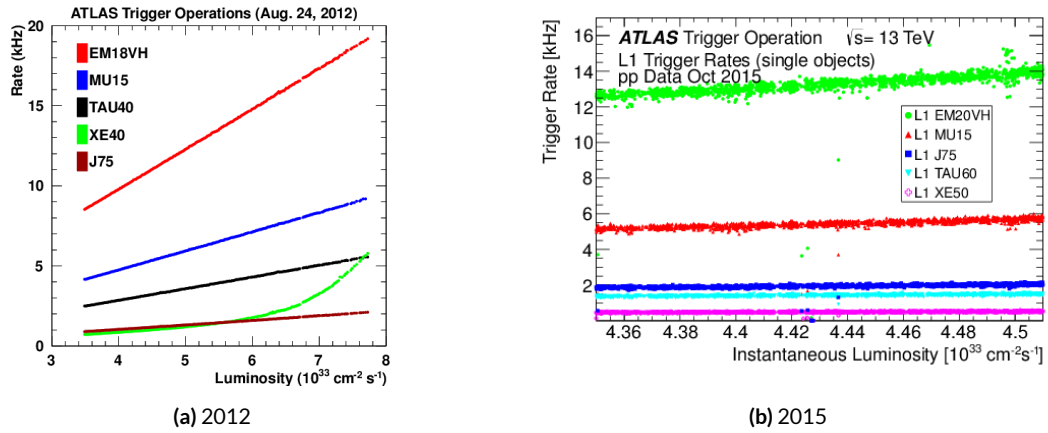


Figure 2.8: ATLAS trigger rates for Level-1 triggers as a function of instantaneous luminosity in 2012 and 2015 operation. These are single object triggers for electromagnetic clusters (EM), muons (MU), jets (J), missing energy (XE), and τ leptons (TAU). The threshold of the trigger is given in the name in GeV. [9]

983 2.2.7 ATLAS DATASETS

984 ATLAS has collected data at center of mass energies of 7, 8, and 13 TeV. Figure 2.9 shows the integrated
 985 luminosity as a function of time for each of the three collected datasets. At $\sqrt{s} = 7$ TeV, ATLAS
 986 recorded 5.08 fb^{-1} . Increased instantaneous luminosity in 2012 led to a larger dataset of 21.3 fb^{-1}
 987 recorded at $\sqrt{s} = 8$ TeV. After Long Shutdown 1 (LS1) of the LHC and a restart in 2015, ATLAS

recorded 3.9 fb^{-1} of data at $\sqrt{s} = 13 \text{ TeV}$. [10, 11]

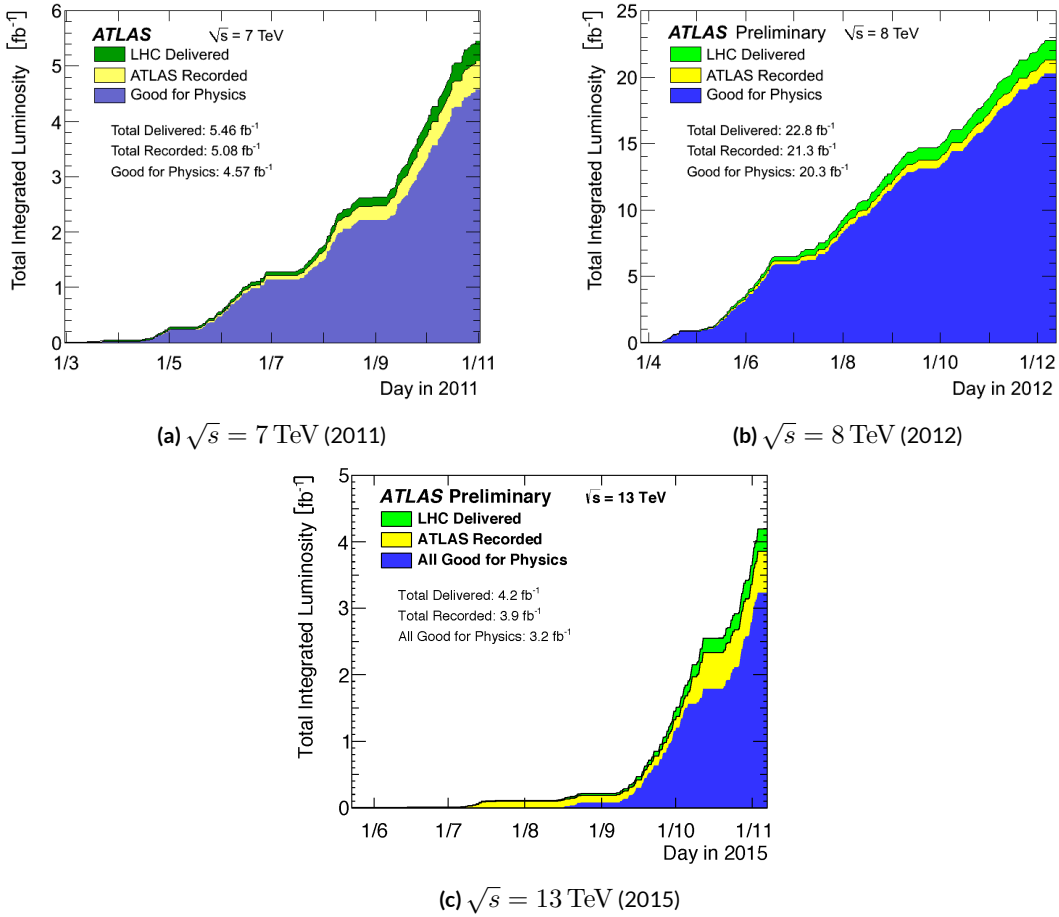


Figure 2.9: Instantaneous luminosity as a function of time for data recorded by ATLAS at different center of mass energies [10, 11]

2.2.8 DETECTOR PERFORMANCE

Table 2.2 summarizes the design requirements for each of the different sub-detectors. This table shows the energy and momentum resolution of each tracking, calorimetry, and muon measurements.

2.3 THE ATLAS MUON NEW SMALL WHEEL UPGRADE

As the LHC continues operation, it is scheduled to be upgraded in several phases to allow it to reach higher instantaneous luminosities and thus collect larger datasets. These conditions will open new doors

	Required resolution
Tracking	$\sigma_{p_T}/p_T = 0.05\% p_T \oplus 1\%$
EM calorimetry	$\sigma_E/E = 10\%/\sqrt{E} \oplus 0.7\%$
Hadronic calorimetry	
Barrel and end-cap	$\sigma_E/E = 50\%/\sqrt{E} \oplus 3\%$
Forward	$\sigma_E/E = 100\%/\sqrt{E} \oplus 10\%$
Muon spectrometer	σ_{p_T}/p_T at $p_T = 1$ TeV

Table 2.2: Performance requirements for the ATLAS detector [7].

for study of rare physics processes but will also present interesting challenges that must be faced. ATLAS will require new detector technologies to cope with the increased background rates in the cavern in these high luminosity conditions. One such upgrade, scheduled to be installed during Long Shutdown 2 (LS2) of the LHC in 2018, is the ATLAS Muon New Small Wheel (NSW) upgrade [12]. The NSW will replace the innermost end-cap wheel of the muon system with new technologies, as this is the part of the muon detector closest to the beam and thus suffers from the highest rates.

2.3.1 MOTIVATION

The motivation of the NSW is two-fold. First, the objective is to alleviate the decreased tracking efficiency that comes in a high rate environment. As figure 2.10, at the LHC design luminosity both the efficiency of recording hits and reconstructing track segments in the MDTs decreases at the LHC design luminosity.

Second, the NSW will work to alleviate the rate of fake triggers arising in the endcap. Figure 2.11 shows the extrapolated trigger rates as a function of the p_T threshold with and without the NSW upgrade. As the figure shows, the NSW upgrade will reduce the trigger rate by an order of magnitude compared to the current endcap trigger system.

2.3.2 NSW DETECTOR TECHNOLOGIES

The NSW will use two new detector technologies - micromesh gaseous structure detectors (micromegas) and small-strip thin gap chambers (sTGCs) [12, 62]. Unlike the previous detectors, both of these detector technologies can be used for tracking or trigger. However, the micromegas is more suited to tracking

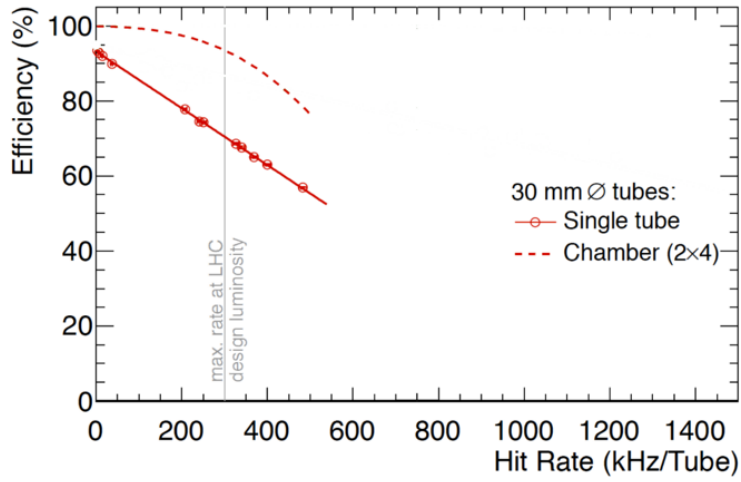


Figure 2.10: MDT tube hit (solid) and segment (dashed) efficiency as a function of hit rate per tube [12]

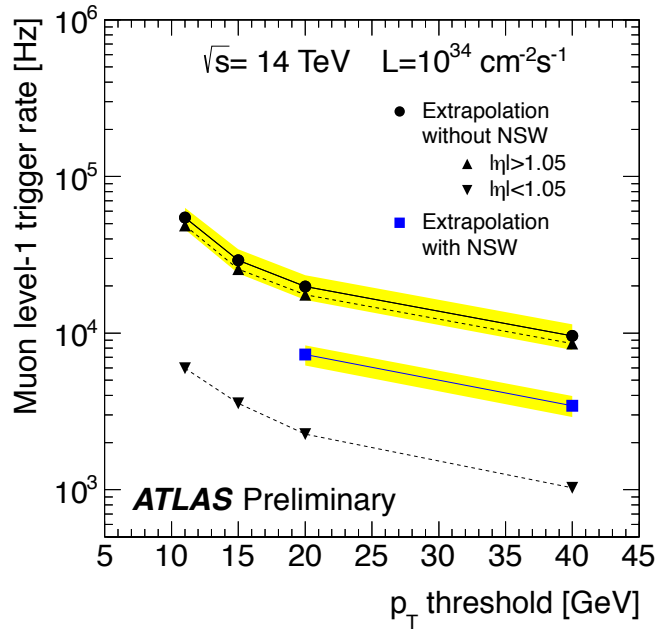


Figure 2.11: Trigger rate as a function of p_T threshold with and without the NSW upgrade [12]

¹⁰¹⁴ because of its good spatial resolution, while the sTGCs have better time resolution and are more suited
¹⁰¹⁵ for the trigger. To maintain a fully redundant system, both technologies are used for both purposes.

1016 **MICROMEGAS**

1017 Micromegas detectors operate using a thin metallic mesh that sits approximately $100\ \mu\text{m}$ away from
1018 the readout electrodes to create the amplification region. Above this mesh, there is a drift region on the
1019 order of a few mm in length capped by a drift electrode. As a charged particle traverses the detector, it
1020 ionizes gas and the electrons drift down towards readout strips. The timing of the drift can be used to
1021 reconstruct the angle of traversal of the particle. This is illustrated in figure 2.12. The micromegas used in
1022 ATLAS will be resistive micromegas, where the readout electrodes are topped with resistive strips [63].
1023 This alleviates the risk of sparking in the large area detectors that ATLAS will use.

1024 In ATLAS, the micromegas drift gap will be 5 mm and the amplification gap will be $128\ \mu\text{m}$. They
1025 are filled with the same gas mixture as the MDTs. They will be stacked in an octuplet in an XXUV-
1026 UVXX geometry, where X refers to straight strips and U and V refer to stero strips at an angle of $\pm 1.5^\circ$.
1027 This arrangement allows for measurement of the azimuthal coordinate and gives a large lever arm be-
1028 tween the straight strips for triggering purposes. Figure 2.12 shows the geometry of a single micromegas
1029 detector as well as its operating principle [12].

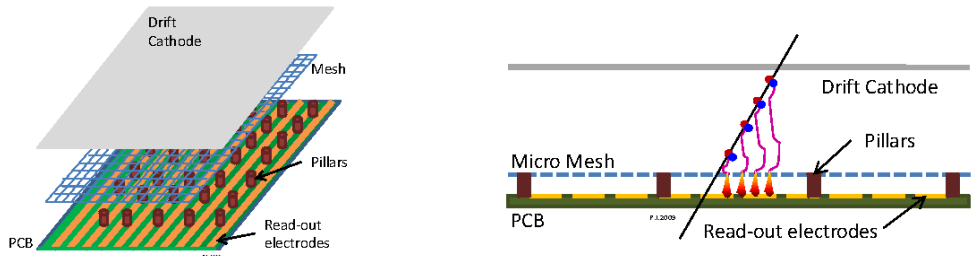


Figure 2.12: Illustrations of the geometry (left) and operating principle (right) of the micromegas detector [12]

1030 **sTGCs**

1031 The sTGCs are similar to the TGCs already described. They consist of gold-plated tungsten wires with
1032 a 1.8 mm pitch between two cathode planes 1.4 mm away from the wire plane. One cathode plane
1033 consists of strips with a 3.2 mm pitch (much smaller pitch than the TGCs), while the other consists
1034 of coarser pads that are used for defining regions of interest in the sTGC trigger algorithm. Figure 2.13
1035 shows the basic detector geometry.

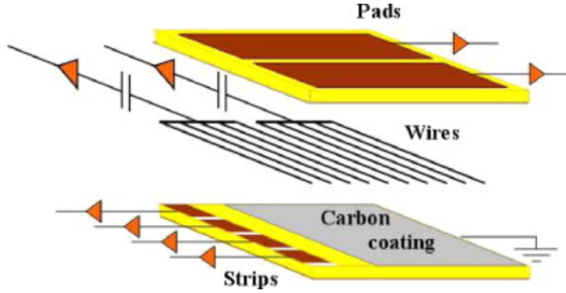


Figure 2.13: Geometry of the sTGC detector [12]

1036 2.3.3 PHYSICS IMPACT

1037 Maintaining low p_T thresholds for muons while still staying within the trigger rate budget at Level 1
 1038 (20 kHz) for the muon system is crucial for physics analyses to be successful in high luminosity condi-
 1039 tions. One realm where the lepton trigger threshold is especially important is in Higgs physics. In the
 1040 $H \rightarrow WW^*$ analysis, one of the W bosons is off shell and tends to decay to soft leptons. In associated
 1041 production of a Higgs with a W , the lepton is also important because the lepton provides the main han-
 1042 dle which allows the event to be triggered. Table 2.3 shows the impact of increasing the trigger thresholds
 1043 on these analyses. It shows that either raising the threshold or using only the barrel both have signifi-
 1044 cant impacts on the signal efficiency. With the NSW, the signal efficiency is largely maintained and the
 1045 triggers can be unprescaled.

Threshold	$H \rightarrow b\bar{b}$ (%)	$H \rightarrow WW^*$ (%)
$p_T > 20$ GeV	93	94
$p_T > 40$ GeV	61	75
$p_T > 20$ GeV (barrel only)	43	72
$p_T > 20$ GeV (with NSW)	90	92

Table 2.3: Signal efficiencies for WH production with $H \rightarrow b\bar{b}$ and $H \rightarrow WW^* \rightarrow \mu\nu qq$ under different trigger configurations [12].

1046 2.4 OBJECT RECONSTRUCTION IN ATLAS

1047 ATLAS analyses first start by requiring the presence of certain reconstructed physics objects in the event.
 1048 This section will present a brief overview of the algorithms used to reconstruct electrons, muons, jets

1049 (including b -jets), and missing energy^{*}. The performance of object reconstruction and measurement will
 1050 also be discussed as these are relevant to the analyses presented later. Figure 2.14 gives an overview of the
 1051 different sub-detectors that each type of particle will interact with in ATLAS.

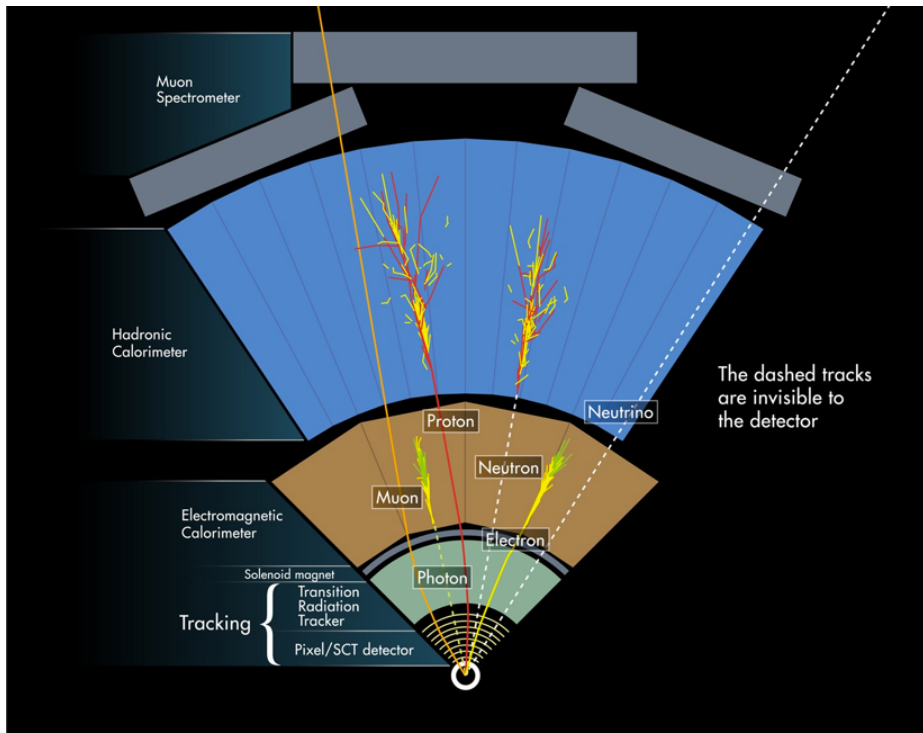


Figure 2.14: Illustration of particle interactions in ATLAS [13]

1052 2.4.I ELECTRONS

1053 Electrons in ATLAS will leave tracks in the inner detector and energy deposits in the electromagnetic
 1054 calorimeter. The algorithm for recognizing the signature of electrons proceeds in two steps: reconstruc-
 1055 tion and identification.

1056 In reconstruction, an electron candidate is formed by matching EM calorimeter deposits with ID
 1057 tracks. The algorithm first chooses seed clusters in the EM calorimeter by using a sliding window algo-
 1058 rithm that searches for towers with transverse energy larger than 2.5 GeV. In addition to seed clusters,
 1059 track candidates must be identified in the ID. The algorithm selects seed tracks with $p_T > 1$ GeV that

*Reconstruction algorithms for other objects, such as photons and τ leptons, are not detailed here as these objects are not used in the presented studies.

1060 do not fit well with a pion hypothesis. Once candidate tracks are selected, they are re-fit with a Gaussian Sum Filter (GSF) algorithm to estimate electron parameters [64]. Finally, an electron candidate is
 1061 formed if at least one track matches to a seed cluster in the calorimeter. The full details of the reconstruction
 1062 algorithm can be found in reference [14].

1063
 1064 Once an electron candidate is present, identification criteria must be applied in order to reject fake
 1065 electrons from background. Many different variables are used for this identification, most of them re-
 1066 lated to the shower shape in the EM calorimeter and the amount of leakage into the hadronic calorime-
 1067 ter, as well as information from the ID and in particular the TRT. There are both cut-based and likelihood-
 1068 based criteria that range from “loose” to “very tight”. For details, see reference [14].

1069
 1070 Figure 2.15 shows the algorithm’s reconstruction efficiency of true electrons for different identification
 1071 criteria as well as the electron energy resolution in simulation [14, 15]. The reconstruction efficiency is
 measured using both Z and J/ψ tag and probe techniques.

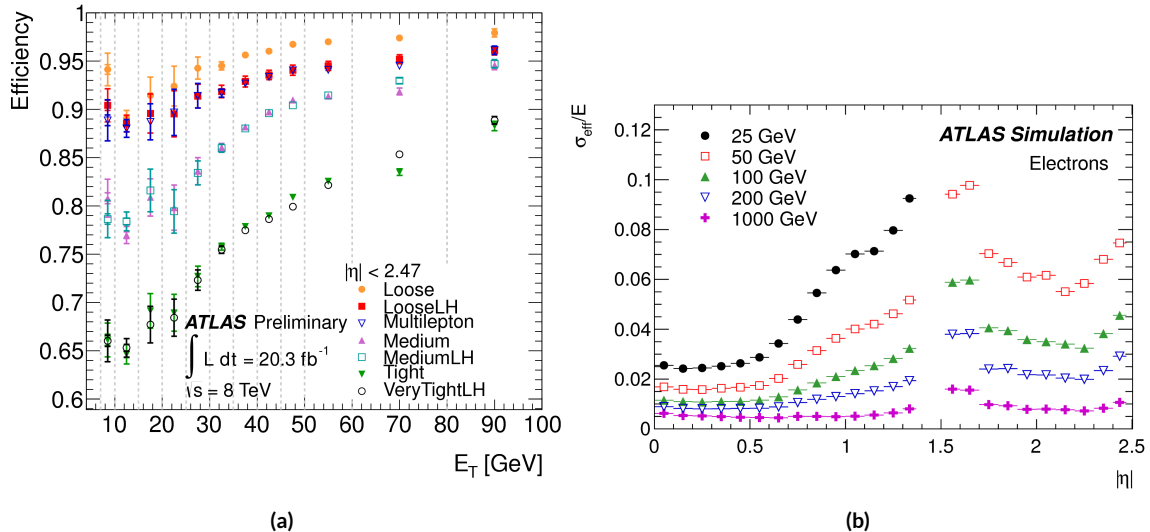


Figure 2.15: Electron performance: (a) reconstruction efficiency as a function of electron E_T [14] (b) energy resolution in simulation as a function of $|\eta|$ for different energy electrons [15]

1072 2.4.2 MUONS

1073 The ATLAS detector is designed to stop most particles before they reach the muon spectrometer. Muons,
 1074 however, are minimum ionizing particles, meaning that they will not lose a significant amount of energy

1075 through interactions with the detector and will thus pass through. Therefore, the muon reconstruction
1076 works to match tracks in the muon spectrometer with tracks in the inner detector.

1077 The first step of reconstruction is to reconstruct local straight line tracks, called segments, in each
1078 muon chamber. Segments are then fit to larger tracks that traverse the entire muon spectrometer. Such
1079 muon tracks are referred to as “standalone” tracks (SA) as they only use information from the muon
1080 spectrometer. The standalone tracks are then matched to tracks in the inner detector to form “com-
1081 bined” (CB) muons, where the combined ID and MS fit are used to determine the momentum and di-
1082 rection of the muon. To improve acceptance, segment-tagged and calorimeter-tagged muons are also
1083 reconstructed. In these cases, ID tracks are matched to segments in the MS and calorimeter deposits con-
1084 sistent with a minimum ionizing particle, respectively. The details of the reconstruction can be found in
1085 reference [16].

1086 As with electrons, once muon candidates are reconstructed they have identification criteria applied to
1087 reduce background. These criteria include the χ^2 match between the ID and MS tracks, the number of
1088 hits in the ID, overall ID and MS track fit quality, and additional variables [16]. The criteria range from
1089 “loose” to “tight” as with electrons.

1090 Figure 2.16 shows the muon reconstruction efficiency (measured with Z and J/ψ tag and probe) and
1091 invariant mass resolution [16].

1092 2.4.3 JETS

1093 When a quark or gluon is produced in collisions, it is not measured directly in ATLAS. Rather, due to
1094 QCD effects, it produces a collimated spray of hadrons in the direction of the original parton, which is
1095 known as a jet. Jets are reconstructed in ATLAS using energy deposits in the hadronic calorimeter. The
1096 first step is build “topological clusters” out of energy deposits in calorimeter cells [65, 66]. This is done
1097 using strategy where seed cells are chosen by picking cells whose energy measurements are four times the
1098 amount of noise expected for that cell. Adjacent cells with at least 2σ energy measurements are added
1099 to the cluster, then a final layer of clusters with energy above 0σ are added. Once calorimeter clusters
1100 are formed, they are clustered further into jet candidates using the anti- k_T jet clustering algorithm [67].

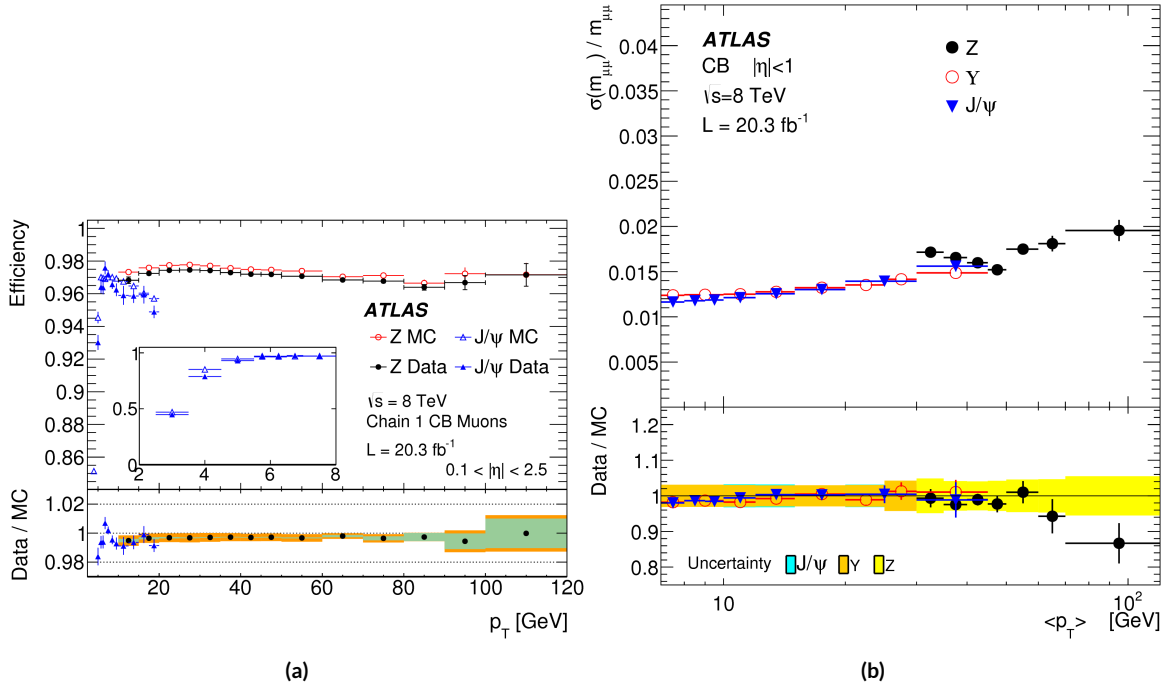


Figure 2.16: Muon performance: (a) reconstruction efficiency as a function of muon p_T (b) dimuon mass resolution as a function of average p_T [16]

This algorithm uses a parameter R that appears in the denominator of the clustering distance metric and defines the radial size of the jet in η - ϕ space.

The energy response of the calorimeter must be properly characterized in order to reconstruct jet energy. Calorimeter clusters can be calibrated either with the EM calibration, where each cluster is assumed to have come from the energy deposit of an electron or photon, or the LCW calibration, where local cluster weights are computed to allow for local calibration of clusters as hadronic or electromagnetic.

The details of the jet energy calibration are not detailed here and are discussed in reference [17].

Figure 2.17 shows the jet energy response after calibration in Monte Carlo as a function of the true p_T of the jet [17].

2.4.4 b -TAGGING

One important aspect of jet physics is the task of identifying the flavor of parton that produced the measured jet. While in general this is very difficult, jets from b -quarks offer an interesting case where such identification is possible. B mesons have a lifetime on the order of 10^{-12} seconds, which makes a $c\tau$

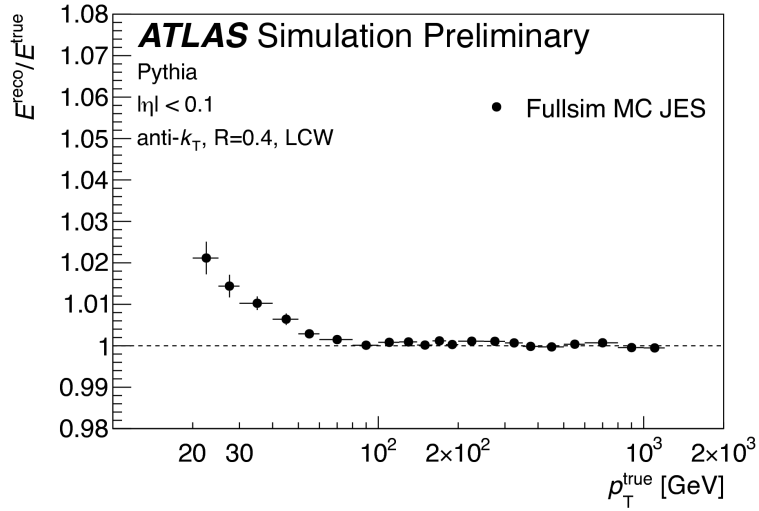


Figure 2.17: Jet energy response after calibration as a function of true p_T in simulation [17]

on the order of millimeters [1]. This type of displaced decay vertex can be identified in detectors like ATLAS and allows b -jets to be distinguished from other flavors of jets[†].

ATLAS uses a multivariate machine learning algorithm to identify jets from b -quarks. The inputs to this algorithm are determined from lower level reconstruction algorithms. There are three distinct algorithms that reconstruct variables which are used as input to the multivariate technique.

The first family is referred to as IPxD (where the x can either be 2 or 3). These algorithms use the transverse and longitudinal impact parameters d_0 and z_0 of the tracks inside a jet to determine their consistency with the primary vertex. They two or three dimensional (hence the x) templates for light flavor, charm, and bottom jets and then evaluate the likelihood of the jet coming from each of these types. The likelihood ratios are used as inputs to the multivariate algorithm.

The next two algorithms used as input are referred to as the secondary vertex (SV) and JetFitter (JF) algorithms. The SV algorithm uses tracks inside the jet to fit for vertices that are displaced from the primary vertex. The JF algorithm attempts to reconstruct the full flight path of the b by looking for multiple displaced vertices along the same line (as B decays often result in subsequent c decays).

In Run 1, the multivariate b -tagging algorithm used a neural network and was referred to as MV1.

[†]Jets from charm quarks can also be detected in this way but they do not live quite as long so the displacement of the vertex is harder to distinguish

1129 The details of this algorithm and its inputs are given in reference [18]. In Run 2, the number of inputs
 1130 was simplified and a boosted decision tree with 24 input variables was used, referred to as MV2. The
 1131 details of this algorithm are in reference [19]. Figure 2.18 shows the performance of each of these algo-
 1132 rithms.

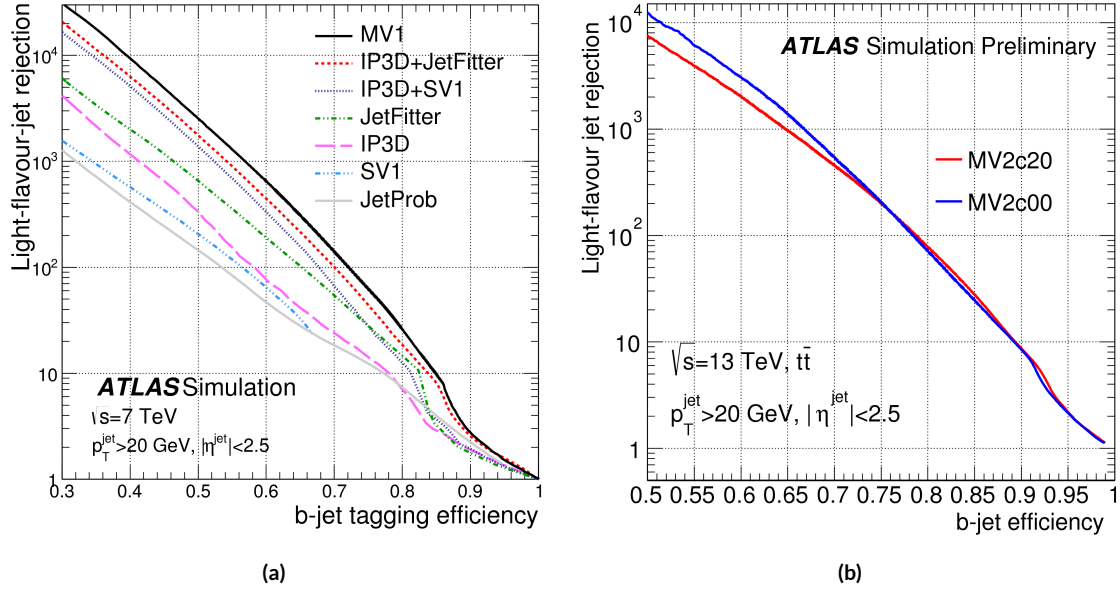


Figure 2.18: Light jet rejection ($1/\text{efficiency}$) vs. b -jet efficiency for MV1 and its input algorithms (a) [18] and MV2 (b) [19] in simulated $t\bar{t}$ events. The numbers in the algorithm names in (b) refer to the fraction of charm events used in the MV2 training.

1133 2.4.5 MISSING TRANSVERSE ENERGY

1134 As noted in figure 2.14, neutrinos produced in ATLAS will pass through the detector without inter-
 1135 acting. The only way of detecting the presence of particles like neutrinos (or BSM particles that are
 1136 long-lived) is to use missing transverse momentum. The basic principle of missing transverse energy is
 1137 to use the momentum balance of the incoming protons to infer the presence of missing particles. The
 1138 net longitudinal momentum of the incoming partons that collide is not known (since each carries an un-
 1139 known fraction of the proton's momentum). However, the protons (and thus incoming partons) have
 1140 no net momentum in the plane transverse to the beam line (the x - y plane). Therefore, if there are no
 1141 un-measured particles in the final state, the transverse momenta of all of the final state particles should

balance. The magnitude of this imbalance is known as missing transverse momentum (E_T^{miss}).

The basic calculation of missing transverse momentum from calorimeter cells is given in equation 2.4 [68].

$$\begin{aligned} E_x^{\text{miss}} &= -\sum_{i=1}^{N_{\text{cell}}} E_i \sin \theta_i \cos \phi_i \\ E_y^{\text{miss}} &= -\sum_{i=1}^{N_{\text{cell}}} E_i \sin \theta_i \sin \phi_i \end{aligned} \quad (2.4)$$

The E_T^{miss} calculation is separated into different terms based on the objects that the calorimeter clusters are associated with. This way, each cell's contribution is calibrated appropriately according to the object. This separation of terms is shown in equation 2.5 [68].

$$\begin{aligned} E_{x(y)}^{\text{miss,calo}} &= E_{x(y)}^{\text{miss},e} + E_{x(y)}^{\text{miss},\gamma} + E_{x(y)}^{\text{miss},\tau} + E_{x(y)}^{\text{miss,jets}} \\ &\quad + E_{x(y)}^{\text{miss,softjets}} + E_{x(y)}^{\text{miss},\mu} + E_{x(y)}^{\text{miss,CellOut}} \end{aligned} \quad (2.5)$$

The CellOut term of the above equation corresponds to calorimeter cells with energy deposits that are not associated with other objects. The soft jets term comes from cells associated to jets with p_T between 7 and 20 GeV, while the jets term comes from jets with $p_T > 20$ GeV. Because muons do not deposit significant energy in the calorimeter, the muon momentum is used for the muon term [68]. The final E_T^{miss} is calculated using equation 2.6.

$$E_T^{\text{miss}} = \sqrt{(E_x^{\text{miss}})^2 + (E_y^{\text{miss}})^2} \quad (2.6)$$

Figure 2.19 shows the resolution of the components of the E_T^{miss} under different pileup suppression techniques [20].

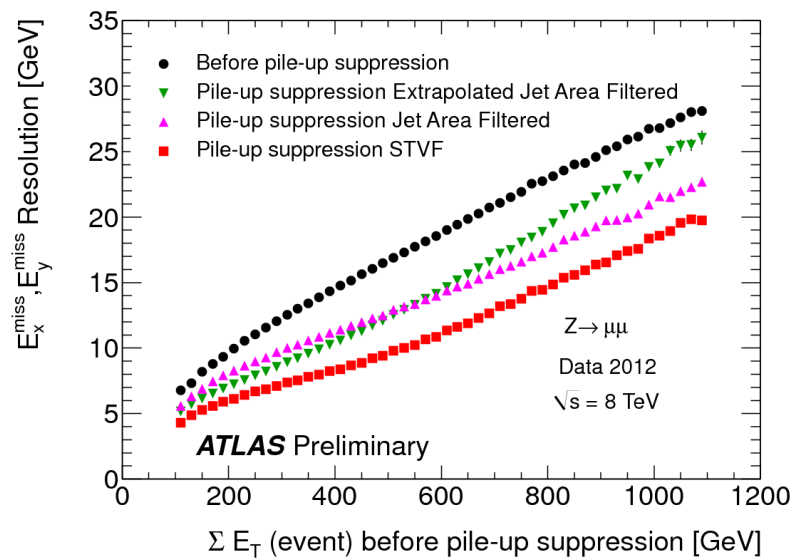


Figure 2.19: Resolution of E_T^{miss} components as a function of $\sum E_T$ before pileup suppression with different pileup techniques [20]

1154

Part II

1155

Observation and measurement of Higgs

1156

boson decays to WW^* in LHC Run I at

1157

$$\sqrt{s} = 7 \text{ and } 8 \text{ TeV}$$

*Basic research is what I am doing when I don't know
what I am doing.*

Wernher von Braun

3

1158

1159 $H \rightarrow WW^* \rightarrow \ell\nu\ell\nu$ Analysis Strategy

1160 3.1 INTRODUCTION

1161 This chapter presents an overview of the strategy for searching for a Higgs boson in the $H \rightarrow WW^* \rightarrow$
1162 $\ell\nu\ell\nu$ decay topology. Its purpose is to define in broad terms how the search and measurement are un-
1163 dertaken, before going into details on the specific sub-categories within the larger analysis. First, the
1164 properties of the Higgs signal are discussed and the associated backgrounds are presented. Next, the ob-
1165 servables used to enhance the signal to background ratio are defined. Finally, the parameters of interest
1166 in the search and measurement will be shown, along with a brief overview of the statistical treatment of
1167 the final Higgs candidates.

1168 Following this chapter, the results of three different studies within the $H \rightarrow WW^* \rightarrow \ell\nu\ell\nu$ channel
1169 are shown. Chapter 4 presents a search for Higgs boson production in gluon fusion mode and the role
1170 of the $H \rightarrow WW^*$ channel in its discovery. Chapter 5 shows the search and first observation in ATLAS
1171 of the Vector Boson Fusion (VBF) production mode of the Higgs in the $H \rightarrow WW^*$ decay channel.

1172 Finally, chapter 6 shows the combined Run 1 $H \rightarrow WW^*$ results for the measurement of the Higgs
1173 cross section and relative coupling strengths to other SM particles.

1174 3.2 THE $H \rightarrow WW^* \rightarrow \ell\nu\ell\nu$ SIGNAL IN ATLAS

1175 The signal studied in this and subsequent chapters is the Higgs boson in the WW^* final state, where
1176 each W boson subsequently decays into a charged lepton and a neutrino. In its simplest decay path, the
1177 final state consists of two neutrinos and two charged leptons, each of which can be either an electron or
1178 a muon. If one or both of the W s decay to τ leptons, only leptonic decays of the τ are considered. This
1179 decay path produces additional neutrinos in the final state but still gives two charged leptons as before.
1180 Neutrinos are not detected in ATLAS, so the final state ultimately consists of two reconstructed leptons
1181 and missing transverse momentum (denoted as E_T^{miss}). Final states where both of the charged leptons
1182 are electrons or muons are referred to as the “same flavor” ($ee/\mu\mu$) final states, while those with one
1183 electron and one muon are referred to as “different flavor” ($e\mu$ or μe).

1184 While the basic final state consists of two leptons and E_T^{miss} , there can be additional objects depend-
1185 ing on the production mode of the Higgs. As described in detail in Chapter 1, if the Higgs is produced
1186 via vector boson fusion production, there will be two additional forward jets in the event. Even in gluon
1187 fusion, one or more jets can be produced through initial state radiation from the incoming gluons. Be-
1188 cause of the varying background composition as a function of jet multiplicity, each bin in this variable
1189 has its own dedicated requirements applied in the search and measurement. The $n_j = 0$ and $n_j = 1$
1190 bins are dedicated to gluon fusion production, while the $n_j \geq 2$ bin has separate dedicated searches for
1191 ggF and VBF production.

1192 Figure 3.1 shows the relative branching fractions for the $H \rightarrow WW^*$ process, calculated from the
1193 Particle Data Group values for the W and τ branching ratios[?]. The largest branching ratio is both
1194 W bosons decaying to quark pairs at 45.44%. The next largest is one W decaying leptonically and the
1195 other decaying to quarks, a branching ratio of 34.18%. In all cases, ℓ denotes either an electron or muon,
1196 and the leptonic branching ratios of the τ are included. For example, the $\ell\nu qq$ final state includes one W
1197 decaying to $e\nu$, $\mu\nu$, or $\tau\nu$. In the case of the $W \rightarrow \tau\nu$ decay, the τ lepton then decays to an electron or

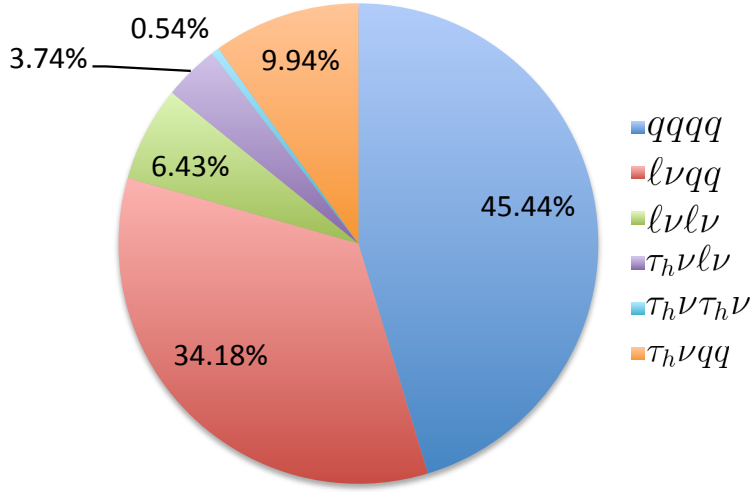


Figure 3.1: Branching ratios for a WW system. q refers to quarks. ℓ can be either an electron or muon, and the leptonic branching ratios of the τ are included. For example, the $\ell\nu qq$ final state includes one W decaying to $e\nu$, $\mu\nu$, or $\tau\nu$. τ_h refer to hadronic decays of the τ .

1198 muon via $\tau \rightarrow \nu_\tau \ell \nu_\ell$. Final states with a τ_h refer to hadronic decays of the τ . The branching ratio to the
 1199 $\ell\nu \ell\nu$ final state is 6.43%.

1200 While the $\ell\nu \ell\nu$ final state is not a large fraction of the branching ratio, there are significant advantages
 1201 in this channel. First, both the $qqqq$ and $\ell\nu qq$ channels suffer from a large QCD multijet background,
 1202 which is often difficult to model. Second, events in the the $\ell\nu \ell\nu$ channel in data can be triggered more
 1203 efficiently due to the presence of two leptons.

1204 **3.3 BACKGROUND PROCESSES**

1205 Many processes from the Standard Model can also produce a final state with two leptons and missing
 1206 transverse momentum . This section lists the dominant backgrounds to Higgs production. It gives gen-
 1207 eral descriptions of how the backgrounds mimic Higgs production and how they can be reduced. Ta-
 1208 ble3.1 summarizes the different processes.

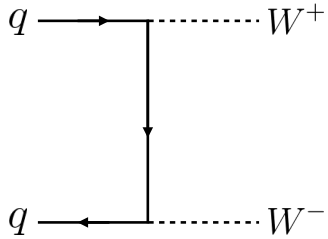


Figure 3.2: Feynman diagram for Standard Model WW production

1209 3.3.1 STANDARD MODEL WW PRODUCTION

1210 Non-resonant Standard Model diboson production, as shown in figure 3.2, is an irreducible background
 1211 to Higgs boson production in the WW final state. It produces the same exact final state objects, namely
 1212 leptonically decaying W bosons. There are no additional objects in the final state that allow for back-
 1213 ground reduction. Therefore the analysis solely relies on the correlations between the leptons to reduce
 1214 this background.

1215 3.3.2 TOP QUARK PRODUCTION

1216 Production of top quarks, either in pairs ($t\bar{t}$ production) or singly (e.g. Wt production), can also mimic
 1217 Higgs production. Because top quarks decay via $t \rightarrow Wb$, top pair production can produce a final state
 1218 with two W bosons that then decay leptonically. In this case, however, there are two additional jets from
 1219 the bottom quarks in the final state. This allows the analysis to veto on the presence of jets identified as
 1220 originating from a b in order to reduce the size of the background.

1221 Single top production can occur via s -channel, t -channel, or associated production (Wt). The mode
 1222 which most closely resembles the Higgs final state is Wt . In this case, there are two real W bosons pro-
 1223 duced, as with $t\bar{t}$. However, the decay of the single top quark will still also produce one b -jet, meaning a
 1224 b veto will reduce this background as well.

1225 Figure 3.3 shows the Feynman diagrams for $t\bar{t}$ and Wt production.

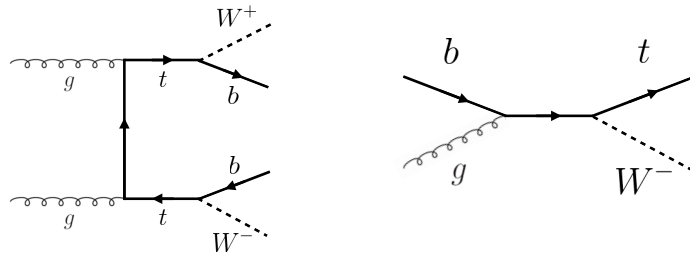


Figure 3.3: Feynman diagrams for top pair production (left) and Wt production (right)

1226 3.3.3 W +JETS BACKGROUND

1227 Single W boson production, in association with jets, is a unique background. The other background
 1228 considered so far have all included real leptons in the final state. In this case, however, only one real lep-
 1229 ton from the decay of a W exists in the final state. The second reconstructed lepton can arise from two
 1230 different cases. First, the lepton may truly be an algorithm “fake”, or a jet misidentified as a lepton by
 1231 either the electron or muon reconstruction algorithms. Second, the lepton may be a real lepton but
 1232 coming from semi-leptonic decays of particles inside the shower of the jet. This background can be re-
 1233 duced by requiring that the reconstructed lepton have little activity surrounding it in the calorimeter
 1234 (also known as an “isolated” lepton). Figure 3.4 shows the Feynman diagram for W +jets production.

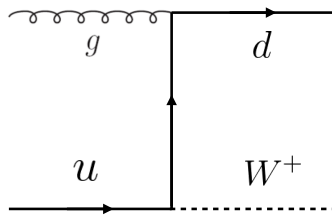


Figure 3.4: An example Feynman diagram of W +jets production

1235 3.3.4 Z/γ^* +JETS BACKGROUND

1236 Production of a Z/γ^* in association with jets (also known as Drell-Yan) is also a background to Higgs
 1237 production. In particular, the same flavor final states have a large Z +jets background, as the Z decays
 1238 into two leptons of the same flavor. (This background also enters the different flavor final state through

¹²³⁹ the leptonic decays of $Z \rightarrow \tau\tau$). Figure 3.5 shows the production of a Z in association with one jet. Be-
¹²⁴⁰ cause there are no neutrinos in this final state, variables like E_T^{miss} can be used to reduce the background.

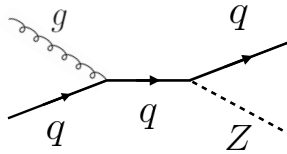


Figure 3.5: An example Feynman diagram of $Z + \text{jets}$ production

¹²⁴¹ 3.3.5 OTHER (SUBDOMINANT) BACKGROUNDS

¹²⁴² There are additional processes which contribute to the background composition but are not produced
¹²⁴³ as frequently as those listed already. The first of these are referred to as VV or “Other diboson” pro-
¹²⁴⁴ cesses and include multiple Standard Model diboson processes, including WZ , ZZ , $W\gamma$, $W\gamma^*$, and
¹²⁴⁵ $Z\gamma$ production. Additionally, there is background from QCD multijet production, where two jets are
¹²⁴⁶ misidentified as leptons.

Category	Process	Description
SM WW	$WW \rightarrow \ell\nu\ell\nu$	Real leptons and neutrinos
Top quark production	$t\bar{t} \rightarrow WbWb \rightarrow \ell\nu b\ell\nu b$ $tW \rightarrow WbW \rightarrow \ell\nu\ell\nu b$ $t\bar{b}, t\bar{q}\bar{b}$	Real leptons, untagged b s Real leptons, untagged b Untagged b , jet misidentified as lepton
Drell-Yan	$Z/\gamma^* \rightarrow ee, \mu\mu$ $Z/\gamma^* \rightarrow \tau\tau \rightarrow \ell\nu\ell\nu$	“Fake” E_T^{miss} Real leptons and neutrinos
Other dibosons	$ZZ \rightarrow \ell\ell\nu\nu$ $W\gamma^*, WZ \rightarrow \ell\nu\ell\ell, ZZ \rightarrow \ell\ell\ell\ell$ $W\gamma, Z\gamma$	Real leptons and neutrinos Unreconstructed leptons γ reconstructed as e , unreconstructed lepton
$W + \text{jets}$	$Wj \rightarrow \ell\nu j$	Jet reconstructed as lepton
QCD multijet	jj	Jets reconstructed as leptons

Table 3.1: A summary of backgrounds to the $H \rightarrow WW^* \rightarrow \ell\nu\ell\nu$ signal

1247 3.4 SHARED SIGNAL REGION SELECTION REQUIREMENTS

1248 As presented in section 3.2, there are many different combinations of objects that can define a $H \rightarrow$
1249 $WW^* \rightarrow \ell\nu\ell\nu$ final state. The multiplicity of jets and the flavor combinations of the leptons both lead
1250 to many potential signal regions. Additionally, signal regions can be optimized separately to be sensi-
1251 tive to the distinct production modes of the Higgs. Gluon fusion, vector boson fusion, and associated
1252 production of a Higgs all lead to unique final state topologies. Figure 3.6 delineates the different signal
1253 regions used in the gluon fusion and vector boson fusion $H \rightarrow WW^*$ analyses. While there are different
1254 optimizations possible in each signal region, there are also some commonly shared selections that will be
1255 described here.

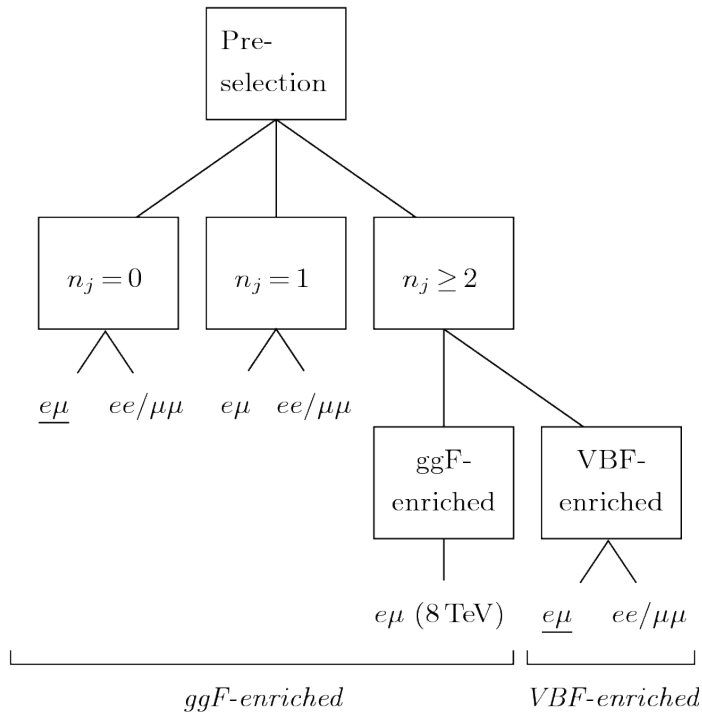


Figure 3.6: An illustration of the unique analysis signal regions[21]

1256 3.4.1 EVENT PRE-SELECTION

1257 Before being sorted into the distinct signal regions, basic requirements are applied on the reconstructed
1258 objects in the event to select Higgs-like event candidates. First, two oppositely charged leptons are re-

1259 quired.

1260 Once the leptons are selected, the last requirement for event pre-selection is the presence of neutrinos.
1261 As neutrinos cannot be detected directly in ATLAS, E_T^{miss} can be used as a proxy for the combined neu-
1262 trino momentum in the transverse plane. In general, it is expected that the signal should have a harder
1263 E_T^{miss} spectrum than backgrounds, especially if those backgrounds did not contain neutrinos. One ad-
1264 ditional consideration when using E_T^{miss} is the fact that mis-measurements of objects in the detector
1265 can lead to imbalances in the transverse plane that are not due to real particles escaping the detector.
1266 One indicator that this is the case is that the E_T^{miss} vector in the transverse plane will be pointing in the
1267 same direction as the mis-measured object. Therefore, a new variable, $E_{T,\text{rel}}^{\text{miss}}$, is used in the pre-selection.
1268 $E_{T,\text{rel}}^{\text{miss}}$ is defined in equation 3.1.

$$E_{T,\text{rel}}^{\text{miss}} = \begin{cases} E_T^{\text{miss}} \sin \Delta\phi_{\text{near}} & \text{if } \Delta\phi_{\text{near}} < \pi/2 \\ E_T^{\text{miss}} & \text{otherwise,} \end{cases} \quad (3.1)$$

1269 If the closest object to the E_T^{miss} vector is within $\pi/2$ radians in the transverse plane, the E_T^{miss} is pro-
1270 jected away from this object. Otherwise, the normal E_T^{miss} vector is used. Figure 3.7 shows a graphical
1271 illustration of this concept.

1272 Once both the lepton and E_T^{miss} pre-selections are made, the analysis can be divided into different
1273 regions according to jet multiplicity.

1274 3.4.2 JET MULTIPLICITY

1275 Jet multiplicity, denoted as n_j , is used to sub-divide the analysis into its distinct signal regions. The rea-
1276 son for this is twofold. First, different jet multiplicity bins will be more or less sensitive to different Higgs
1277 production modes. For example, the $n_j \geq 2$ region is more sensitive to VBF production because of
1278 the two high momentum jets produced at matrix element level. For gluon fusion production to enter
1279 this bin, two initial state radiation jets must be emitted. Second, background composition varies greatly
1280 in different bins of n_j . Figure 3.8 shows the jet multiplicity in both the different flavor and same flavor
1281 regions. It also shows the background composition in the bins of n_b . There are a few clear trends from

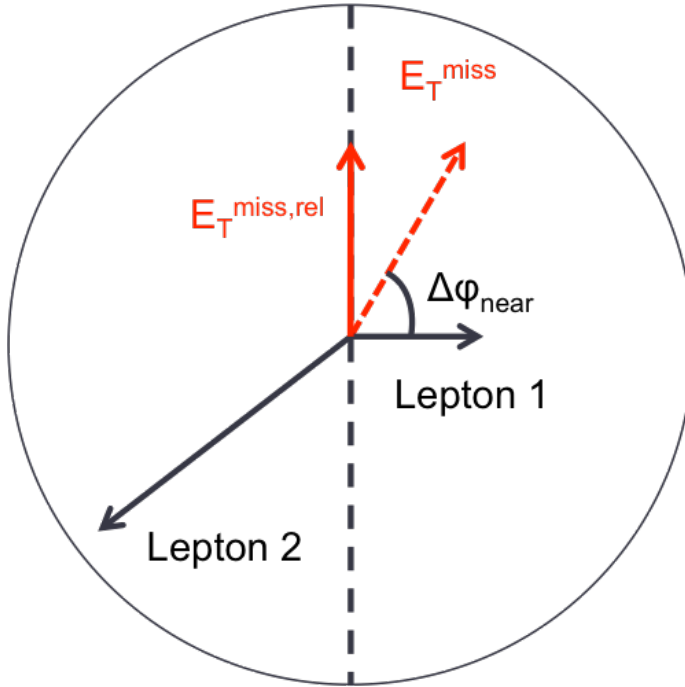


Figure 3.7: A graphical illustration of the $E_{T,\text{rel}}^{\text{miss}}$ calculation

1282 this distribution. The first is that the Drell-Yan background dominates in the same flavor channels for
 1283 $n_j \leq 1$. Second, the top background becomes a clear contributor to the total background for $n_j \geq 1$.
 1284 Lastly, the SM WW production dominates in the $n_j = 0$ bin, as it is an irreducible background to
 1285 $H \rightarrow WW^*$ production. Because of these distinct features, each jet multiplicity bin is treated separately.

1286 3.5 BACKGROUND REDUCTION IN SAME-FLAVOR FINAL STATES

1287 As described in section 3.4.2, the background composition of the same flavor final states is unique to that
 1288 of the different flavor states. In particular, Drell Yan processes play a much larger role because the Z/γ^*
 1289 decays to same flavor leptons. Because real neutrinos are absent in the Z/γ^* decays to ee and $\mu\mu$, a re-
 1290 quirement on E_T^{miss} should largely reduce the background. However, as this section will demonstrate,
 1291 with increasing pileup conditions the resolution of the calorimeter-based E_T^{miss} degrades greatly. There-
 1292 fore, two new variables for Z/γ^* background reduction are constructed and described in this section.

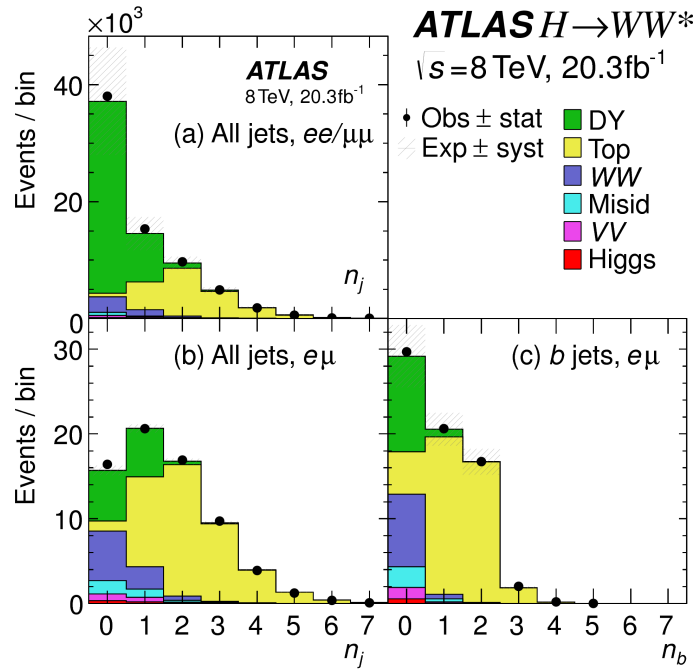


Figure 3.8: Predicted backgrounds (compared with data) as a function of n_j (a and b) and n_b (c)

1293 3.5.1 PILEUP AND E_T^{miss} RESOLUTION

1294 Secondary interactions of protons in the colliding bunches of the LHC (known as pileup interactions,
 1295 described in detail in Chapter 2) deposit energy into the ATLAS calorimeter on top of the energy that
 1296 comes from the hard scatter process that is being searched for or analyzed. The calculation of E_T^{miss} is
 1297 fundamentally Poissonian, as summing up all of the energy deposits in individual calorimeter cells or
 1298 clusters is similar to a counting experiment. Thus, the energy resolution scales as \sqrt{E} , just as the error on
 1299 a mean of N in a Poisson distribution is \sqrt{N} . As more energy is deposited in the calorimeter, the E_T^{miss}
 1300 resolution degrades, meaning that the E_T^{miss} resolution is particularly sensitive to LHC instantaneous
 1301 luminosity conditions.

1302 Figure 3.9 shows an event display of a $Z/\gamma^* + \text{jets}$ event candidate with the twenty-five reconstructed
 1303 primary vertices. This display illustrates that while the interaction of interest only has tracks coming
 1304 from the hardest primary vertex, all of the secondary interactions will deposit energy in the calorimeter as
 1305 well.

1306 Figure 3.10 shows the RMS of the E_T^{miss} distribution in $Z \rightarrow \mu\mu$ events (where there are no real neu-

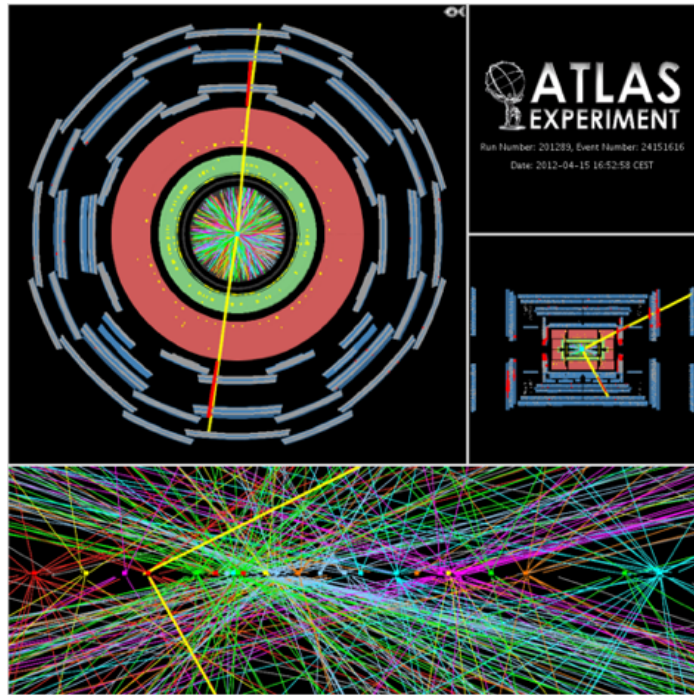


Figure 3.9: An event display of a Z/γ^* + jets event illustrating the effect of pileup interactions

trinos) as a function of the number of the average number of interactions. Under 2011 LHC conditions, this RMS was approximately 9 GeV, while under 2012 running conditions the resolution worsened to 12 GeV. This worsening dilutes the E_T^{miss} variable's ability to reduce the Z/γ^* background.

3.5.2 TRACK-BASED DEFINITIONS OF MISSING TRANSVERSE MOMENTUM

Because the increasing number of secondary proton-proton interactions degrades calorimeter-based E_T^{miss} resolution, a new variable using only contributions from the primary interaction vertex is necessary to further reduce the Z/γ^* background. While it is not possible to associate calorimeter energy deposits with a particular vertex, individual charged particle tracks in the Inner Detector are associated to unique vertices. Thus, two track-based definitions of missing transverse momentum , using only tracks coming from the primary vertex in the event, are used in the analysis. The simplest variable, $p_T^{\text{miss}(\text{trk})}$, is the vectorial sum of the p_T of all of the tracks from the primary vertex and the selected leptons (excluding the tracks associated with the selected leptons to avoid double counting). This is defined in equa-

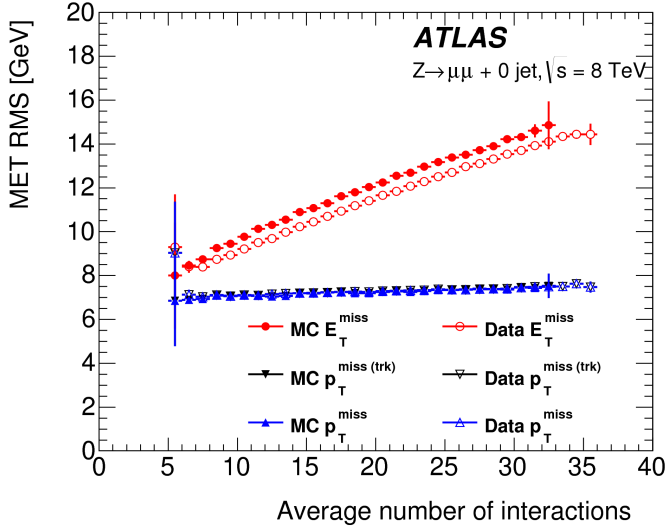


Figure 3.10: The RMS of different missing transverse momentum definitions as a function of the average number of interactions per bunch crossing

tion 3.2.

$$\mathbf{p}_T^{\text{miss}(\text{trk})} = - \left(\sum_{\text{selected leptons}} \mathbf{p}_T + \sum_{\text{other tracks}} \mathbf{p}_T \right), \quad (3.2)$$

In events with hard jets, a better resolution on the missing transverse momentum is obtained by including the calorimeter based measurement of the hard jets rather than the track based measurements. Thus, another variable, p_T^{miss} , is defined, using the nominal measurements of p_T for the selected leptons and jets and using tracks rather than calorimeter clusters for the soft component of the missing transverse momentum. This is defined in equation 3.3.

$$\mathbf{p}_T^{\text{miss}} = - \left(\sum_{\text{selected leptons}} \mathbf{p}_T + \sum_{\text{selected jets}} \mathbf{p}_T + \sum_{\text{other tracks}} \mathbf{p}_T \right), \quad (3.3)$$

Figure 3.10 illustrates that these two new variables accomplish their intended purpose. The resolution as a function of mean number of interactions for both $p_T^{\text{miss}(\text{trk})}$ and p_T^{miss} is much flatter compared to the dependence for E_T^{miss} .

Figure 3.11a shows the difference between the true and reconstructed values of missing transverse mo-

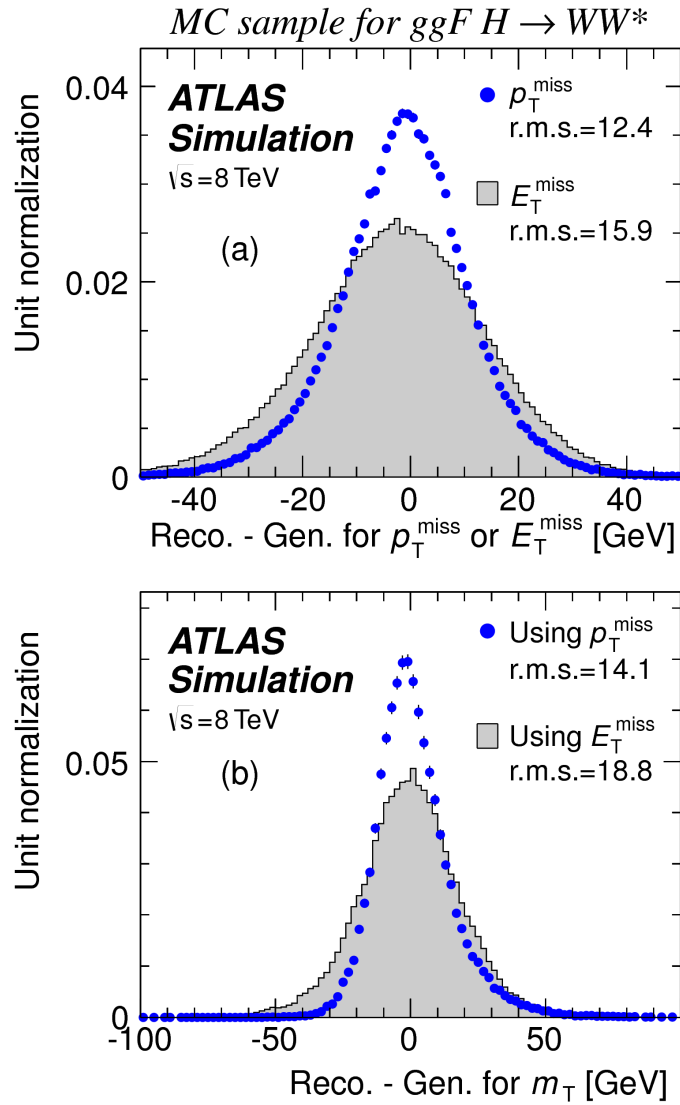


Figure 3.11: The difference between the true and reconstructed values of the missing transverse momentum (a) and m_T (b) in a gluon fusion signal sample

1329 mentum using both the track-based p_T^{miss} and calorimeter based E_T^{miss} . The RMS of the distribution

1330 improves by 3.5 GeV when using p_T^{miss} .

1331 3.5.3 Distinguishing Z/γ^* +JETS AND $H \rightarrow WW^*$ TOPOLOGIES

1332 The track-based definitions of missing transverse momentum were constructed to mitigate degrading

1333 performance as a function of pileup. However, an additional variable can be constructed to exploit kine-

matic and topological differences between the Z/γ^* background and $H \rightarrow WW^*$ signal. Because there
 1334 are no real neutrinos in the final state (in the case of $Z/\gamma^* \rightarrow ee, \mu\mu$ decays), the dilepton system of a
 1335 Z/γ^* will be balanced with the jets produced in the hard scatter. A new variable, f_{recoil} , is constructed
 1336 to estimate the balance between the dilepton system and the jets in the quadrant opposite the dilepton
 1337 vector in the transverse plane. It is defined in equation 3.4. The numerator of f_{recoil} is the magnitude of
 1338 the vectorial sum of the p_T of jets in the quadrant opposite the dilepton system, weighted by each jet's Jet
 1339 Vertex Fraction (JVF, described in chapter 2). The denominator is the magnitude of the dilepton p_T .
 1340

$$f_{\text{recoil}} = \left| \sum_{\text{jets } j \text{ in } \wedge} \text{JVF}_j \cdot \mathbf{p}_T^j \right| / p_T^{\ell\ell}. \quad (3.4)$$

1341 Figure 3.12 shows a shape comparison of the distribution of f_{recoil} in a simulated $Z/\gamma^* + \text{jets}$ sample,
 1342 a $H \rightarrow WW^*$ signal sample, and other backgrounds that contain real neutrinos. The $Z/\gamma^* + \text{jets}$ events
 1343 tend to be more balanced between the dilepton system and recoiling jets, while the processes containing
 1344 real neutrinos are less balanced in the transverse plane. Thus, a requirement on f_{recoil} will also reduce
 1345 the $Z/\gamma^* + \text{jets}$ background while maintaining a good signal efficiency.

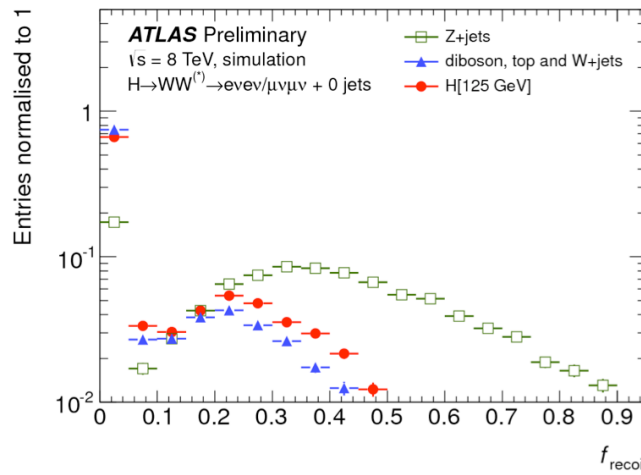


Figure 3.12: Comparison of f_{recoil} distributions for $Z/\gamma^* + \text{jets}$, $H \rightarrow WW^*$, and other backgrounds with real neutrinos.

1346 **3.5.4 OPTIMIZING BACKGROUND REDUCTION SELECTION REQUIREMENTS**

1347 The requirements on $p_T^{\text{miss(trk)}}$ and f_{recoil} used to reduce the Z+jets background must be optimized
 1348 to maximize their efficacy. Figure 3.13 shows an early attempt to optimize the combination of the two
 1349 requirements in the gluon fusion zero jet bin. Each bin shows the expected signal significance if the
 1350 $p_{T,\text{rel}}^{\text{miss(trk)}}$ is required to be greater than the left edge of the bin and the f_{recoil} is required to be less than
 1351 the top edge of the bin. The figure shows that the best signal significance comes from requiring low val-
 1352 ues of $f_{\text{recoil}} (< 0.05)$ and $p_{T,\text{rel}}^{\text{miss(trk)}}$ values greater than 45 GeV.

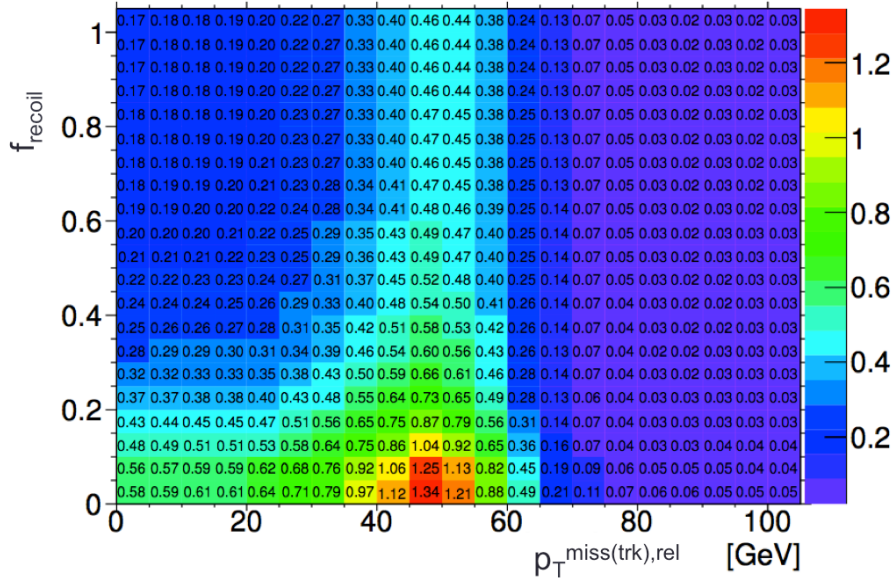


Figure 3.13: Signal significance as a function of required value for f_{recoil} and $p_{T,\text{rel}}^{\text{miss(trk)}}$ in the ggF $H \rightarrow WW^*$ with $n_j = 0$

1353 **3.6 PARAMETERS OF INTEREST AND STATISTICAL TREATMENT**

1354 As with any search or measurement, there are particular parameters of the Higgs that the $H \rightarrow WW^*$
 1355 analysis is interested in measuring. In this case, the parameters of interest are the mass of the Higgs bo-
 1356 son and its production cross section. Because the $H \rightarrow WW^* \rightarrow \ell\nu\ell\nu$ process does not have a closed
 1357 final state, it is not possible to measure the full invariant mass of the particle that may have produced
 1358 the final state. However, a proxy for the invariant mass using transverse plane information can be de-

1359 fined. This is described in more detail in section 3.6.1. The second parameter of interest is the ratio of the
 1360 measured cross section to that expected from the Standard Model Higgs, which is denoted a μ . This is
 1361 defined in equation 3.5.

$$\mu = \frac{\sigma}{\sigma_{\text{SM}}} \quad (3.5)$$

1362 All of the likelihoods used in the statistical analysis of the final signal region events are paramaterized
 1363 as a function of μ . μ is a natural variable for hypothesis testing, as $\mu = 0$ corresponds to a background
 1364 only hypothesis and $\mu = 1$ corresponds exactly to a Standard Model Higgs.

1365 3.6.1 TRANSVERSE MASS

1366 Because the longitudinal information about the neutrinos is not attainable, the $H \rightarrow WW^* \rightarrow \ell\nu\ell\nu$
 1367 analysis uses a mass variable, the transverse mass, that exploits information in the transverse plane as a
 1368 proxy for the full invariant mass. The transverse mass is defined in equation 3.6.

$$m_T = \sqrt{(E_T^{\ell\ell} + p_T^{\text{miss}})^2 - |\mathbf{p}_T^{\ell\ell} + \mathbf{p}_T^{\text{miss}}|^2}, \quad (3.6)$$

1369 Here the $E_T^{\ell\ell}$ and $p_T^{\ell\ell}$ are the transverse energy and momentum of the dilepton system, while p_T^{miss} is
 1370 a proxy for the transverse momentum of the di-neutrino system. The track-based p_T^{miss} is used in the m_T
 1371 rather than the calorimeter based E_T^{miss} because it has a better resolution on the true transverse mass.
 1372 Figure 3.11b shows the improvement in the RMS of the difference between the true and reconstructed
 1373 transverse mass in a ggF signal sample. The RMS improves by 4.7 GeV using p_T^{miss} in the m_T calcula-
 1374 tion.

1375 3.6.2 STATISTICAL TREATMENT^{*}

1376 LIKELIHOOD FUNCTION

1377 The statistical analysis of final event candidates is framed as a hypothesis test, where the null hypothe-
1378 sis is background-only (no Standard Model Higgs). The first step in the analysis is to form a likelihood
1379 function for the data. In its simplest form, this likelihood is the probability of observing the number
1380 of events seen in the final signal region given knowledge of the signal strength. Because observation of
1381 events is fundamentally a Poisson counting experiment, this simple likelihood can be expressed as a Pois-
1382 son probability of observing N events given a total number of predicted signal and background events.
1383 This basic likelihood is shown in equation 3.7.

$$\mathcal{L}(\mu) = P(N|\mu S + B) \quad (3.7)$$

1384 Here, P is the Poisson probability density function, N is the total number of observed events, μ is
1385 the signal strength, S is the predicted number of signal events, and B is the predicted number of back-
1386 ground events.

1387 In particle physics, certain background estimates are commonly normalized in so-called “control” re-
1388 gions and those predictions are scaled by the same normalization factor in the signal region. This leads
1389 to a slightly more complicated likelihood, which is a function of both the signal strength and the back-
1390 ground normalization. This is shown in equation 3.8.

$$\mathcal{L}(\mu, \theta) = P(N|\mu S + \theta B) P(N_{\text{CR}}|\theta B_{\text{CR}}) \quad (3.8)$$

1391 Here, θ is a so-called “nuisance parameter”, a parameter that is not a primary parameter of interest but
1392 still enters the likelihood. The second Poisson term adds an extra term to the likelihood, enforcing the
1393 fact that the background normalization must be consistent with the number of observed events in data
1394 in the control region, N_{CR} .

1395 So far, these two formulations of likelihoods have assumed a single signal region and do not take into

*Many thanks to Aaron Armbruster, whose thesis[69] inspired parts of this section.

1396 account any shape information of potential discriminating variables. The $H \rightarrow WW^*$ analysis is di-
 1397 vided into many different categories, and we can perform the same counting experiment described above
 1398 in each individual category. As mentioned in section 3.6.1, the transverse mass is used as the primary dis-
 1399 criminating variable in many of the $H \rightarrow WW^*$ sub-analyses, so additionally we can perform the same
 1400 counting experiment in each bin of the m_T distribution to incorporate some shape information. Thus,
 1401 the total likelihood becomes a product over signal regions and bins of the m_T distribution. Finally, there
 1402 are usually many backgrounds that are normalized in control regions, so the new formulation of the like-
 1403 lihood takes this into account as well by including a product over control regions in the second Poisson
 1404 term. All of these modifications are shown in equation 3.9.

$$\mathcal{L}(\mu, \theta) = \prod_{\substack{\text{SRs } i \\ \text{bins } b}} P\left(N_{ib} \middle| \mu S_{ib} + \sum_{\text{bkg } k} \theta_k B_{kib}\right) \prod_{\text{CRs } l} P\left(N_l \middle| \sum_{\text{bkg } k} \theta_k B_{kl}\right) \quad (3.9)$$

1405 The final step to get the full likelihood used in the analysis is to add nuisance parameters for the sys-
 1406 tematic uncertainties. In cases where the uncertainty does not affect the shape of m_T bin-by-bin, each
 1407 systematic uncertainty ϵ is allowed to affect the expected event yields through a linear response function
 1408 of the nuisance parameter, namely $\nu(\theta) = (1 + \epsilon)^\theta$. If instead the uncertainty does affect the shape,
 1409 the effect is instead parameterized by $\nu_b(\theta) = 1 + \epsilon_b \theta$. The value of the nuisance parameters for the
 1410 systematic uncertainty are constrained with a Gaussian term that is added to the likelihood as well. This
 1411 is of the form $g(\delta|\theta) = e^{-(\delta-\theta)^2/2}/\sqrt{2\pi}$, where δ is the central value and θ is a nuisance parameter.
 1412 Finally, a last term is added to account for the statistical uncertainty in the Monte Carlo samples used,
 1413 which adds an additional poisson term. The full likelihood used in the final statistical analysis is defined

¹⁴¹⁴ in equation 3.10.

$$\begin{aligned}\mathcal{L}(\mu, \boldsymbol{\theta}) = & \prod_{\substack{\text{SRs i} \\ \text{bins b}}} P\left(N_{ib} \middle| \mu S_{ib} \cdot \prod_{\substack{\text{sig.} \\ r}} \nu_{br}(\theta_r) + \sum_{\text{bkg k}} \theta_k B_{kib} \cdot \prod_{\substack{\text{bkg.} \\ \text{syst.} \\ s}} \nu_{bs}(\theta_s)\right) \\ & \cdot \prod_{\text{CRs l}} P\left(N_l \middle| \sum_{\text{bkg k}} \theta_k B_{kl}\right) \\ & \cdot \prod_{\substack{\text{syst.} \\ t}} g(\delta_t | \theta_t) \cdot \prod_{\text{bkg k}} P(\xi_k | \zeta_k \theta_k)\end{aligned}\tag{3.10}$$

¹⁴¹⁵ In the fourth term of the equation, quantifying uncertainty due to finite Monte Carlo sample size, ξ
¹⁴¹⁶ represents the central value of the background prediction, θ is the associated nuisance parameter, $\zeta =$
¹⁴¹⁷ $(B/\delta B)^2$, where δB is the statistical uncertainty of B .

¹⁴¹⁸ The best fit value of the signal strength μ is determined by finding the values of μ and $\boldsymbol{\theta}$ that maxi-
¹⁴¹⁹ mize the likelihood, while setting $\delta = 0$ and $\xi = \zeta$.

¹⁴²⁰ Once the likelihood is defined, a test statistic must be built for use in hypothesis testing.

¹⁴²¹ TEST STATISTIC

¹⁴²² To distinguish whether the data match a background only or background and signal hypothesis, a test
¹⁴²³ statistic must be used. The $H \rightarrow WW^*$ analysis used the profile likelihood technique[70]. The first step
¹⁴²⁴ in formulating this test statistic is to define the profile likelihood ratio, shown in equation 3.11.

$$\lambda(\mu) = \frac{\mathcal{L}(\mu, \hat{\theta}_\mu)}{\mathcal{L}(\hat{\mu}, \hat{\theta})}\tag{3.11}$$

¹⁴²⁵ Here $\hat{\theta}_\mu$ is the value of θ that maximizes the likelihood for the choice of μ being tested. Additionally,
¹⁴²⁶ $\hat{\theta}$ and $\hat{\mu}$ represent the values of θ and μ that gives the overall maximum value of the likelihood.

¹⁴²⁷ Once this is defined, a test statistic q_μ is constructed. This is shown in equation 3.12.

$$q_\mu = -2 \ln \lambda(\mu)\tag{3.12}$$

1428 A higher value of q_μ means that the data are more incompatible with the hypothesized value of μ , and
1429 q_0 then corresponds to the value of the test statistic for the background only hypothesis. A p_0 value is
1430 then defined to quantify the compatibility between the data and the null hypothesis. The p_0 value is the
1431 probability of obtaining a value of q_0 larger than the observed value, and this is shown in equation 3.13.

$$p_0 = \int_{q_0^{\text{obs}}}^{\infty} f(q_\mu | \mu = 0) dq_\mu \quad (3.13)$$

1432 Here $f(q_\mu)$ is the probability distribution function of the test statistic. Finally, the p_0 value can be
1433 converted into a signal significance, using the formula in equation 3.14, or the one-sided tail of the Gaussian distribution.

$$Z_0 = \sqrt{2} \operatorname{erf}^{-1}(1 - 2p_0) \quad (3.14)$$

1435 The threshold for discovery used in particle physics is $Z_0 \geq 5$, more commonly known as a value of
1436 5σ .

The real voyage of discovery consists not in seeking new landscapes, but in having new eyes.

Marcel Proust

4

1437

1438
1439

The discovery of the Higgs boson and the role of the $H \rightarrow WW^* \rightarrow \ell\nu\ell\nu$ channel

1440 4.1 INTRODUCTION

1441 This chapter presents the results of the search for the Higgs boson in 4.8 fb^{-1} collected at $\sqrt{s} = 7 \text{ TeV}$
1442 and 5.8 fb^{-1} at $\sqrt{s} = 8 \text{ TeV}$. The results of three searches at $\sqrt{s} = 8 \text{ TeV}$ in the $H \rightarrow WW^* \rightarrow \ell\nu\ell\nu$
1443 , $H \rightarrow \gamma\gamma$, and $H \rightarrow ZZ \rightarrow 4\ell$ channels are combined with results of searches at $\sqrt{s} = 7 \text{ TeV}$
1444 in the same search channels (as well as the $H \rightarrow \tau\tau$ production and associated production searches for
1445 $H \rightarrow b\bar{b}$). The results of this combination are a 5.9σ detection of a new particle consistent with a Higgs
1446 boson. Rather than going into detail for all of the different Higgs decay searches, this chapter will discuss
1447 the three most sensitive channels and in particular focus on $H \rightarrow WW^* \rightarrow \ell\nu\ell\nu$. While the focus is
1448 on WW^* , some of the ZZ^* and $\gamma\gamma$ results are shown for completeness. The results not discussed here

1449 can be found in the ATLAS Higgs discovery publication[[22](#)].

1450 **4.2 DATA AND SIMULATION SAMPLES**

1451 The data sample used for the following results was taken in 2011 and 2012 at center of mass energies of 7
1452 and 8 TeV, respectively, with 4.8 fb^{-1} collected at 7 TeV and 5.8 fb^{-1} collected at 8 TeV. Higgs pro-
1453 duction in the gluon fusion and vector boson fusion modes is modeled with **POWHEG** for the hard scat-
1454 tering event and **PYTHIA** for the showing and hadronization. Associated production of a Higgs with a
1455 vector boson or top quarks is modeled via **PYTHIA**.

1456 Table 4.1 shows the Monte Carlo generators used for modeling the signal and background processes
1457 relevant for the three analyses to be discussed.

Process	Generator
$\text{ggF}, \text{VBF } H$	POWHEG + PYTHIA
$WH, ZH, t\bar{t}H$	PYTHIA
$W + \text{jets}, Z/\gamma^* + \text{jets}$	ALPGEN + HERWIG
$t\bar{t}, tW, tb$	MC@NLO + HERWIG
tqb	ACERMC + PYTHIA
$q\bar{q} \rightarrow WW$	MC@NLO + HERWIG
$gg \rightarrow WW$	GG2WW+ HERWIG
$q\bar{q} \rightarrow ZZ$	POWHEG + PYTHIA
$gg \rightarrow ZZ$	GG2ZZ+ HERWIG
WZ	MADGRAPH+ PYTHIA , HERWIG
$W\gamma + \text{jets}$	ALPGEN + HERWIG
$W\gamma^*$	MADGRAPH+ PYTHIA
$q\bar{q}/gg \rightarrow \gamma\gamma$	SHERPA

Table 4.1: Monte carlo generators used to model signal and background for the Higgs search[[22](#)].

1458 **4.3 $H \rightarrow WW \rightarrow e\nu\mu\nu$ SEARCH**

1459 The $H \rightarrow WW \rightarrow e\nu\mu\nu$ search is unique compared to the ZZ and $\gamma\gamma$ channels. The Higgs mass can-
1460 not be fully reconstructed due to the presence of neutrinos in the final state, so the transverse mass m_T
1461 is used as the final discriminating variable. Compared to the other channels, there are more backgrounds

1462 here as well, as discussed in chapter 3. The same flavor final states are excluded from this search due to
1463 high pileup in the 8 TeV dataset.

1464 4.3.1 EVENT SELECTION

1465 The analysis requires two opposite charge isolated leptons, with the leading (sub-leading) lepton required
1466 to have $p_T > 25(15)$ GeV. The events are separated into different signal regions depending on which
1467 flavor of lepton is leading ($e\mu$ for leading electron, μe for leading muon). Strict lepton quality cuts are
1468 applied to the sample to reduce backgrounds from fake leptons.

1469 Jets are reconstructed with the anti- k_T algorithm with a radius parameter $R = 0.4$. The jets are
1470 required to have $p_T > 25$ GeV and $|eta| < 4.5$, with jets in the tracking volume required to have a
1471 jet vertex fraction of 0.5 and jets in the forward region required to have $p_T > 30$ GeV. The analysis is
1472 separated into three different signal regions based on jet multiplicity: $n_j = 0, 1, \geq 2$.

1473 To indicate the presence of neutrinos in the event, a requirement of $E_{T,\text{rel}}^{\text{miss}} > 25$ GeV is made*. This
1474 requirement significantly reduces the QCD multijet and Z/γ^* + jets backgrounds. Figure 4.1 shows the
1475 distribution of n_j in data and simulation after applying these “pre-selection” requirements.

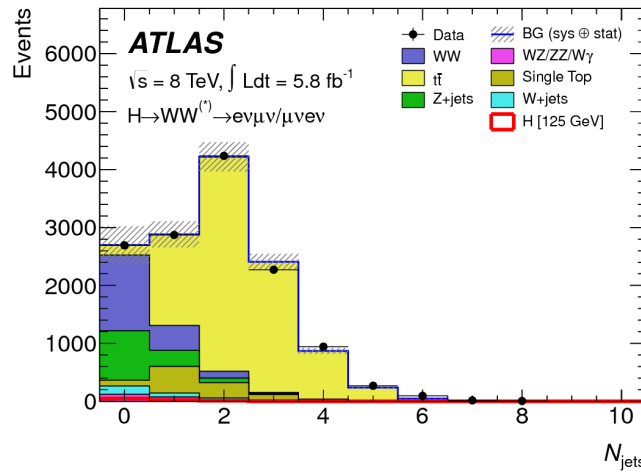


Figure 4.1: Jet multiplicity distribution in data and MC after applying lepton, jet, and $E_{T,\text{rel}}^{\text{miss}}$ selections. The WW and top backgrounds have been normalized using control samples, and the hashed band indicates the total uncertainty on the prediction. [22]

*For the definition of $E_{T,\text{rel}}^{\text{miss}}$, see chapter 3

1476 Additional selections are applied to require the dilepton topology to correspond to that of a SM
1477 Higgs. The requirements are presented here - more detailed discussion on the motivation for each re-
1478 quirement is saved for Chapter 5. In all of the jet multiplicity channels, the dilepton system is required to
1479 have a small gap in azimuthal angle, $\Delta\phi_{\ell\ell} < 1.8$. Similarly, the $m_{\ell\ell}$ is required to be less than 50 GeV
1480 in the lower jet multiplicity channels and less than 80 GeV in the $n_j \geq 2$ channel. In the $n_j = 0$
1481 channel, the magnitude of the dilepton p_T , $p_T^{\ell\ell}$, is required to be greater than 30 GeV.

1482 In the higher jet multiplicity channels ($n_j \geq 1$), the top background is a more important component
1483 and must be reduced. The total transverse momentum p_T^{sum} is thus required to be less than 30 GeV.
1484 Additionally, the di- τ invariant mass $m_{\tau\tau}$ (dilepton mass computed under the assumption that the neu-
1485 trinos from the τ decay are emitted collinear to the charged leptons) is used to reject $Z \rightarrow \tau\tau$ events by
1486 requiring $|m_{\tau\tau} - m_Z| > 25$ GeV. These variables are also discussed in more detail in Chapter 5.

1487 In the $n_j \geq 2$ channel, requirements are made to isolate the VBF contribution to Higgs production.
1488 The kinematics of the two leading jets are used to make these requirements. In particular, the event must
1489 have $\Delta y_{jj} > 3.8$ and $m_{jj} > 500$ GeV, along with a veto on having any additional jets with rapidity
1490 between the two leading jets.

1491 4.3.2 BACKGROUND ESTIMATION

1492 The details of the background estimation techniques used in the $H \rightarrow WW^* \rightarrow \ell\nu\ell\nu$ analysis are dis-
1493 cussed in section 5.5. As that section refers to a later iteration of the analysis, a general discussion is given
1494 here for completeness. The dominant backgrounds are SM WW production and top (both pair and
1495 single) production, and these backgrounds have their normalizations estimated from dedicated control
1496 regions while their shapes are taken from simulation.

1497 The control sample for the Standard Model WW background is defined by making the same require-
1498 ments as the signal region with the $m_{\ell\ell}$ requirement inverted (now requiring $m_{\ell\ell} > 80$ GeV) and
1499 removing the $\Delta\phi_{\ell\ell}$ requirement. This creates a control sample that is 70% (40%) pure in the 0(1)-jet
1500 region. The correction to the pure MC-based background estimate is quantified by defining a normal-
1501 ization factor β which is the ratio of the data yield to the MC yield ($N_{\text{data}}/N_{\text{MC}}$) in this control sample.

1502 Table 4.2 shows the WW normalization factors in the $n_j = 0$ and $n_j = 1$ bins (the $n_j \geq 2$ estimate is
 1503 taken directly from MC).

n_j	β_{WW}	β_t
= 0	1.06 ± 0.06	1.11 ± 0.06
= 1	0.99 ± 0.15	1.11 ± 0.05
≥ 2	-	1.01 ± 0.26

Table 4.2: Normalization factors (ratio of data and MC yields in a control sample) for the Standard Model WW and top backgrounds in the $H \rightarrow WW^* \rightarrow \ell\nu\ell\nu$ analysis [22]. Only statistical uncertainties are shown.

1504 The top background estimate is also computed separately in each jet multiplicity bin. In the $n_j = 0$
 1505 channel, the background is first normalized using data after pre-selection requirements with no selection
 1506 on n_j . Then, a dedicated b -tagged control sample is used to evaluate the ratio of one-jet to two-jet events
 1507 in data. The details of this technique are shown in reference [71]. In the $n_j = 1$ and the $n_j \geq 2$ regions,
 1508 the top background is normalized in a control sample where the signal region selections are applied,
 1509 but the b -jet veto is reversed and the Higgs topology requirements on $m_{\ell\ell}$ and $\Delta\phi_{\ell\ell}$ are removed. The
 1510 resulting normalization factors for these techniques are shown in table 4.2.

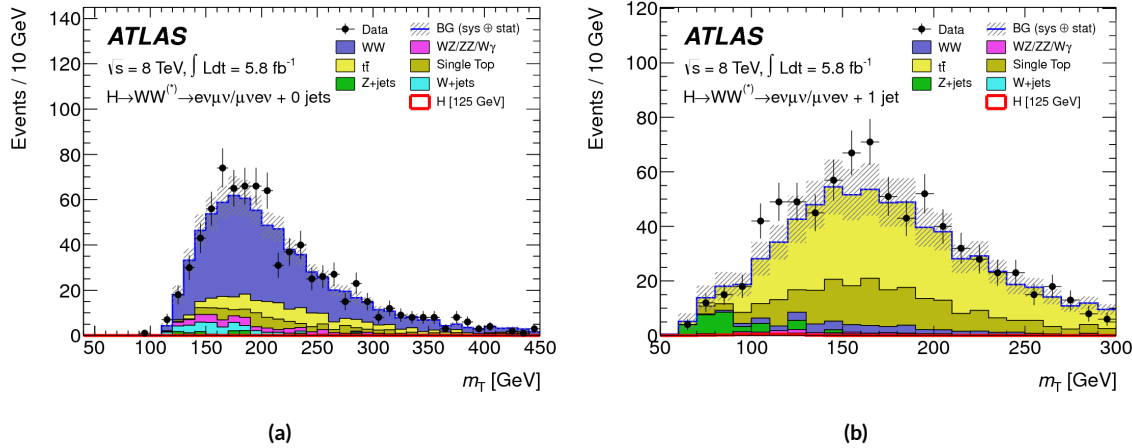


Figure 4.2: Comparison of m_T between data and simulation in the $n_j = 0$ WW (a) and $n_j = 1$ top (b) control samples [22]

1511 The control samples which are used for background normalization can also be used to validate the
 1512 modeling of the m_T distribution for each background. Figure 4.2 shows the comparison between data

1513 and MC for the m_T distribution after correcting the normalization of the backgrounds in the WW and
 1514 top control regions. Good agreement between data and simulation is seen in both cases.

1515 The $W + \text{jets}$ background estimate is taken entirely from data using a control sample with one well
 1516 reconstructed lepton and one anti-identified lepton. All other backgrounds are taken purely from simu-
 1517 lation.

1518 4.3.3 SYSTEMATIC UNCERTAINTIES

1519 The systematic uncertainties that have the largest impact on the analysis are the theoretical uncertainties
 1520 associated with the signal cross section, and these are shared with the ZZ^* and $\gamma\gamma$ channels. The un-
 1521 certainties resulting from variations of the QCD scale are $+7\% / -8\%$ on the final singal yield. Those
 1522 coming from variations of the parton distribution function (PDF) used in the simulation add a $\pm 8\%$
 1523 uncertainty on the yield. The uncertainties on the branching ratios of the Higgs are $\pm 5\%$.

1524 The main experimental uncertainties come from variations of the jet energy scale (JES), jet energy
 1525 resolution, pile-up, E_T^{miss} , b -tagging efficiency, $W + \text{jets}$ background estimate, and integrated luminosity.
 1526 For more details, see reference [22].

1527 4.3.4 RESULTS

1528 Table 4.3 shows the signal and background yields in the final signal region after normalizing the back-
 1529 grounds according to the methods described above.

	$n_j = 0$	$n_j = 1$	$n_j \geq 2$
Signal	20 ± 4	5 ± 2	0.34 ± 0.07
WW	101 ± 13	12 ± 5	0.10 ± 0.14
Other dibosons	12 ± 3	1.9 ± 1.1	0.10 ± 0.10
$t\bar{t}$	8 ± 2	6 ± 2	0.15 ± 0.10
Single top	3.4 ± 1.5	3.7 ± 1.6	-
$Z/\gamma^* + \text{jets}$	1.9 ± 1.3	0.10 ± 0.10	-
$W + \text{jets}$	15 ± 7	2 ± 1	-
Total background	142 ± 16	26 ± 6	0.35 ± 0.18
Observed in data	185	38	0

Table 4.3: Data and expected yields for signal and background in the final $H \rightarrow WW^* \rightarrow \ell\nu\ell\nu$ signal region.
 Uncertainties shown are both statistical and systematic. [22]

1530 Figure 4.3 shows the m_T distribution in the $n_j \leq 1$ channels for 8 TeV data. (No events are observed
 1531 in data in the $n_j \geq 2$ channels in this dataset). The excess shown here relatively flat as a function of
 1532 hypothesized Higgs mass. The combined 7 and 8 TeV data gives an excess with local significance of 2.8σ
 1533 with an expected significance of 2.3σ , corresponding to a μ measurement of 1.3 ± 0.5 .

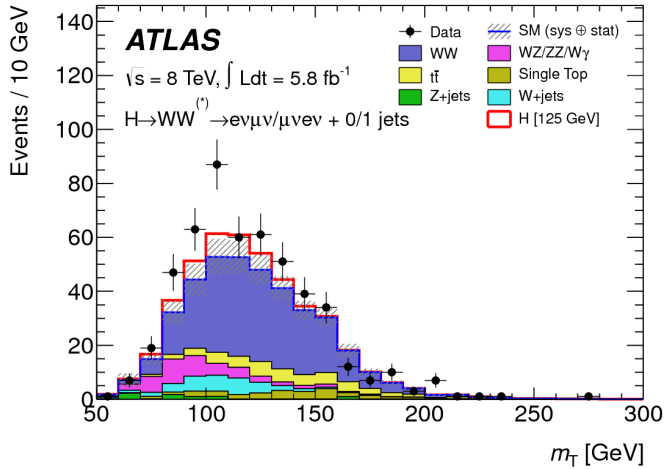


Figure 4.3: m_T distribution in the $H \rightarrow WW \rightarrow e\nu\mu\nu$ $n_j \leq 1$ channels for 8 TeV data[22].

1534 4.4 $H \rightarrow \gamma\gamma$ SEARCH

1535 The $H \rightarrow \gamma\gamma$ search is in essence a search for a peaked excess above the falling SM diphoton mass spec-
 1536 trum, with $m_{\gamma\gamma}$ as the ultimate discriminating variable. Events are selected by requiring two isolated
 1537 photons, with the leading (sub-leading) photon required to have $E_T > 40(30)$ GeV. In the 8 TeV
 1538 data, the photons are required to pass cut-based identification criteria consistent with a photon in the
 1539 electromagnetic calorimeter and little leakage in the hadronic calorimeter.

1540 The main challenges for this analysis are accurate mass reconstruction and background estimation.
 1541 In order to accurately reconstruct the invariant mass of the di-photon system, both the energy and di-
 1542 rection of the photons must be measured well. Therefore, the identification of the primary vertex of the
 1543 hard interaction is particularly important, and is done using a multivariate likelihood which combines
 1544 information about the photon direction and vertex position. The background is modeled with a falling
 1545 spectrum in $m_{\gamma\gamma}$ that is parameterized by different functions depending on the category of the event.

1546 4.4.1 RESULTS

1547 The resulting diphoton mass spectrum is shown in figure 4.4. The best fit mass value in the $\gamma\gamma$ channel
 1548 alone in the combined 7 and 8 TeV data is 126.5 GeV. The local significance at this point is 4.5σ , with
 1549 an expected significance of 2.5σ . Therefore, the measured signal strength μ is 1.8 ± 0.5 in this channel.

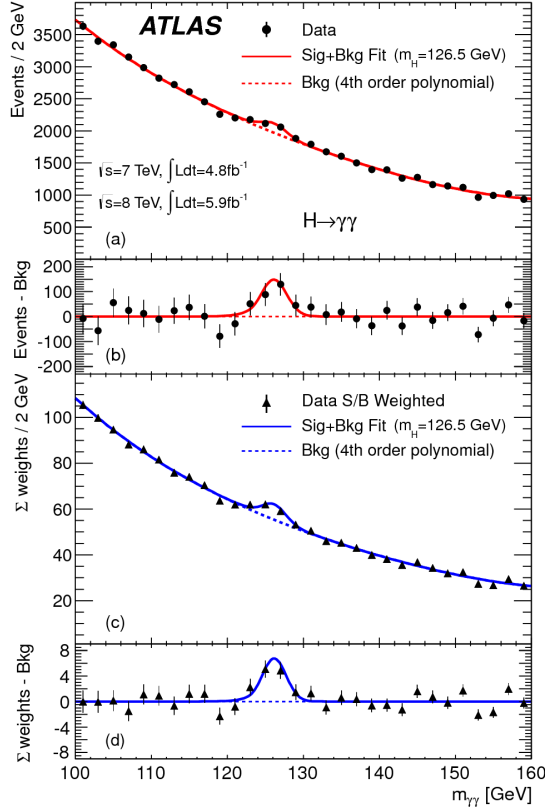


Figure 4.4: Diphoton mass spectrum in 7 and 8 TeV data. Panel a) shows the unweighted data distribution superimposed on the background fit, while panel c) shows the data where each event category is weighted by its signal to background ratio. Panels b) and d) show the respective distributions with background subtracted[22].

1550 4.5 $H \rightarrow ZZ \rightarrow 4\ell$ SEARCH

1551 The $H \rightarrow ZZ \rightarrow 4\ell$ analysis searches for a Standard Model Higgs boson decaying to two Z bosons,
 1552 each of which decays to a pair of same flavor, opposite charge isolated leptons. The ultimate discriminat-
 1553 ing variable is $m_{4\ell}$, or the invariant mass of the four selected leptons. The ℓ denotes an e or μ as with the
 1554 $H \rightarrow WW^* \rightarrow \ell\nu\ell\nu$ analysis.

1555 Four distinct signal regions are constructed depending on the flavors of the final state, additionally
 1556 separated by the flavor of the leading lepton pair. These are referred to as $4e$, $2e2\mu$, $2\mu2e$, 4μ .

1557 The main backgrounds in the $H \rightarrow ZZ \rightarrow 4\ell$ search are continuum ZZ^* production, $Z + \text{jets}$ pro-
 1558 duction, and $t\bar{t}$. The $m_{4\ell}$ distribution for background is estimated from simulation. The normalization
 1559 of the SM ZZ^* background is also taken from MC simulation, while the $Z + \text{jets}$ and $t\bar{t}$ normalizations
 1560 are taken from data-driven methods.

1561 **4.5.1 RESULTS**

1562 Figure 4.5 shows the $m_{4\ell}$ spectrum measured in the 7 and 8 TeV datasets. The total number of events
 1563 observed in the window between 120 and 130 GeV is 13, with 6 events in the 4μ channel, 2 events in
 1564 the $4e$ channel, and 5 events in the $2e2\mu/2\mu2e$. The best fit μ value in the combined 7 and 8 TeV data
 1565 occurs at 125 GeV and is measured to be 1.2 ± 0.6 . The observed significance at this mass is 3.6σ , with
 1566 an expected significance of 2.7σ .

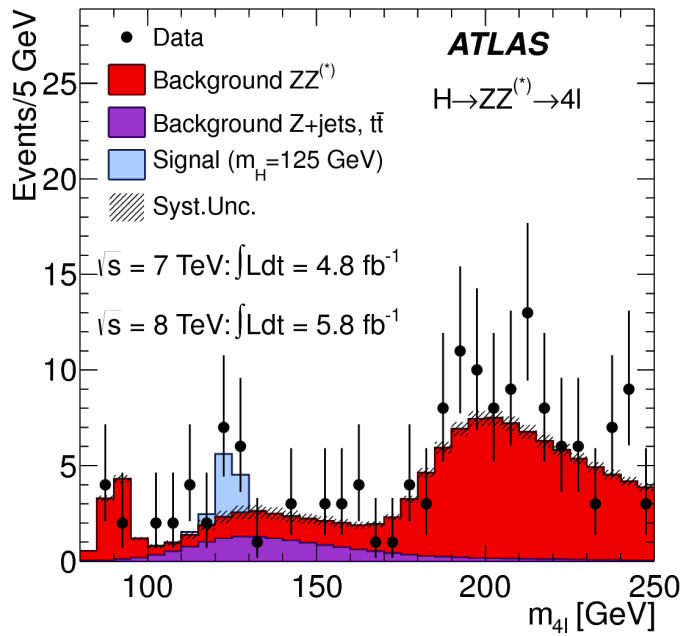


Figure 4.5: Four lepton invariant mass spectrum ($m_{4\ell}$) in 7 and 8 TeV data compared to background estimate. A 125 GeV SM Higgs signal is shown in blue[22].

1567 4.6 COMBINED RESULTS

1568 The statistical interpretation of the combined results is undertaken as described in section 3.6.2, with a
 1569 hypothesis test based on a likelihood ratio parameterized by the Higgs signal strength μ . The null hy-
 1570 pothesis corresponds to $\mu = 0$, while the SM Higgs corresponds to $\mu = 1$.

1571 Table 4.4 summarizes the properties of the individual channels as well as the significances of the ex-
 1572 cesses seen. The most significant observed local excess comes from the $\gamma\gamma$ channel. Figure 4.6 shows a
 1573 comparison of the observed local p_0 values as a function of hypothesized mass for the three different
 1574 search channels. Both the ZZ^* and $\gamma\gamma$ channels have very peaked excesses, while the WW^* excess can
 1575 be seen as very broad because the m_T distribution does not provide detailed information about the true
 1576 Higgs mass.

Channel	Fit var.	Observed Z_l	Expected Z_l	$\hat{\mu}$
$H \rightarrow ZZ^* \rightarrow 4\ell$	$m_{4\ell}$	3.6	2.7	1.2 ± 0.6
$H \rightarrow \gamma\gamma$	$m_{\gamma\gamma}$	4.5	2.5	1.8 ± 0.5
$H \rightarrow WW^* \rightarrow e\nu\mu\nu$	m_T	2.8	2.3	1.3 ± 0.5
Combined	-	6.0	4.9	1.4 ± 0.3

Table 4.4: Summary of the expected and observed significance and measured signal strengths in the combined 7 and 8 TeV datasets for the Higgs discovery analysis[22].

1577 Figure 4.7 shows the combined exclusion limit, p_0 , and signal strength. The highest local excess comes
 1578 at a value of 126.5 GeV and corresponds to a 6.0σ observed excess.

1579 Figure 4.8 shows a comparison of the measured signal strengths between the different Higgs search
 1580 channels. All measured μ are consistent with unity within their uncertainty, and the combined μ mea-
 1581 surement is 1.4 ± 0.3 .

1582 The likelihood can also be computed in a two-dimensional plane of m_H and μ , and this is shown in
 1583 figure 4.9. The figure shows that while the $\gamma\gamma$ and ZZ^* channels have very good mass resolution, the
 1584 excess in WW^* covers a broad mass range. The banana shape of the WW^* result is due to the fact that
 1585 the excess in this channel can either be explained by increasing the signal strength or by changing the
 1586 mass (and thus the cross section). The two parameters are correlated due to the lack of mass sensitivity in
 1587 this channel.

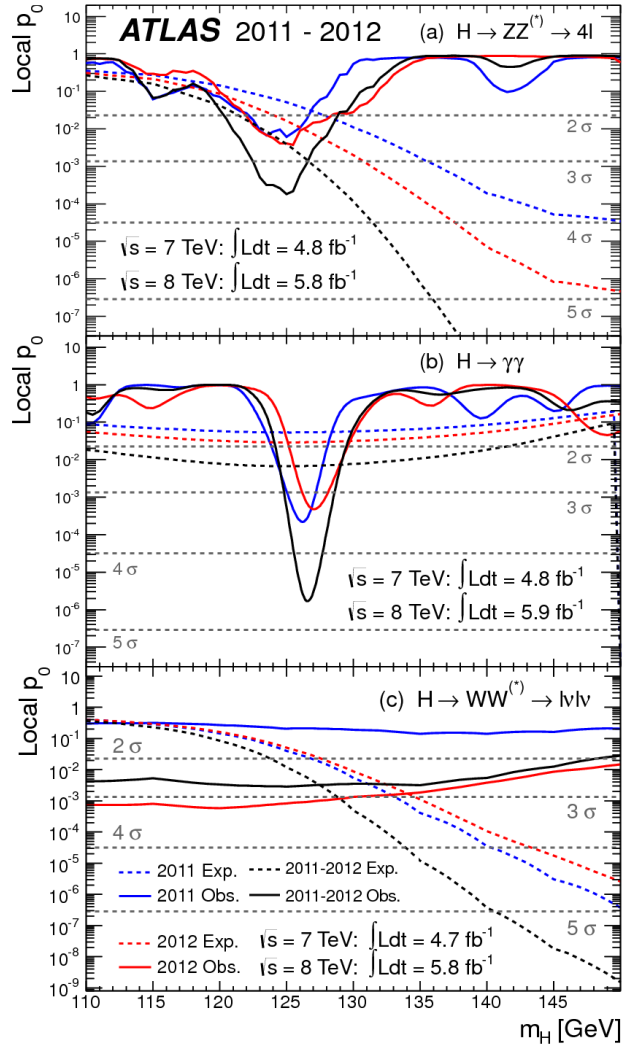


Figure 4.6: Local p_0 distribution as a function of hypothesized Higgs mass for the $H \rightarrow ZZ^* \rightarrow 4\ell$ (a), $H \rightarrow \gamma\gamma$ (b), and $H \rightarrow WW^* \rightarrow \ell\nu\ell\nu$ (c) channels. Dashed curves show expected results, while solid curves show observed. Red curves are from 7 TeV data, blue curves from 8 TeV, and black curved combined[22].

Because multiple Higgs mass points are searched for, the local significance must be corrected for a look-elsewhere effect to compute a true global significance. The global significance for finding a Higgs anywhere in the mass range of 110 GeV to 600 GeV is 5.1σ . This increases slightly to 5.3σ if only mass range from 110 to 150 GeV.

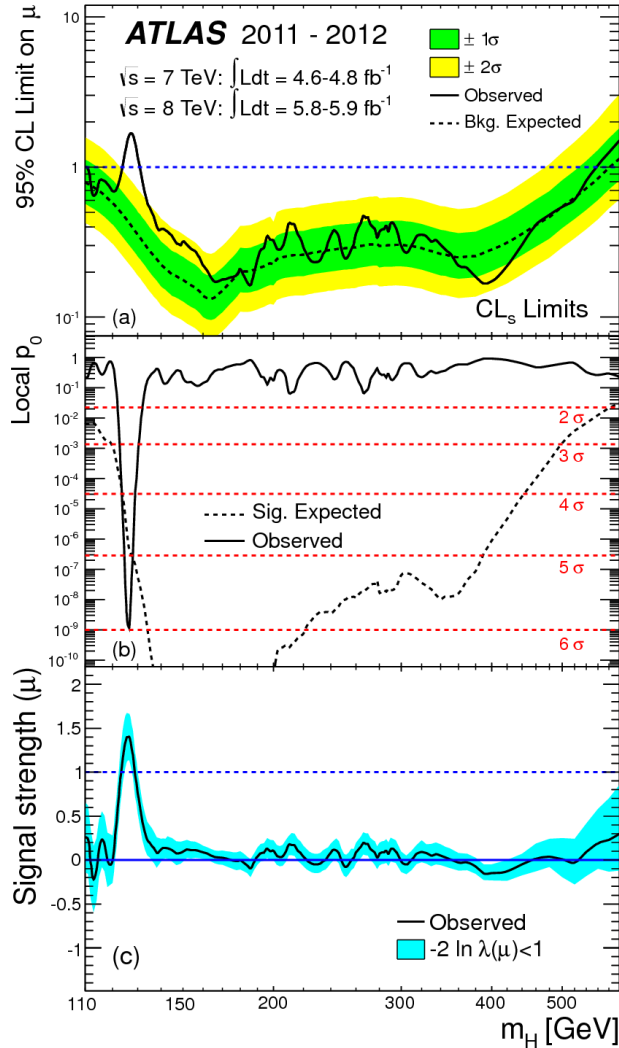


Figure 4.7: Combined 95% CL limits (a), local p_0 values (b), and signal strength measurement (c) as a function of Higgs mass[22].

1592 4.7 CONCLUSION

1593 A search for the production of a Standard Model Higgs boson was conducted in 4.8 fb^{-1} collected at
 1594 $\sqrt{s} = 7 \text{ TeV}$ and 5.8 fb^{-1} at $\sqrt{s} = 8 \text{ TeV}$. A new particle consistent with the Higgs boson was
 1595 observed, with a mass of 126.5 GeV and a global (local) significance of $5.1(6.0)\sigma$. This is the first dis-
 1596 covery level observation of a particle consistent with the Higgs.

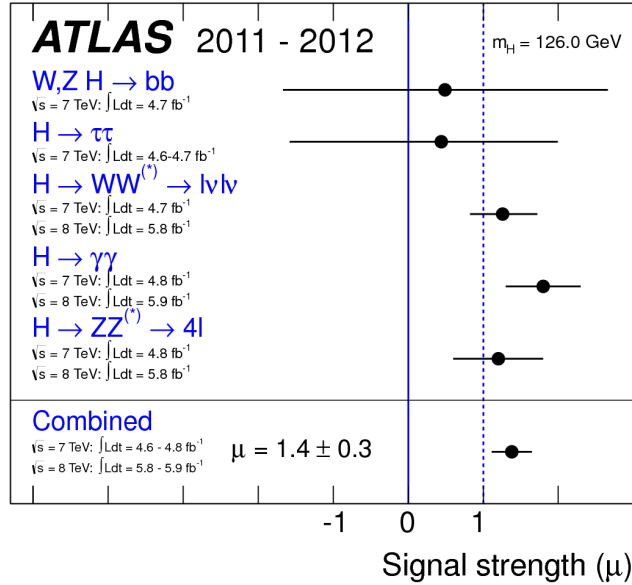


Figure 4.8: Comparison of measured signal strength μ for a 126 GeV Higgs in the 7 and 8 TeV datasets[22].

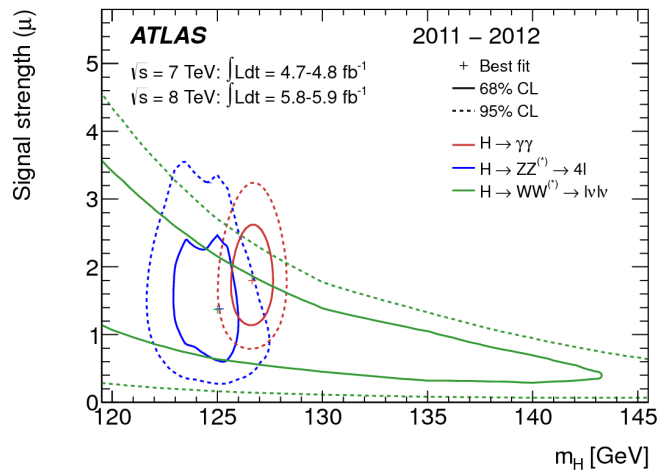


Figure 4.9: Two dimensional likelihood as a function of signal strength μ and Higgs mass m_H [22].

*The imagination of nature is far, far greater than the
imagination of man.*

Richard Feynman

5

1597

1598

Observation of Vector Boson Fusion

1599

production of $H \rightarrow WW^* \rightarrow \ell\nu\ell\nu$

1600 5.1 INTRODUCTION

1601 After the discovery of a particle consistent with the Higgs boson, the $H \rightarrow WW^*$ analysis had two main
1602 goals. The first goal was to increase the sensitivity of the analysis to fully confirm that the $H \rightarrow WW^*$
1603 process did indeed exist. The second goal was to characterize the particle as much as possible, including
1604 searching for the lower cross-section production modes, in order to confirm that it was indeed a Higgs
1605 boson. This chapter presents a dedicated search for Vector Boson Fusion (VBF) production of a Higgs
1606 boson decaying via the $H \rightarrow WW^* \rightarrow \ell\nu\ell\nu$ mode. First, basics of the topology of VBF production
1607 are presented. Then, the details of the analysis are shown, including signal region definition, background
1608 estimation techniques, and systematic uncertainties. Finally, the results of the analysis are presented. As

1609 will be shown, this analysis is the first and most sensitive observation of the VBF production mode of the
1610 Higgs on ATLAS.

1611 In the VBF channel, there are both a selection requirement based signal region analysis (known as the
1612 “cut-based”) and a multivariate analysis which uses a boosted decision tree (known as the BDT analysis).
1613 The focus of this chapter will be on the cut-based signal region, as this is an important component of the
1614 VBF analysis and in particular acts as strong validation for the final BDT result. Connections between
1615 the cut-based and BDT analyses will be discussed where appropriate.

1616 5.2 DATA AND SIMULATION SAMPLES

1617 The results presented here are with 20.3 fb^{-1} taken at $\sqrt{s} = 8 \text{ TeV}$ and 4.5 fb^{-1} taken at $\sqrt{s} = 7 \text{ TeV}$.
1618 The details of the LHC and detector conditions during this period are given in Chapter 2. The trigger
1619 selection defining the dataset is discussed in section 5.2.1. The simulation samples used for signal and
1620 background modeling are given in section 5.2.2.

1621 5.2.1 TRIGGERS

1622 The analysis uses a combination of single lepton and dilepton triggers to allow lowering of the p_T thresh-
1623 olds and increased signal acceptance. The p_T threshold on the leptons is a particularly important consid-
1624 eration for this signal. Because the second W produced in the decay can be off-shell, it tends to pro-
1625 duce lower momentum leptons. Thus, being able to lower the p_T threshold while still maintaining
1626 a low background rate is critical. Figure 5.1 shows an example of the subleading lepton p_T for a VBF
1627 $H \rightarrow WW^*$ signal compared to the corresponding $t\bar{t}$ background. Note that the lepton p_T spectrum is
1628 considerably softer in the signal sample.

1629 As discussed in Chapter 2, there are multiple levels in the ATLAS trigger system, and there are differ-
1630 ent p_T thresholds imposed for the leptons at each level. Additionally, some triggers have a loose selection
1631 on the isolation of the lepton (looser than that applied offline in the analysis object selection). Table 5.1
1632 shows the thresholds used for single lepton triggers, while table 5.2 shows the thresholds coming from
1633 di-lepton triggers. The single lepton trigger efficiency for muons that pass the analysis object selection is

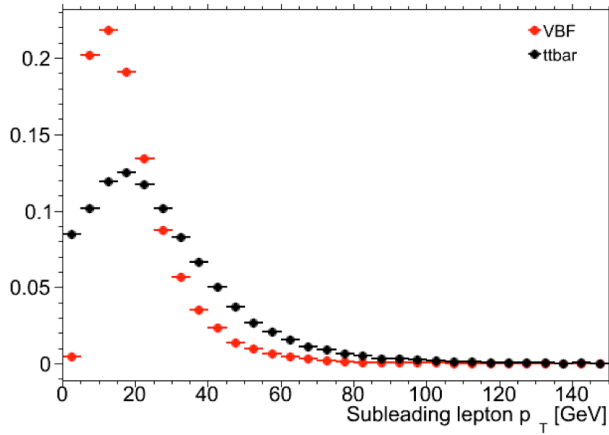


Figure 5.1: A comparison of the subleading lepton p_T spectrum between VBF $H \rightarrow WW^*$ production and $t\bar{t}$ background

1634 70% for muons in the barrel region ($|\eta| < 1.05$) and 90% in the endcap region. The electron trigger ef-
1635 ficiency increases with electron p_T but the average is approximately 90%. These efficiencies are measured
1636 by combined performance and trigger signature groups[72, 73].

	Level-1 threshold	High-level threshold
Electron	18	$24i$
	30	60
Muon	15	$24i$
		36

Table 5.1: Single lepton triggers used for electrons and muons. A logical “or” of the triggers listed for each lepton type is taken. Units are in GeV, and the i denotes an isolation requirement in the trigger.

	Level-1 threshold	High-level threshold
ee	10 and 10	12 and 12
$\mu\mu$	15	18 and 8
$e\mu$	10 and 6	12 and 8

Table 5.2: Di-lepton triggers used for different flavor combinations. The two thresholds listed refer to leading and sub-leading leptons, respectively. The di-muon trigger only requires a single lepton at level-1.

1637 The combination of all triggers shown gives good efficiency for signal events. This efficiency is sum-
1638 marized in table 5.3. The relative improvement in efficiency by adding the dilepton triggers is also shown
1639 in the same table. The largest gain comes in the $\mu\mu$ channel. Overall the trigger selection shows a good
1640 efficiency for $H \rightarrow WW^*$ signal events.

Channel	Trigger efficiency	Gain from 2ℓ trigger
ee	97%	9.1%
$\mu\mu$	89%	18.5%
$e\mu$	95%	8.3%
μe	81%	8.2%

Table 5.3: Trigger efficiency for signal events and relative gain of adding a dilepton trigger on top of the single lepton trigger selection. The first lepton is the leading, while the second is the sub-leading. Efficiencies shown here are for the ggF signal in the $n_j = 0$ category but are comparable for the VBF signal.

1641 5.2.2 MONTE CARLO SAMPLES

1642 Modeling of signal and background processes in the signal region, in particular for the m_T distribution,
 1643 is an important consideration for the final interpretation of the analysis. Therefore, careful consideration
 1644 must be paid to which Monte Carlo (MC) generators are used for specific processes. With the exception
 1645 of the $W + \text{jet}$ and multijet backgrounds, the m_T shape used as the final discriminant is taken from simu-
 1646 lation. (Many backgrounds are normalized from data, as described in section 5.5).

1647 Table 5.4 shows the MC generators used for the signal and background processes, as well as their cross
 1648 sections. In order to include corrections up to next-to-leading order (NLO) in the QCD coupling con-
 1649 stant α_s , the `POWHEG` [74] generator is often used. In some cases, only leading order generators like
 1650 `ACERMC` [75] and `GG2VV` [76] are available for the process in question. If the process requires good
 1651 modeling for very high parton multiplicities, the `SHERPA` [77] and `ALPGEN` [78] generators are used
 1652 to provide merged calculations for five or fewer additional partons. These matrix element level calcula-
 1653 tions must then be additionally matched to models of the underlying event, hadronization, and parton
 1654 shower. There are four possible generators for this: `SHERPA`, `PYTHIA 6`[79], `PYTHIA 8`[80], or `HERWIG`
 1655 [81] + `JIMMY` [82]. The simulation additionally requires an input parton distribution function (PDF).
 1656 The `CT10`[83] PDFs are used for `SHERPA` and `POWHEG` simulated samples, while `CTEQ6Li`[84] is used
 1657 for `ALPGEN + HERWIG` and `ACERMC` simulations. The Drell-Yan samples are reweighted to the `MRST`
 1658 [85] PDFs, as these are found to give the best agreement between data and simulation.

1659 Once the basic hard scattering process is simulated, it must be passed through a detector simulation
 1660 and additional pile-up events must be overlaid. The pile-up events are modeled with `PYTHIA 8`, and the

Process	MC generator	$\sigma \cdot \mathcal{B}$ (pb)
Signal		
ggF	$H \rightarrow WW^*$ POWHEG +PYTHIA 8	0.435
VBF	$H \rightarrow WW^*$ POWHEG +PYTHIA 8	0.0356
VH	$H \rightarrow WW^*$ PYTHIA 8	0.0253
WW		
$q\bar{q} \rightarrow WW$ and $qg \rightarrow WW$	POWHEG +PYTHIA 6	5.68
$gg \rightarrow WW$	GG2VV +HERWIG	0.196
$(q\bar{q} \rightarrow W) + (q\bar{q} \rightarrow W)$	PYTHIA 8	0.480
$q\bar{q} \rightarrow WW$	SHERPA	5.68
VBS $WW + 2$ jets	SHERPA	0.0397
Top quarks		
$t\bar{t}$	POWHEG +PYTHIA 6	26.6
Wt	POWHEG +PYTHIA 6	2.35
$tq\bar{b}$	ACERMC +PYTHIA 6	28.4
$t\bar{b}$	POWHEG +PYTHIA 6	1.82
Other dibosons (VV)		
$W\gamma$ ($p_T^\gamma > 8$ GeV)	ALPGEN +HERWIG	369
$W\gamma^*$ ($m_{\ell\ell} \leq 7$ GeV)	SHERPA	12.2
WZ ($m_{\ell\ell} > 7$ GeV)	POWHEG +PYTHIA 8	12.7
VBS $WZ + 2$ jets	SHERPA	0.0126
($m_{\ell\ell} > 7$ GeV)		
$Z\gamma$ ($p_T^\gamma > 8$ GeV)	SHERPA	163
$Z\gamma^*$ (min. $m_{\ell\ell} \leq 4$ GeV)	SHERPA	7.31
ZZ ($m_{\ell\ell} > 4$ GeV)	POWHEG +PYTHIA 8	0.733
$ZZ \rightarrow \ell\ell\nu\nu$ ($m_{\ell\ell} > 4$ GeV)	POWHEG +PYTHIA 8	0.504
Drell-Yan		
Z ($m_{\ell\ell} > 10$ GeV)	ALPGEN +HERWIG	16500
VBF $Z + 2$ jets	SHERPA	5.36
($m_{\ell\ell} > 7$ GeV)		

Table 5.4: Monte Carlo samples used to model the signal and background processes[21].

ATLAS detector is simulated with GEANT4[86]. Because of the unique phase space of the $H \rightarrow WW^*$ analysis, events are sometimes filtered at generator level to allow for more efficient generation of relevant events. The efficiency of the trigger in MC simulation does not always match the measured efficiency in

1664 data, so trigger scale factors are applied to correct the MC efficiency to the data. These are derived by the
1665 combined performance groups[[72](#), [73](#)].

1666 5.3 OBJECT SELECTION

1667 In order to define the signal region, the analysis must first select the objects to be considered. The de-
1668 tails of the object reconstruction algorithms are discussed in Chapter 2, while this section gives specific
1669 selection cuts used in the $H \rightarrow WW^*$ analysis.

1670 The first step in this process is to select a primary vertex candidates. The event’s primary vertex is the
1671 vertex with the largest sum of p_T^2 for associated tracks and is required to have at least three tracks with
1672 $p_T > 450$ MeV. Many of the object selection cuts are then made relative to this chosen primary vertex.

1673 5.3.1 MUONS

1674 The analysis uses combined muon candidates, where a track in the Inner Detector has been matched
1675 to a standalone track in the Muon Spectrometer. The track parameters are combined statistically in the
1676 muon reconstruction algorithm[[16](#)]. The muons are required to be within $|\eta| < 2.5$ and have a $p_T >$
1677 10 GeV. To reduce backgrounds coming from mis-reconstructed leptons, there are requirements on
1678 the impact parameter of the muon relative to the primary vertex. The transverse impact parameter d_0
1679 is required to be small relative to its estimated uncertainty, the exact cut value being $d_0/\sigma_{d_0} < 3$. The
1680 longitudinal impact parameter z_0 must satisfy $|z_0 \sin \theta| < 1$ mm.

1681 As discussed previously, the muons must also be isolated. There are two types of lepton isolations
1682 that are calculated: track-based and calorimeter-based. For muons, the track-based isolation is defined
1683 using the scalar sum $\sum p_T$ for tracks with $p_T > 1$ GeV (excluding the muon’s track) within a cone of
1684 $\Delta R = 0.3$ (0.4) for muon with $p_T > 15$ GeV ($10 < p_T < 15$ GeV). The final isolation requirement
1685 is made my requiring that this scalar sum be no more than a certain fraction of the muon’s p_T . This re-
1686 quirement varies with muon p_T and the exact cuts are defined in table 5.5.

1687 The calorimeter-based muon isolation is defined using as a $\sum E_T$ calculated from calorimeter cells
1688 using the same cone size as the track-based isolation but excluding cells with $\Delta R < 0.05$ around the

1689 muon. This requirement is also defined as a cut on the ratio of the sum to the muon p_T and varies with
1690 muon p_T . The cut values are also given in table 5.5.

1691 The isolation requirements loosen as a function of p_T to allow for larger signal acceptance. At low p_T ,
1692 the isolation is tightened to reduce the $W + \text{jets}$ background which arises from a misidentified lepton.

p_T range (GeV)	Calorimeter isolation	Track isolation
10 – 15	0.06	0.06
15 – 20	0.12	0.08
20 – 25	0.18	0.12
> 25	0.30	0.12

Table 5.5: p_T dependent isolation requirements for muons. Muons are required to have the amount of calorimeter or track based cone sums be less than this fraction of their p_T .

1693 5.3.2 ELECTRONS

1694 Electrons are identified by matching reconstructed clusters in the electromagnetic calorimeter with tracks
1695 in the inner detector. The electrons are identified using a likelihood based method[14, 64] which takes
1696 into account the shower shapes in the calorimeter, the matching of tracks to clusters, and the amount of
1697 transition radiation in the TRT. The electrons are required to have $|\eta| < 2.47$, and candidates in the
1698 transition region between the barrel and endcap ($1.37 < |\eta| < 1.52$) are excluded. As the muons, the
1699 electrons are required to have transverse impact parameter significance < 3 , while in the longitudinal
1700 direction they must have $|z_0 \sin \theta| < 0.4$ mm. Some electron requirements also vary with electron E_T ,
1701 and these requirements are summarized in table 5.6.

1702 The isolation for electrons are defined similarly to the muons but with unique cuts on the objects in-
1703 cluded. The track-based isolation is defined using tracks with $p_T > 400$ MeV with cone sizes as defined
1704 previously. The calorimeter-based isolation also uses the same cone size as the muon, but here the cells
1705 within a 0.125×0.175 area in $\eta \times \phi$ around the electron cluster's barycenter are excluded. The other
1706 difference with respect to muons is that the denominator of the isolation ratio is the electron's E_T rather
1707 than p_T . The isolation cuts very with electron E_T and are defined in table 5.6.

1708 The electron is also required to not be consistent with a vertex coming from a photon conversion.

p_T range (GeV)	Quality cut	Calorimeter isolation	Track isolation
10 – 15	Very tight LH	0.20	0.06
15 – 20	Very tight LH	0.24	0.08
20 – 25	Very tight LH	0.28	0.10
> 25	Medium	0.28	0.10

Table 5.6: p_T dependent requirements for electrons. Electrons are required to have the amount of calorimeter or track based cone sums be less than this fraction of their E_T .

1709 5.3.3 JETS

1710 Jets are clustered with the anti- k_T reconstruction algorithm using a radius parameter of $R = 0.4$. They
 1711 are required to have a jet vertex fraction (JVF) of at least 50%, meaning that half of the tracks associated
 1712 with the jet originated from the primary vertex. Jets with no tracks associated (i.e. those outside the ac-
 1713 ceptance of the ID) do not have this requirement applied. Jets are required to have $p_T > 25$ GeV if
 1714 they are within the tracking acceptance ($|\eta| < 2.4$). Jets with $2.4 < |\eta| < 4.5$ are required to have
 1715 $p_T > 30$ GeV. This tighter requirement reduces jets from pileup in the region where JVF requirements
 1716 cannot be applied. The two highest p_T jets in the event are referred to as the “VBF” jets and used to com-
 1717 pute various analysis selections later.

1718 Identification of b -jets is done using the MV1 algorithm and is limited to the acceptance of the ID
 1719 ($|\eta| < 2.5$). The operating point of MV1 that is used is the one that is 85% efficient for identifying true
 1720 b -jets. This operating point has a 10.3% of mis-tagging a light quark jet as a b -jet. In order to improve
 1721 the rejection of b -jets, a lower threshold than the nominal p_T threshold described above is used. For the
 1722 purposes of counting the number of b -jets, jets with p_T down to 20 GeV are used.

1723 5.3.4 OVERLAP REMOVAL

1724 There are some cases where certain reconstructed objects will overlap and one will have to be chosen
 1725 (for example, an electron and a jet in the calorimeter). First, the case of lepton overlap is dealt with. If
 1726 an electron candidate extends into the muon spectrometer, it is removed. If a muon or electron have a
 1727 $\Delta R < 0.1$, the electron is removed and the muon is kept. If two electron candidates overlap within
 1728 the same radius, then the higher E_T electron is kept. Next, the overlap between leptons and jets is con-

1729 sidered. If an electron and jet are within $\Delta R < 0.3$ of one another, the electron is kept and the jet is
1730 removed. However, if a muon and jet overlap within $\Delta R < 0.3$, the jet is kept (as it is likely that the
1731 muon is the result of a semileptonic decay inside the jet).

1732 Once the overlap removal is complete, the final set of objects used in the analysis is defined.

1733 **5.4 ANALYSIS SELECTION**

1734 The VBF analysis uses two distinct selections. The first is a more standard selection, referred to as “cut-
1735 based”, that applies requirements on the VBF variables and uses m_T as the final discriminating variable.
1736 The second is a looser selection that uses a Boosted Decision Tree (BDT) score as the final discriminator
1737 in order to take advantage of the detailed correlations between the VBF variables. While the BDT analy-
1738 sis is ultimately more sensitive, the cut-based serves as an important component of the analysis. First, the
1739 cut-based allows for confirming the modeling and validity of many variables used as input to the BDT.
1740 Second, because this is the first use of such an MVA technique in the $H \rightarrow WW^*$ analysis, the cut-based
1741 selection allows confirmation of the final BDT result with a more traditional analysis. The cut-based
1742 techniques are the focus of this chapter, but connections to the BDT result will be illustrated when ap-
1743 propriate.

1744 One important note is that because this analysis is dedicated to the measurement of the VBF pro-
1745 duction mode of the Higgs, events coming from gluon fusion production with the Higgs decaying via
1746 $H \rightarrow WW^* \rightarrow \ell\nu\ell\nu$ are treated as background events. This will be seen throughout the various
1747 predictions shown.

1748 **5.4.I COMMON PRE-SELECTION**

1749 Both the cut-based and BDT analyses have a common pre-selection that is applied before the main signal
1750 region requirements. The requirements on leptons are common to all n_j bins. The analysis requires two
1751 oppositely charged leptons, with the leading lepton required to have $p_T > 22$ GeV while the subleading
1752 lepton must have $p_T > 10$ GeV. Next, to remove low mass Z/γ^* events, a cut on the dilepton mass
1753 $m_{\ell\ell} > 10$ (12) GeV is applied in the different (same) flavor channel. In the same flavor channels, there is

1754 an additional veto placed on the region around the Z peak, requiring that $|m_{\ell\ell} - m_Z| > 15$ GeV.

1755 There are also requirements on the amount of missing transverse momentum in the event. These
1756 are only applied in the same flavor channels, as in the different flavor channels $t\bar{t}$ is the dominant back-
1757 ground in $n_j \geq 2$. The BDT analysis requires $p_T^{\text{miss}} > 40$ GeV and $E_T^{\text{miss}} > 45$ GeV. The cut-
1758 based analysis must select more tightly on these variables to have maximal sensitivity and thus requires
1759 $p_T^{\text{miss}} > 50$ GeV and $E_T^{\text{miss}} > 55$ GeV.

1760 Finally, because this analysis is focused on VBF, a requirement on the jet multiplicity is placed, with
1761 $n_j \geq 2$. Additionally, the analysis requires that there are no jets identified as b-quarks in the event, or
1762 $n_b = 0$.

1763 5.4.2 CUT-BASED SELECTION

1764 The cut-based selection places sequential requirements on variables reconstructed from the VBF jets in
1765 order to increase the signal to background ratio.

1766 GENERAL BACKGROUND REDUCTION

1767 Top pair production is the primary background in the $n_j \geq 2$ bin. Even though $n_b = 0$ is required,
1768 an additional variable is constructed to further suppress the top background. There is often additional
1769 QCD radiation that accompanies the $t\bar{t}$ system when it is produced. Therefore, a variable which tests for
1770 the presence of this additional radiation, p_T^{sum} , is constructed. It is defined in equation 5.1.

$$p_T^{\text{sum}} = p_T^{\ell\ell} + p_T^{\text{miss}} + \sum p_T^j \quad (5.1)$$

1771 The first cut after pre-selection in the cut-based analysis requires $p_T^{\text{sum}} < 15$ GeV to further suppress
1772 $t\bar{t}$ production.

1773 In the different flavor channels, a cut is made to reduce the contamination from $Z \rightarrow \tau\tau$ decays. The
1774 di- τ invariant mass, $m_{\tau\tau}$, is constructed by assuming that the neutrinos from the τ decays were collinear
1775 with the leptons[?]. The analysis requires that this mass not be consistent with a Z by requiring $m_{\tau\tau} <$
1776 $m_Z - 25$ GeV.

1777 VBF TOPOLOGICAL CUTS

1778 The characteristic feature of VBF production of the Higgs is the presence of two additional forward jets
1779 coming from the incoming partons which radiate the vector bosons that make the Higgs. These jets are
1780 forward because the outgoing partons still carry the longitudinal momentum of the incoming partons.
1781 Figure 5.2 shows the distribution of the η for the leading jet in a VBF event compared to a background
1782 top pair production event. As can be seen, the VBF jets tend to be more forward in η , while the $t\bar{t}$ jets are
1783 more central.

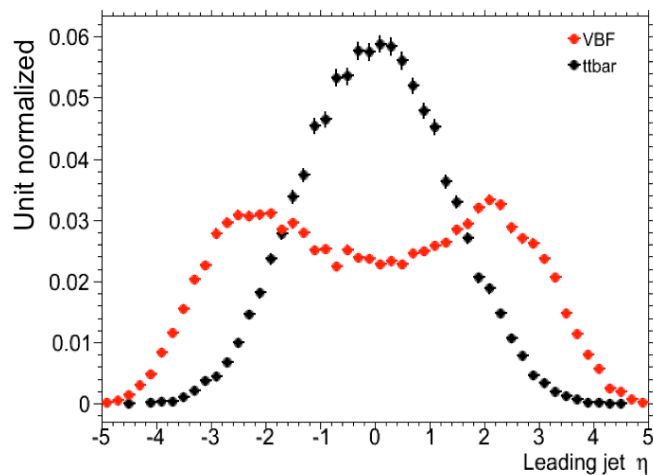


Figure 5.2: Leading jet η in VBF $H \rightarrow WW^*$ (red) and $t\bar{t}$ (black)

1784 Because the cross section for VBF production is an order of magnitude smaller than gluon fusion pro-
1785 duction, these forward jets must be used in order to better reduce background and achieve a good signal
1786 to background ratio. The dedicated VBF search selection requirements are constructed to maximally
1787 exploit the features of the unique VBF topology.

1788 Requirements on the VBF jets are collectively referred to as the “VBF topological cuts”. First, a re-
1789 quirement on the dijet invariant mass of the VBF jets, m_{jj} , is placed, requiring $m_{jj} > 600$ GeV. Next,
1790 the event is required to have a large gap in rapidity between the two VBF jets, or $\Delta y_{jj} > 3.6$. Both
1791 of these cuts put tight requirements on the presence of two forward, high p_T jets moving in opposite

1792 directions in the longitudinal plane.

1793 Beyond requiring the presence of the two forward VBF jets, the analysis also vetoes on the presence
1794 of any additional jets that fall between the two VBF jets. This cut is referred to as the central jet veto, or
1795 CJV. Any events with a third jet with $p_T > 20$ GeV whose rapidity is between the region defined by the
1796 two VBF jets are vetoed. This can be expressed in terms of a variable called the jet centrality, defined in
1797 equation 5.2.

$$C_{j3} = \left| \eta_{j3} - \frac{\eta_{j1} + \eta_{j2}}{2} \right| / \frac{|\eta_{j1} - \eta_{j2}|}{2}, \quad (5.2)$$

1798 Here, η_{j1} and η_{j2} are the pseudorapidities of the leading and subleading jets, respectively, while η_{j3} is
1799 the pseudorapidity of the extra jet in the event (if one exists). Intuitively, C_{j3} is zero when η_{j3} is directly
1800 centered between the two jets and unity when η_{j3} is aligned with either of the VBF jets. Thus, the CJV
1801 can be expressed as a requirement that $C_{j3} > 1$.

1802 The decay products of the Higgs tend to be central as well. Thus, the analysis also requires that both
1803 leptons in the analysis fall within the rapidity gap defined by the jets. This cut is referred to as the outside
1804 lepton veto, or OLV. A quantitative way to define the cut is to require that the centrality of each lepton
1805 (defined analogously to that of the third jet in equation 5.2) correspond to the lepton being within the jet
1806 rapidity gap, or $C_\ell < 1$ for both leptons.

1807 Figure 5.3a-c shows the m_{jj} , Δy_{jj} , and $C_{\ell 1}$ variables at the stage where all previous cuts in the se-
1808 quence have been made. The agreement between data and Monte Carlo is good, and the bottom panels
1809 show their power in discriminating the VBF signal from the background processes.

1810 The final signal region is also split into two bins of m_{jj} , with the first bin corresponding to $600 \text{ GeV} <$
1811 $m_{jj} < 1 \text{ TeV}$ and the second bin corresponding to $m_{jj} > 1 \text{ TeV}$. The first bin has more statistics but
1812 also a larger contribution from background, while the second bin has lower statistics but a 1:1 signal to
1813 background ratio.

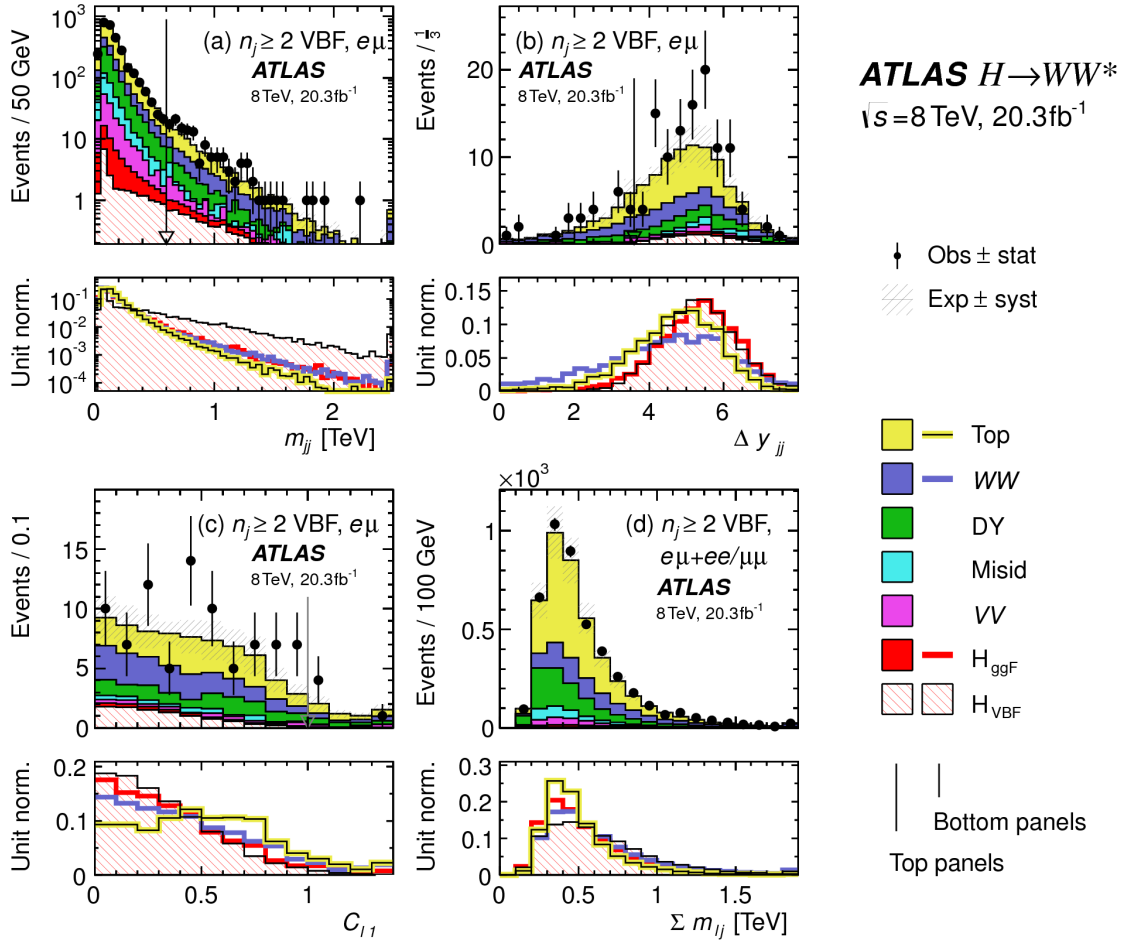


Figure 5.3: Distributions of (a) m_{jj} , (b) Δy_{jj} , (c) $C_{\ell 1}$, and (d) $\sum m_{ij}$, for the VBF analysis. The top panels compare simulation and data, while the bottom panels show normalized distributions for all background processes and signal[21].

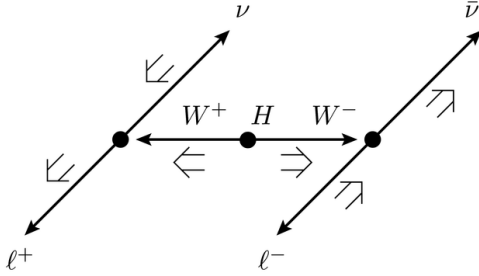


Figure 5.4: A cartoon of the WW final state. Momenta are represented with thin arrows, spins with thick arrows. [21]

1814 **HIGGS TOPOLOGICAL CUTS**

1815 The final state leptons will exhibit unique correlations due to the fact that they are arising from the decay
 1816 of a spin zero resonance. In particular, the spins of the final state leptons and neutrinos must all cancel,
 1817 as shown in figure 5.4. Because the neutrino has a left handed chirality and the anti-neutrino has a right
 1818 handed chirality (in the massless neutrino approximation), the spin and momentum of the particles
 1819 will be anti-aligned and aligned, respectively. In the transverse plane, the momenta of all four final state
 1820 objects must cancel as well. With the constraint of having both the momenta and the spin alignments
 1821 cancel, the final state kinematics strongly prefer having a small angle between the leptons in the trans-
 1822 verse plane (low $\Delta\phi_{\ell\ell}$). This angular correlation will also lead to low values of the di-lepton invariant
 1823 mass $m_{\ell\ell}$. These unique signal final state kinematic correlations will be exploited to define the ultimate
 1824 signal region.

1825 The analysis places additional requirements on the final state leptons. Two requirements on dilepton
 1826 kinematics are made that are common with lower multiplicity jet bins as well. The angle between leptons
 1827 in the transverse plane, $\Delta\phi_{\ell\ell}$, is required to be less than 1.8 radians. Additionally, the dilepton mass $m_{\ell\ell}$
 1828 is required to be less than 50 GeV.

1829 The cut-based analysis uses m_T as the final discriminating variable as in the ggF focused analysis. The
 1830 optimal number of bins in m_T was found to be three bins, with the bin boundaries at 80 and 130 GeV.

1831 Table 5.7 shows the data and estimated signal and background yields from simulation as each cut de-
 1832 scribed above is made. The table shows how each cut reduces specific backgrounds and how the overall

1833 signal to background ratio grows through the cutflow.

1834 Figure 5.5 shows an ATLAS event display of a candidate event in the final signal region.

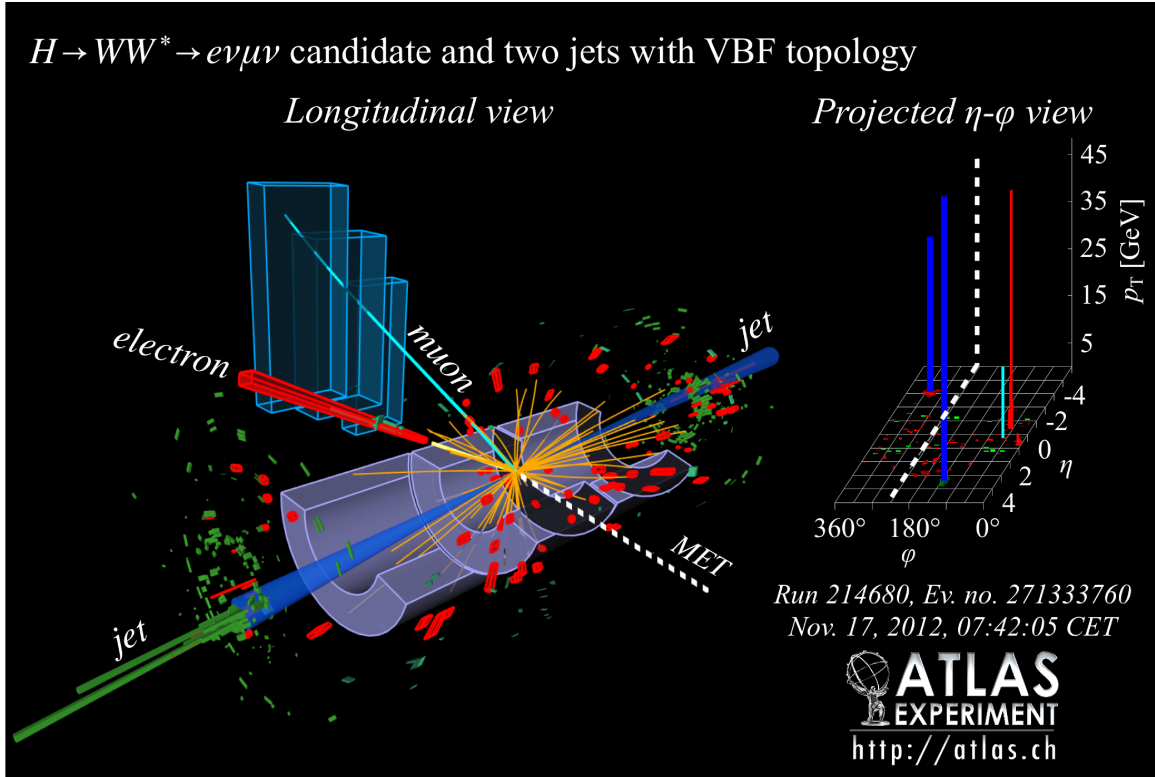


Figure 5.5: Event display of a VBF candidate event[21].

1835 5.4.3 BDT-BASED SELECTION

1836 The boosted decision tree based analysis takes a different philosophy compared to the cut-based. Rather
1837 than cutting sequentially on many variables, the BDT analysis uses many of these variables as inputs
1838 to the BDT and the output BDT score (O_{BDT}) as the final discriminant. The BDT is trained with the
1839 VBF $H \rightarrow WW^*$ simulation as the signal samples and all other processes as background, including ggF
1840 $H \rightarrow WW^*$ production. While the BDT based analysis is treated as a separate result, it has significant
1841 overlap with the cut-based selection.

Table 5.7: Event selection for the $n_j \geq 2$ VBF analysis in the 8 TeV cut-based analysis[21].

Selection	Summary										Composition of N_{bkg}							
	$N_{\text{obs}}/N_{\text{bkg}}$	N_{obs}	N_{bkg}	N_{signal}	N_{ggF}	N_{VBF}	N_{VH}	N_{WW}^{QCD}	N_{WW}^{EW}	$N_{t\bar{t}}$	N_t	N_{top}	N_{Wj}	N_{jj}	N_{VV}	N_{misid}	$N_{\text{Drell-Yan}}$	$N_{ee/\mu\mu} N_{\tau\tau}^{\text{QCD}}$
$e\mu$ sample	1.00 ± 0.00	61434	61180	85	32	26	1350	68	51810	2970	847	308	380	51	3260	46		
$n_b = 0$	1.02 ± 0.01	7818	7700	63	26	16	993	43	3000	367	313	193	273	35	2400	29		
$p_T^{\text{sum}} < 15$	1.03 ± 0.01	5787	5630	46	23	13	781	38	1910	270	216	107	201	27	2010	23		
$m_{\tau\tau} < m_Z - 25$	1.05 ± 0.02	3129	2970	40	20	9.9	484	22	1270	177	141	66	132	7.6	627	5.8		
$m_{jj} > 600$	1.31 ± 0.12	131	100	2.3	8.2	—	18	8.9	40	5.3	1.8	2.4	5.1	0.1	15	1.0		
$\Delta y_{jj} > 3.6$	1.33 ± 0.13	107	80	2.1	7.9	—	11.7	6.9	35	5.0	1.6	2.3	3.3	—	11.6	0.8		
$C_{j3} > 1$	1.36 ± 0.18	58	43	1.3	6.6	—	6.9	5.6	14	3.0	1.3	1.3	2.0	—	6.8	0.6		
$C_{\ell 1} < 1, C_{\ell 2} < 1$	1.42 ± 0.20	51	36	1.2	6.4	—	5.9	5.2	10.8	2.5	1.3	1.3	1.6	—	5.7	0.6		
$m_{\ell\ell}, \Delta\phi_{\ell\ell}, m_\tau$	2.53 ± 0.71	14	5.5	0.8	4.7	—	1.0	0.5	1.1	0.3	0.3	0.3	0.6	—	0.5	0.2		
<hr/>																		
$ee/\mu\mu$ sample	0.99 ± 0.01	26949	27190	31	14	10.1	594	37	23440	1320	230	8.6	137	690	679	16		
$n_b, p_T^{\text{sum}}, m_{\tau\tau}$	1.03 ± 0.03	1344	1310	13	8.0	4.0	229	12.0	633	86	26	0.9	45	187	76	1.5		
$m_{jj}, \Delta y_{jj}, C_{j3}, C_\ell$	1.39 ± 0.28	26	19	0.4	2.9	0.0	3.1	3.1	5.5	1.0	0.2	0.0	0.7	3.8	0.7	0.1		
$m_{\ell\ell}, \Delta\phi_{\ell\ell}, m_\tau$	1.63 ± 0.69	6	3.7	0.3	2.2	0.0	0.4	0.2	0.6	0.2	0.2	0.0	0.1	1.5	0.3	0.1		

1842 PRE-TRAINING SELECTION AND BDT INPUTS

1843 Before training, the common preselection cuts described in section 5.4.1 are applied. Additionally, the
1844 central jet veto and outside lepton veto described in section 5.4.2 are applied. The BDT has eight input
1845 variables, six of which are also variables that are used in the cut-based analysis. The six shared variables
1846 are p_T^{sum} , m_{jj} , Δy_{jj} , $m_{\ell\ell}$, $\Delta\phi_{\ell\ell}$, and m_T . The seventh variable input in the BDT is a combination of
1847 the variables used to do the OLV in the cut-based analysis. The BDT uses as input the sum of lepton
1848 centralities, or $\sum C_\ell = C_{\ell 1} + C_{\ell 2}$. The final BDT input variable, $\Sigma m_{\ell j}$, is constructed to account for
1849 the correlations between the jets and leptons in the event. It is the sum of the invariant masses of all four
1850 possible lepton-jet combinations.

1851 Figure 5.3d shows the agreement between data and simulation for the $\Sigma m_{\ell j}$ variable, as well as show-
1852 ing its discriminating power. Figure 5.6 shows the distributions of the Higgs topological variables that
1853 are shared between the cut-based and BDT analyses. Figure 5.7 shows the distributions of the VBF topo-
1854 logical variables shared between the cut-based and BDT analyses. In both cases, the VBF yield has been
1855 scaled by a factor of 50 to better show the shape difference compared to the backgrounds.

1856 Table ?? summarizes the cuts applied for the cut-based and analyses, as well as which variables are used
1857 as input to the BDT.

1858 5.5 BACKGROUND ESTIMATION

1859 This section describes the procedures used to estimate backgrounds for the VBF analysis in both the
1860 cut-based and BDT analyses.

1861 5.5.1 GENERAL STRATEGY

1862 Most of the backgrounds in the VBF analysis have shapes estimated from Monte Carlo simulation but
1863 normalizations derived from control regions in data. In essence, a normalization factor (denoted with
1864 β or abbreviated as NF) is derived by scaling the MC yield in the control region to the corresponding
1865 yield in data. Once this factor is derived, it can be used to scale the MC estimate of the background in the

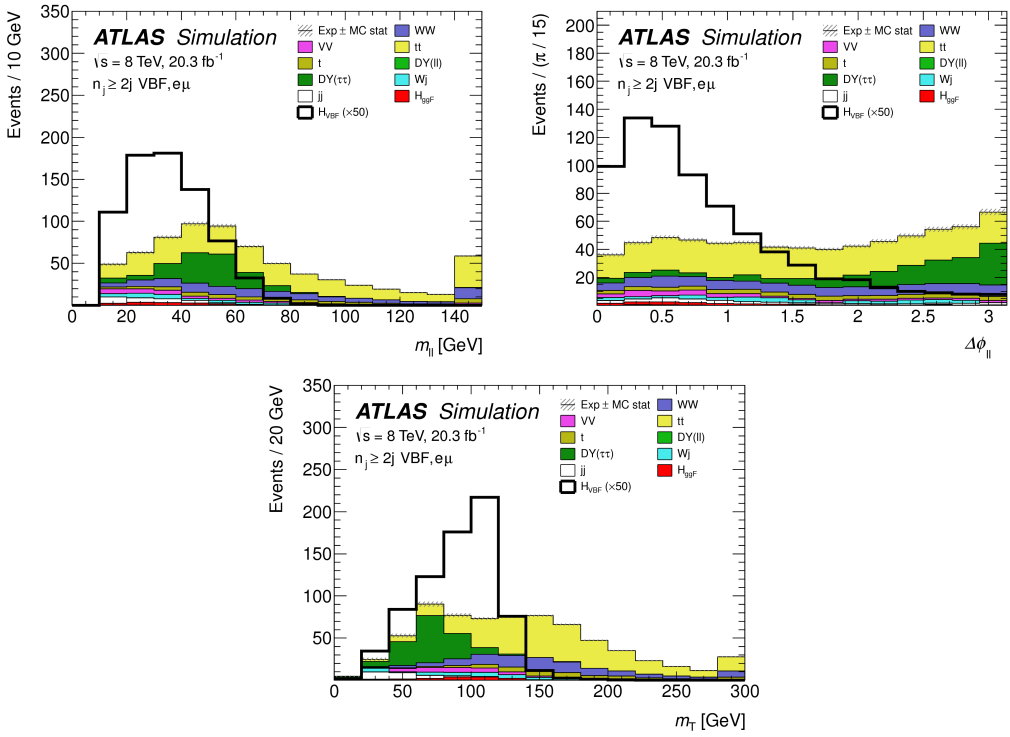


Figure 5.6: Distributions of $m_{\ell\ell}$ (top left), $\Delta\phi_{\ell\ell}$ (top right), and m_T (bottom), Higgs topology variables used in the selection requirements of the cut-based signal region and as inputs to the BDT result. These are plotted after all of the BDT pre-training selection cuts[21].

1866 signal region. This is illustrated in equation 5.3.

$$B_{\text{SR}}^{\text{est}} = B_{\text{SR}} \times \frac{N_{\text{CR}}}{B_{\text{CR}}} \equiv B_{\text{SR}} \times \beta \quad (5.3)$$

1867 Here, B denotes the MC yield prediction in the denoted region, while N denotes the observed num-

1868 ber of events in data in the denoted region.

1869 Another way of writing the same equation, in terms of an extrapolation factor α rather than a nor-
 1870 malization factor β . The overall calculation is exactly the same. However, when phrased in this way, it
 1871 shows how the uncertainty on the background estimation can be reduced. This is shown in equation 5.4.

$$B_{\text{SR}}^{\text{est}} = N_{\text{CR}} \times \frac{B_{\text{SR}}}{B_{\text{CR}}} \equiv N_{\text{CR}} \times \alpha \quad (5.4)$$

1872 Phrased this way, the equation shows that with enough statistics in the control region, a large theoret-

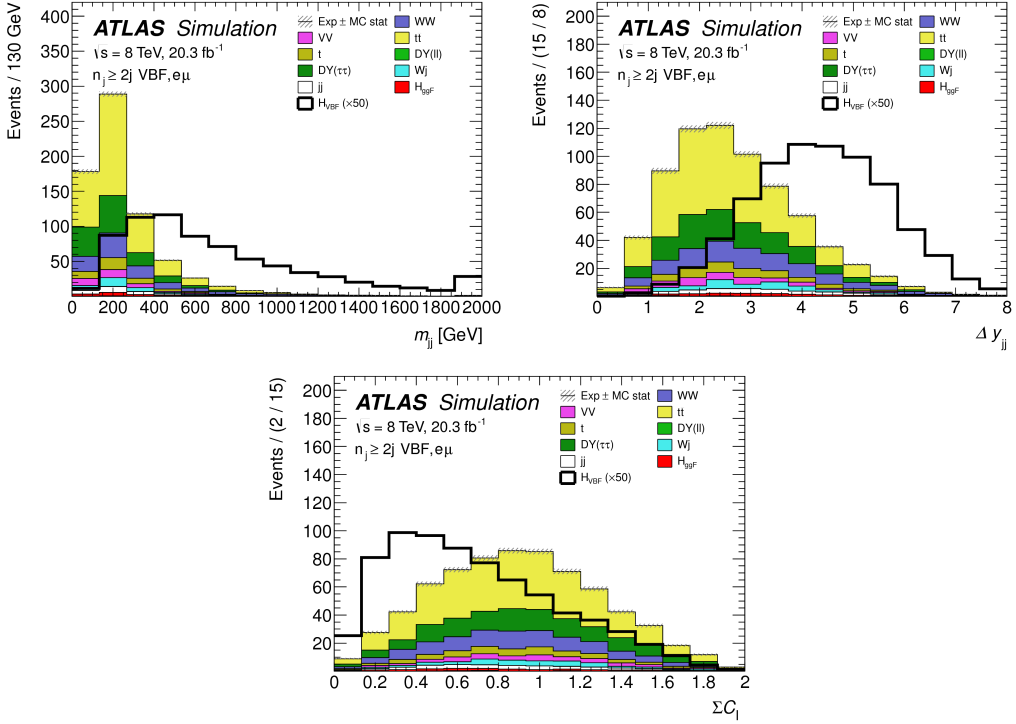


Figure 5.7: Distributions of m_{jj} (top left), Δy_{jj} (top right), $\sum C_\ell$ (bottom), VBF topology variables used in the selection requirements of the cut-based signal region and as inputs to the BDT result. These are plotted after all of the BDT pre-training selection cuts[21].

ical uncertainty on the overall background yield in the signal region can be replaced by a small statistical uncertainty coming from the number of data events in the CR and a smaller theoretical uncertainty on the extrapolation from the control region to the signal region.

5.5.2 TOP BACKGROUND

The normalization factor β_t for the top background in the VBF analysis is derived in a region required to have one b-tagged jet, or $n_b = 1$. In the cut-based analysis, normalization factors are computed at every stage of the cutflow by applying the appropriate cuts in the CR. These NF are then applied to the $t\bar{t}$ and single top event yields in the SR. In the BDT analysis, a single normalization factor is computed for each bin of O_{BDT} after applying the BDT pre-training cuts described previously. The computed normalization factors are derived with all flavor combinations combined in order to decrease statistical uncertainty. Additionally, in the BDT analysis, BDT bins 2 and 3 are merged for the same reason.

1884 Table 5.8 shows the evolution of the β_t through the cut-based selection. Table 5.9 shows the value
 1885 of the β_t in each bin of O_{BDT} . In all cases, the computed factors are relatively consistent with unity,
 1886 with the largest discrepancy coming in bin 1 of O_{BDT} . The normalization factors in the bins of O_{BDT}
 1887 are also consistent with those derived in the cut-based signal region, increasing confidence in the BDT
 1888 estimation.

Cut	β_t
$p_T^{\text{sum}} < 15 \text{ GeV}$	1.03 ± 0.01
$m_{\tau\tau} < m_Z - 25$	1.05 ± 0.01
$m_{jj} > 600 \text{ GeV}$	0.96 ± 0.06
$\Delta y_{jj} > 3.6$	1.02 ± 0.08
CJV	1.13 ± 0.16
OLV	1.01 ± 0.19
$m_{jj} < 1 \text{ TeV}$	0.94 ± 0.19
$m_{jj} > 1 \text{ TeV}$	1.48 ± 0.66

Table 5.8: Top normalization factors computed at each stage of the cut-based selection. Uncertainties are statistical only.

O_{BDT}	β_t
Bin0	1.09 ± 0.02
Bin1	1.58 ± 0.15
Bin2	0.95 ± 0.31
Bin3	0.95 ± 0.31

Table 5.9: Top normalization factors computed for each bin of O_{BDT} . Uncertainties are statistical only.

1889 Figure 5.8 shows the m_{jj} and O_{BDT} distributions in the top control region. Overall the modeling
 1890 looks consistent with the data.

1891 While these normalization factors can be computed and applied to the expected background yields
 1892 listed in tables like table 5.7, in the end the normalization of the top background is profiled (meaning
 1893 there is a dedicated Poisson constraint) and allowed to float in the final statistical fit.

1894 5.5.3 $Z/\gamma^* \rightarrow \tau\tau$ BACKGROUND

1895 In the different flavor channels, the $Z/\gamma^* \rightarrow \tau\tau$ background is an important one. Di-tau production
 1896 can produce an $e\mu$ final state if each τ lepton decays to a different flavor lepton.

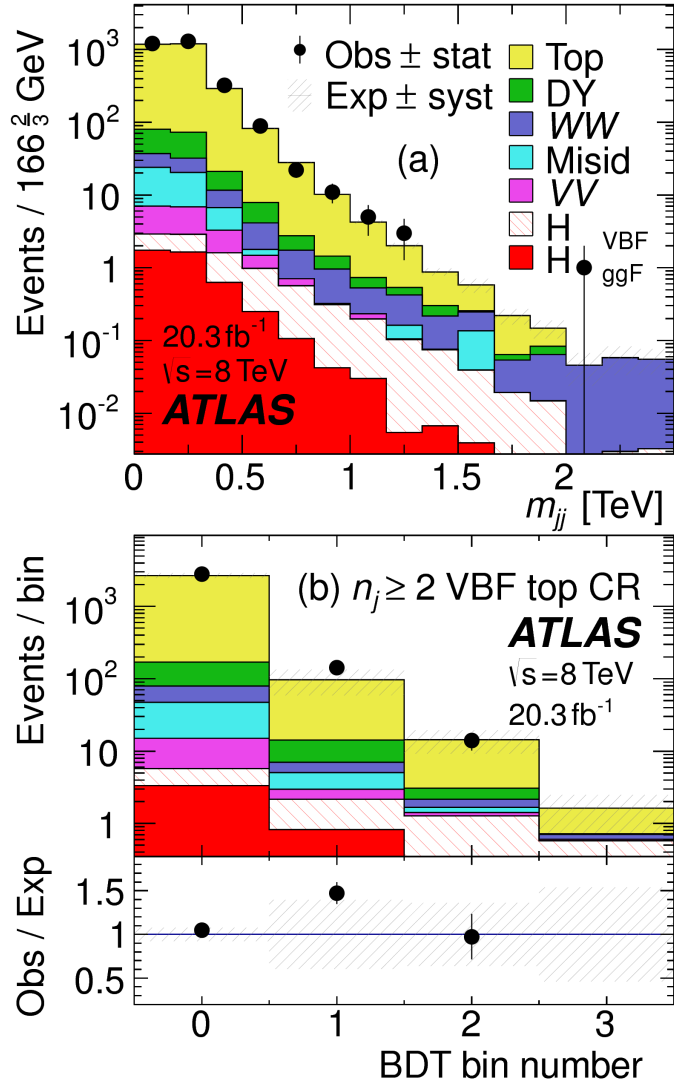


Figure 5.8: Distributions of m_{jj} (a) and O_{BDT} (b) in the VBF $n_b = 1$ top CR [21].

1897 In the BDT analysis, a single normalization factor for the background is derived. A control region is
 1898 defined using the pre-training selection cuts, except requiring that $|m_{\tau\tau} - m_Z| < 25 \text{ GeV}$ so that
 1899 the region is enriched in $Z/\gamma^* \rightarrow \tau\tau$ background. Additional requirements of $m_{\ell\ell} < 80(75) \text{ GeV}$
 1900 in the different (same) flavor channel, as well as $O_{\text{BDT}} > -0.48$ are applied to increase the purity of
 1901 the region. The final $\beta_{Z/\gamma^* \rightarrow \tau\tau}$ is calculated to be 0.9 ± 0.3 (statistical uncertainty only). Because of
 1902 the small contribution of this background in the BDT analysis and the large statistical uncertainty, no
 1903 additional systematics are calculated. The final SR estimate is scaled by this β and not allowed to float in

1904 the fit.

1905 The cut-based corrections are a bit more involved because they need to be applied cut by cut through
 1906 the cutflow, as well as in the final signal region for the fit. The region is defined including all SR cuts
 1907 up to the $Z/\gamma^* \rightarrow \tau\tau$ veto, which is instead made into a Z mass peak requirement as for the BDT
 1908 region. The $m_{\ell\ell}$ cut from the BDT region is included as well. The cut-based approach aims to correct
 1909 the normalization of the $Z/\gamma^* \rightarrow \tau\tau$ background in two ways. First, an overall normalization factor is
 1910 computed from the control region. However, the VBF topological cuts are not included in this region,
 1911 and applying them as is done in the top CR is not feasible due to limited statistics. So, instead, correction
 1912 factors (CF) to the cut efficiencies of the VBF cuts are derived in a same flavor $Z \rightarrow \ell\ell$ control region,
 1913 which has significantly more statistics. The CF is simply the ratio of the cut efficiencies in data and MC
 1914 derived in this region. In the end, the overall background estimate is given by equation 5.5.

$$N_{Z/\gamma^* \rightarrow \tau\tau}^{\text{est}} = B_{Z/\gamma^* \rightarrow \tau\tau}^{\text{SR}} \times \beta_{\tau\tau} \times \frac{\epsilon_{\text{VBF cuts}}^{\text{data}}}{\epsilon_{\text{VBF cuts}}^{\text{MC}}} \quad (5.5)$$

1915 The hypothesis is that while the normalization correction must be derived in a dedicated region, the
 1916 efficiency of the VBF cuts should not be sensitive to the type of Z/γ^* process and thus the larger control
 1917 region can be exploited to derive the CF. Figure 5.9 shows a shape comparison for the m_{jj} variable in
 1918 $Z \rightarrow \tau\tau$ events in the signal region and $Z \rightarrow \ell\ell$ events in the control region. The figure shows that the
 1919 shapes are indeed comparable and thus any CF derived in the same flavor control region can reliably be
 1920 applied in the signal region.

1921 Table 5.10 shows the overall normalization factor $\beta_{\tau\tau}$ and the efficiency correction factors for the var-
 1922 ious VBF topological cuts. In general, the statistical uncertainties on the cut efficiency corrections are
 1923 quite good, and the MC tends to underestimate the efficiency of the VBF cuts for the $Z/\gamma^* \rightarrow \tau\tau$ back-
 1924 ground. The overall normalization factor is also consistent with that calculated for the BDT analysis.

1925 5.5.4 $Z/\gamma^* \rightarrow \ell\ell$ BACKGROUND

1926 In the same flavor channels, the $Z/\gamma^* \rightarrow \ell\ell$ background is dominant and thus must be estimated
 1927 correctly. In both the BDT and cut-based analyses, the background is estimated using the so-called

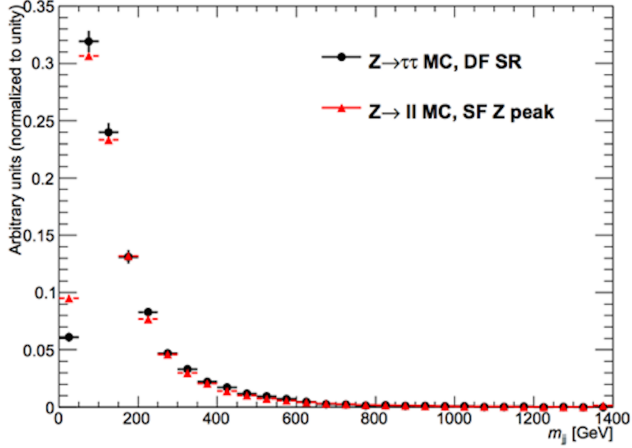


Figure 5.9: Comparison of m_{jj} shape in a same flavor $Z \rightarrow \ell\ell$ control region and the VBF cut-based signal region.

$\beta_{\tau\tau}$	0.97 ± 0.04
Cut	Correction factors
$m_{jj} > 600$ GeV	1.09 ± 0.01
$\Delta y_{jj} > 3.6$	1.14 ± 0.02
CJV	1.20 ± 0.02
OLV	1.17 ± 0.03
$m_{jj} < 1$ TeV	1.17 ± 0.06
$m_{jj} > 1$ TeV	1.18 ± 0.13

Table 5.10: $Z/\gamma^* \rightarrow \tau\tau$ correction factors for the VBF cut-based analysis. Uncertainties are statistical only.

“ABCD” method. The ABCD method creates four different regions by defining cuts on two variables. One of the regions (A) is the signal region, while the other regions are defined by inverting one of both of the cuts. in this case, the two variables used are $m_{\ell\ell}$ and E_T^{miss} , because inverting either of the SR cuts on these variables will give regions rich in the $Z/\gamma^* \rightarrow \ell\ell$ background. Figure 5.10 illustrates the general strategy for each region.

In both of the cut-based and BDT analyses, the Z peak region is defined with $|m_{\ell\ell} - m_Z| < 15$ GeV. In the cut-based analysis, low $m_{\ell\ell}$ corresponds to $m_{\ell\ell} < 50$ GeV (this defines the cut-based SR) while in the BDT it is $m_{\ell\ell} < 75$ GeV. In the cut-based, high and low E_T^{miss} are defined as opposite ends of the 55 GeV cut applied for the signal region definition. The BDT low E_T^{miss} region is between 25 and 45 GeV, while the high E_T^{miss} region is $E_T^{\text{miss}} > 45$ GeV.

Once the regions are defined, the final signal region background estimate is done by taking the esti-

Region A (SR)	Region C
High E_T^{miss}	High E_T^{miss}
Low $m_{\ell\ell}$	Z peak
Region B	Region D
Low E_T^{miss}	Low E_T^{miss}
Low $m_{\ell\ell}$	Z peak

Figure 5.10: General illustration of the ABCD region definitions for $Z/\gamma^* \rightarrow \ell\ell$ background estimation.

1939 mate in region B and extrapolating it to the signal region (A) by multiplying it by the ratio of regions
 1940 C and D. Effectively, the Z peak region is used to estimate the efficiency of the E_T^{miss} cut in data, and
 1941 then this efficiency is applied in the low $m_{\ell\ell}$ region. An additional correction is also applied for the non-
 1942 closure of the method in MC. This is summarized in equations 5.6 and 5.7.

$$N_{Z/\gamma^* \rightarrow \ell\ell}^{\text{SR}} = N_{Z/\gamma^* \rightarrow \ell\ell}^{\text{B}} \times \frac{N_{Z/\gamma^* \rightarrow \ell\ell}^{\text{C}}}{N_{Z/\gamma^* \rightarrow \ell\ell}^{\text{D}}} \times f_{\text{corr}} \quad (5.6)$$

$$f_{\text{corr}} = \frac{B_{\text{MC}}^{\text{A}}/B_{\text{MC}}^{\text{B}}}{B_{\text{MC}}^{\text{C}}/B_{\text{MC}}^{\text{D}}} \quad (5.7)$$

1943 Here, the N refer to data yields in each region with the non Z/γ^* backgrounds subtracted, while B
 1944 refer to the Z/γ^* yields in MC in each region.

1945 A normalization factor $\beta_{\ell\ell}$ is computed for each analysis as the ratio of the predicted data yield to
 1946 the MC yield in the SR. The shape of the BDT distribution is taken from data region B, while the shape
 1947 of the m_T distribution in the cut-based analysis is taken from Z/γ^* MC in the SR. The values of the
 1948 $\beta_{\ell\ell}$ in the cut-based and BDT analyses from this method are summarized in table 5.11. They are quite
 1949 consistent with one another within the statistical uncertainties. In the cut-based analysis, the same cut
 1950 efficiency correction factors shown in table 5.10 are also applied (in product with the $\beta_{\ell\ell}$) in the same
 1951 flavor channels to this background, as they were derived in the Z peak region.

	β_t
BDT Bin 1	1.01 ± 0.15
BDT Bin 2	0.89 ± 0.28
Cut-based	0.81 ± 0.21

Table 5.11: $Z/\gamma^* \rightarrow \ell\ell$ normalization factors for cut-based and BDT analyses. Uncertainties are statistical only.

1952 5.5.5 WW AND OTHER DIBOSON BACKGROUNDS

1953 The WW and other diboson backgrounds have both their shape and normalization taken from MC
 1954 simulation. They are validated in dedicated control regions and found to agree with data well.

1955 As WW is the largest of these backgrounds and is irreducible, validating the estimate is of particular
 1956 importance. The validation region is constructed by requiring the pre-selection cuts on leptons and $m_{\ell\ell}$,
 1957 $n_b = 0$, and $m_T > 100$ GeV. The m_{T2} variable[?] is an additional discriminant that will isolate
 1958 the WW background, and a requirement of $m_{T2} > 160$ GeV is placed to define the WW validation
 1959 region. This cut gives a 60% purity for the validation region. The derived normalization factor in the
 1960 region is 1.15 ± 0.19 and is thus consistent with unity. Figure 5.11 shows the m_{T2} distribution and how
 1961 it distinguishes the WW background.

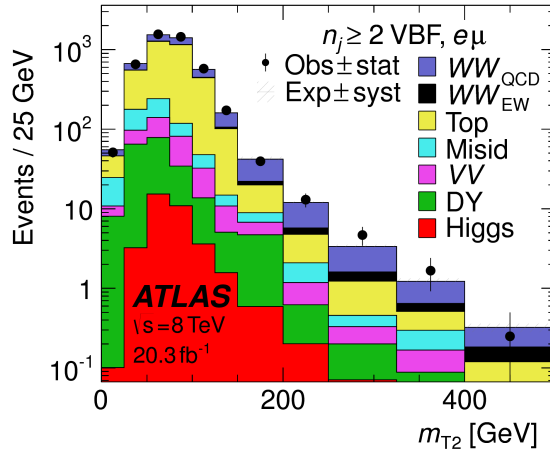


Figure 5.11: Distribution of m_{T2} in the WW validation region of the VBF analysis[21].

1962 5.5.6 HIGGS PRODUCTION VIA GLUON-GLUON FUSION

1963 Because this analysis is dedicated to measuring the VBF contribution to Higgs production, the com-
1964 ponent of Higgs production from gluon-gluon fusion is treated as a background. The shape is taken
1965 directly from simulation, using the generators described in table 5.4. In the final combined fit of all dif-
1966 ferent signal regions, the normalization is controlled by either a combined signal strength parameter μ ,
1967 which controls the normalization of both ggF and VBF production, or a separate parameter μ_{ggF} de-
1968 pending on the interpretation being presented in the final results.

1969 5.5.7 BACKGROUNDS WITH MISIDENTIFIED LEPTONS

1970 As discussed previously, the $W + \text{jets}$ and QCD multijet backgrounds are derived with fully data-driven
1971 methods. These backgrounds do not make a large contribution to the final VBF signal region but their
1972 estimation methods are discussed briefly here.

1973 $W + \text{jets}$ BACKGROUND

1974 The $W + \text{jets}$ background enters the signal region by having one of the jets mis-reconstructed as a lep-
1975 ton. The background is estimated by constructing a control sample with two leptons, where one lepton
1976 passes the usual lepton quality cuts but the second lepton fails one of those cuts (also known as the “anti-
1977 identified” lepton). This control region is rich in the $W + \text{jets}$ contribution because if a second lepton is
1978 reconstructed in a $W + \text{jets}$ event it is likely to be poor quality. The purity of this $W + \text{jets}$ control sample
1979 is 85% to 90% depending on the exact configuration of leptons in the final state.

1980 The signal region estimate of $W + \text{jets}$ is estimated by extrapolation from the control sample to the sig-
1981 nal region using extrapolation factors derived in a $Z + \text{jets}$ control sample in data. The extrapolation fac-
1982 tor is the ratio of the number of lepton candidates satisfying all quality criteria to the number of lepton
1983 candidates anti-identified. This ratio is measured in bins of p_T and η . Thus, the final signal region esti-
1984 mate (binned as the extrapolation factor is binned) is simply the number of events in the anti-identified
1985 lepton control sample multiplied by the extrapolation factor derived from the $Z + \text{jets}$ control sample.

1986 Figure 5.12 shows the extrapolation factors derived for electrons and muons.

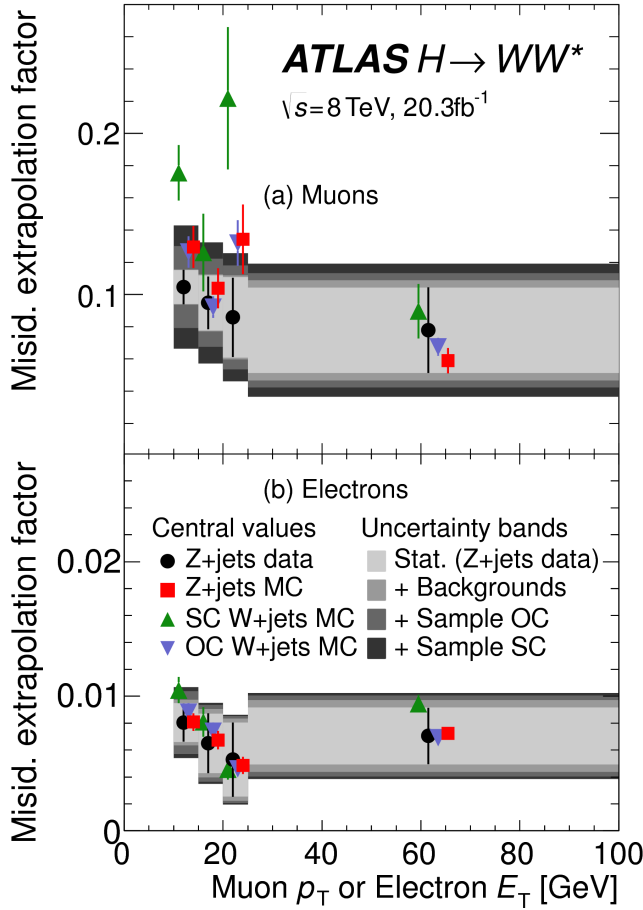


Figure 5.12: Extrapolation factors for the $W+jets$ estimate derived for muons (a) and electrons (b) as a function of lepton p_T [21].

1987 QCD MULTIJET BACKGROUND

1988 The method for estimating the multijet background is very similar to the $W+jets$ estimation method.
 1989 The control sample in this case has two anti-identified leptons but otherwise satisfies all signal region
 1990 requirements. The extrapolation factor is estimated from a multijet sample and applied twice to the
 1991 control sample.

1992 5.5.8 BACKGROUND COMPOSITION IN FINAL SIGNAL REGION

1993 After all of these estimation procedures, the final signal region composition can be calculated. The esti-
 1994 mated yields are all shown in table 5.7. Figure 5.13 shows the relative percentages of the different back-

1995 ground for the different flavor and same flavor final states. In $e\mu$, the leading backgrounds are top back-
 1996 grounds, ggF Higgs, and SM WW production. In $ee/\mu\mu$, the leading background is Drell-Yan, fol-
 1997 lowed by top and ggF Higgs.

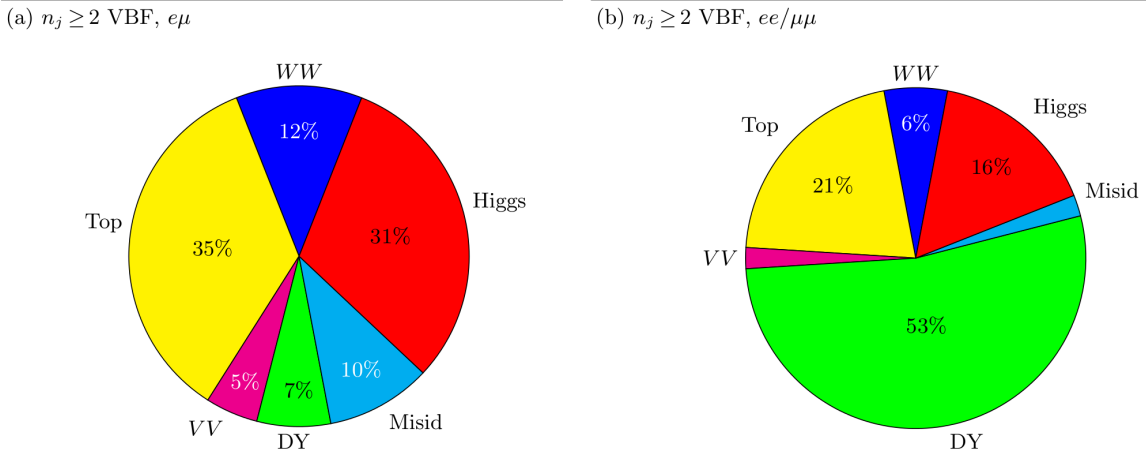


Figure 5.13: Background composition in final VBF signal region[21].

1998 5.6 SYSTEMATIC UNCERTAINTIES

1999 There are two main types of systematic uncertainties that are assessed for the analysis. First, theoreti-
 2000 cal uncertainties associated with the various signal and background yield estimates are discussed. Then,
 2001 experimental uncertainties due to detector effects are shown. Normalization uncertainties refer to uncer-
 2002 tainties that affect the cross section of the process in question in the signal region being probed. Shape
 2003 uncertainties refer to systematic uncertainties that affect the shape of the final discriminating variable
 2004 (either m_T or O_{BDT}).

2005 5.6.1 THEORETICAL UNCERTAINTIES

2006 There are four main components to theoretical uncertainties assigned to signal and background pro-
 2007 cesses taken from Monte Carlo. Each one is a different source of variation in the overall acceptance for
 2008 that process. The first involves variation of the QCD renormalization and factorization scales used in
 2009 the calculation. In this case, the two scales are varied independently and simultaneously by factors of
 2010 two high or low and quantifying the resulting variation in normalization and shape for the process. This

2011 approximates the correction to the cross section that would come from including the next order of the
 2012 QCD calculation (referred to as scale uncertainty). Next, there is an uncertainty associated with the PDF
 2013 set used in generating the events. The uncertainty eigenvectors for the given PDF set are studied, and the
 2014 envelope of maximal variation is taken as an uncertainty. Finally, there are two uncertainties associated
 2015 with the choice of MC software (referred to as PDF uncertainty). An uncertainty associated with the
 2016 generator chosen for the hard scattering process is evaluated by keeping the parton showering software
 2017 constant but varying the matrix element generator and taking the maximal variation as an uncertainty
 2018 (referred to as the generator uncertainty). The converse variation can also be done, where the matrix ele-
 2019 ment generator remains constant and the generator used for the underlying event/parton shower mod-
 2020 eling is varied (referred to as the UE/PS uncertainty). In cases where the background is normalized in a
 2021 control region, the systematic uncertainty arises from variations of the extrapolation factor α between
 2022 the CR and the SR, which can affect the normalization of the background in the SR.

2023 There are two additional uncertainties that are applied to the Higgs processes as well. First, there are
 2024 uncertainties assigned to the Higgs total production cross section. Then, there are uncertainties assigned
 2025 based on the fact that the analysis is done in exclusive jet bins and it is possible for signal events to mi-
 2026 grate from one bin to the next depending on the presence or absence of jets. These are assigned using the
 2027 Jet Veto Efficiency (JVE) procedure[?] for ggF events and the Stewart-Tackmann (ST) method[87] for
 2028 VBF production.

2029 Table 5.12 shows the total theory uncertainties on the backgrounds in the cut-based analysis. These are
 2030 the sum in quadrature of the uncertainties from each of the variations described above.

Process	Theory syst. (%)
ggF H	48
Top	26
QCD WW	37
$Z/\gamma^* \rightarrow \tau\tau$	6.1

Table 5.12: Systematic uncertainties for various processes in the cut-based VBF analysis, given in units of % change in yield.
Values are given for the low m_{jj} signal region.

2031 Figures 5.14 and 5.15 show the variations in the extrapolation factor from the PDF and QCD uncer-
 2032 tainties on the top background estimate, binned in m_T , for the cut-based analysis. In both cases, there

2033 was no significant shape uncertainty but normalization uncertainties were assigned according to the
 2034 maximal variation. These uncertainties enter into the 26% total uncertainty on top quoted in table 5.12.
 2035 While the estimate for the same-flavor $Z/\gamma^* \rightarrow \ell\ell$ background is data-driven, there is still a sys-
 2036 tematic uncertainty taken for the non-closure of the method in Monte Carlo. This is taken as the max-
 2037 imum of the deviation of the non-closure factor f_{corr} from unity and its uncertainty, or $\max(|1 -$
 2038 $f_{\text{corr}}|, \delta f_{\text{corr}})$. For the cut-based analysis this non-closure uncertainty 23%, while for the BDT analy-
 2039 sis it is 17%.

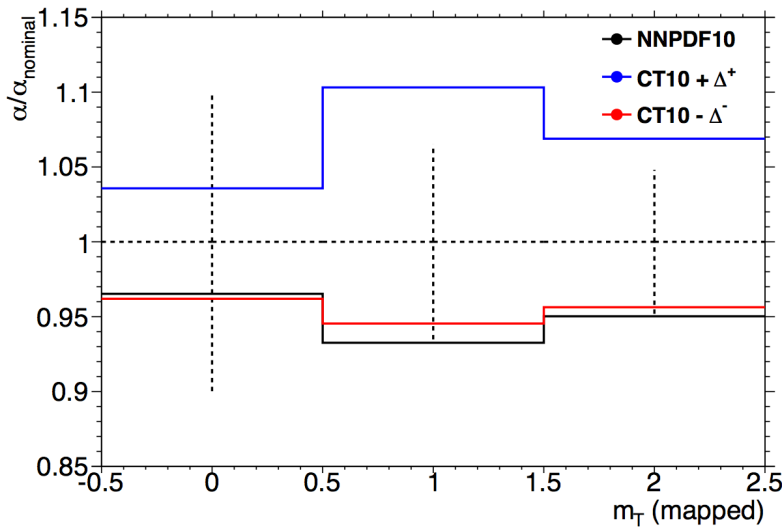


Figure 5.14: Variations in the top background extrapolation factor in the cut-based analysis due to PDF uncertainties, binned in m_T .

2040 5.6.2 EXPERIMENTAL UNCERTAINTIES

2041 In this analysis, the theoretical uncertainties end up being the most dominant, but there are some ex-
 2042 perimental uncertainties that make a contribution as well. The first is the uncertainty on the measured
 2043 integrated luminosity, which affects backgrounds whose normalization is taken from MC and is mea-
 2044 sured to be 2.8% in the 8 TeV dataset [88]. The dominant sources of uncertainty overall are uncertainties
 2045 on the jet energy scale and resolution and the b -tagging efficiency. Additional sources include lepton
 2046 uncertainties on identification, resolution, and trigger efficiency, as well as uncertainties on the missing
 2047 transverse momentum .

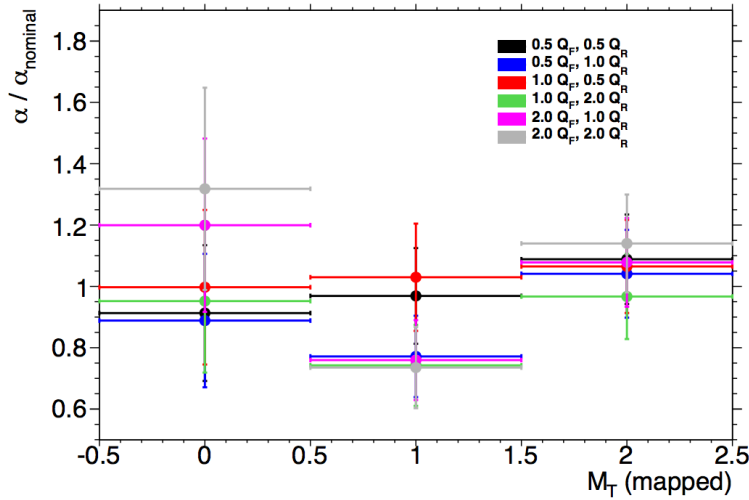


Figure 5.15: Variations in the top background extrapolation factor in the cut-based analysis due to QCD scale uncertainties, binned in m_T .

2048 The jet energy scale uncertainty is split into several independent components, including jet-flavor
 2049 dependent calorimeter response uncertainties, uncertainties on modeling of pile-up interactions, uncer-
 2050 tainties on extrapolation from the central to forward detector regions, and MC non-closure [89]. The
 2051 uncertainty on energy scale for jets used in this analysis ranges from 1% to 7% depending on the jet p_T
 2052 and η . The jet energy resolution varies from 5% to 20%, with uncertainties ranging from 2% to 40%
 2053 (the largest uncertainties occurring at the selection threshold).

2054 The b-tagging efficiency is independently measured in data samples enriched in dileptonic decays of
 2055 $t\bar{t}$ events or in events where a muon is reconstructed in the vicinity of a jet[90, 91]. The efficiencies and
 2056 their uncertainties are binned in p_T and decomposed into uncorrelated components using an eigenvec-
 2057 tor method[?]. Uncertainties on the efficiency range from 1% to 7.8%. The uncertainty on the rate of
 2058 misidentification of c -jets as b -jets ranges from 6-14%, while the uncertainty on the rate of light jet mis-
 2059 tagging ranges from 9-19% depending on p_T and η .

2060 The total experimental uncertainties on different signal and background components are summa-
 2061 rized in table 5.13. They are compared to the level of other statistical and systematic uncertainties as well.
 2062 Overall, the experimental uncertainties are sub-dominant compared to the statistical and theoretical
 2063 uncertainties.

Sample	Total error	Stat. error	Expt. syst. err.	Theo. syst. err.
$n_j \geq 2$ VBF-enriched				
N_{sig}	13	-	6.8	12
N_{bkg}	9.2	4.7	6.4	4.5
N_{WW}	32	-	14	28
N_{top}	15	9.6	7.6	8.5
N_{misid}	22	-	12	19
N_{VV}	20	-	12	15
$N_{\tau\tau} (\text{DY})$	40	25	31	2.9
$N_{ee/\mu\mu} (\text{DY})$	19	11	15	-

Table 5.13: Composition of the post-fit uncertainties (in %) on the total signal (N_{sig}), total background (N_{bkg}), and individual background yields in the VBF analysis[21].

2064 5.7 RESULTS

2065 While the combined results of all the $H \rightarrow WW^*$ sub-analyses will be discussed in the next chapter, this
 2066 section presents the results of the VBF specific analysis and interpretations.

2067 As table 5.7 shows, the final cut-based signal region contains 20 events in data with $m_T < 150$ GeV,
 2068 14 coming from the $e\mu$ channel and 6 coming from the $ee + \mu\mu$ channel. The BDT analysis has many
 2069 more candidates due to its looser selection, and the yields in each bin of O_{BDT} are shown in table 5.14.

2070 Figure 5.16(a) shows the final distribution of data candidates compared to the expected m_T distri-
 2071 bution for signal and background. The data are very consistent with a VBF Higgs hypothesis. Fig-
 2072 ure 5.16(b) shows where the data candidates fall in the two-dimensional binning of m_T and m_{jj} used
 2073 in the fit for the cut-based analysis.

2074 Figure 5.17 shows the distributions of O_{BDT} and m_T in the VBF BDT analysis. Again the data are
 2075 quite consistent with a VBF Higgs hypothesis.

2076 Because the cut-based result is used as a validation for the BDT analysis and the two signal regions are
 2077 not fully orthogonal, it is interesting to explore which events overlap between the two analyses. Of the
 2078 twenty events in the cut-based signal region, only seven were not selected by the BDT analysis, while the
 2079 other thirteen also enter the BDT signal region. Figure ?? shows where the different analysis candidates
 2080 lie in the m_{jj} - m_T plane. This shows clearly that the advantage of the BDT analysis is that it can extract

(a) Before the BDT classification

Selection	Summary						Composition of N_{bkg}											
	$N_{\text{obs}}/N_{\text{bkg}}$	N_{obs}	N_{bkg}	N_{signal}	N_{ggF}	N_{VBF}	N_{VH}	N_{WW}	$N_{\text{WW}}^{\text{NEW}}$	$N_{\text{WW}}^{\text{QCD}}$	N_t	N_{missid}	N_{Wj}	N_{ij}	N_{VV}	$N_{e\mu/\mu\mu}$	$N_{\tau\tau}^{\text{QCD}}$	$N_{\tau\tau}^{\text{NEW}}$
$e\mu$ sample	1.04 ± 0.04	718	689	13	15	2.0	90	II	327	42	29	23	31	—	2.2	130	2	—
$ee/\mu\mu$ sample	1.18 ± 0.08	469	397	6.0	7.7	0.9	37	3	132	17	5.2	1.2	10.1	—	168	23	1	—

(b) Bins in O_{BDT}

$e\mu$ sample	Bins in O_{BDT}																	
	Bin 0 (not used)	Bin 1	Bin 2	Bin 3	Bin 4	Bin 5	Bin 6	Bin 7	Bin 8	Bin 9	Bin 10	Bin 11	Bin 12	Bin 13	Bin 14	Bin 15	Bin 16	Bin 17
$ee/\mu\mu$ sample	1.91 ± 0.08	396	345	3.8	1.3	0.8	33	2	123	16	4.1	1.1	8.8	137	20.5	0.5	—	—
Bin 0 (not used)	0.82 ± 0.14	53	45	1.5	2.2	0.1	3.0	0.5	10.4	1.8	0.8	0.2	0.9	26	1.7	0.1	—	—
Bin 1	1.77 ± 0.49	14	7.9	0.6	2.5	—	0.8	0.3	1.1	0.2	0.2	—	0.3	4.4	0.3	0.1	—	—
Bin 2	6.52 ± 2.87	6	0.9	0.2	1.7	—	0.1	0.2	0.2	—	—	—	—	0.7	—	—	—	—
Bin 3	5.41 ± 2.32	6	1.1	0.4	3.1	—	0.3	0.2	0.3	0.1	—	—	0.1	—	0.1	0.1	0.1	0.1

Table 5.14: Event selection for the VBF BDT analysis. The event yields in (a) are shown after the preselection and the additional requirements applied before the BDT classification (see text). The event yields in (b) are given in bins in O_{BDT} after the classification[21].

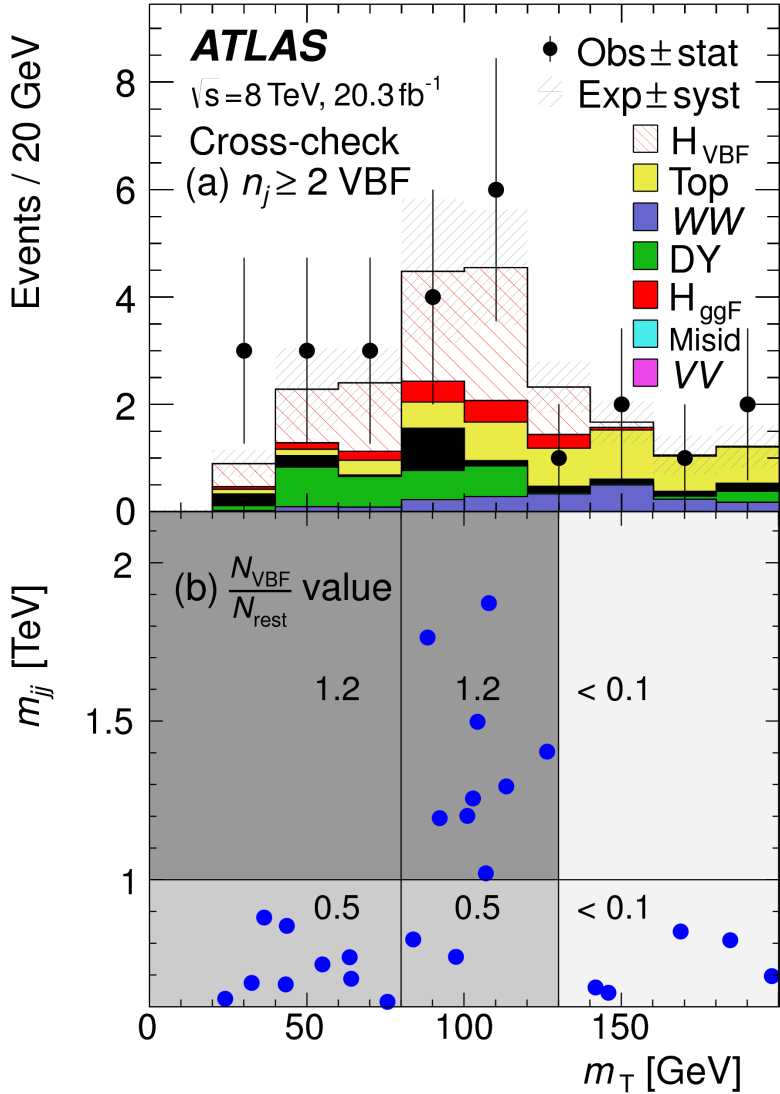


Figure 5.16: Postfit distributions in the cut-based VBF analysis. Panel (a) shows the one-dimensional m_T distribution, while (b) shows the data candidates split into the bins of m_T and m_{jj} used in the final fit[21].

2081 signal candidates lower m_{jj} region due to its ability to recognize correlations with other variables.
 2082 While the context of these results in the broader $H \rightarrow WW^*$ statistical analysis will be presented
 2083 in the next chapter, the significance of the VBF observation can be shown here. In the BDT analysis,
 2084 the expected signal significance was 2.7σ , while the observed significance was 3.1σ . In the cut-based
 2085 analysis, the expected significance was 2.1σ and the observed significance was 3.0σ . The compatibility
 2086 between these two results can be evaluated by computing the probability of observing a larger difference

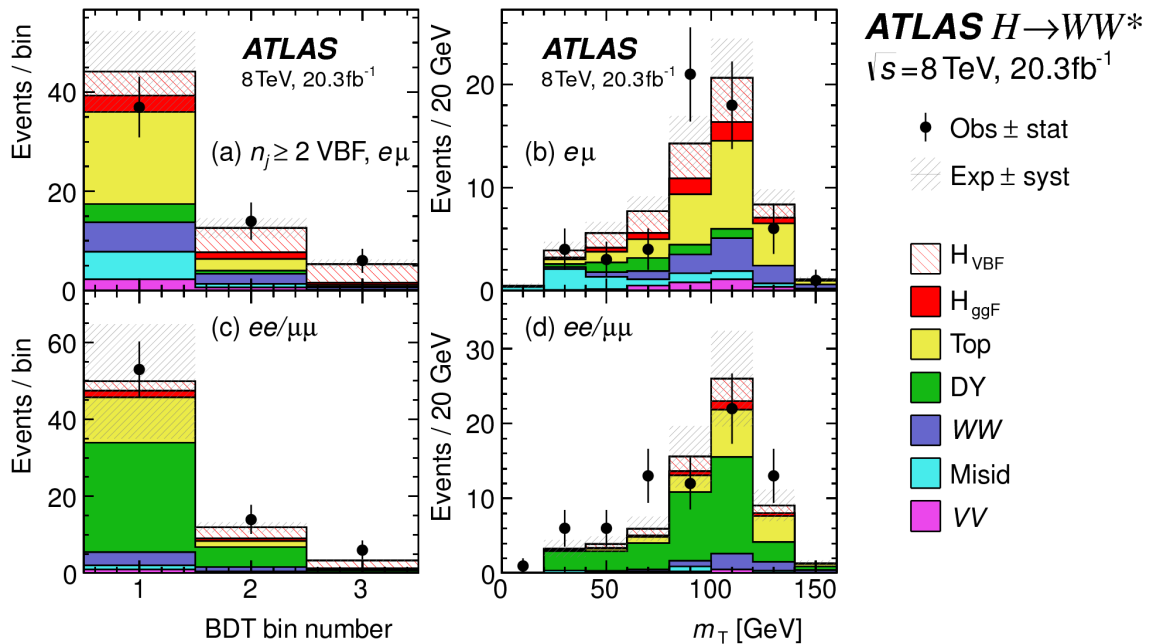


Figure 5.17: Postfit distributions in the BDT VBF analysis[21].

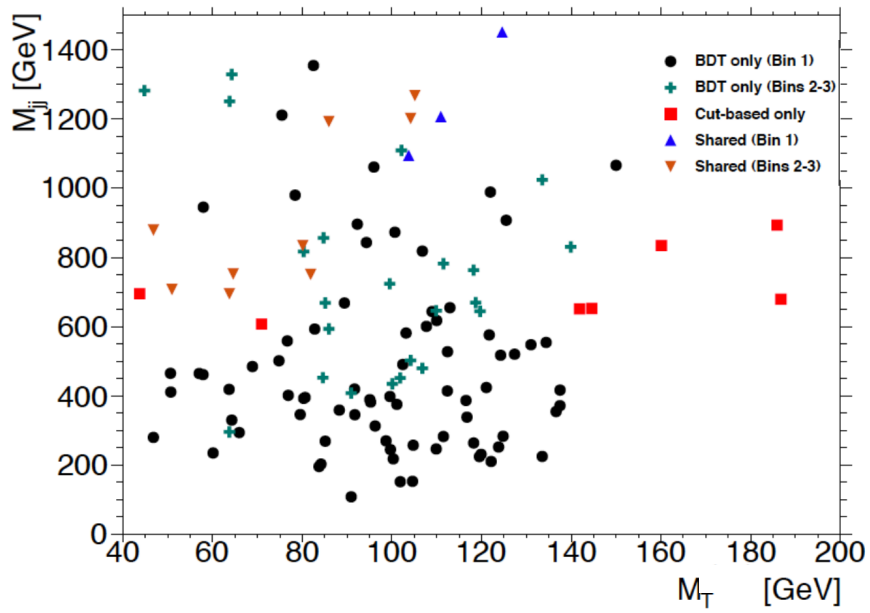


Figure 5.18: Overlap between cut-based and BDT VBF signal region candidates in the m_{jj} - m_T plane.

2087 in Z_0 values than the one measured. Using toy Monte Carlo with the ggF signal strength fixed to unity
2088 and considering only statistical uncertainties, this probability is computed to be 79%, indicating good
2089 agreement between the analyses.

2090 This result represents the first observation of the vector boson fusion production of a Higgs boson.

*The feeling is less like an ending than just another
starting point.*

Chuck Palahniuk

6

2091

2092

Combined Run I $H \rightarrow WW^* \rightarrow \ell\nu\ell\nu$

2093

results

2094 6.1 INTRODUCTION

2095 In the final statistical analysis of $H \rightarrow WW^* \rightarrow \ell\nu\ell\nu$, the dedicated gluon-gluon fusion and vector
2096 boson fusion sensitive signal regions are all combined into a single fit to determine the main parameters
2097 of interest, the Higgs signal strength μ and mass m_H . Therefore, while the specific requirements applied
2098 for the VBF sensitive analysis are discussed in chapter 5, the final measurement of these parameters can
2099 only be discussed in combination with the results of the ggF dedicated analysis. For example, because
2100 ggF Higgs production is considered a background in the VBF analysis, the ggF dedicated signal regions
2101 can actually constrain the normalization of this background in the VBF dedicated region.

2102 This chapter presents the combined interpretation of results in the $H \rightarrow WW^* \rightarrow \ell\nu\ell\nu$ analysis

SR category i			Fit var.
n_j , flavor	$\otimes m_{\ell\ell}$	$\otimes p_T^{\ell 2}$	
$n_j = 0$			
$e\mu$	$\otimes [10, 30, 55]$	$\otimes [10, 15, 20, \infty]$	$\otimes [e, \mu]$
$ee/\mu\mu$	$\otimes [12, 55]$	$\otimes [10, \infty]$	m_T
$n_j = 1$			
$e\mu$	$\otimes [10, 30, 55]$	$\otimes [10, 15, 20, \infty]$	$\otimes [e, \mu]$
$ee/\mu\mu$	$\otimes [12, 55]$	$\otimes [10, \infty]$	m_T
$n_j \geq 2$ ggF			
$e\mu$	$\otimes [10, 55]$	$\otimes [10, \infty]$	m_T
$n_j \geq 2$ VBF			
$e\mu$	$\otimes [10, 50]$	$\otimes [10, \infty]$	O_{BDT}
$ee/\mu\mu$	$\otimes [12, 50]$	$\otimes [10, \infty]$	O_{BDT}

Table 6.1: All signal regions definitions input into final statistical fit[21].

for gluon fusion and vector boson fusion Higgs production. First, the results of the dedicated gluon fusion search are presented. Then, a comparison of the individual production mode signal strengths (μ_{ggF} and μ_{VBF} and a measurement of the combined signal strength (μ) are shown. Subsequently, the measured values of the Higgs couplings to fermions and vector bosons is presented. Finally, the cross section measurement for ggF and VBF production are shown.

6.2 RESULTS OF DEDICATION GLUON FUSION $H \rightarrow WW^* \rightarrow \ell\nu\ell\nu$ SEARCH

The details of the dedicated gluon fusion $H \rightarrow WW^* \rightarrow \ell\nu\ell\nu$ search are not discussed in this thesis and instead left to more comprehensive sources[21]. However, a brief summary of the results are essential for describing the results of the full analysis and interpreting the results of the dedicated VBF search in this broader context.

Table 6.1 shows the individual signal regions that were input into the final statistical fit. The ggF dedicated bins use m_T as their discriminating variable and are separated into bins of p_T of the subleading lepton as well. The VBF dedicated bin uses the O_{BDT} distribution as its final discriminant.

Table 6.2 shows the yields in the various signal regions in both data and expected signal and back-

2117 grounds. The yields for signal and background are all scaled according to the final normalizations calcu-
2118 lated in the fit.

	N_{obs}	N_{bkg}	N_{ggF}	N_{VBF}
$n_j = 0$	3750	3430 ± 90	300 ± 50	8 ± 4
$n_j = 1$	1596	1470 ± 40	102 ± 26	17 ± 5
$n_j \geq 2, \text{ggF } e\mu$	1017	960 ± 40	37 ± 11	13 ± 1.4
$n_j \geq 2, \text{VBF}$	130	99 ± 9	7.7 ± 2.6	21 ± 3

Table 6.2: Post-fit yields in the different ggF and VBF dedicated signal regions[21].

2119 Figure 6.1 shows the final post-fit m_T distribution in the $n_j \leq 1$ regions. The data are very consistent
2120 with the hypothesis of ggF Higgs production.

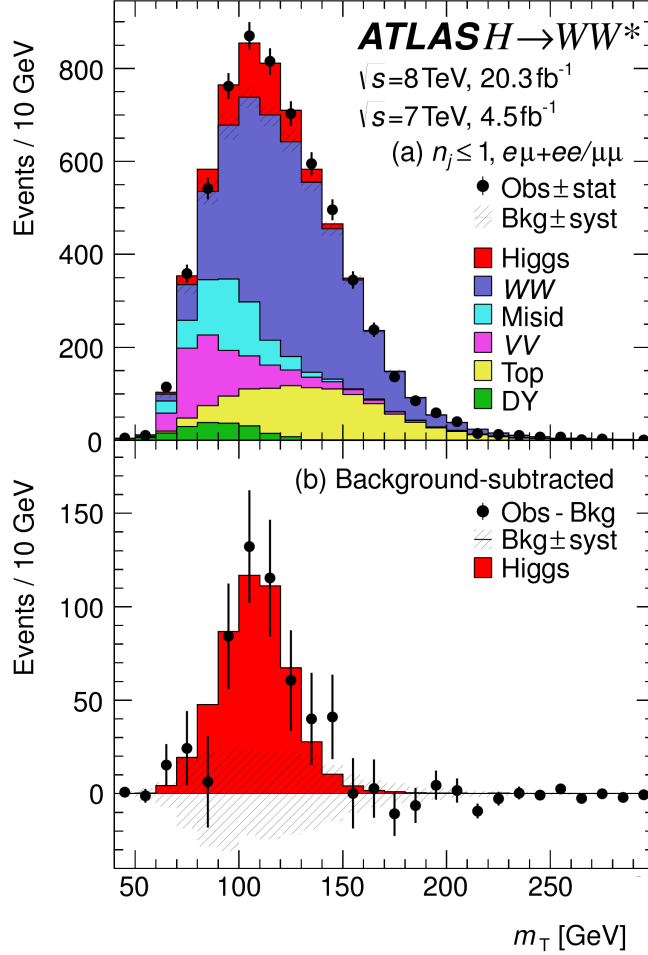


Figure 6.1: Post-fit m_T distribution in the $n_j \leq 1$ regions[21].

2121 These yields are used as input, along with the VBF results in chapter 5, for the physical interpretation
2122 of results presented in subsequent sections.

2123 **6.3 SIGNAL STRENGTH MEASUREMENTS IN ggF AND VBF PRODUCTION**

2124 When all of the signal regions are combined in the fit, there can be a combined measurement of the sig-
2125 nal strength as well as the individual ggF and VBF signal strengths. The combined signal strength is the
2126 ratio of the sum of the gluon fusion and VBF cross sections to the theory prediction, or a singal strength
2127 for the total Higgs production cross section that this analysis is sensitive to. The final measured com-
2128 bined signal strength μ is measured shown in equation 6.1.

$$\begin{aligned} \mu &= 1.09 \quad {}^{+0.16}_{-0.15} (\text{stat.}) \quad {}^{+0.08}_{-0.07} \left(\begin{array}{l} \text{expt} \\ \text{syst} \end{array} \right) \quad {}^{+0.15}_{-0.12} \left(\begin{array}{l} \text{theo} \\ \text{syst} \end{array} \right) \quad \pm 0.03 \left(\begin{array}{l} \text{lumi} \\ \text{syst} \end{array} \right) \\ &= 1.09 \quad {}^{+0.16}_{-0.15} (\text{stat}) \quad {}^{+0.17}_{-0.14} (\text{syst}) \\ &= 1.09 \quad {}^{+0.23}_{-0.21}. \end{aligned} \tag{6.1}$$

2129 Figure 6.2 gives the best fit signal strength $\hat{\mu}$ as a function of hte hypothesized Higgs mass. The value
2130 at 125.36 GeVcorresponds to the μ quoted in equation 6.1. This value of the Higgs mass is used because
2131 it is the most precise mass measurement from ATLAS, a result of the combined $\gamma\gamma$ and ZZ mass mea-
2132 surements[?].

2133 As explained in chapter 3, a probability p_0 can be computed using the test statistic q_0 to quantify the
2134 probability that the background could fluctuate to produce an excess at least as large as the one observed
2135 in the data. The local p_0 value is shown in figure 6.3 as a function of m_H . The minimum p_0 value is
2136 at $m_H = 130$ GeV and coresponds to a significance of 6.1σ . The curve is relatively flat and the sig-
2137 nificance is the same at 125.36 GeVwithin the quoted precision. The expected significance for a signal
2138 with strength $\mu = 1.0$ is 5.8σ . This represents the first discovery level significance measurement in the
2139 $H \rightarrow WW^* \rightarrow \ell\nu\ell\nu$ analysis.

2140 All the results presented so far in this section have been for the combined gluon fusion and VBF pro-
2141 duction modes. However, each signal strength can be calculated separately in the likelihood as well.
2142 There are two ways to do this. First, the likelihood can be parameterized in terms of a single parameter,

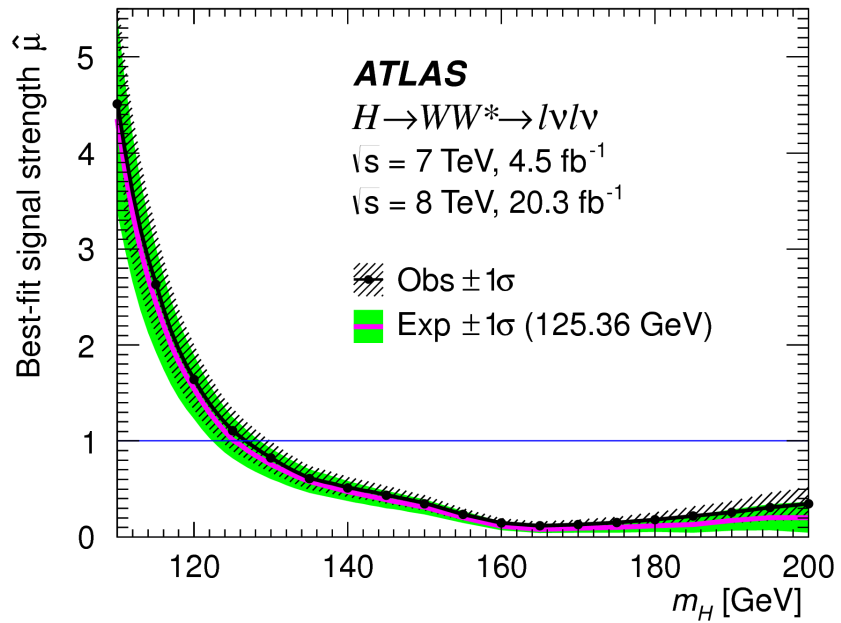


Figure 6.2: Best fit signal strength $\hat{\mu}$ as a function of hypothesized m_H [21].

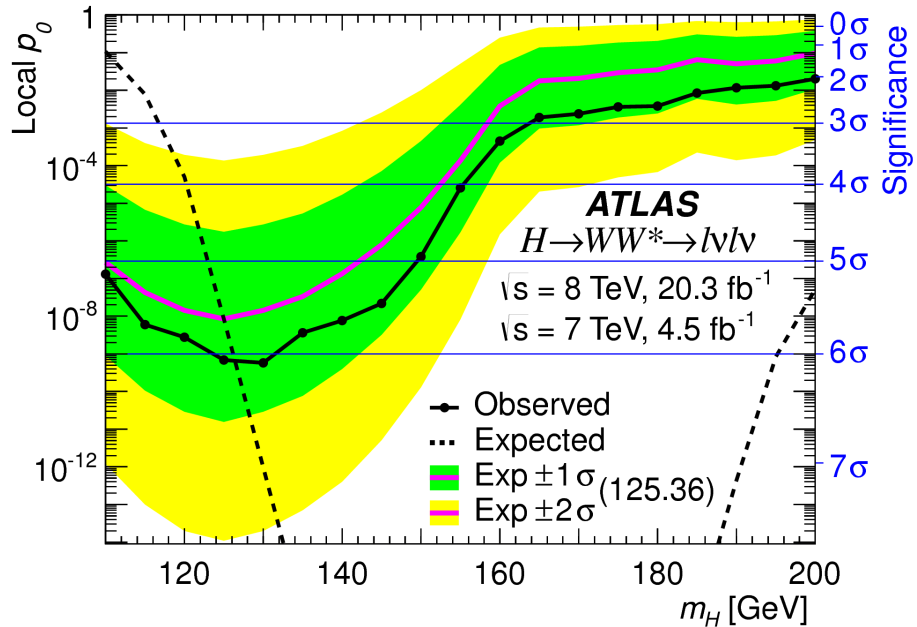


Figure 6.3: Local p_0 as a function of m_H [21].

²¹⁴³ the ratio of the VBF and gluon fusion signal strengths. With this method, the significance of the VBF
²¹⁴⁴ observation can be evaluated. Figure 6.4 shows the likelihood as a function of the ratio $\mu_{\text{VBF}}/\mu_{\text{ggF}}$.

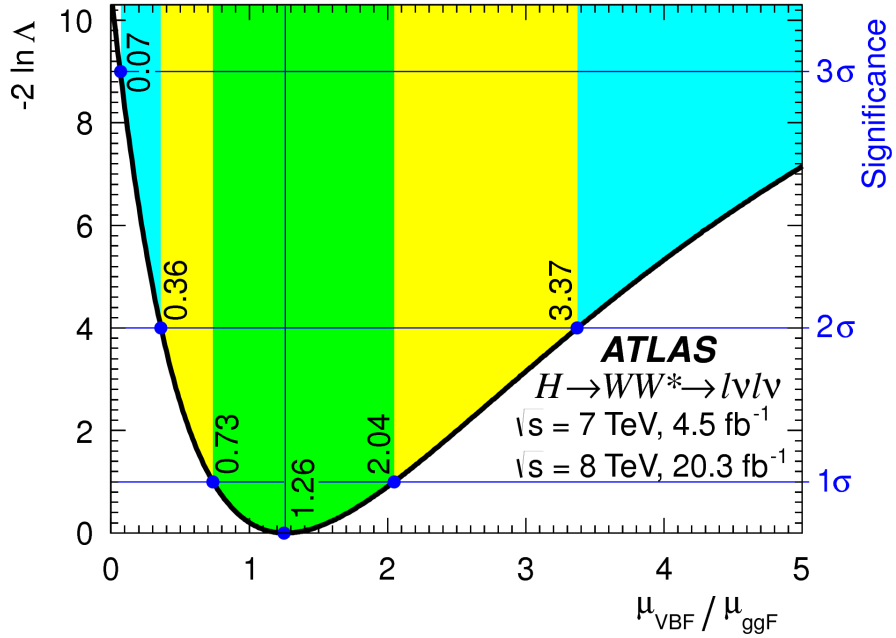


Figure 6.4: Likelihood as a function of $\mu_{\text{VBF}} / \mu_{\text{ggF}}$ [21].

2145 The best fit value of the ratio of signal strengths is shown in equation 6.2. Within the quoted uncer-
 2146 tainties, it is consistent with a ratio of unity.

$$\frac{\mu_{\text{VBF}}}{\mu_{\text{ggF}}} = 1.26^{+0.61} (\text{stat.})^{+0.50} (\text{syst.}) = 1.26^{+0.79}_{-0.53} \quad (6.2)$$

2147 The null hypothesis for VBF production corresponds to a ratio of $\mu_{\text{VBF}} / \mu_{\text{ggF}} = 0$. The likelihood
 2148 in figure 6.4 gives a significance of 3.2σ at $\mu_{\text{VBF}} / \mu_{\text{ggF}} = 0$, as quoted in chapter 5.

2149 In addition to the ratio of signal strengths, each signal strength can be varied independently in the
 2150 likelihood as well. Figure 6.5 shows the two dimensional likelihood scan in the $\mu_{\text{ggF}}-\mu_{\text{VBF}}$ plane. The
 2151 best fit values of the two signal strengths are shown in equation 6.3. Both are consistent with unity
 2152 within their uncertainties.

$$\begin{aligned} \mu_{\text{ggF}} &= 1.02 \pm 0.19^{+0.22}_{-0.18} = 1.02^{+0.29}_{-0.26} \\ \mu_{\text{VBF}} &= 1.27 \pm 0.44^{+0.29}_{-0.40} = 1.27^{+0.53}_{-0.45}. \end{aligned} \quad (6.3)$$

(stat.) (syst.)

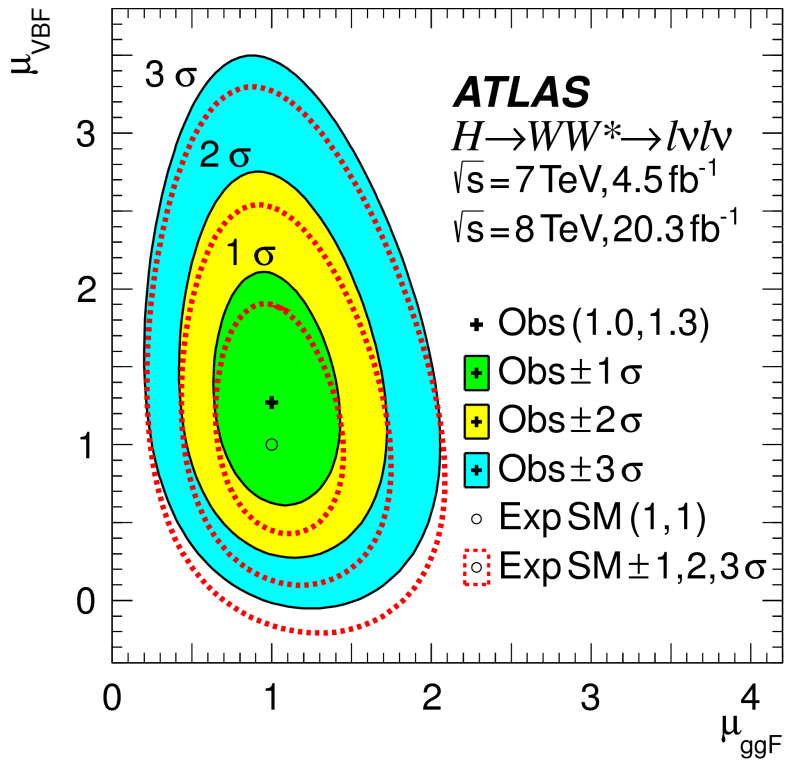


Figure 6.5: Likelihood scan as a function of μ_{VBF} and μ_{ggF} [21].

2153 6.4 MEASUREMENT OF HIGGS COUPLINGS TO VECTOR BOSONS AND FERMIONS

2154 Similar to the parameterization of signal strength, the couplings of the Higgs to fermions and bosons can
 2155 also be parameterized. The parameter of interest in this case is κ , or the ratio of the measured coupling
 2156 to the standard model expectation. Both the fermion and boson couplings have these so-called scale fac-
 2157 tors, κ_F for fermions and κ_V for bosons. Gluon fusion production is sensitive to the fermion couplings
 2158 through the top quark loops in its production, while VBF production is sensitive to the vector boson
 2159 couplings in its production. Both modes are sensitive to the vector boson couplings in their decays. The
 2160 signal strengths will have dependence on the coupling scale factors as described in equation 6.4[2].

$$\begin{aligned} \mu_{\text{ggF}} &\propto \frac{\kappa_F^2 \cdot \kappa_V^2}{(\mathcal{B}_{H \rightarrow f\bar{f}} + \mathcal{B}_{H \rightarrow gg}) \kappa_F^2 + (\mathcal{B}_{H \rightarrow VV}) \kappa_V^2} \\ \mu_{\text{VBF}} &\propto \frac{\kappa_V^4}{(\mathcal{B}_{H \rightarrow f\bar{f}} + \mathcal{B}_{H \rightarrow gg}) \kappa_F^2 + (\mathcal{B}_{H \rightarrow VV}) \kappa_V^2}. \end{aligned} \quad (6.4)$$

2161 Figure 6.6 shows the two-dimensional likelihood scan of κ_F and κ_V . The best-fit values are given in
 2162 equation 6.5. The best-fit values are consistent with unity within their uncertainties.

$$\begin{aligned} \kappa_F &= 0.93 & +0.24 & +0.21 & = 0.93 & +0.32 \\ && -0.18 & -0.14 && -0.23 \\ \kappa_V &= 1.04 & +0.07 & +0.07 & = 1.04 & \pm 0.11. \end{aligned} \quad (6.5)$$

(stat.) (syst.)

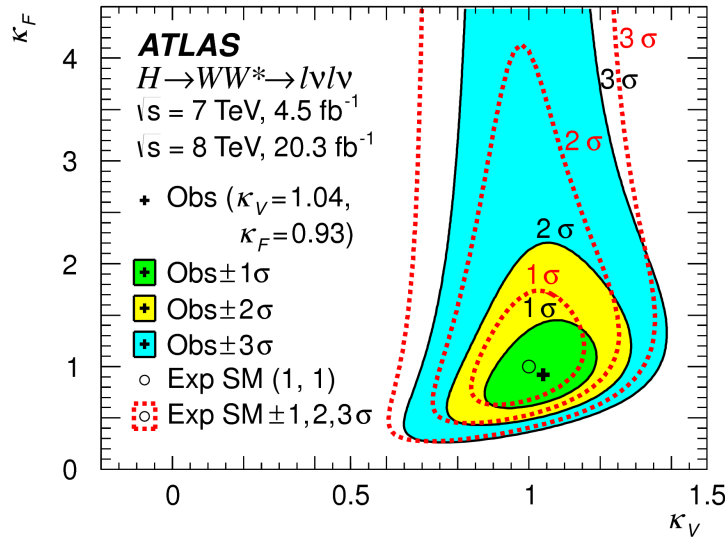


Figure 6.6: Likelihood scan as a function of κ_F and κ_V [21].

2163 6.5 HIGGS PRODUCTION CROSS SECTION MEASUREMENT

2164 Another measurement that comes naturally from the signal strength numbers quoted earlier is the pro-
 2165 duction cross section and 7 and 8 TeV for both gluon fusion and VBF production. The general equa-
 2166 tion for calculating the cross section is given in equation 6.6.

$$\begin{aligned} (\sigma \cdot \mathcal{B}_{H \rightarrow WW^*})_{\text{obs}} &= \frac{(N_{\text{sig}})_{\text{obs}}}{\mathcal{A} \cdot \mathcal{C} \cdot \mathcal{B}_{WW \rightarrow \ell\nu\ell\nu}} \cdot \frac{1}{\int L dt} \\ &= \hat{\mu} \cdot (\sigma \cdot \mathcal{B}_{H \rightarrow WW^*})_{\text{exp}} \end{aligned} \quad (6.6)$$

2167 $(N_{\text{sig}})_{\text{obs}}$ is the number of events observed in data. \mathcal{A} is the geometric and kinematic acceptance of
 2168 the detector, while \mathcal{C} is the efficiency of the signal region selection for events that are reconstructed in the
 2169 detector. The branching ratio of a WW system to leptons must also be divided out. The production
 2170 cross section depends on the center of mass energy and the production mode desired (gluon fusion or
 2171 VBF), and so three separate cross section measurements are quoted in equation 6.7.

$$\begin{aligned}
 \sigma_{\text{ggF}}^{\text{7TeV}} \cdot \mathcal{B}_{H \rightarrow WW^*} &= 2.0 \pm 1.7 {}^{+1.2}_{-1.1} = 2.0 {}^{+2.1}_{-2.0} \text{ pb} \\
 \sigma_{\text{ggF}}^{\text{8TeV}} \cdot \mathcal{B}_{H \rightarrow WW^*} &= 4.6 \pm 0.9 {}^{+0.8}_{-0.7} = 4.6 {}^{+1.2}_{-1.1} \text{ pb} \\
 \sigma_{\text{VBF}}^{\text{8TeV}} \cdot \mathcal{B}_{H \rightarrow WW^*} &= 0.51 {}^{+0.17}_{-0.15} {}^{+0.13}_{-0.08} = 0.51 {}^{+0.22}_{-0.17} \text{ pb.}
 \end{aligned} \tag{6.7}$$

(stat.) (syst.)

2172 The predicted cross section values for gluon fusion are 3.3 ± 0.4 pb at 7 TeV and 4.2 ± 0.5 pb
 2173 at 8 TeV, consistent with the measured values within their uncertainties. For vector boson fusion, the
 2174 predicted cross section is 0.35 ± 0.02 pb, again consistent with the measured value.

2175 6.6 CONCLUSION

2176 The combined analysis of the gluon fusion and vector boson fusion processes in $H \rightarrow WW^* \rightarrow \ell\nu\ell\nu$
 2177 in the 7 and 8 TeV datasets has yielded the first discovery level significance for Higgs production in this
 2178 decay channel. Additionally, precise measurements of the couplings to vector bosons and fermions are
 2179 given. Finally, signal strengths and cross sections for each production mode are measured. Figure 6.7
 2180 shows the $H \rightarrow WW^* \rightarrow \ell\nu\ell\nu$ measurements in comparison with other Higgs decay channels in
 2181 ATLAS. The measurement of signal strength from this channel remains the most sensitive in both the
 2182 gluon fusion and VBF production modes for the Run 1 dataset.

ATLAS

Individual analysis

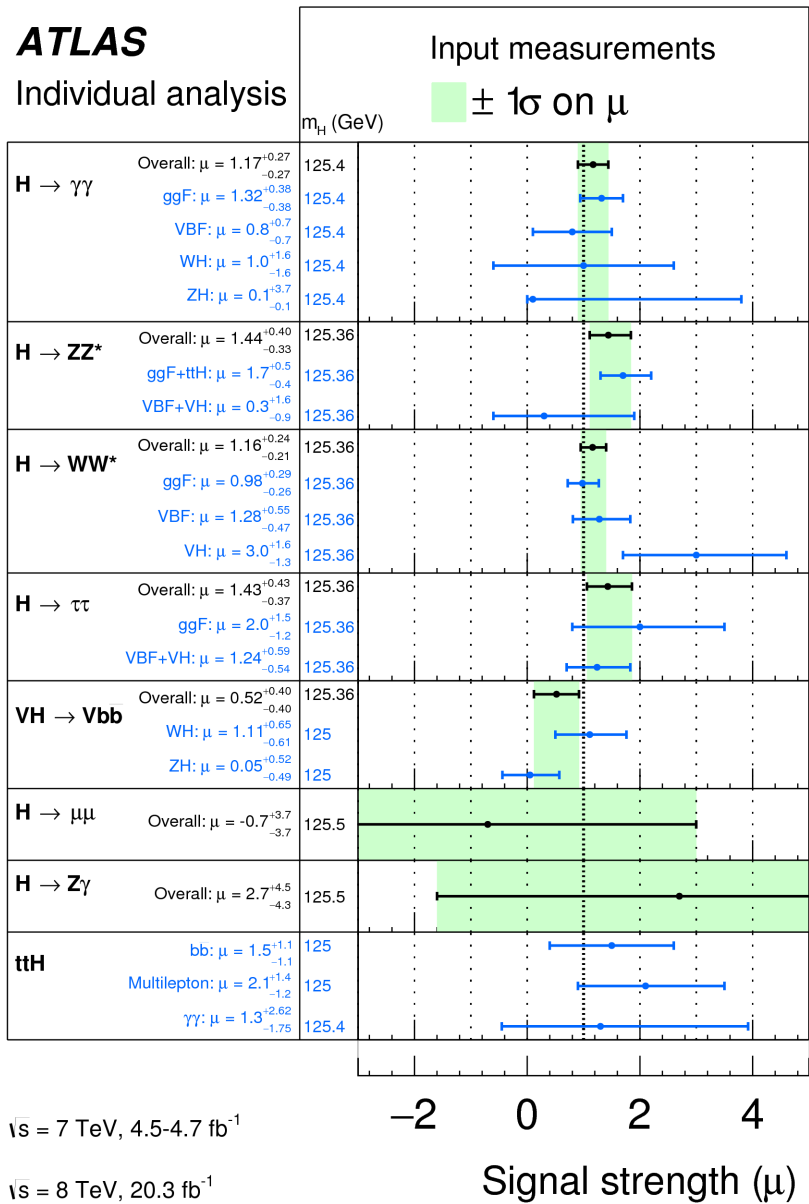


Figure 6.7: Comparison of signal strength measurements in different Higgs decay channels on ATLAS[23].

2183

Part III

2184

Search for Higgs pair production in the

2185

$HH \rightarrow b\bar{b}b\bar{b}$ channel in LHC Run 2 at $\sqrt{s} =$

2186

13 TeV

*Passion is in all great searches and is necessary to all
creative endeavors.*

W. Eugene Smith

7

2187

2188 Search for Higgs pair production in boosted 2189 $b\bar{b}b\bar{b}$ final states

2190 7.1 INTRODUCTION

2191 After the discovery of the Higgs boson in the ATLAS Run 1 dataset and the subsequent measurements
2192 of its properties, the Higgs transformed into a potential tool in searches for physics beyond the Stan-
2193 dard Model. The pair production cross section of the Higgs can be enhanced through BSM physics.
2194 Studying di-Higgs production also probes the Higgs self-coupling, shedding light on the structure
2195 of the Higgs potential. This chapter presents a search for resonant production of a Higgs pair in the
2196 $X \rightarrow HH \rightarrow b\bar{b}b\bar{b}$ final state in 3.2 fb^{-1} of data collected at $\sqrt{s} = 13 \text{ TeV}$. In particular, this
2197 chapter focuses on a search for this final state in the regime where m_X is large ($\gtrsim 1 \text{ TeV}$) and the Higgs
2198 bosons in the decay are significantly boosted. A tailored selection for this boosted selection, using novel

2199 techniques in jet substructure and b -tagging, is discussed. Then, the data-driven background estimate is
 2200 presented. Finally, the results of the search are shown. The signal models used as benchmarks are a spin-
 2201 2 Randall Sundrum graviton (RSG) and a narrow width spin-0 resonance. These models are described
 2202 in more detail in Chapter 1. Limits on signal models are reserved for the next chapter where the results of
 2203 this chapter are combined with the results of a separate selection dedicated to the lower m_X regime.

2204 **7.2 MOTIVATION**

2205 With the center of mass energy increase from $\sqrt{s} = 8$ TeV to $\sqrt{s} = 13$ TeV, the LHC and ATLAS
 2206 are able to probe new resonances at higher mass scales than previously accessible in Run 1. This is a
 2207 powerful motivator for searching for a new resonance in the early 13 TeV data. Figure 7.1 shows the
 2208 ratios of parton luminosities between 8 and 13 TeV for different resonance masses. For a resonance of
 2209 $M_X = 2$ TeV, the cross section at $\sqrt{s} = 13$ TeV is roughly a factor of 10 larger than at $\sqrt{s} = 8$ TeV.

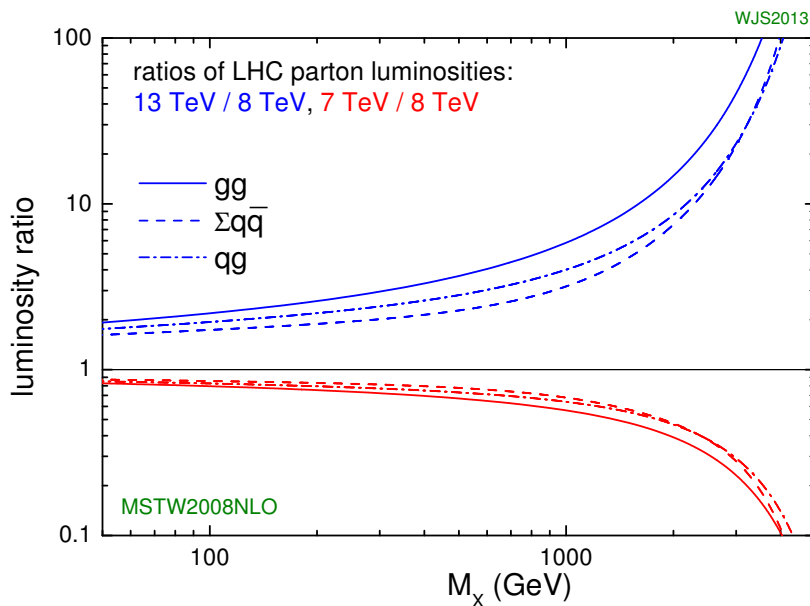


Figure 7.1: Parton luminosity ratios as a function of resonance mass M_X for 13/8 TeV and 7/8 TeV [24].

2210 Higgs pair production offers a vast array of unprobed regions of phase space where searches for BSM
 2211 physics can be made. Chapter 1 discusses some possibilities for both resonant and non-resonant enhance-

ment of the di-Higgs production cross section. Given the increased mass reach of the LHC in Run 2, it is particularly important to focus on resonant searches at high m_X . One consideration when conducting a search in the HH final state is which decay modes of the Higgs to consider. Figure 7.2 shows the branching ratio of the HH final state for different combinations of decays of each individual Higgs. As the largest branching ratio for the 125 GeV Higgs is $H \rightarrow b\bar{b}$, the $HH \rightarrow b\bar{b}b\bar{b}$ branching ratio is also the largest at 33%.

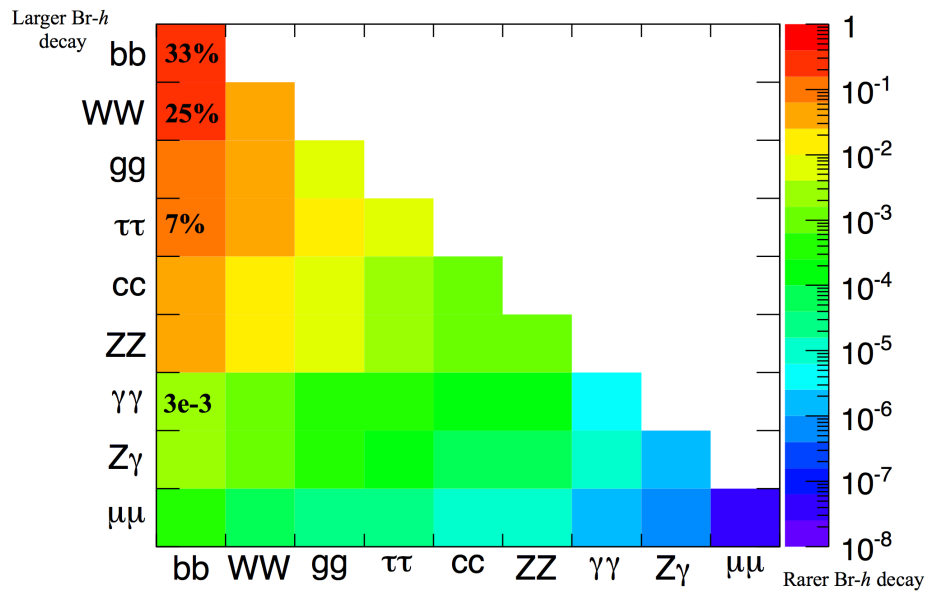


Figure 7.2: Summary of HH branching ratios [25].

At high m_X , the Higgs bosons resulting from the decay of a heavy resonance will have large p_T^* . The ΔR between the decay products of the Higgs is inversely proportional to the Higgs p_T , as shown in equation ??.

$$\Delta R \approx \frac{2m}{p_T} \quad (7.1)$$

Figure 7.3 shows the minimum ΔR between truth level B decay vertices in simulation samples for Randall-Sundrum gravitons of different masses. The figure shows that as the mass of the graviton increases, the ΔR distribution between the b quarks in the Higgs decay tends to shift to lower values. Be-

*In the limit that $m_H \ell \ell m_X$, the Higgs p_T is roughly $m_X/2$.

cause of this effect, it is necessary to tailor a selection to target these merged b -jets.

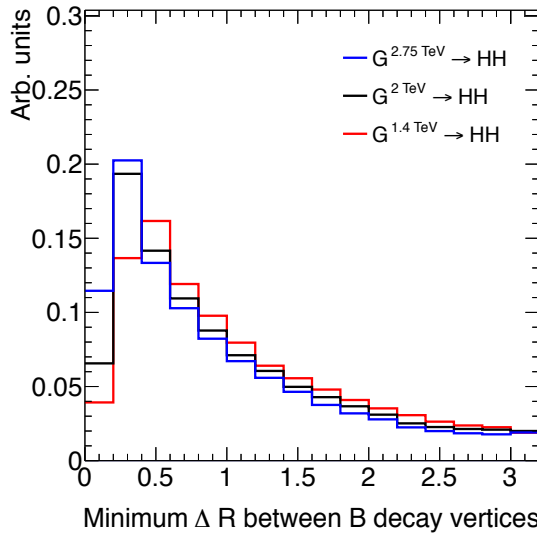


Figure 7.3: Minimum ΔR between B decay vertices for different RSG masses in a $G_{\text{KK}}^* \rightarrow HH \rightarrow 4b$ sample with $c = 1$

7.3 DATA AND SIMULATION SAMPLES

7.3.1 SIGNAL MODELS

While the resonance search is by its nature generic (as it is a simple search for a peak in the $4b$ invariant mass spectrum), there are two signal models that the selection requirements have been optimized for. The first is Randall-Sundrum (RSG) model, where a tower of massive spin-2 Kaluza-Klein gravitons is predicted. The second is a heavy narrow spin-0 resonance, the so-called “heavy Higgs”. This type of resonance arises, for example, in the two Higgs doublet model (2HDM). More details about the physics of these models and their motivation is given in chapter 1.

Signal graviton (G_{KK}^*) events are generated at leading order (LO) with **MADGRAPH5 v2.2.2** [92].

The PDF set used is the **NNPDF2.3 LO** set [93]. For modeling parton shower and hadronization in jets, **PYTHIA 8.186** is used with the A14 tune [80, 94]. The free parameters in the RSG model are the graviton mass and the coupling constant $c \equiv k/\bar{M}_{\text{Pl}}$ [†]. Both the production cross section and width of the

[†] k is the curvature constant for the warped extra dimension and \bar{M}_{Pl} is the Planck mass divided by 8π

graviton are proportional to c^2 . Samples are generated at both $c = 1$ and $c = 2$ for a variety of mass points between 300 GeV and 3 TeV.

The second signal sample is a heavy spin-0 resonance H with a fixed width of $\Gamma_H = 1$ GeV. This is generated with **MADGRAPH5** and uses the **CT10** PDF set [83]. The parton shower and hadronization are handled by **HERWIG ++** with the **CTEQ6L1** PDF set and the **UEEE5** event tune [84, 95, 96]. Because the width and branching ratios depend on 2HDM parameters, each mass point generated with this fixed width corresponds to a different point in the 2HDM parameter phase space. Mass points are generated between 300 GeV and 1 TeV as with the RSG signal samples.

7.3.2 BACKGROUND SAMPLES

While the dominant **QCD** multijet background is estimated with a fully data-driven method, the sub-dominant backgrounds $t\bar{t}$ and $Z + \text{jets}$ are modeled with some input from simulation.

$t\bar{t}$ events are simulated at next-to-leading order (NLO) with the **POWHEG-BOX** version 1 generator using the **CT10** PDF set [97]. The parton shower, hadronization, and underlying event are simulated with **PYTHIA 6.428** with the **CTEQ6L1** PDF set [79]. The Perugia 2012 tune is used [98]. NNLO **QCD** corrections to the cross sections are computed in **Top++ 2.0** [99]. The top quark mass is set to 172.5 GeV. The shapes of distributions in $t\bar{t}$ are taken from MC while the normalization is taken from data.

Finally, the $Z + \text{jets}$ background is simulated with **PYTHIA 8.186** and the **NNPDF2.3** LO PDF set. This background is negligible compared to the others and is taken fully from MC.

7.3.3 DATA SAMPLE AND TRIGGER

This analysis is done on 3.2 fb^{-1} of data taken in 2015 at $\sqrt{s} = 13$ TeV. The details of the machine conditions during this time can be found in Chapter 2. Only data which was taken during stable beam conditions with all detectors functioning is used. Events must pass a trigger which requires a single 360 GeV large radius ($R = 1.0$) jet to be reconstructed in the HLT. Figure 7.4 shows the trigger efficiency for various trigger options as a function of graviton mass. Above $m_G > 1$ TeV, the single large radius jet trigger is 99% efficient for events passing the signal selection.

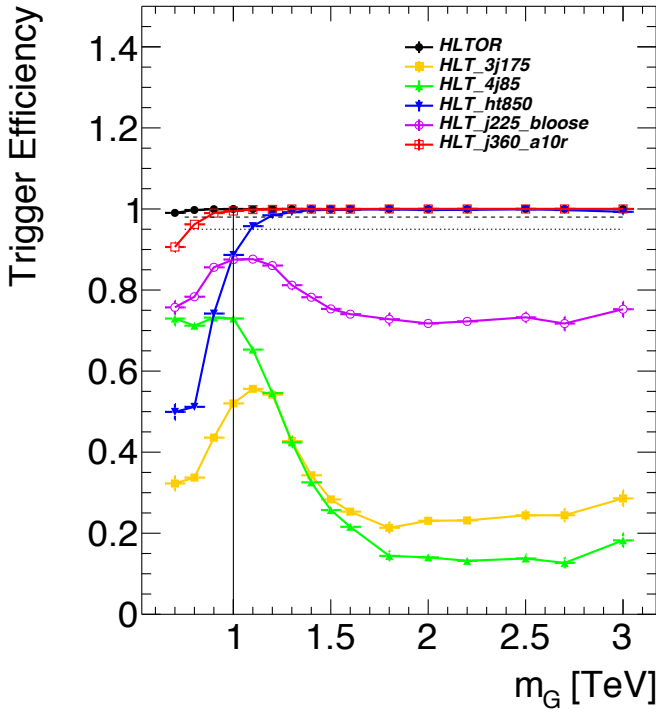


Figure 7.4: Trigger efficiency for events passing all signal region selections as a function of mass in $G_{KK}^* \rightarrow HH \rightarrow 4b$ samples with $c = 1$ [26]. In the trigger names, “j” refers to a jet or jets. “ht” refers to H_T , the scalar sum of transverse momenta in the event. “bloose” refers to a loose b -tagging requirement applied to the jet. “a10r” refers to anti- k_T jets with $R = 1.0$. The numbers at the end are the thresholds on the given quantity in GeV.

2262 7.4 EVENT RECONSTRUCTION AND OBJECT SELECTION

2263 The boosted selection first begins by defining a unique set of objects that can be exploited to increase
 2264 signal efficiency in the kinematic regime where the final state b -jets are very merged.

2265 7.4.1 LARGE RADIUS ($R = 1.0$) JETS

2266 The first step towards reconstructing the final state is to define objects that can be used to measure the
 2267 kinematics of the Higgs bosons. In the boosted selection anti- k_T jets with a radius parameter of 1.0
 2268 are used. These jets are much larger in angular size than the typical $R = 0.4$ jets and are intended to
 2269 encompass both jets resulting from the Higgs decay[‡]. The jets are built from clusters in the calorimeter

[‡]This is in contrast to the resolved selection, which uses two $R = 0.4$ anti- k_T jets for each Higgs

2270 calibrated with local calibration weighting [17].

2271 Because of the large extent of these jets, great care must be taken to remove potential contributions of
2272 calorimeter clusters from pile-up. This is done using a technique called jet trimming [100]. With trim-
2273 ming, the constituents of the large radius jet are re-clustered with a smaller radius with the k_T algorithm.
2274 Then, these so-called subjets are removed from the larger jet if $p_T^{\text{subjet}}/p_T^{\text{jet}} < f_{\text{cut}}$. In this analysis, the
2275 subjet radius is $R = 0.2$ and $f_{\text{cut}} = 0.05$. Trimming has been shown to improve the mass resolution
2276 of large radius jets. Figure 7.5 shows the effect of trimming on the large radius jet mass (M_J). Because
2277 the large radius jet fully contains the higgs decay products, its invariant mass should correspond to the
2278 125 GeV mass of the Higgs. The trimming algorithm brings the jet mass much closer to the expected
2279 Higgs mass and improves the mass resolution.

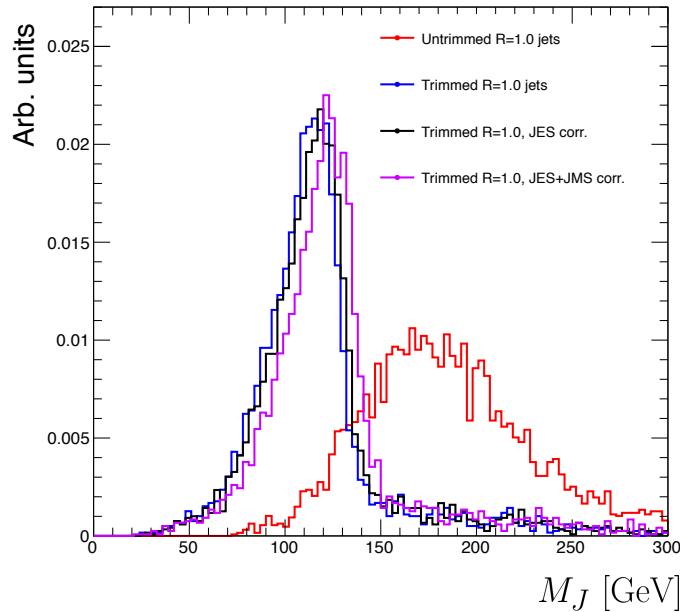


Figure 7.5: Comparison of untrimmed and trimmed jet masses for large radius jets in a RSG sample with $m_{G_{\text{KK}}^*} = 1 \text{ TeV}$. JES (JMS) refers to the standard jet energy (mass) scale calibration for ATLAS [17].

2280 The large radius jets are required to satisfy $250 < p_T < 1500 \text{ GeV}$. They must also be within
2281 $|\eta| < 2.0$ in order to ensure that the full jet is within the inner detector tracking volume. Finally, they
2282 are required to have $M_J > 50 \text{ GeV}$. The upper p_T cut and lower threshold on mass are applied to
2283 correspond to the kinematic range where uncertainties are available in ATLAS calibrations [101, 102].

2284 7.4.2 TRACK JETS AND b -TAGGING

2285 Because the b -jets from boosted Higgs decays are so close together (as illustrated in figure 7.3), narrow ra-
2286 dius jets are required to fully resolve both b -jets. The minimum radius feasible for jets based on calorime-
2287 ter deposits is determined by the calorimeter granularity. However, because b -tagging relies on informa-
2288 tion from the inner detector, it is possible to define another type of jet that can have a smaller radius and
2289 better b -tagging resolution. These jets are called “track jets” [27, 102].

2290 Track jets are formed by applying the usual anti- k_T clustering algorithm to tracks that are required
2291 to be consistent with the primary vertex. After the jet axis has been determined using these tracks, a sec-
2292 ond step of track association is also performed to add tracks that can be useful for b -tagging [27]. In this
2293 analysis, the tracks are clustered with a radius parameter of $R = 0.2$. This radius has been shown to
2294 give good performance in boosted Higgs tagging [27, 102]. Figure 7.6 shows a comparison among dif-
2295 ferent track jet radii of the efficiency for reconstructing two b -jets from each Higgs in a RSG sample as a
2296 function of mass. Track jets with radius of 0.2 give the best performance, especially at high mass.

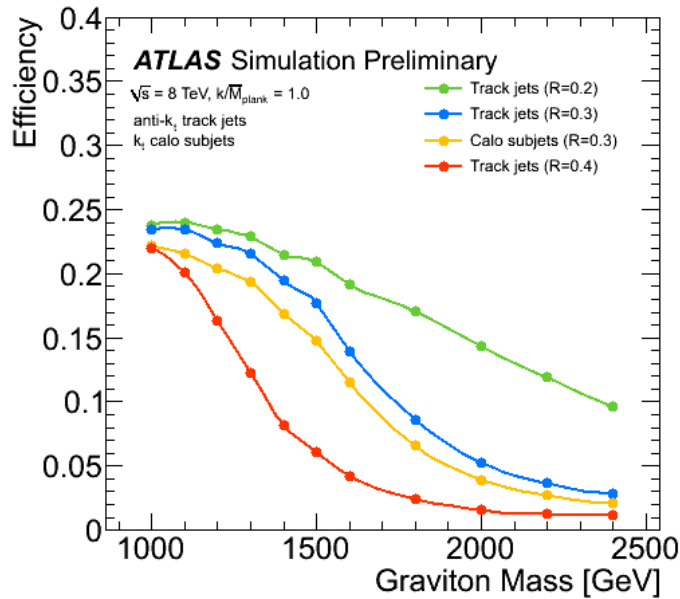


Figure 7.6: Efficiency of finding two b -jets from each Higgs in an RSG event using calorimeter jets with $R = 0.3$ or different track jet radii [27]

2297 In this analysis, track jets are required to have $p_T > 10$ GeV and $|\eta| < 2.5$. They must also have at

2298 least two tracks.

2299 **7.4.3 MUONS**

2300 Muons are used in this study to correct the four-momenta of calorimeter jets by accounting for semi-
2301 leptonic b decays. The muons used are combined ID and MS muons which must satisfy tight identifica-
2302 tion requirements [16]. The muons must have $p_T > 4 \text{ GeV}$ and $|\eta| < 2.5$. Table 7.1 summarizes the
2303 object requirements described in this section.

	R	p_T	$ \eta $	M
Calorimeter jets	1.0	$250 < p_T < 1500 \text{ GeV}$	< 2.0	$> 50 \text{ GeV}$
Track jets	0.2	$> 10 \text{ GeV}$	< 2.5	-
Muons	-	4 GeV	< 2.5	-

2304 **Table 7.1:** Summary of requirements on objects used in the $X \rightarrow HH \rightarrow b\bar{b}b\bar{b}$ search

2304 **7.5 EVENT SELECTION**

2305 The first requirement in the boosted selection is for ≥ 2 large radius jets satisfying the selections outlined
2306 above. The two highest momentum large-R jets in the event are referred to as “Higgs candidates”. The
2307 leading jet is required to have $p_T > 350 \text{ GeV}$.

2308 Track jets satisfying the object selections are matched to Higgs candidate jets via ghost association [103].
2309 Each Higgs candidate must have at least 2 track jets associated with it. These basic requirements are illus-
2310 trated in figure 7.7

2311 The QCD multijet background produces less central jets than high mass resonances, so there is an ad-
2312 ditional requirement that the two Higgs candidates be close together in η . The large-R jets are required
2313 to satisfy $|\Delta\eta(JJ)| < 1.7$.

2314 The final set of requirements ensures that the Higgs candidates are consistent with expected proper-
2315 ties of the 125.0 GeV Higgs. First, a variable (X_{hh}) is defined to measure the consistency of both of the

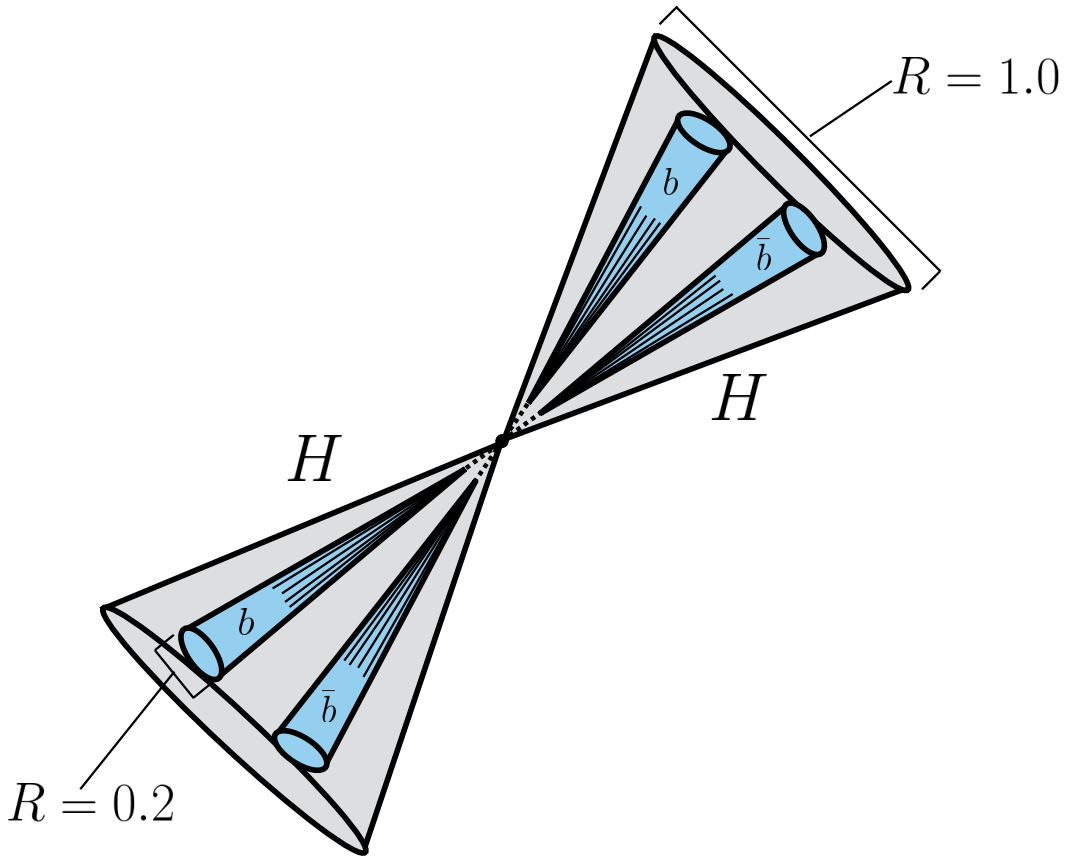


Figure 7.7: Illustration of the boosted selection requirements on Higgs candidates. Each large-radius calorimeter jet (Higgs candidate) must contain two track jets

²³¹⁶ Higgs candidate jets with the SM Higgs mass. This is shown in equation 7.2.

$$X_{hh} = \sqrt{\left(\frac{M_J^{\text{lead}} - 124 \text{ GeV}}{0.1 M_J^{\text{lead}}}\right)^2 + \left(\frac{M_J^{\text{sublead}} - 115 \text{ GeV}}{0.1 M_J^{\text{sublead}}}\right)^2} \quad (7.2)$$

²³¹⁷ The mass values in the X_{hh} formula are optimized to maximize signal efficiency. The sub-leading jet
²³¹⁸ typically has a lower mass due to semi-leptonic b decays and final state radiation. X_{hh} effectively acts as
²³¹⁹ a χ^2 measurement of the consistency of the two Higgs candidate masses with the signal hypothesis. The
²³²⁰ denominators of each term ($0.1 M$) give the uncertainty on the mass measurement for the large radius
²³²¹ jets. Events are required to satisfy $X_{hh} < 1.6$.

²³²² The last requirement applied is on the number of b -tagged track jets. There are two signal regions de-

fined. The first requires exactly four b -tagged track jets, two in each Higgs candidate (known as the 4 signal region). At high resonance masses, this requirement is inefficient, so an additional signal region requiring only three b -tagged track jets is also defined (known as the 3 b signal region). While this has a larger background it is also more efficient for high resonance masses. For both signal regions, threshold on MV2 score is chosen such that the algorithm is 77% efficiency in finding true b -jets[§]. Different working points were tested and this was found to be optimal. Appendix A has more details on this optimization.

Before making the requirement on X_{hh} , the masses of the Higgs candidates are corrected for semi-leptonic b decays using muons with the criteria outlined in the previous section. Any muons within a $\Delta R < 0.2$ of a b -tagged track jet have their four-momenta added to the four-momentum of the Higgs candidate. This correction does not affect the pre-selection requirements but does affect the X_{hh} requirement and the final invariant mass distribution used.

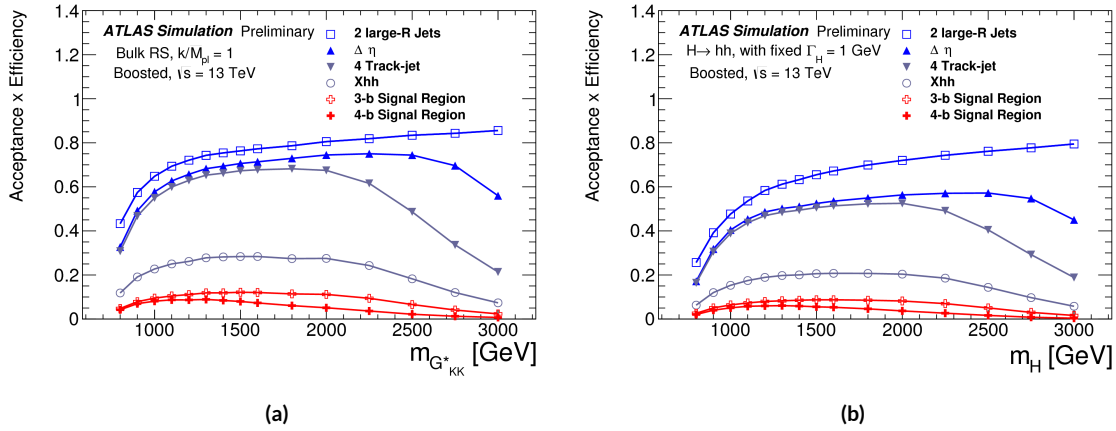


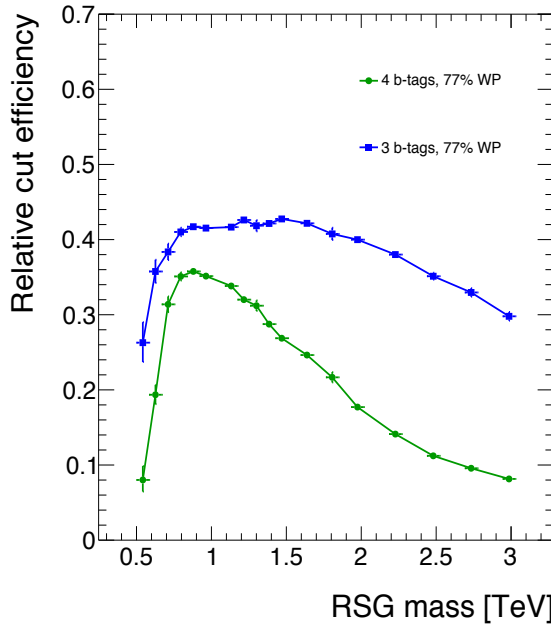
Figure 7.8: Acceptance \times efficiency as a function of mass for (a) RSG and (b) narrow heavy scalar signal models [28].

Figure 7.8 shows the product of acceptance and efficiency as a function of mass for both the RSG and narrow heavy scalar resonance signal models. After $m_X > 1$ TeV, the efficiency of the 4 b requirement begins to decline. After $m_X > 2$ TeV, the efficiency of requiring two track jets in each Higgs candidate begins to decline as well. Both of these behaviors illustrate the difficulty of resolving the merged decay

[§]The specific MV2 algorithm chosen is MV2c20, where the fraction of charm events used in the training is 20%

2339 products at high mass. More details on the degradation of the b -tagging efficiency at high masses are
2340 shown in appendix B.

2341 Figure 7.9 shows a more detailed comparison of the signal efficiency in the $3b$ vs $4b$ signal regions for
2342 the RSG model. The efficiencies shown here are relative to all prior selection requirements.



2343 **Figure 7.9:** Efficiency of requiring 3 or 4 b -tagged track jets vs. RSG mass. The efficiency quoted is relative to the previous
2344 selection requirements (rather than an absolute efficiency).

2345 The final discriminating variable used in the boosted analysis is M_{2J} , the invariant mass of the two
2346 Higgs candidates. In order to improve the mass resolution, the four-momenta of each Higgs candidate
2347 are scaled by m_h/M_J . The effect of this correction is small in the boosted analysis but is done for consis-
2348 tency with the resolved selection.

2349 Table 7.2 shows the effect of the selection requirements on signal and background simulations as well
2350 as data.

2349 7.6 DATA-DRIVEN BACKGROUND ESTIMATION

2350 The largest background to this final state is QCD multijet production, constituting 80-90% of the total
2351 background. Because of the difficulties in modeling higher order QCD processes, this background is

Selection	Data	$m_{G_{KK}^*} = 1\text{TeV}$	$m_{G_{KK}^*} = 2\text{TeV}$	$t\bar{t}$	$Z+\text{jets}$
N(fiducial large-R jets) ≥ 2	2202396	23.3	0.48	32345.2	4255.7
leading large-R jet $p_T > 350\text{ GeV}$	1873741	22.9	0.48	26511.7	3649.9
Both large-R jet $m > 50\text{ GeV}$	1854625	21.2	0.47	24369.8	3575.8
Both large-R jet $p_T < 1500\text{ GeV}$	1853601	21.2	0.46	24346.5	3572.9
$ \Delta\eta(JJ) < 1.7$	1435273	20.8	0.44	20751.0	3265.8
≥ 2 track-jets per large-R jet	1224727	19.8	0.40	18234.5	2692.6
$3 b\text{-tags}, X_{hh} < 1.6$	316	3.4	0.067	46.7	2.0
$4 b\text{-tags}, X_{hh} < 1.6$	20	2.9	0.030	1.4	0.0

Table 7.2: Effect of boosted selection on data, RSG signal models, $t\bar{t}$, and $Z+\text{jets}$. The numbers from simulation are normalized with the MC generator cross section and do not take into account the data driven estimates described in section 7.6 [33].

estimated with a fully data-driven method. The only other non-negligible background is $t\bar{t}$, constituting the other 10-20%. Due to the presence of $t\bar{t}$ in the sideband region where the QCD background will be estimated, the normalization of the QCD and $t\bar{t}$ backgrounds are simultaneously estimated.

7.6.1 MASS REGION DEFINITIONS

The first step in the data-driven background estimate is to define a sideband mass region where the background normalization can be derived. Additionally, a control region is defined where the background estimate can be validated. The control (CR) and sideband (SB) regions are defined using a radial distance in the two-dimensional large-R jet mass plane, R_{hh} , which is defined in equation 7.3.

$$R_{hh} = \sqrt{(M_J^{\text{lead}} - 124\text{ GeV})^2 + (M_J^{\text{sublead}} - 115\text{ GeV})^2} \quad (7.3)$$

Events in the sideband region are required to fail the signal region $X_{hh} < 1.6$ requirement and have $R_{hh} > 35.8\text{ GeV}$. The control region consists of those events which are not in the signal or sideband regions. Figure 7.10 shows the definition of the signal, control, and sideband mass regions.

Table 7.3 summarizes the mass region selections for the three different regions used in the analysis.

*The $Z+\text{jets}$ background is a sub-percent level contribution

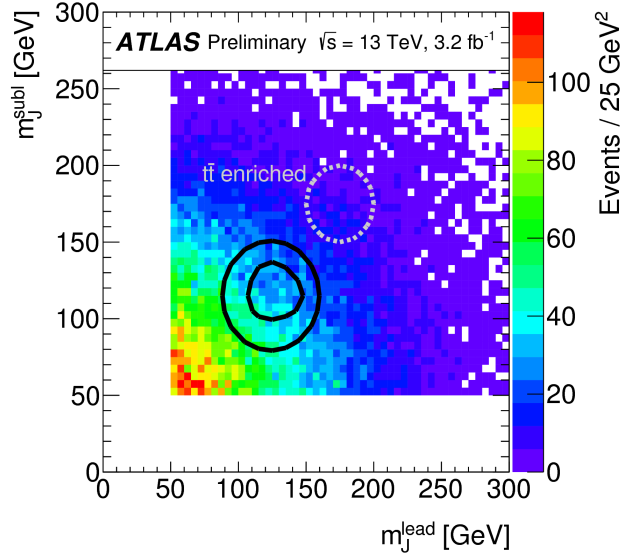


Figure 7.10: M_J^{sublead} vs. M_J^{lead} in a 2 b -tag data sample. The signal region is defined by the inner black contour ($X_{hh} < 1.6$) and the sideband region is defined by the outer contour ($R_{hh} > 35.8 \text{ GeV}$). The region between the black contours is the control region. The mass region which is enriched in $t\bar{t}$ background is also shown for illustration. [28]

Region	Requirement	Notes
Signal Region (SR)	$X_{hh} < 1.6$	-
Control Region (CR)	$R_{hh} < 35.8 \text{ GeV}$ and $X_{hh} > 1.6$	Used for validation of background estimates
Sideband Region (SB)	$R_{hh} > 35.8 \text{ GeV}$	Used to derive background normalization

Table 7.3: Mass region definitions used for background estimation

2364 7.6.2 BACKGROUND ESTIMATION

2365 The method for estimating the background in this analysis is similar to the ABCD method presented in
 2366 Chapter 5. In this case, the two handles used to define different regions for the estimate are the number
 2367 of b -tagged track jets and the mass regions. A region requiring exactly two b -tagged track jets in one large-
 2368 R jet (referred to as the 2-tag or 2 b region) is defined for use in the background estimate. The number of
 2369 expected background events in the 3 b and 4 b signal regions is then given by equation 7.4.

$$N_{\text{bkg}}^{3(4)-\text{tag},\text{SR}} = \mu_{\text{Multijet}} N_{\text{Multijet}}^{2-\text{tag},\text{SR}} + \beta_{t\bar{t}} N_{t\bar{t}}^{3(4)-\text{tag},\text{SR}} + N_{Z+\text{jets}}^{3(4)-\text{tag},\text{SR}} \quad (7.4)$$

2370 In this equation, $N_{\text{bkg}}^{3(4)\text{-tag}}$ is the expected number of background events in the $3b$ or $4b$ signal re-
 2371 gions. $N_{\text{Multijet}}^{2\text{-tag}}$ is the number of multijet events in the 2-tag region. $N_{t\bar{t}}^{3(4)\text{-tag}}$ is the number of $t\bar{t}$
 2372 events predicted in the MC for the $3b$ or $4b$ signal region, and the variable is similarly defined for the
 2373 $Z+\text{jets}$ background. The $\beta_{t\bar{t}}$ parameter is a scale factor used to correct the normalization of the $t\bar{t}$ esti-
 2374 mate in the signal region. μ_{Multijet} is an extrapolation factor that is derived in the sideband region and
 2375 used to estimate the ratio of 2-tag events to 3(4)-tag events in the signal region. It is defined in equa-
 2376 tion 7.5.

$$\mu_{\text{Multijet}} = \frac{N_{\text{Multijet}}^{3(4)\text{-tag,SB}}}{N_{\text{Multijet}}^{2\text{-tag,SB}}} = \frac{N_{\text{data}}^{3(4)\text{-tag,SB}} - \beta_{t\bar{t}} N_{t\bar{t}}^{3(4)\text{-tag,SB}} - N_{Z+\text{jets}}^{3(4)\text{-tag,SB}}}{N_{\text{data}}^{2\text{-tag,SB}} - \beta_{t\bar{t}} N_{t\bar{t}}^{2\text{-tag,SB}} - N_{Z+\text{jets}}^{2\text{-tag,SB}}} \quad (7.5)$$

2377 The $t\bar{t}$ scale factor ($\beta_{t\bar{t}}$) and the QCD multijet extrapolation factor (μ_{Multijet}) are estimated together
 2378 in a simultaneous fit in the sideband region. Then, the number of events in the 2-tag signal region is
 2379 used, along with the $t\bar{t}$ estimate in the $3b$ and $4b$ signal regions and μ_{Multijet} , to estimate the total num-
 2380 ber of background events in the two final signal regions. The shape of the final discriminant M_{2J} is also
 2381 taken from the 2-tag signal region where there are more statistics. This method is illustrated graphically
 2382 in figure 7.11.

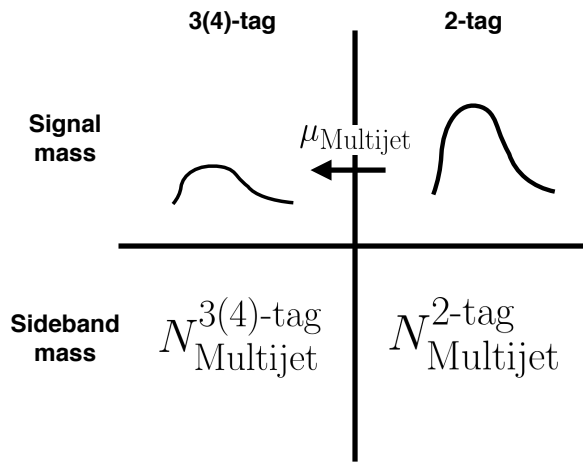


Figure 7.11: An illustration of the data-driven background estimation technique for the boosted analysis

2383 In the $3b$ region, the fit yields values of $\mu_{\text{Multijet}} = 0.160 \pm 0.03$ and $\beta_{t\bar{t}} = 1.02 \pm 0.09$. In the $4b$

region, the fit gives $\mu_{\text{Multijet}} = 0.0091 \pm 0.0007$ and $\beta_{t\bar{t}} = 0.82 \pm 0.39$. The uncertainties quoted are statistical only. The larger uncertainties in the $4b$ values indicate the lower statistics available in that region.

Figure 7.12 shows the distributions of data and background estimates in the $3b$ and $4b$ sideband regions after the background fit has been done. The normalizations are constrained from the fit to match that of the data, but good modeling of the shape of the mass of the leading large-R jet is seen as well. The shapes of the kinematic distributions in the $4b$ region are taken from the $3b$ region due to the better MC statistics in that region.

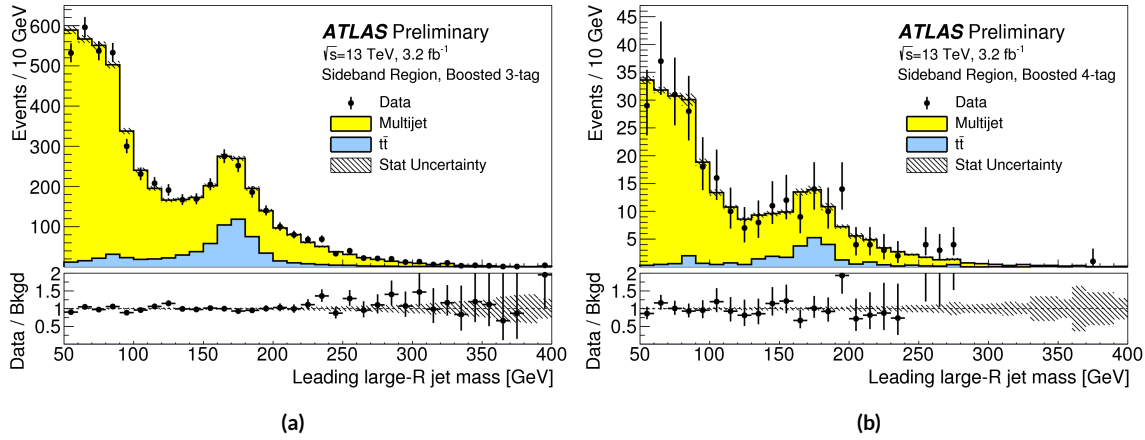


Figure 7.12: Leading large-R jet mass in the $3b$ (a) and $4b$ (b) sideband regions. The multijet and $t\bar{t}$ backgrounds are estimated using the data-driven methods described above. Because their normalizations are derived in the sideband region, the total background normalization is constrained by default to match the normalization of the data [28].

7.6.3 BACKGROUND SHAPE FIT

As mentioned in the previous section, the background shape in the 3-tag and 4-tag signal regions is taken from the 2-tag signal mass region. Due to the limited statistics available, the background shapes are additionally smoothed after being extrapolated to the 3-tag and 4-tag signal regions. Only the data in the range $900 < M_{2J} < 2000$ GeV is included in the fit due to the limited statistics available above 2 TeV. Both the $t\bar{t}$ and QCD multijet background are independently fit with an exponential shape, $y = e^{ax+b}$. Other shapes are considered and used for the systematic uncertainties. Table 7.4 shows the fit values for

the parameters. Because both the $3b$ and $4b$ QCD shapes come from the 2-tag region, the slopes derived are very similar.

	a	b
QCD ($4b$)	0.00545 ± 0.00021	5.44 ± 0.24
$t\bar{t}$ ($4b$)	0.00746 ± 0.00021	4.88 ± 0.36
QCD ($3b$)	0.00545 ± 0.00021	8.30 ± 0.24
$t\bar{t}$ ($3b$)	0.00746 ± 0.00021	8.58 ± 0.36

Table 7.4: Parameters derived for exponential fit to background M_{2J} shape in the $3b$ and $4b$ signal regions [33]

7.6.4 VALIDATION OF BACKGROUND ESTIMATE

The background estimate can be validated by using the method to estimate the number of events in the control mass region rather than the signal mass region. Figure 7.13 shows the M_{2J} distribution in the $3b$ and $4b$ control regions, comparing data and background estimates. In both cases, both the background shape and normalization are consistent with the data, indicating good agreement. The ratio of data to the background estimates is also fit to a line in the figure to test for any shape difference. The slope of the line is within 1σ (from the fit uncertainties) of flat, further indicating that the data is consistent with the background estimate in the control region.

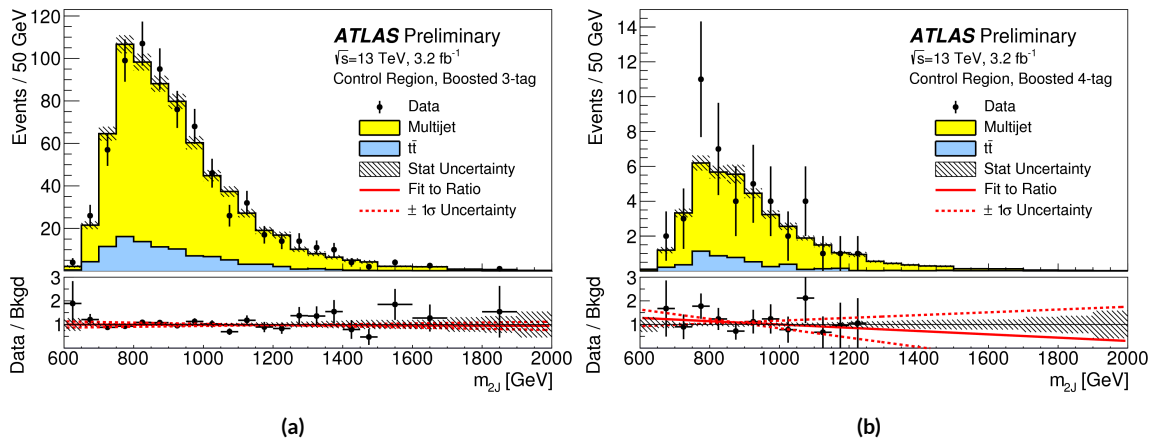


Figure 7.13: Di-jet invariant mass (M_{2J}) in the $3b$ (a) and $4b$ (b) control regions. The multijet and $t\bar{t}$ backgrounds are estimated using the data-driven methods described above [28].

Table 7.5 shows the yields in data and background estimates in the 3-tag and 4-tag sideband and con-

2410 trol regions. Again, here, it can be seen that the total number of predicted background events from the
2411 data driven method is consistent with the number of data events in the region.

Sample (3-tag)	Sideband Region	Control Region
Multijet	4328 ± 27	607 ± 10
$t\bar{t}$	683.5 ± 8.1	99.6 ± 3.1
$Z+jets$	31.8 ± 3.7	7.7 ± 1.8
Total	5043 ± 28	715 ± 11
Data	5043	724
Sample (4-tag)	Sideband Region	Control Region
Multijet	247.4 ± 1.5	34.7 ± 0.6
$t\bar{t}$	28.4 ± 1.5	5.1 ± 0.7
$Z+jets$	3.4 ± 1.2	0.6 ± 0.5
Total	279.2 ± 2.5	40.3 ± 1.0
Data	279	45

Table 7.5: The number of events in data and predicted background events in the boosted 3-tag and 4-tag sideband and control regions. The uncertainties shown are statistical only.[28]

2412 7.7 SYSTEMATIC UNCERTAINTIES

2413 The systematic uncertainties in this analysis can be divided into two broad categories. The first type is
2414 uncertainties associated with the modeling of the signal processes. The second type of uncertainty is
2415 associated with both the shape and normalization of the background prediction.

2416 7.7.1 SIGNAL MODELING UNCERTAINTIES

2417 The signal modeling uncertainty has three main components: theoretical uncertainty on the acceptance,
2418 experimental uncertainties on the large-R jets, and experimental uncertainties on the track jets related to
2419 b -tagging. In this analysis the experimental uncertainties are the most significant.

2420 The first uncertainty on signal modeling is the theoretical uncertainty on the acceptance. As explained
2421 in section 5.6.1, there are four components to this uncertainty. The first is related to missing higher order
2422 terms from the matrix element calculations which is estimated by varying the QCD renormalization and

2423 factorization scales. The second is uncertainty due to the PDF set used. The third is a generator uncer-
2424 tainty which is estimated by modifying the generator used to model the underlying event and hadroniza-
2425 tion. Finally, there is an uncertainty associated with the modeling of the initial state and final state radia-
2426 tion (ISR/FSR). The total theoretical uncertainty on the signal yield is 3%, and this is dominated by the
2427 ISR/FSR modeling.

2428 There are uncertainties on the large-R jets in both the jet energy scale (JES) and jet energy resolution
2429 (JER) as well as the jet mass scale (JMS) and jet mass resolution (JMR). These are evaluated using $\sqrt{s} =$
2430 8 TeV data from Run 1 of ATLAS and extrapolated to the Run 2 beam and detector conditions using
2431 MC[¶]. The details of these uncertainties can be found in reference [104].

2432 Uncertainties on the track jets are related to the b -tagging efficiency. The total uncertainty on the sig-
2433 nal yield due to b -tagging is evaluated by propagating variations of the b -tagging efficiency through the
2434 boosted selection requirements. The uncertainties are calculated jet-by-jet and parameterized as a func-
2435 tion of b -jet p_T and η [105]. For high p_T b -jets (with $p_T > 300$ GeV), the uncertainties are extrapolated
2436 using MC simulation from the lower p_T b -jets [106].

2437 Table 7.6 shows the systematic uncertainties on the signal normalization for models with $m_{G_{KK}^*} =$
2438 1.5 TeV and both $c = 1$ and $c = 2$ as well as a narrow width heavy scalar. The dominant uncertainty
2439 comes from b -tagging and this uncertainty is larger in the 4-tag region than the 3-tag region.

2440 7.7.2 BACKGROUND UNCERTAINTIES

2441 Uncertainties on the QCD multijet background normalization and shape are estimated using the control
2442 mass region. As shown previously, the background predictions in the control region match with the
2443 data yields within the statistical uncertainty in both the 3-tag and 4-tag control regions. As an additional
2444 protection, the statistical uncertainty on the background prediction in the control region is assigned as a
2445 systematic uncertainty on the normalization of the QCD background.

2446 Additional robustness tests are done by varying the definition of the control mass region and the b -
2447 tagging requirements used to define the 2-tag sample. In all cases, the effect of the variations is found to

[¶]The uncertainties are correspondingly larger due to the uncertainty of this extrapolation.

Source	Background		G_{KK}^*	H
	$c = 1$	$c = 2$		
Luminosity	-	5.0	5.0	5.0
3-tag				
JER	< 1	< 1	< 1	< 1
JES	2	< 1	< 1	< 1
JMR	1	12	12	11
JMS	5	14	13	17
b -tagging	1	23	22	23
Theoretical	-	3	3	3
Multijet Normalization	3	-	-	-
Statistical	2	1	1	1
Total	7	31	30	33
4-tag				
JER	< 1	< 1	< 1	< 1
JES	< 1	< 1	< 1	< 1
JMR	4	12	13	13
JMS	5	13	13	14
b -tagging	2	36	36	36
Theoretical	-	3	3	3
Multijet Normalization	14	-	-	-
Statistical	3	1	1	1
Total	15	42	42	43

Table 7.6: Summary of systematic uncertainties in the total background and signal event yields (expressed in %) in the boosted 3-tag and 4-tag signal regions. Systematic uncertainties on the signal normalization are shown for models with $m_{G_{KK}^*} = 1.5$ TeV and both $c = 1$ and $c = 2$ as well as a narrow width heavy scalar.

²⁴⁴⁸ be within the statistical uncertainties on the background normalization in the control region.

²⁴⁴⁹ Shape uncertainties on the background are evaluated using two techniques. First, as shown in figure 7.13, the ratio between the data and background prediction is fit with a linear function. The uncertainties on the slope of this fit are assigned as shape uncertainties. An additional uncertainty is assigned ²⁴⁵⁰ by using alternate power law fit functions for the smoothing of the background shape. Table 7.7 shows ²⁴⁵¹ the alternate shapes used. The largest difference between the nominal fit function and the alternates, ²⁴⁵² taking into account the 1σ uncertainty band on each fit as well, is taken as a shape uncertainty. ²⁴⁵³

Functional Form
$f_1(x) = p_0(1-x)^{p_1}x^{p_2}$
$f_2(x) = p_0(1-x)^{p_1}e^{p_2 x^2}$
$f_3(x) = p_0(1-x)^{p_1}x^{p_2} x$
$f_4(x) = p_0(1-x)^{p_1}x^{p_2} \ln x$
$f_5(x) = p_0(1-x)^{p_1}(1+x)^{p_2} x$
$f_6(x) = p_0(1-x)^{p_1}(1+x)^{p_2} \ln x$
$f_7(x) = \frac{p_0}{x}(1-x)^{p_1-p_2} \ln x$
$f_8(x) = \frac{p_0}{x^2}(1-x)^{p_1-p_2} \ln x$

Table 7.7: Alternate fit functions used to model the M_{JJ} distribution in the QCD multijet background. In the equations, $x = M_{JJ}/\sqrt{s}$.

2455 The uncertainties on the $t\bar{t}$ background are obtained by propagating the various experimental varia-
 2456 tions (JES, JER, JMS, JMR, b -tagging) through the analysis selection requirements. Table 7.6 summarizes
 2457 the background uncertainties in the 3-tag and 4-tag regions.

2458 7.8 RESULTS

2459 Table 7.8 shows the observed yields in the 3-tag and 4-tag signal regions for the boosted analysis com-
 2460 pared to the predicted number of background events. In the 3-tag region, 316 events are observed with
 2461 a predicted background of 285 ± 19 . In the 4-tag region, 20 events are observed with a predicted back-
 2462 ground of 14.6 ± 2.4 . Figure 7.14 shows the M_{JJ} distribution in the 3-tag and 4-tag regions. There are
 2463 some small excesses in the data, in particular in the 3-tag region around $M_{JJ} \approx 900$ GeV and in the
 2464 region of $1.6 < M_{JJ} < 2.0$ TeV. The significance of these excesses will be evaluated in the next chapter
 2465 in the statistical combination with the resolved results.

Sample	Signal Region (3-tag)	Signal Region (4-tag)
Multijet	235 ± 14	13.5 ± 2.4
$t\bar{t}$	48 ± 22	1.2 ± 1.0
$Z+jets$	2.0 ± 2.2	-
Total	285 ± 19	14.6 ± 2.4
Data	316	20
$G_{KK}^*(1000 \text{ GeV}), c = 1$	3.4 ± 0.9	2.9 ± 1.1

Table 7.8: Observed yields in the 3-tag and 4-tag signal regions for the boosted analysis compared to the predicted number of background events Errors correspond to the total uncertainties in the predicted event yields. The yields for a graviton with $m_{G_{KK}^*} = 1 \text{ TeV}$ and $c = 1$ are also shown. [28]

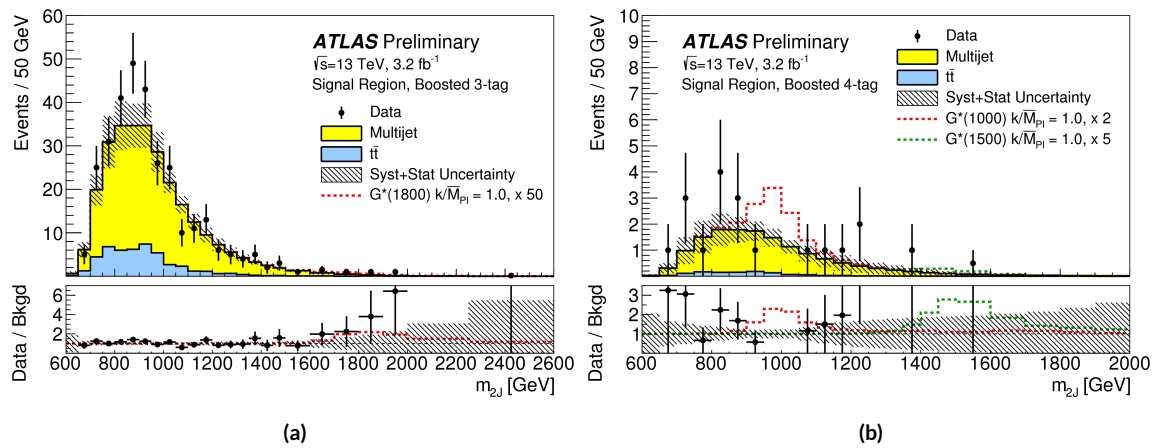


Figure 7.14: Di-jet invariant mass (M_{2J}) in the $3b$ (a) and $4b$ (b) signal regions. The multijet and $t\bar{t}$ backgrounds are estimated using the data-driven methods described above. In the $3b$ region, a graviton signal with $m_{G_{KK}^*} = 1.8 \text{ TeV}$ and $c = 1$ is overlaid, with the cross section multiplied by a factor of 50 so that the signal is visible. In the $4b$ region, signals with $m_{G_{KK}^*} = 1.0 \text{ TeV}$ and $m_{G_{KK}^*} = 1.5 \text{ TeV}$ are overlaid, both with $c = 1$ and the yields multiplied by factors of 2 and 5 respectively [28].

This is a really enlightening quote.

Tomo Lazovich

8

2466

2467

Combined limits from boosted and resolved searches

2468

2469 8.1 INTRODUCTION

2470 In order to cover the full mass range of possible resonances decaying to di-Higgs final states, two distinct
2471 tailored selections were produced. The resolved selection is more sensitive in the mass range of $400 < m_X < 1100$ GeV while the boosted selection is more sensitive to masses in the range $1100 < m_X <$
2472 3000 GeV. Chapter 7 presents the details of the boosted selection and results. In setting limits on spin-2
2473 Randall-Sundrum graviton (RSG) and narrow width heavy scalar (H) models, the results of the boosted
2474 selection are combined with the results of the resolved selection to cover the full mass range.
2475

2476 This chapter presents limits on signal models resulting from the $X \rightarrow HH \rightarrow b\bar{b}b\bar{b}$ search in both
2477 the resolved and boosted selections. It first presents a brief overview of the resolved results that go into

2478 the limit setting. Then, an overview of the statistical methods used for the search and limit setting is
2479 given. Finally, limits on the RSG and heavy scalar models are presented.

2480 **8.2 RESOLVED RESULTS**

2481 The details of the resolved selection will not be presented here and can be found in reference [28]. In
2482 basic terms, the selection searches for four $R = 0.4$ b-tagged calorimeter jets (where each pair of jets is
2483 one Higgs candidate). This is distinct from the boosted methodology which searches for merged decay
2484 products. The backgrounds to the resolved selection are the same as those presented in Chapter 7 for the
2485 boosted analysis.

2486 Table 8.1 shows the results for data yields and expected background in the resolved signal region. Fig-
2487 ure 8.1 shows the M_{2J} distribution in the resolved signal region. The total number of events is consis-
2488 tent with the prediction and no significant excess is seen. One event in the boosted 4-tag signal is shared
2489 with the resolved signal region and has a mass of 852 GeV.

Sample	Signal Region Yield
Multijet	43.3 ± 2.3
$t\bar{t}$	4.3 ± 3.0
$Z + \text{jets}$	-
Total	47.6 ± 3.8
Data	46
SM hh	0.25 ± 0.07
$G_{\text{KK}}^*(800 \text{ GeV}), c = 1$	5.7 ± 1.5

Table 8.1: Observed yields in the resolve selection 4-tag signal region compared to the predicted number of background events Errors correspond to the total uncertainties in the predicted event yields. The yields for a graviton with $m_{G_{\text{KK}}^*} = 800 \text{ GeV}$ and $c = 1$ are also shown. [28]

2490 **8.3 SEARCH TECHNIQUE AND RESULTS**

2491 The statistical technique used for the search in this analysis is the same as that used in the $H \rightarrow WW^*$
2492 analysis presented in section 3.6.2. The test statistic q_0 is used to define the p -values which measure the

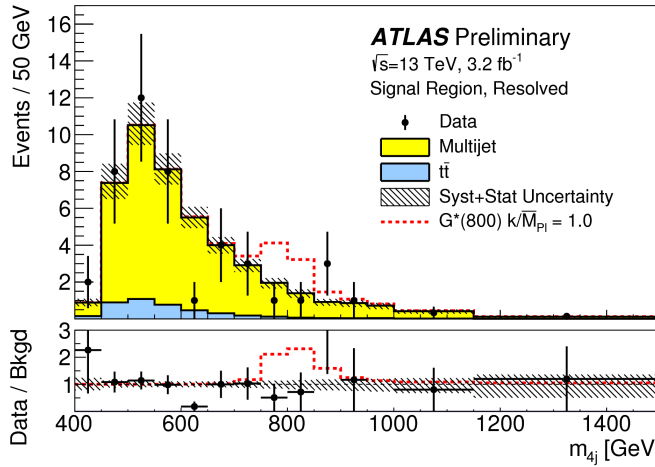


Figure 8.1: Di-jet invariant mass (M_{2J}) in the resolved signal region. Agraviton signal with $m_{G^*_\text{KK}} = 800 \text{ GeV}$ and $c = 1$ is overlaid. [28].

compatibility of the data with the background-only hypothesis corresponding to a signal strength $\mu = 0$.

Local p_0 values are computed to quantify the probability that the background could produce a fluctuation greater than or equal to the one observed in the data. In the resolved analysis, no significant excesses are observed. The largest discrepancy with respect to the background only hypothesis occurs near a resonance mass of 900 GeV and is found to be less than 2σ in significance.

In the boosted selection, the largest local excess is a broad excess in the $3b$ signal region that begins near $M_{2J} \approx 1.7 \text{ GeV}$. Assuming a G^*_KK with this mass and $c = 1.0$, the local significance of this excess is 2.0σ .

8.4 LIMIT SETTING

In the absence of any significant excess observed in the data, limits on different signal models can be set. This section describes the limit setting procedure and presents combined results of the resolved and boosted analyses.

2506 8.4.1 LIMIT SETTING PROCEDURE

2507 The procedure used for setting exclusion limits in this analysis is the CL_s method [107]. The first step in
 2508 setting the limits is to define a test statistic which will be used. For limit setting, the test statistic is shown
 2509 in equation 8.1.

$$\tilde{q}_\mu = \begin{cases} -2 \ln \frac{L(\mu, \hat{\theta}(\mu))}{L(0, \hat{\theta}(0))} & \hat{\mu} < 0 \\ -2 \ln \frac{L(\mu, \hat{\theta}(\mu))}{L(\hat{\mu}, \hat{\theta})} & 0 \leq \hat{\mu} < \mu \\ 0 & \hat{\mu} > \mu \end{cases} \quad (8.1)$$

2510 In the above equation, μ is the value of the signal strength under test, $\hat{\mu}$ is the best fit μ , $\hat{\theta}$ is the
 2511 best fit value of the nuisance parameters, $\hat{\theta}$ is the best fit value of the nuisance parameters under the fixed
 2512 μ value, and L is the Poisson likelihood of the data (as described in section 3.6.2).

2513 The test statistic \tilde{q}_μ is constructed to protect against two interesting corner cases when setting the
 2514 upper limit on the cross section. First, it protects against negative signal strengths μ which are unphys-
 2515 ical. Second, it does not count excesses in the data larger than those expected by a signal strength μ as
 2516 evidence against the μ hypothesis.

2517 The CL_s statistic is constructed by taking a ratio of two probabilities. CL_{s+b} is the probability that
 2518 the signal+background hypothesis would produce a value of the test statistic that is less than or equal
 2519 to the observed value*. CL_b is the probability that the background only hypothesis will pro-
 2520 duce a value of the test statistics less than or equal to the observed. The CL_s statistic is then the ratio
 2521 $\text{CL}_{s+b}/\text{CL}_b$. A 95% upper limit on the cross section is set at the value of μ that makes the CL_s statistic
 2522 less than 5%.

2523 In practice, the limits are computed numerically within an asymptotic approximation for the distri-
 2524 bution of the test statistic \tilde{q}_μ . The details of this approximation can be found in reference [70].

2525 The resolved and boosted analyses are combined using a very simple procedure rather than a full sta-
 2526 tistical combination. For each mass point tested, the limit which gives the most stringent constraint is

*Lower values of \tilde{q}_μ mean better compatibility

used. This means that for mass points below 1.1 TeV the resolved signal region is used, while at and above this point the combination of the orthogonal $3b$ and $4b$ boosted signal regions is used.

8.4.2 LIMIT SETTING RESULTS

Figure 8.2 shows the combined 95% upper bounds as a function of mass for three different models: G_{KK}^* with $c = 1$, G_{KK}^* with $c = 2$, and a narrow heavy scalar H .

The cross section of $\sigma(pp \rightarrow G_{\text{KK}}^* \rightarrow hh \rightarrow b\bar{b}b\bar{b})$ with $c = 1$ is constrained to be less than 70 fb for masses in the range $600 < m_{G_{\text{KK}}^*} < 3000$ GeV. For the RSG model with $c = 2$, cross sections limits between 40 fb and 200 fb are set for the mass range of $500 < m_{G_{\text{KK}}^*} < 3000$ GeV. Masses in the range of $475 < m_{G_{\text{KK}}^*} < 785$ GeV are excluded with $c = 1$ (with an exclusion of the range 465 to 745 GeV expected). Masses less than 980 GeV are excluded with $c = 2$ (with an exclusion for masses less than 1 TeV expected).

In the heavy Higgs model, the cross section upper limits for $\sigma(pp \rightarrow H \rightarrow hh \rightarrow b\bar{b}b\bar{b})$ ranges from 30 to 300 fb in the mass range of $500 < m_H < 3000$ GeV.

The resolved analysis can also set an upper limit on the Standard Model di-Higgs production cross section discussed in chapter 3. The upper limit on $\sigma(pp \rightarrow hh \rightarrow b\bar{b}b\bar{b})$ in the Standard Model is constrained to be less than 1.22 pb.

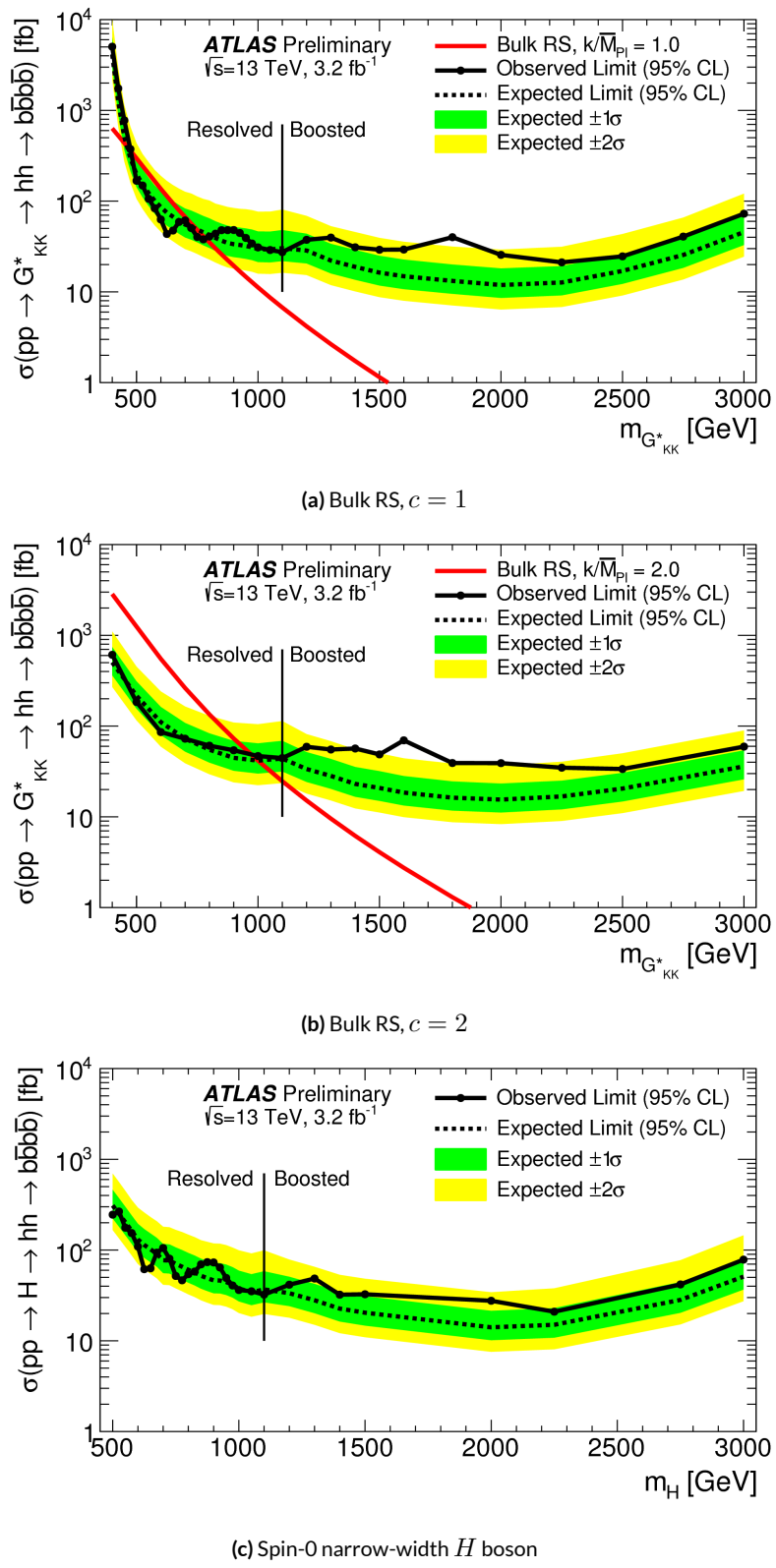


Figure 8.2: Expected and observed upper limit as a function of mass for G^*_{KK} in the RSG model with (a) $c = 1$ and (b) $c = 2$, as well as (c) H with fixed $\Gamma_H = 1$ GeV, at the 95% confidence level in the CL_s method. [28]

2543

Part IV

2544

Looking ahead

9

2545

2546

Conclusion

2547 This dissertation presented two distinct studies: the observation and measurement of the Higgs boson
2548 in the $H \rightarrow WW^* \rightarrow \ell\nu\ell\nu$ channel at $\sqrt{s} = 7$ TeV and $\sqrt{s} = 8$ TeV and a search for Higgs pair
2549 production in the $HH \rightarrow b\bar{b}b\bar{b}$ channel at $\sqrt{s} = 13$ TeV with the ATLAS detector in pp collisions at
2550 the Large Hadron Collider.

2551 In the $H \rightarrow WW^* \rightarrow \ell\nu\ell\nu$, results from both the discovery of the Higgs boson and the full
2552 ATLAS Run 1 dataset were presented. With the full 20.3 fb^{-1} at $\sqrt{s} = 8$ TeV and 4.2 fb^{-1} at $\sqrt{s} =$
2553 7 TeV, ATLAS achieved discovery level significance in the $H \rightarrow WW^*$ channel alone and obtained
2554 the first observation of vector boson fusion production in that channel. The combined signal strength
2555 is measured to be $\mu = 1.09^{+0.23}_{-0.21}$. The total observed significance of the $H \rightarrow WW^*$ process is ob-
2556 served to be 6.1σ (with 5.8σ expected). Advanced methods for background reduction and estimation,
2557 particularly in same-flavor lepton final states, are shown. The VBF signal strength is measured to be
2558 $\mu_{\text{VBF}} = 1.27^{+0.53}_{-0.45}$ with an observed significance of 3.2σ (with 2.7σ expected).

These results required many novel innovations. The increase of pileup interactions in the higher instantaneous luminosity LHC conditions of 2012 led to a degradation of missing transverse momentum resolution. As a result, the prominent Z/γ^* +jets background of the same flavor $H \rightarrow WW^* \rightarrow \ell\nu\ell\nu$ final states increased greatly. New variables, including a track-based missing transverse momentum and a measurement of the balance between the dilepton system and recoiling jets, allowed for significant reduction of this background. In the VBF channel, selections were optimized to exploit the unique VBF final state topology. Incorporating these variables into a boosted decision tree technique allowed the analysis to exceed the 3σ observation threshold.

At $\sqrt{s} = 13$ TeV, a search for Higgs pair production in the $b\bar{b}b\bar{b}$ final state with 3.2 fb^{-1} was conducted. A signal region optimized for the boosted final states arising from high mass resonances was constructed. This signal region utilized large-radius calorimeter jets and b -tagging with small radius track jets to maximize the signal acceptance. No significant excesses were observed, and upper limits on cross sections are placed for spin-2 Randall Sundrum gravitons (RSG) and narrow spin-0 resonances. The cross section of $\sigma(pp \rightarrow G_{\text{KK}}^* \rightarrow hh \rightarrow b\bar{b}b\bar{b})$ with $k/\bar{M}_{\text{Pl}} = 1$ is constrained to be less than 70 fb for masses in the range $600 < m_{G_{\text{KK}}^*} < 3000 \text{ GeV}$. For the RSG model with $k/\bar{M}_{\text{Pl}} = 2$, cross sections limits between 40 fb and 200 fb are set for the mass range of $500 < m_{G_{\text{KK}}^*} < 3000 \text{ GeV}$. The cross section upper limits for $\sigma(pp \rightarrow H \rightarrow hh \rightarrow b\bar{b}b\bar{b})$ ranges from 30 to 300 fb in the mass range of $500 < m_H < 3000 \text{ GeV}$.

A

2577

2578

Optimization of b -tagging working point in

2579

$X \rightarrow HH \rightarrow b\bar{b}b\bar{b}$ search

2580 To the $3b$ and $4b$ signal regions in the boosted $X \rightarrow HH \rightarrow b\bar{b}b\bar{b}$ search, the MV₂ algorithm with a
2581 20% fraction of charm events in training is used (MV_{2c20}). Once the algorith is selected, an efficiency
2582 working point must also be chosen. This working point defines the efficiency with which true b -jets
2583 are tagged and also fixes the overall background rejection of the algorithm. Higher efficiency working
2584 points accept more true b -jets but also allow for more background. Five different working points (70%,
2585 77%, 80%, 85%, 90%) are tested. With each working point, the full data driven background estimation
2586 method is run to quantify the amount of background that will be present in the final signal region. The
2587 significance is quantified using the median discovery significance for signal and background with Poisson

2588 errors, given in equation A.1 [108].

$$Z = \sqrt{2 \left((s + b) \ln \left(1 + \frac{s}{b} \right) - s \right)} \quad (\text{A.1})$$

2589 Note that in the limit where s is much smaller than b , this equation reduces to the more well known

2590 s/\sqrt{b} .

2591 Figure A.1 shows the estimated significance as a function of signal mass in RSG $c = 1$ models for
 2592 the $3b$ and $4b$ signal regions. The 77% working point gives the best performance over a wide range of
 2593 masses in the $4b$ signal region. As this is the region which contributes the most to the total discovery
 2594 significance, the 77% efficiency working point is chosen for the analysis.

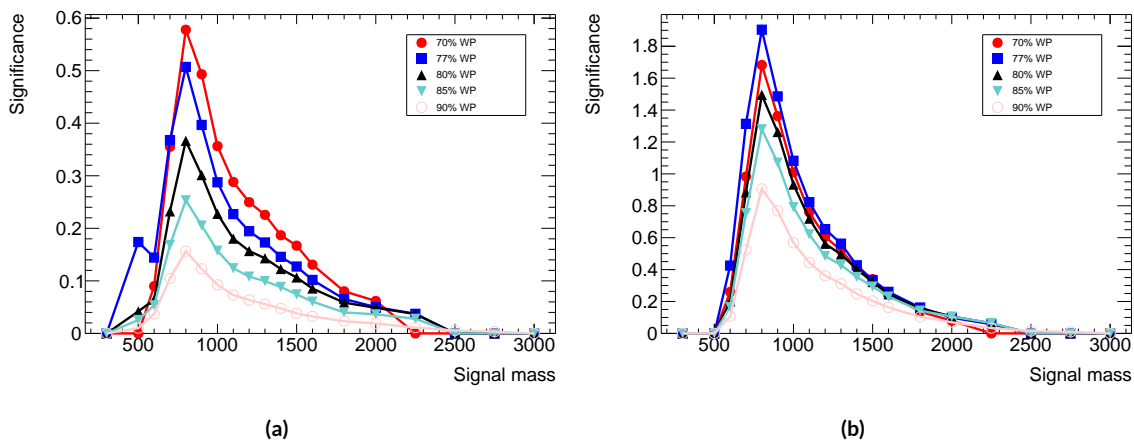


Figure A.1: Estimated significance as a function of signal mass for RSG $c = 1$ models in the $3b$ (a) and $4b$ (b) regions for different b -tagging efficiency working points

B

2595

2596

b-tagging performance at high p_T

2597 One of the limiting factors of the signal acceptance in the *FourB full* search at high resonance masses is
2598 the degradation of the *b*-tagging efficiency for high p_T jets. This appendix presents a study of the under-
2599 lying causes of this degradation.

2600 **B.1 MV2 ALGORITHM OVERVIEW**

2601 The MV2 algorithm is a boosted decision tree incorporating twenty-four input variables constructed
2602 from three lower level input algorithms: IPxD, SV1, and JetFitter. IPxD uses the two and three dimen-
2603 sional impact parameter information of tracks in the jet to construct templates for light, charm, and bot-
2604 tom quarks and compute likelihood ratios. SV1 is a secondary vertex reconstruction algorithm. JetFitter
2605 attempts to fit to the full decay chain of the B hadron, looking for multiple decay vertices aligned along a
2606 single axis. Figure B.1 summarizes the inputs to MV2.

IP2D and IP3D (6 inputs)	SV1 (8 inputs)	JetFitter (8 inputs)
$\log(p_b/p_u)$	Mass	Mass
$\log(p_b/p_c)$	Energy fraction	Energy fraction
$\log(p_c/p_u)$	# tracks at vertex	# vertices
	# 2 track vertices	# tracks at vertex
	Lxy	# 1 track vertices
	L3d	# 2 track vertices
	3D significance	3D significance
	ΔR	ΔR
Kinematics (2 inputs)		
	p_T	
	η	

Figure B.1: Summary of the inputs to the MV2 b -tagging algorithm

2607 **B.2 CHANGES IN MV2 SCORE AT HIGH p_T**

2608 The degradation of b -tagging at high p_T was studied in particular in the context of RSG models at high
 2609 mass. Figure B.2 shows the p_T of the leading track jet inside of the leading calorimeter jet in RSG events.
 2610 At high $m_{G_{KK}^*}$, the p_T spectrum of track jets is much harder than at lower masses due to the increased
 2611 Higgs p_T .

2612 Figure B.3 shows the MV2c20 algorithm score for the leading and subleading track jets inside of the
 2613 leading calorimeter jet. In both cases, it can be seen that at higher RSG masses the MV2 score shifts to-
 2614 wards more background like (negative) values. Additionally, this effect is more pronounced in the lead-
 2615 ing track jet than the subleading.

2616 To understand what is causing this change in the MV2c20 score, the same comparisons can be made
 2617 for the input variables of MV2c20. The focus in these comparisons will be on the leading track jet as
 2618 this is the one seen to have the largest difference in MV2 score. Figure B.4 shows the log likelihood ratio
 2619 $\log(p_b/p_u)$ from the IP3D (three dimensional impact parameter) algorithm. At higher masses, the IP3D
 2620 likelihood ratio distribution does become more background-like.

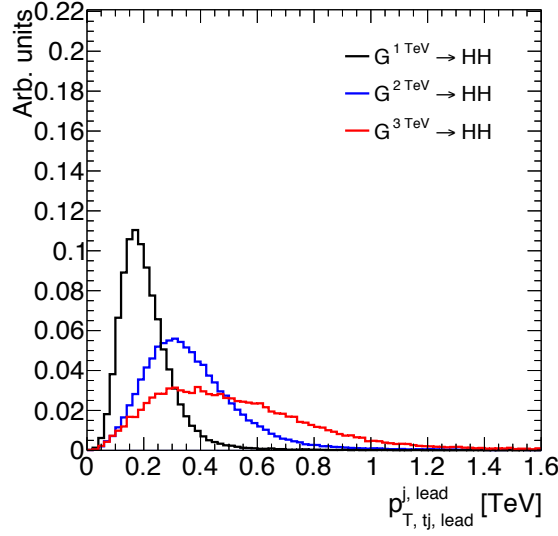


Figure B.2: p_T of the leading track jet in the leading calorimeter jet for different signal masses in RSG $c = 1$ models

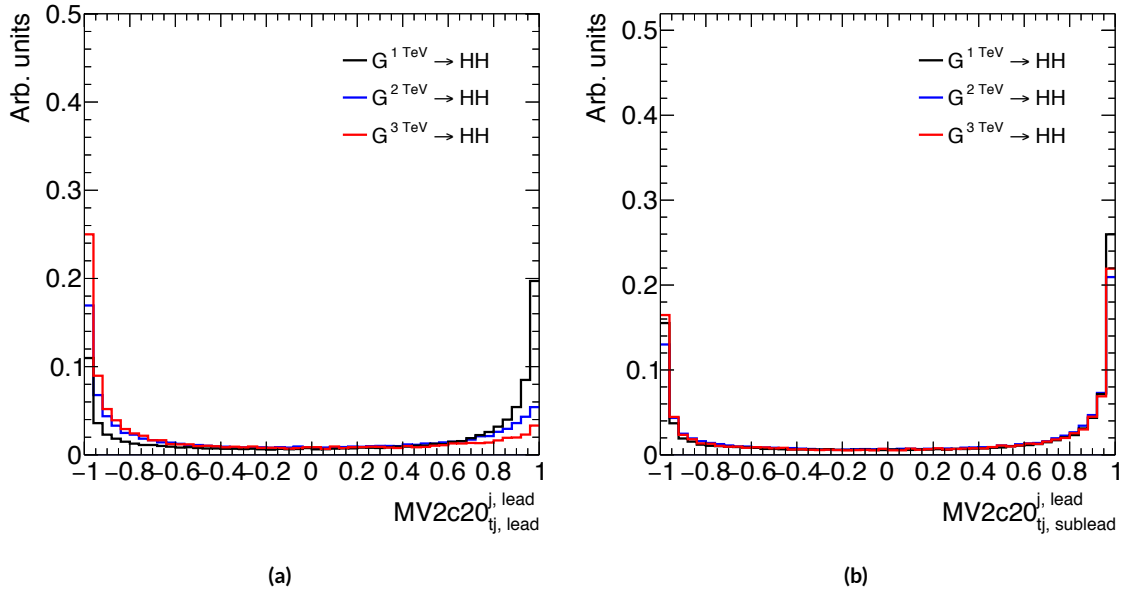


Figure B.3: MV2c20 score for the leading track jet (a) and subleading track jet (b) of the leading calorimeter jet for different signal masses in RSG $c = 1$ models

2621 Figure B.5 shows the mass and number of tracks at the secondary vertex computed by the SVI algo-
 2622 rithm. When there is no secondary vertex found, the algorithm assigns a default negative value for these
 2623 quantities. Both of these distributions show that there is a significantly larger fraction of jets where no
 2624 secondary vertex is found in the high mass samples compared to the $m_{G_{KK}^*} = 1$ TeV sample. The SVI

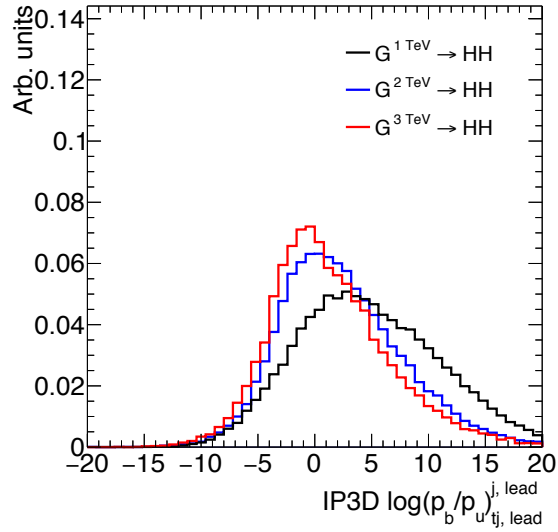


Figure B.4: IP3D log-likelihood ratio ($\log(p_b/p_u)$) of the leading track jet in the leading calorimeter jet for different signal masses in RSG $c = 1$ models

algorithm's inability to find a secondary vertex could be an important factor in the overall MV₂ score shift, as this eliminates eight of the input variables that would normally contribute information to the algorithm.

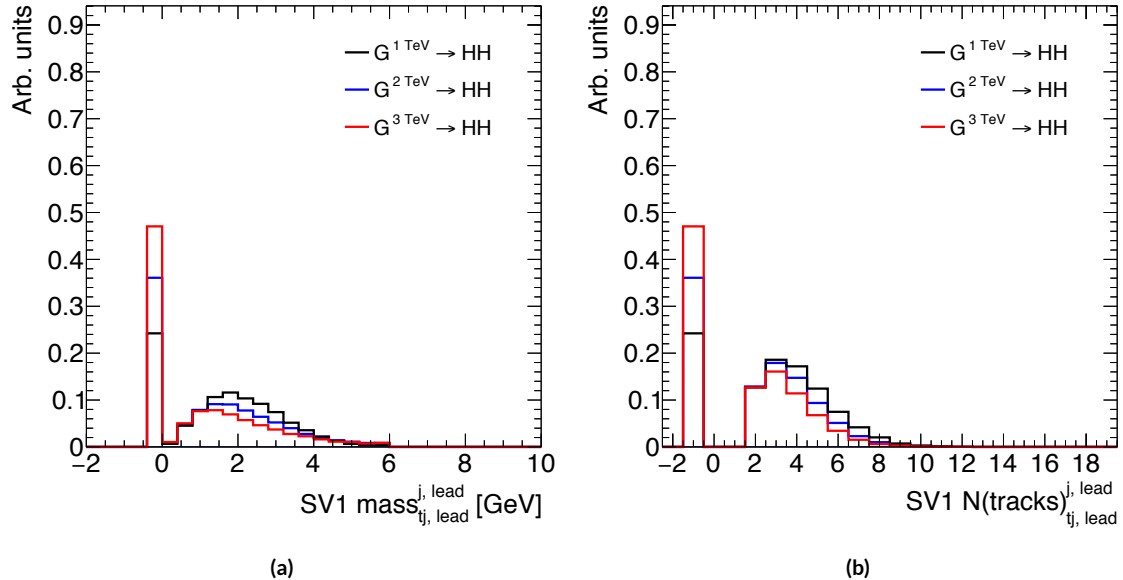


Figure B.5: Mass (a) and number of tracks (b) for the secondary vertices computed with the SV1 algorithm. When no secondary vertex is found, the quantites are assigned to default negative values.

2628 Figure B.6 shows the same quantities for the JetFitter algorithm. In this case, there is also a change in
 2629 the fraction of jets which have their secondary vertices successfully reconstructed, but this change is not
 2630 as drastic as that seen in SVI. There is also an increase in the number of jets which have high values of
 2631 mass.

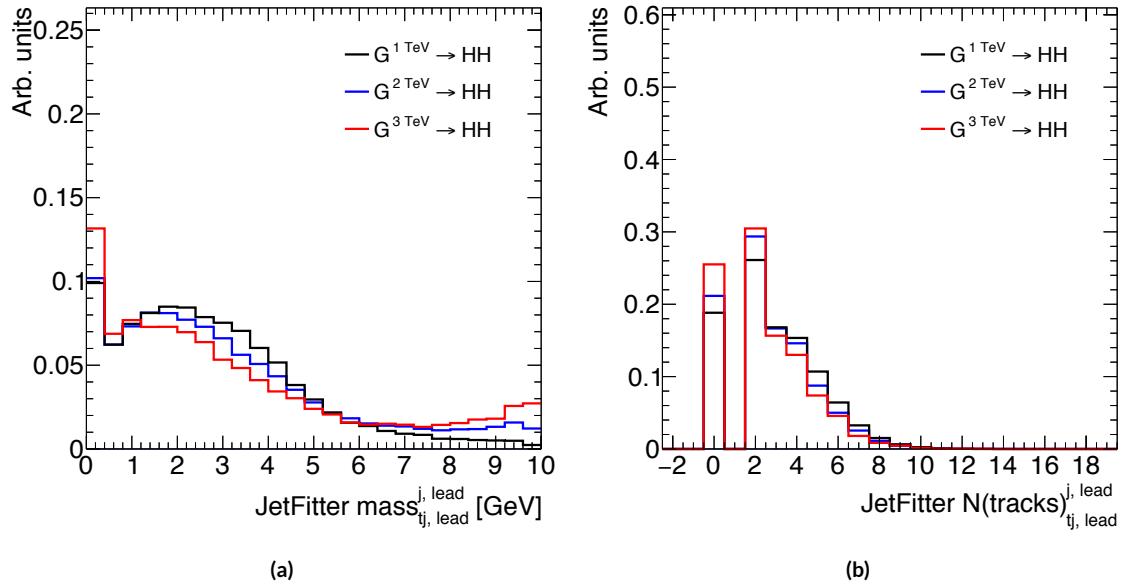


Figure B.6: Mass (a) and number of tracks (b) for vertices computed with the JetFitter algorithm. When no vertices are found, the quantities are assigned to default negative values.

References

2632

- 2633 [1] K. A. Olive et al. Review of Particle Physics. *Chin. Phys.*, C38:090001, 2014. doi: 10.1088/1674-1137/38/9/090001.
- 2635 [2] LHC Higgs Cross Section Working Group, S. Heinemeyer, C. Mariotti, G. Passarino, and R. Tanaka (Eds.). Handbook of LHC Higgs Cross Sections: 3, Higgs Properties. 2013.
- 2637 [3] Kaustubh Agashe, Hooman Davoudiasl, Gilad Perez, and Amarjit Soni. Warped Gravitons at the LHC and Beyond. *Phys. Rev.*, D76:036006, 2007. doi: 10.1103/PhysRevD.76.036006.
- 2639 [4] Johan Alwall, Michel Herquet, Fabio Maltoni, Olivier Mattelaer, and Tim Stelzer. MadGraph 5:Going Beyond. *JHEP*, 1106:128, 2011. doi: 10.1007/JHEP06(2011)128.
- 2641 [5] Howard E. Haber and Oscar Stål. New LHC benchmarks for the \mathcal{CP} -conserving two-Higgs-doublet model. *Eur. Phys. J.*, C75(10):491, 2015. doi: 10.1140/epjc/s10052-015-3697-x.
- 2643 [6] Lyndon Evans. The Large Hadron Collider. In Holstein, BR and Haxton, WC and Jawahery, A, editor, *ANNUAL REVIEW OF NUCLEAR AND PARTICLE SCIENCE, VOL 61*, volume 61 of *Annual Review of Nuclear and Particle Science*, pages 435–466. 2011. doi: {10.1146/annurev-nucl-102010-130438}.
- 2647 [7] ATLAS Collaboration. The ATLAS experiment at the CERN Large Hadron Collider. *JINST*, 3: So8003, 2008. doi: 10.1088/1748-0221/3/08/So8003.
- 2648 [8] Track Reconstruction Performance of the ATLAS Inner Detector at $\sqrt{s} = 13$ TeV. Technical Report ATL-PHYS-PUB-2015-018, CERN, Geneva, Jul 2015. URL <http://cds.cern.ch/record/2037683>.
- 2652 [9] ATLAS Collaboration. ATLAS Trigger Operations Public Results. 2015. URL <https://twiki.cern.ch/twiki/bin/view/AtlasPublic/TriggerOperationPublicResults>.
- 2654 [10] ATLAS Collaboration. ATLAS Luminosity Public Results, Run 1. 2012. URL <https://twiki.cern.ch/twiki/bin/view/AtlasPublic/LuminosityPublicResults>.
- 2656 [11] ATLAS Collaboration. ATLAS Luminosity Public Results, Run 2. 2015. URL <https://twiki.cern.ch/twiki/bin/view/AtlasPublic/LuminosityPublicResultsRun2>.

- 2658 [12] T Kawamoto, S Vlachos, L Pontecorvo, J Dubbert, G Mikenberg, P Iengo, C Dallapiccola,
2659 C Amelung, L Levinson, R Richter, and D Lellouch. New Small Wheel Technical Design Re-
2660 port. Technical Report CERN-LHCC-2013-006. ATLAS-TDR-020, CERN, Geneva, Jun 2013.
2661 URL <https://cds.cern.ch/record/1552862>. ATLAS New Small Wheel Technical Design
2662 Report.
- 2663 [13] Joao Pequenao and Paul Schaffner. An computer generated image representing how ATLAS
2664 detects particles. Jan 2013. URL <https://cds.cern.ch/record/1505342>.
- 2665 [14] Electron efficiency measurements with the ATLAS detector using the 2012 LHC proton-proton
2666 collision data. Technical Report ATLAS-CONF-2014-032, CERN, Geneva, Jun 2014. URL
2667 <https://cds.cern.ch/record/1706245>.
- 2668 [15] Georges Aad et al. Electron and photon energy calibration with the ATLAS detector using LHC
2669 Run 1 data. *Eur. Phys. J.*, C74(10):3071, 2014. doi: 10.1140/epjc/s10052-014-3071-4.
- 2670 [16] Georges Aad et al. Measurement of the muon reconstruction performance of the ATLAS detec-
2671 tor using 2011 and 2012 LHC proton–proton collision data. *Eur. Phys. J.*, C74(11):3130, 2014. doi:
2672 10.1140/epjc/s10052-014-3130-x.
- 2673 [17] Monte Carlo Calibration and Combination of In-situ Measurements of Jet Energy Scale, Jet En-
2674 ergy Resolution and Jet Mass in ATLAS. Technical Report ATLAS-CONF-2015-037, CERN,
2675 Geneva, Aug 2015. URL <http://cds.cern.ch/record/2044941>.
- 2676 [18] Georges Aad et al. Performance of *b*-Jet Identification in the ATLAS Experiment. 2015.
- 2677 [19] Expected performance of the ATLAS *b*-tagging algorithms in Run-2. Technical Report ATL-
2678 PHYS-PUB-2015-022, CERN, Geneva, Jul 2015. URL <http://cds.cern.ch/record/2037697>.
- 2679 [20] Performance of Missing Transverse Momentum Reconstruction in ATLAS studied in Proton-
2680 Proton Collisions recorded in 2012 at 8 TeV. Technical Report ATLAS-CONF-2013-082, CERN,
2681 Geneva, Aug 2013. URL <http://cds.cern.ch/record/1570993>.
- 2682 [21] ATLAS Collaboration. Observation and measurement of Higgs boson decays to WW* with the
2683 ATLAS detector. *Phys. Rev. D*, 92(012006), 2015.
- 2684 [22] Georges Aad et al. Observation of a new particle in the search for the Standard Model Higgs
2685 boson with the ATLAS detector at the LHC. *Phys. Lett.*, B716:1–29, 2012. doi: 10.1016/j.physletb.
2686 2012.08.020.
- 2687 [23] Georges Aad et al. Measurements of the Higgs boson production and decay rates and coupling
2688 strengths using pp collision data at $\sqrt{s} = 7$ and 8 TeV in the ATLAS experiment. *Eur. Phys. J.*,
2689 C76(1):6, 2016. doi: 10.1140/epjc/s10052-015-3769-y.

- 2691 [24] W.J. Stirling. 7/8 and 13/8 TeV LHC luminosity ratios. 2013. URL http://www.hep.ph.ic.ac.uk/~wstirlin/plots/lhclumi7813_2013_v0.pdf.
- 2692
- 2693 [25] J Alison. Experimental Studies of hh. Oct 2014. URL <http://cds.cern.ch/record/1952581>.
- 2694
- 2695 [26] Baojia (Tony) Tong. Private communication.
- 2696 [27] Flavor Tagging with Track Jets in Boosted Topologies with the ATLAS Detector. Technical Report ATL-PHYS-PUB-2014-013, CERN, Geneva, Aug 2014. URL <https://cds.cern.ch/record/1750681>.
- 2697
- 2698 [28] Search for pair production of Higgs bosons in the $b\bar{b}b\bar{b}$ final state using proton-proton collisions at $\sqrt{s} = 13$ TeV with the ATLAS detector. Technical Report ATLAS-CONF-2016-017, CERN, Geneva, Mar 2016. URL <https://cds.cern.ch/record/2141006>.
- 2700
- 2701
- 2702 [29] Christopher G. Tully. *Elementary particle physics in a nutshell*. 2011.
- 2703 [30]
- 2704 [31] Mike Lamont for the LHC team. The First Years of LHC Operation for Luminosity Production. International Particle Accelerator Conference, 2013. URL https://accelconf.web.cern.ch/accelconf/IPAC2013/talks/moyab101_talk.pdf.
- 2705
- 2706
- 2707 [32] Paul Collier for the LHC team. LHC Machine Status. CERN Resource Review Board, 2015.
- 2708 URL <https://cds.cern.ch/record/2063924/files/CERN-RRB-2015-119.PDF>.
- 2709
- 2710 [33] Qi Zeng. Private communication.
- 2711
- 2712 [34] Serguei Chatrchyan et al. Observation of a new boson at a mass of 125 GeV with the CMS experiment at the LHC. *Phys. Lett.*, B716:30–61, 2012. doi: 10.1016/j.physletb.2012.08.021.
- 2713
- 2714 [35] David Griffiths. *Introduction to elementary particles*. 2008.
- 2715
- 2716 [36] F. Halzen and Alan D. Martin. *QUARKS AND LEPTONS: AN INTRODUCTORY COURSE IN MODERN PARTICLE PHYSICS*. 1984. ISBN 0471887412, 9780471887416.
- 2717
- 2718 [37] Matthew D. Schwartz. *Quantum Field Theory and the Standard Model*. Cambridge University Press, 2014. ISBN 1107034736, 9781107034730. URL <http://www.cambridge.org/us/academic/subjects/physics/theoretical-physics-and-mathematical-physics/quantum-field-theory-and-standard-model>.
- 2719
- 2720 [38] S. Dawson. Introduction to electroweak symmetry breaking. In *High energy physics and cosmology. Proceedings, Summer School, Trieste, Italy, June 29-July 17, 1998*, pages 1–83, 1998. URL <http://alice.cern.ch/format/showfull?sysnb=0301862>.
- 2721

- 2722 [39] S. L. Glashow. Partial Symmetries of Weak Interactions. *Nucl. Phys.*, 22:579–588, 1961. doi:
2723 10.1016/0029-5582(61)90469-2.
- 2724 [40] Steven Weinberg. A Model of Leptons. *Phys. Rev. Lett.*, 19:1264–1266, 1967. doi: 10.1103/
2725 PhysRevLett.19.1264.
- 2726 [41] A. Salam. *Elementary Particle Theory*. Almqvist and Wiksell, Stockholm, 1968.
- 2727 [42] J. Iliopoulos S.L. Glashow and L. Maiani. D2:1285, 1970.
- 2728 [43] R. Keith Ellis, W. James Stirling, and B. R. Webber. QCD and collider physics. *Camb. Monogr.
2729 Part. Phys. Nucl. Phys. Cosmol.*, 8:1–435, 1996.
- 2730 [44] P. W. Higgs. Broken symmetries and the masses of gauge bosons. 13:508, 1964.
- 2731 [45] P. W. Higgs. Spontaneous symmetry breakdown without massless bosons. 145:1156, 1966.
- 2732 [46] F. Englert and R. Brout. Broken symmetry and the mass of gauge vector mesons. 13:321, 1964.
- 2733 [47] G. S. Guralnik, C. R. Hagen, and T. W. .B. Kibble. Global conservation laws and massless parti-
2734 cles. *Phys. Rev. Lett.*, 13:585, 1964. doi: 10.1103/PhysRevLett.13.585.
- 2735 [48] Matthew J. Dolan, Christoph Englert, and Michael Spannowsky. New Physics in LHC Higgs
2736 boson pair production. *Phys. Rev.*, D87(5):055002, 2013. doi: 10.1103/PhysRevD.87.055002.
- 2737 [49] Roberto Contino, Margherita Ghezzi, Mauro Moretti, Giuliano Panico, Fulvio Piccinini, and
2738 Andrea Wulzer. Anomalous Couplings in Double Higgs Production. *JHEP*, 08:154, 2012. doi:
2739 10.1007/JHEP08(2012)154.
- 2740 [50] R. Grober and M. Muhlleitner. Composite Higgs Boson Pair Production at the LHC. *JHEP*, 06:
2741 020, 2011. doi: 10.1007/JHEP06(2011)020.
- 2742 [51] Lisa Randall and Raman Sundrum. A Large mass hierarchy from a small extra dimension. *Phys.
2743 Rev. Lett.*, 83:3370–3373, 1999. doi: 10.1103/PhysRevLett.83.3370.
- 2744 [52] A. Liam Fitzpatrick, Jared Kaplan, Lisa Randall, and Lian-Tao Wang. Searching for the Kaluza-
2745 Klein Graviton in Bulk RS Models. *JHEP*, 09:013, 2007. doi: 10.1088/1126-6708/2007/09/013.
- 2746 [53] Julien Baglio, Otto Eberhardt, Ulrich Nierste, and Martin Wiebusch. Benchmarks for Higgs Pair
2747 Production and Heavy Higgs boson Searches in the Two-Higgs-Doublet Model of Type II. *Phys.
2748 Rev.*, D90(1):015008, 2014. doi: 10.1103/PhysRevD.90.015008.
- 2749 [54] G. C. Branco, P. M. Ferreira, L. Lavoura, M. N. Rebelo, Marc Sher, and Joao P. Silva. Theory
2750 and phenomenology of two-Higgs-doublet models. *Phys. Rept.*, 516:1–102, 2012. doi: 10.1016/j.
2751 physrep.2012.02.002.

- 2752 [55] Jose M. No and Michael Ramsey-Musolf. Probing the Higgs Portal at the LHC Through Reso-
 2753 nant di-Higgs Production. *Phys. Rev.*, D89(9):095031, 2014. doi: 10.1103/PhysRevD.89.095031.
- 2754 [56] Lyndon R Evans and Philip Bryant. LHC Machine. *J. Instrum.*, 3:S08001, 164 p, 2008. URL
 2755 <https://cds.cern.ch/record/1129806>. This report is an abridged version of the LHC
 2756 Design Report (CERN-2004-003).
- 2757 [57] CMS Collaboration. The cms experiment at the cern lhc. *Journal of Instrumentation*, 3(08):
 2758 S08004, 2008. URL <http://stacks.iop.org/1748-0221/3/i=08/a=S08004>.
- 2759 [58] LHCb Collaoration. The LHCb Detector at the LHC. *JINST*, 3:S08005, 2008. doi: 10.1088/
 2760 1748-0221/3/08/S08005.
- 2761 [59] ALICE Collaboration. The alice experiment at the cern lhc. *Journal of Instrumentation*, 3(08):
 2762 S08002, 2008. URL <http://stacks.iop.org/1748-0221/3/i=08/a=S08002>.
- 2763 [60] ATLAS Collaboration. Luminosity Determination in pp Collisions at $\sqrt{s} = 7$ TeV Using the
 2764 ATLAS Detector at the LHC. *Eur. Phys. J.*, C 71:1630, 2011. doi: 10.1140/epjc/s10052-011-1630-5.
- 2765 [61] M Capeans, G Darbo, K Einsweiller, M Elsing, T Flick, M Garcia-Sciveres, C Gemme, H Perneg-
 2766 ger, O Rohne, and R Vuillermet. ATLAS Insertable B-Layer Technical Design Report. Tech-
 2767 nical Report CERN-LHCC-2010-013, ATLAS-TDR-19, CERN, Geneva, Sep 2010. URL
 2768 <https://cds.cern.ch/record/1291633>.
- 2769 [62] Y Giomataris, Ph. Rebourgeard, J.P. Robert, and G. Charpak. Micromegas: a high-granularity
 2770 position-sensitive gaseous detector for high particle-flux environments. *Nuclear Instruments
 2771 and Methods in Physics Research Section A: Accelerators, Spectrometers, Detectors and As-
 2772 sociated Equipment*, 376(1):29 – 35, 1996. ISSN 0168-9002. doi: [http://dx.doi.org/10.1016/0168-9002\(96\)00175-1](http://dx.doi.org/10.1016/0168-9002(96)00175-1). URL <http://www.sciencedirect.com/science/article/pii/0168900296001751>.
- 2775 [63] T Alexopoulos, J. Burnens, R. de Oliveira, G. Glonti, O. Pizzirusso, V. Polychronakos,
 2776 G. Sekhniaidze, G. Tsipolitis, and J. Wotschack. A spark-resistant bulk-micromegas chamber for
 2777 high-rate applications. *Nuclear Instruments and Methods in Physics Research Section A: Acceler-
 2778 ators, Spectrometers, Detectors and Associated Equipment*, 640(1):110 – 118, 2011. ISSN 0168-9002.
 2779 doi: <http://dx.doi.org/10.1016/j.nima.2011.03.025>. URL <http://www.sciencedirect.com/science/article/pii/S0168900211005869>.
- 2781 [64] Improved electron reconstruction in ATLAS using the Gaussian Sum Filter-based model for
 2782 bremsstrahlung. Technical Report ATLAS-CONF-2012-047, CERN, Geneva, May 2012. URL
 2783 <https://cds.cern.ch/record/1449796>.

- 2784 [65] W Lampl, S Laplace, D Lelas, P Loch, H Ma, S Menke, S Rajagopalan, D Rousseau, S Snyder,
 2785 and G Unal. Calorimeter Clustering Algorithms: Description and Performance. Technical
 2786 Report ATL-LARG-PUB-2008-002, ATL-COM-LARG-2008-003, CERN, Geneva, Apr 2008.
 2787 URL <https://cds.cern.ch/record/1099735>.
- 2788 [66] Georges Aad et al. Topological cell clustering in the ATLAS calorimeters and its performance in
 2789 LHC Run 1. 2016.
- 2790 [67] Matteo Cacciari, Gavin P. Salam, and Gregory Soyez. The Anti-k(t) jet clustering algorithm.
 2791 *JHEP*, 04:063, 2008. doi: 10.1088/1126-6708/2008/04/063.
- 2792 [68] Georges Aad et al. Performance of Missing Transverse Momentum Reconstruction in Proton-
 2793 Proton Collisions at 7 TeV with ATLAS. *Eur. Phys. J.*, C72:1844, 2012. doi: 10.1140/epjc/
 2794 s10052-011-1844-6.
- 2795 [69] Aaron James Armbruster. Discovery of a Higgs Boson with the ATLAS detector. 2013. CERN-
 2796 THESIS-2013-047.
- 2797 [70] G. Cowan, K. Cranmer, E. Gross, and O. Vitells. Asymptotic formulae for likelihood-based tests
 2798 of new physics. *Eur. Phys. J.*, C 71:1554, 2011. doi: 10.1140/epjc/s10052-011-1554-0.
- 2799 [71] ATLAS Collaboration. Limits on the production of the Standard Model Higgs Boson in pp
 2800 collisions at $\sqrt{s} = 7$ TeV with the ATLAS detector. *Eur. Phys. J.*, C 71:1728, 2011. doi: 10.1140/
 2801 epjc/s10052-011-1728-9.
- 2802 [72] ATLAS Collaboration. Performance of the ATLAS muon trigger in pp collisions at $\sqrt{s} = 8$
 2803 TeV. *Eur. Phys. J. C*, (arXiv:1408.3179. CERN-PH-EP-2014-154):75. 19 p, Aug 2014. URL <https://cds.cern.ch/record/1749694>.
- 2804
- 2805 [73] ATLAS collaboration. Electron trigger performance in 2012 ATLAS data, 2015. ATLAS-COM-
 2806 DAQ-2015-091.
- 2807 [74] Paolo Nason. A new method for combining NLO QCD with shower Monte Carlo algorithms.
 2808 *JHEP*, 11:040, 2004.
- 2809 [75] B. P. Kersevan and E. Richter-Was. The Monte Carlo event generator AcerMC version 2.0 with
 2810 interfaces to PYTHIA 6.2 and HERWIG 6.5. 2004.
- 2811 [76] Nikolas Kauer and Giampiero Passarino. Inadequacy of zero-width approximation for a light
 2812 Higgs boson signal. 2012.
- 2813 [77] T. Gleisberg, Stefan. Hoeche, F. Krauss, M. Schonherr, S. Schumann, et al. Event generation with
 2814 SHERPA 1.1. *JHEP*, 0902:007, 2009. doi: 10.1088/1126-6708/2009/02/007.

- 2815 [78] Michelangelo L. Mangano et al. ALPGEN, a generator for hard multiparton processes in
 2816 hadronic collisions. *JHEP*, 0307:001, 2003. doi: 10.1088/1126-6708/2003/07/001.
- 2817 [79] Torbjorn Sjostrand, Stephen Mrenna, and Peter Z. Skands. PYTHIA 6.4 Physics and Manual.
 2818 *JHEP*, 0605:026, 2006. doi: 10.1088/1126-6708/2006/05/026.
- 2819 [80] Torbjorn Sjostrand, Stephen Mrenna, and Peter Z. Skands. A Brief Introduction to PYTHIA 8.1.
 2820 *Comput.Phys.Commun.*, 178:852–867, 2008. doi: 10.1016/j.cpc.2008.01.036.
- 2821 [81] G. Corcella et al. HERWIG 6: An event generator for hadron emission reactions with interfering
 2822 gluons (including super-symmetric processes) . *JHEP*, 01:010, 2001. doi: 10.1088/1126-6708/2001/
 2823 01/010.
- 2824 [82] J. M. Butterworth, Jeffrey R. Forshaw, and M. H. Seymour. Multiparton interactions in photo-
 2825 production at HERA. *Z. Phys.*, C 72:637, 1996. doi: 10.1007/s002880050286.
- 2826 [83] Jun Gao, Marco Guzzi, Joey Huston, Hung-Liang Lai, Zhao Li, et al. The CT10 NNLO Global
 2827 Analysis of QCD. *Phys.Rev.*, D89:033009, 2014. doi: 10.1103/PhysRevD.89.033009.
- 2828 [84] P. M. Nadolsky. Implications of CTEQ global analysis for collider observables. *Phys. Rev.*, D 78:
 2829 013004, 2008. doi: 10.1103/PhysRevD.78.013004.
- 2830 [85] A. Sherstnev and R. S. Thorne. Parton distributions for the LHC. *Eur. Phys. J.*, C 55:553, 2009.
 2831 doi: 10.1140/epjc/s10052-008-0610-x.
- 2832 [86] S. Agostinelli et al. GEANT4, a simulation toolkit. *Nucl. Instrum. Meth.*, A 506:250, 2003. doi:
 2833 10.1016/S0168-9002(03)01368-8.
- 2834 [87] I. Stewart and F. Tackmann. Theory uncertainties for Higgs mass and other searches using jet
 2835 bins. *Phys. Rev.*, D 85:034011, 2012. doi: 10.1103/PhysRevD.85.034011.
- 2836 [88] ATLAS Collaboration. Luminosity Determination in pp Collisions at $\sqrt{s} = 7$ TeV Using the
 2837 ATLAS Detector at the LHC. *Eur. Phys. J.*, C 71:1630, 2011. doi: 10.1140/epjc/s10052-011-1630-5.
- 2838 [89] Jet energy scale and its systematic uncertainty in proton-proton collisions at $\sqrt{s} = 7$ tev with
 2839 atlas 2011 data. *ATLAS-CONF-2013-004*, 2013.
- 2840 [90] Calibrating the b -tag efficiency and mistag rate in 35 pb^{-1} of data with the atlas detector.
 2841 *ATLAS-CONF-2011-089*, 2011.
- 2842 [91] ATLAS Collaboration. Measurement of the b -tag Efficiency in a Sample of Jets Containing
 2843 Muons with 5 fb^{-1} of Data from the ATLAS Detector. *ATLAS-CONF-2012-043*, 2012. URL
 2844 <http://cdsweb.cern.ch/record/1435197>.

- 2845 [92] J. Alwall et al. The automated computation of tree-level and next-to-leading order differential
 2846 cross sections, and their matching to parton shower simulations. *JHEP*, 07:079, 2014.
- 2847 [93] Richard D. Ball et al. Parton distributions with LHC data. *Nucl. Phys. B*, 867:244, 2013.
- 2848 [94] ATLAS Collaboration. ATLAS Run 1 Pythia8 tunes. (ATL-PHYS-PUB-2014-021), Nov 2014.
 2849 URL <https://cds.cern.ch/record/1966419>.
- 2850 [95] M. Bahr et al. Herwig++ Physics and Manual. *Eur. Phys. J. C*, 58:639–707, 2008. doi: 10.1140/
 2851 epjc/s10052-008-0798-9.
- 2852 [96] Stefan Gieseke, Christian Rohr, and Andrzej Siódak. Colour reconnections in Herwig++. *Eur.*
 2853 *Phys. J. C*, 72:2225, 2012. doi: 10.1140/epjc/s10052-012-2225-5.
- 2854 [97] Simone Alioli, Paolo Nason, Carlo Oleari, and Emanuele Re. A general framework for imple-
 2855 menting NLO calculations in shower Monte Carlo programs: the POWHEG BOX. *JHEP*, 06:
 2856 043, 2010.
- 2857 [98] Peter Zeiler Skands. Tuning Monte Carlo Generators: The Perugia Tunes. *Phys. Rev. D*, 82:
 2858 074018, 2010. doi: 10.1103/PhysRevD.82.074018.
- 2859 [99] Michal Czakon and Alexander Mitov. Top++: A Program for the Calculation of the Top-Pair
 2860 Cross-Section at Hadron Colliders. 2011.
- 2861 [100] D. Krohn, J. Thaler, and L.-T. Wang. Jet Trimming. *JHEP*, 02:084, 2010. doi: 10.1007/
 2862 JHEP02(2010)084.
- 2863 [101] ATLAS Collaboration. Identification of Boosted, Hadronically Decaying W Bosons and Com-
 2864 parisons with ATLAS Data Taken at $\sqrt{s} = 8$ TeV. 2015.
- 2865 [102] Expected Performance of Boosted Higgs ($\rightarrow b\bar{b}$) Boson Identification with the ATLAS Detector
 2866 at $\sqrt{s} = 13$ TeV. Technical Report ATL-PHYS-PUB-2015-035, CERN, Geneva, Aug 2015. URL
 2867 <https://cds.cern.ch/record/2042155>.
- 2868 [103] Matteo Cacciari and Gavin P. Salam. Pileup subtraction using jet areas. *Phys. Lett. B*, 659:119,
 2869 2008. doi: 10.1016/j.physletb.2007.09.077.
- 2870 [104] ATLAS Collaboration. Identification of boosted, hadronically-decaying W and Z bosons in
 2871 $\sqrt{s} = 13$ TeV Monte Carlo Simulations for ATLAS. (ATL-PHYS-PUB-2015-033), Aug 2015.
 2872 URL <https://cds.cern.ch/record/2041461>.
- 2873 [105] ATLAS Collaboration. Calibration of b -tagging using dileptonic top pair events in a combina-
 2874 torial likelihood approach with the ATLAS experiment. (ATLAS-CONF-2014-004), 2014. URL
 2875 <http://cds.cern.ch/record/1664335>.

- 2876 [106] ATLAS Collaboration. Performance of b -Jet Identification in the ATLAS Experiment. 2015.
- 2877 [107] Alexander L. Read. Presentation of search results: The CL(s) technique. *J. Phys. G*, 28:2693,
2878 2002. doi: 10.1088/0954-3899/28/10/313.
- 2879 [108] Glen Cowan, Eilam Gross. Discovery significance with statistical uncertainty in the background
2880 estimate. 2008. URL <http://www.pp.rhul.ac.uk/~cowan/stat/notes/SigCalcNote.pdf>.
- 2881



THIS THESIS WAS TYPESET using L^AT_EX, originally developed by Leslie Lamport and based on Donald Knuth's T_EX.

The body text is set in 11 point Egenolff-Berner Garamond, a revival of Claude Garamont's humanist typeface. The above illustration, *Science Experiment 02*, was created by Ben Schlitter and released under CC BY-NC-ND 3.0. A template that can be used to format a PhD dissertation with this look & feel has been released under the permissive AGPL license, and can be found online at github.com/asm-products/Dissertate or from its lead author, Jordan Suchow, at suchow@post.harvard.edu.